January 2016

QUANTITATIVE MODELING OF SCALING OF PATTERNS AND RECEPTOR SIGNALING IN MORPHOGENESIS

Md Shahriar Karim
Purdue University

Graduate School Form
30 Updated 12/26/2015

PURDUE UNIVERSITY
GRADUATE SCHOOL
Thesis/Dissertation Acceptance

This is to certify that the thesis/dissertation prepared

By Md. Shahriar Karim

Entitled

QUANTITATIVE MODELING OF SCALING OF PATTERNS AND RECEPTOR SIGNALING IN MORPHOGENESIS

For the degree of Doctor of Philosophy

Is approved by the final examining committee:

David M. Umulis
Chair

Doraiswami Ramkrishna

Gregery T. Buzzard

Kevin V. Solomon

To the best of my knowledge and as understood by the student in the Thesis/Dissertation Agreement, Publication Delay, and Certification Disclaimer (Graduate School Form 32), this thesis/dissertation adheres to the provisions of Purdue University's "Policy of Integrity in Research" and the use of copyright material.

Approved by Major Professor(s): David M. Umulis

Approved by: Bernard A. Engel 12/9/2016

Head of the Departmental Graduate Program Date

QUANTITATIVE MODELING OF SCALING OF PATTERNS AND RECEPTOR SIGNALING IN MORPHOGENESIS

A Dissertation

Submitted to the Faculty

of

Purdue University

by

Md. Shahriar Karim

In Partial Fulfillment of the

Requirements for the Degree

of

Doctor of Philosophy

December 2016

Purdue University

West Lafayette, Indiana

To my mother Sufia Begum,

To my father Md. Abdul Hamid,

To my wife Antara Chowdhury, and

To my family and relatives.

ACKNOWLEDGMENTS

First and foremost, I thank to almighty Allah for granting me the opportunity and strength to pursue my doctoral study, and for all the kindness that He bestowed upon me.

I would like to express my sincere gratitude to my advisor and committee chair Professor David M. Umulis for the consistent support, guidance, and encouragement that he provided since I joined his research lab. He has been a source of motivation, and has always been helpful to me throughout all the difficult times during my graduate life at Purdue University.

I am also grateful to all my committee members: Professor Gregery T. Buzzard from the Dept. of Mathematics, Professor Doraiswami Ramakrishna from the Dept. of Chemical Engineering, and Professor Kevin Solomon from the Dept. of Ag. and Biological Engineering at Purdue University for their comments and suggestions in finishing my research and writing this dissertation. This dissertation would not have been possible without their helpful comments, constructive criticisms, and suggestions. I also express my gratitude to Professor Ann E. Rundell, who passed away months before this dissertation was completed (May she rest in peace). She helped me immensely with her inquisitive comments and constructive criticisms during our regular research group meetings. I would like to give thanks to Professr Hans G. Othmer from the University of Minnesota for his time in my research. I also express my sincere thanks to Professor Mary C. Mullins of the University of Pennsylvania for all her comments and suggestions in helping me finish my research.

I would like to thank Dr. James A. Dutko for our collaboration during the research. I am grateful to him for all his comments, and numerous skype sessions we used to discuss our research problem. I am very appreciative to my fellow lab-mates for their cooperation, comments on my research, and more importantly, for the time they

spent engaging me in discussions related to this dissertation. I would like to extend my sincere thanks to all my friends and colleagues who are in USA and in my home country, Bangladesh. I also want to say thanks to the ABE graduate office staff, who have always been so cordial and cooperative with me. I am also grateful for the excellent environment for study and research that Purdue University provided to me over the years.

Finally, I would like to acknowledge my parents for all of their support through my good and bad times, and never faltered in extending their encouragement for any of my dreams. Specially, I want to say thanks to my mother, for she always kept confidence in all my endeavors. Without her support, I would not be able to pursue dreams this far in life. I also say thanks to my brothers and relatives, (specially, my aunt Rina Azad) who have always been the source of immense inspiration in my life. I would like to say thanks to my in-laws for their well wishes and love. I am grateful to my teachers from my elementary schools who helped me developing morals and values at the beginning of my academic life. Last but not the least, I would like to express my sincere thanks to my wife Antara Chowdhury for all the love, support and cooperation she extended throughout the course of finishing this dissertation. Also, a very special thanks to her, for she happily tolerated all my unusual work habits as a graduate student.

TABLE OF CONTENTS

Page

Page

Page

LIST OF TABLES

LIST OF FIGURES

Figure Page

Figure Page

Figure Page

Figure Page

Figure Page

Figure Page

Figure Page

Figure Page

Figure Page

SYMBOLS

m	Morphogen
M	Modulator
α	Signaling strength
S	Stiffness ratio
γ	Surface enhancement factor
T_{ss}	Steady state time
ξ	dimensionless spatial variable
D_{m0}	Intrinsic diffusion coefficient of morphogens
D_{M0}	Intrinsic diffusion coefficient of modulators
$k_{\delta m}$	Intrinsic decay coefficient of morphogens
$k_{\delta m}$	Intrinsic decay coefficient of modulators
S	Receptor recruited during secondary receptor recruitment
R_3	Alk 3/6 receptor
R_8	Alk 2/8 receptor
R_{II}	Type II receptor
L	System length
K_D	Dissociation constant
DL	Decay length
ν	Regulatory parameters
l_i	System size variable
ψ	Decay length of morphogen

ABBREVIATIONS

BMP	Bone Morphogenetic Protein
ADMP	Antidorsalizing morphogenetic protein
TCS	Two Component System
SIV	Scale-invariance
RBST	Robustness
SS	Steady state
BDF	Backward Differentiation Formulas
FDM	Finite Difference Method
PDE	Partial Differential Equation
ODE	Ordinary Differential Equation
EC	Expanded Chain-rule (non-divergence form of PDE)
DIV	Divergence form of PDE

NOMENCLATURE

B2	BMP2 homodimer
B7	BMP7 homodimer
B27	BMP2/7 heterodimer
Alk3/6	Type I BMP receptor
Alk2/8	Type I BMP receptor
BR	BMP:Receptor complex
BRS	Tertiary complex
Acvr1	Type of Alk 3/6 receptor
BmpR1	Type of Alk 2/8 receptor

ABSTRACT

Karim, Md. Shahriar Ph.D., Purdue University, December 2016. Quantitative Modeling of Scaling of Patterns and receptor signaling in morphogenesis. Major Professor: David M. Umulis.

Organs and tissue development often experience perturbations, but developmental processes seem to replicate a common body template to maintain appropriate proportions and positions. The key signaling factors that guide a number of those processes are known as morphogens. Developing cells sense their respective positional information from a graded morphogen profile, and differentiate into patterns. Remarkably, patterns are highly robust and reproducible among species, and the underlying mechanisms associated with such high degrees of precision are still enigmatic. In addition, details of the signal, such as the Bone Morphogenetic Protein (BMP) signal, that transmit patterning information to a group of homogenous cells to differentiate is not well understood. Determining how developmental processes ensure robust patterning in the presence of perturbations maintain structural precision by scaling, and what regulatory mechanisms act to ensure robust and reproducible patterning are two longstanding questions that need unraveling. Moreover, determining the mechanisms by which BMP homodimers dominate signaling in developing zebrafish embryos and other contexts is a key factor in understanding developmental regulation for a classic morphogen patterning.

To answer these questions, this work has developed a set of mathematical models to evaluate and interrogate potential signaling networks and regulatory motifs. These models identify scaling mechanisms, test hypotheses on heterodimer dominance during signal transduction, and show how patterning systems function. For the scaling problem, this research proposes a Two Component System (TCS) mech-

anism, where a morphogen (m) and a modulator (M) interact reciprocally to alter the transport and reaction properties of each other spatially. An exhaustive parametric and network motif screen is conducted for several TCS variants under the reaction-diffusion-advection paradigm with spatially varying coefficients. Our analysis revealed a number of candidate networks and minimal regulatory motifs that achieve the precision needed for a developing species to ensure perfect development. Computational models of patterning signals, namely the Bone Morphogenetic Protein (BMP) mediated signal, were developed to analyze the receptor oligomerization that forms heterotetrameric receptor associations in BMP signaling. The oligomerization model disproves previous kinetic based hypotheses of heterodimer dominance, and identify other theoretical conditions to acquire it. Finally, the model predicts that heterodimer dominance provides a larger dynamic range and a higher concentration of morphogen activity, making it a robust sensor responding wide ranges of morphogen concentrations fundamental to a morphogen gradient system. Moreover, stochastic analysis of oligomerization steps reveal that recruitment of type II receptors during the receptor oligomerization by itself does not tend to lower noise in receptor signaling, an outcome that can be applied later in developing a complete probabilistic model of receptor oligomerization events.

The computational arrangements and frameworks developed in this research have wider applications– for instance, illustration of a large-scale screen of a reaction-diffusion-advection systems with spatially varying coefficients is a novel strategy to perform a large-scale screen of such system and could have wider applications in other areas. Additionally, our mathematical framework on the dynamics of a tetrameric complex formation and oligomerization steps could be applicable to other signaling pathways that require trimeric/tetrameric complex formation on the cell surface to elicit signaling.

1. INTRODUCTION

From cells to species to populations, patterns happen at all stages of biological existence. The exact details of patterning mechanisms in various systems may differ; however, they often follow a common structure to generate patterns. This structure includes i) a signal that conveys patterning information, ii) mechanisms and extracellular machinery to detect and to transmit this signal downstream, and finally, iii) a downstream signaling network that interprets information transmitted by the signal. Although there are numerous biological signals and pathways actively involved in species development, this body of work primarily focuses on morphogen [1–7] mediated signaling and pattern formation, and considers mechanistic models to identify mechanisms that aid in scaling and discovering the exact details of the underlying signaling complex that transmit patterning information.

To ensure perfect and precise species development, signaling must happen at the right time and right place during the early stages of development. Despite the presence of perturbations, developmental processes are highly robust and reproducible, and demonstrate shape and size adaptation in order to maintain proportionate development of every species' constitutive organs and tissues [8–12]. For instance, embryo size and shape frequently vary substantially both within and between species, but the adult develops with a perfectly proportioned and positioned organs and tissues [12,13]. The property by which species resolves such perturbations during development is known as scaling [9]. Failure to achieve scaling, and signaling precision during development, may lead to numerous lethal consequences, such as birth defects and developmental disorders [14, 15]. As an example, digit formation in vertebrates may be defective if the underlying morphogen signals, Fibroblast Growth Factor (FGF) and Sonic hedgehog (Shh), are not tightly controlled [16–18] in the presence of system size variation and environmental perturbations. Also, branching morphogenesis

within species requires remarkable precision and reproducibility, and morphogens play an important role in branching networks, such as in lung development [18–20] and limb formation in mammals [19, 21].

While transmitting patterning information to an underlying field of cells, morphogens interact with a large number of extracellular factors [6, 7, 22] that refine signal distributions and regulate the phenotypic response of the system. Despite the availability of molecular data on numerous developmental processes, very little is known about the underlying mechanisms needed to achieve the required precision during species development. Therefore, longstanding questions- how developmental processes within species maintain such precision and finding out which regulatory mechanisms act individually, or in concert, to obtain scaling of patterns at different stages of development - continues to be of great interest to the scientific community. Specifically, in this research, we are primarily interested in the patterns that take place during the early stages of embryonic development, and the patterning signal that is mediated by the Bone Morphogenetic Proteins (BMPs). BMPs act as morphogens that pattern the dorsal-ventral (D/V) axis during the embryonic development both in vertebrates and invertebrates.

Biochemical and cell-based signaling data suggests that BMP signaling is likely to be regulated by low concentration (nano and sub-nanomolar) BMP activity. For example, Decapentaplegic (Dpp) signaling in Drosophila S2 cell line begins to saturate signaling at low concentration ranges between 0.1 nM to 1 nM [23]. In addition, not only the binding between BMP and its family of receptors are tight, BMP-receptor interactions are comparatively slow in many species [24, 25]. The combined effects of tight binding, low concentration, and slow kinetics create a long-duration stochastic deviation from the mean level of BMP signaling [26]. However, BMP-mediated processes appear to be carefully controlled and resilient *in vivo*, suggesting that the pathway evolved to either tolerate or mitigate stochastic fluctuations associated with receptor-ligand bindings. The impact of noise in BMP-mediated signaling has often been overlooked elsewhere [22, 27, 28], and it is unclear if noise is mitigated through

receptor oligomerization steps. Thus, to identify mechanisms of noise suppression in BMP signaling, we need further investigation on receptor recruitment events, and one of the interesting questions would be to see if recruitment of type II receptors during receptor oligomerization by itself tends to lower noise in receptor signaling.

Moreover, in multiple contexts, it has been seen that BMP heterodimers demonstrate stronger signaling activity than BMP homodimers [6, 29–34]. Why the BMP heterodimers signal more strongly than BMP homodimers or as the sole signaling ligand in BMP signaling, it is still unknown, and further attention is needed to unravel what drives the heterodimer dominant mechanism. Further complicating the matter, the structure of obligate dimer-bound Type I receptor (Alk 2/8) is not determined yet, and thus, the affinity of a heterodimer and Alk2/8 binding can not be confirmed [6]. Therefore, based on the existing data and our current understanding of dimer-receptor interactions, no obvious conclusion can be drawn on the potential reasons of heterodimer dominance in BMP signaling, and to circumvent the lack of molecular data, we develop computational models of dimer-receptor interactions to identify mechanisms of heterodimer dominance in BMP signaling.

Computational models have been extensively used to analyze BMP signaling and the roles of BMP-regulators on BMP dynamics for decades [2,7,22,27,29,35–37]. Models on BMP signaling are primarily used to test the mechanisms behind BMP signal regulation and to identify testable hypotheses that can explain robustness, scaling, and the dynamics of BMP signaling. Our current explanations of the mechanisms of heterodimer dominance are insufficient, and the question lacks experimental evidence and adequate molecular data. To investigate the mechanisms of heterodimer dominance in BMP signaling, in this research, we rely on computational models and develop dimer-receptor interaction networks to understand all the receptor oligomerization steps. Later, we used the models to identify mechanisms that favor heterodimer dominance in BMP signaling. We also actively collaborated with the laboratory of Dr. Mary Mullins at the University of Pennsylvania to experimentally validate our proposed hypotheses.

In general, this research adopted both deterministic and stochastic approaches to develop physiologically relevant computational models, and used the models to analyze patterning systems related to embryonic development. The models were are used to test and verified different hypotheses, to propose new hypotheses on the heterodimer dominance in BMP signaling. A reaction-diffusion (RD) paradigm was used to develop computational models for scaling problem, and later the model was used to identify the mechanisms of signaling precision in the presence of perturbations. Computational models developed in this work to analyze various biological systems have wider applications, and could be used beyond the scope of the biological systems considered in this research.

1.1 Morphogens in pattern formation

Morphogens are a group of molecules that are secreted from a localized source, and upon secretion they undergo long range transport away from the source, creating a concentration gradient between a source and a sink [1–5] region. An extracellular gradient of morphogen provides positional information to a field of cells and differentiates them into distinct cell patterns. Cells in the field sense their respective positional information by responding to a predefined threshold of morphogen concentration [1, 5, 38] and assume cell fates in a concentration specific manner (a schematic diagram on how morphogen signaling works in context of development is demonstrated in Fig.1.1).

More than half a century ago, in 1952, Alan Turing [4] introduced the concept of morphogens, proposing that a chemical substance can generate patterns required during morphogenesis through a reaction-diffusion mechanism. Specifically, Turing proposed that if two chemical species, termed as activator and long-range inhibitor, interacting with each other and diffuse in a system with dissimilar diffusion coefficients, repetitive patterns as observed in many species in nature are generated. Later, Lewis Wolpert used the classical French Flag Model [39] to explain the concept of

morphogen and its role in conveying cell position information during species development (demonstrated schematically in Fig. 1.1). The way a morphogen functions is shown in Fig.1.1 upon secretion from a localized source, the morphogen forms a sharp gradient over a region. Subsequently, when a homogenous field of cells is exposed to the already formed morphogen gradient, cells interpret the graded profile of morphogen to differentiate into patterns in a concentration specific (demonstrated here in Fig. 1.1 arbitrary thresholds p, q) manner. That is, a local concentration of morphogens transmit positional information and induce cells to attain specific cell fates when a cell reads out the morphogen gradient using its extracellular machinery.

In the classical morphogen patterning view [39–41], cells respond to an extracellular morphogen gradient and interpret their respective positional cues to differentiate into distinct cell types based on the signals they receive [4,5]. For instance, Bone Morphogenetic Proteins (BMPs) act as a morphogen to regulate the pattern formation of the dorsal-ventral axis of both vertebrate and invertebrate development [6, 29, 42]. When exposed to a gradient of morphogen such as BMPs, cells sense the extracellular level of morphogen through a family of transmembrane receptors and activate pathways downstream of morphogen activity. This signaling, mediated by morphogens, translates extracellular positional information to an organismal phenotype through dose dependent gene expressions [42], and is commonly seen throughout the animal kingdom.

A large number of molecules have already been identified as morphogens. For instance, Decapentaplegic(Dpp) in Drosophila wing imaginal disc development [43], Bicoid activity in A/P axis patterning of Drosophila [44], Activin in Xenopus embryo [45, 46], Retinoic Acid [47, 48] and Sonic hedgehog (Shh) in limb development in vertebrates, Wingless (Wnt) in wing imaginal disc, etc. [49, 50] act as morphogens during development. Thus, studying morphogen signaling and morphogen mediated patterning is crucial as it directly affects numerous lethal diseases. In fact, aberrant morphogen signaling can often lead to developmental disorders [14]. However, the primary focus in this work is on the Bone Morphogenetic Proteins (BMPs) that

direct dorsal-ventral pattern formation both in vertebrates and invertebrates during development.

Bone Morphogenetic Proteins (BMPs) act as morphogens both in vertebrates and invertebrates, and actively participate in dorsal-ventral (D/V) patterning during the early stages of embryonic development. BMP-mediated patterning of cells generally follows a common set of regulatory steps during development: i) secretion of BMPs from a localized source, ii) creation of a spatially non-uniform distribution away from a BMP source by diffusion, and iii) biochemical interactions with receptors and other extracellular factors [2, 13, 27, 51–54] to transmit the extracellular information downstream. The family of receptors for BMPs is structurally similar [55], but they exhibit varied affinities for different versions of BMP ligands [55].

1.2 Morphogen dispersal mechanisms in pattern formation

How morphogens generate a concentration gradient upon secretion from a localized source is still debatable and is not fully understood [56, 57]. Several approaches to explain mechanisms of morphogen dispersals have been proposed, i.e., the transport of morphogens happens because of diffusion, or a cell-based transportation of morphogens forms the required concentration gradient. In diffusion-based models [3, 4, 35, 39], extracellular movement of morphogens occurs because of diffusive transport. On the basis of the presence of hindrance to diffusive transports, diffusion based models are subdivided into a number of categories [56, 58] - such as, free diffusion (diffusion-decay) models, hindered diffusion (reaction-diffusion), facilitated diffusion, etc. In reaction-diffusion models [1, 3, 39, 40], morphogens transiently bind with other extracellular particles while transporting away by diffusion, or face hindrances because of the tortuous paths that they traverse. The binding molecules for morphogens could be membrane receptors, or other molecules that can regulate morphogen signaling extracellularly, and a few examples of those regulators would be HSPG, Dally, Dally-like, SBPs (reviewed in [7, 59]). Also, in hindered diffusion,

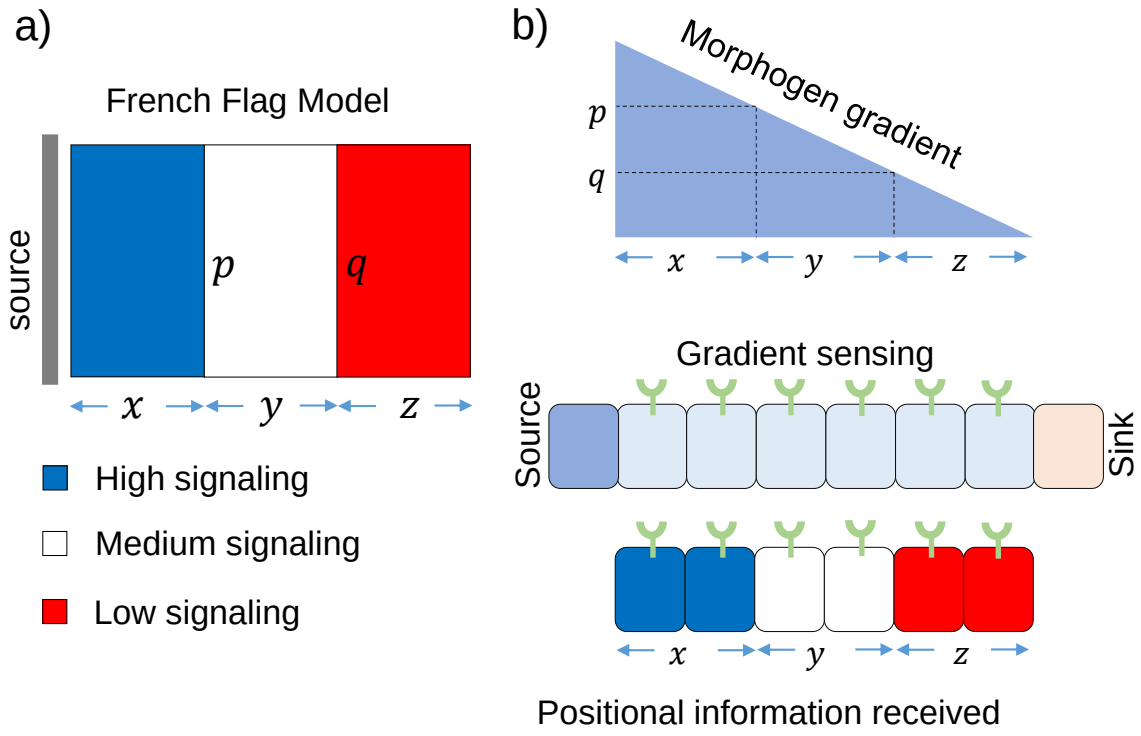

Fig. 1.1. French Flag Model and morphogen mediated pattern formation: a) In the French Flag Model, regions colored in blue, white and red along the horizontal axis with equal width can be made analogous to a homogeneous field of cells. A signaling gradient, such as the morphogen gradient, is interpreted by a field of homogeneous cells in order to acquire each cell's positional value. Depending on the intensity of signal (as demonstrated by threshold p, q) different sets of genes turn on, and the different colors in French Flag Model resembles the manifestation of a threshold-based gene expression. b) Morphogens are secreted from a source and then undergoes a long range transport away from the source, creating a sharp concentration gradient between the source and sink. This concentration gradient of morphogen provides the positional information to each of the receiving cells and the positional information is interpreted by responding to predefined threshold conditions of morphogen concentration. For example, cells exposed to more than a threshold p would become blue, whereas cells that are exposed to morphogen concentration between thresholds p and q would be white. Such a threshold-based readout of morphogen signaling by a homogenous field of cells to differentiate into patterns is analogous to the colored patterns of a French flag model as demonstrated in part a.

the diffusivity of morphogens doesnt remain constant, since morphogens bind with receptors they leave less numbers of free morphogens to diffuse at any given time, whereas in models that consider free diffusion, the diffusivity of morphogens remain unchanged over the course of time.

In cell-based mechanisms of morphogen dispersal, morphogens bind to the cell surface, and are endocytosed inside the cell. Subsequently, morphogens residing inside the cell are released again to the cell surface by exocytosis. Gradient formation by a series of endocytosis and exocytosis is known as the transcytosis model of morphogen dispersal [60,61]. In transcytosis, the diffusivity of morphogens is treated as negligible, and gradient formation solely depends on the rounds of uptake and the release of morphogens only. There are other mechanisms proposed to explain the formation of morphogen gradients that include cytoneme-mediated gradient formation, bucket brigade models [62]. For example, in cytoneme based models, structures similar to filopodia emanate from cells and create a contact to the source of morphogens in order to mediate the transport of morphogens.

However, quantitative analysis of morphogen data posits diffusion-based morphogen dispersal as a more viable transport model for gradient formation [3, 35]. Interestingly, new experimental evidence further corroborates the plausibility of a diffusion-based explanation of gradient formation. For example, gradient formation in morphogens such as Nodal/Lefty, Fibroblast Growth Factor (FGF), and Decapentaplegic (Dpp) are largely formed by diffusion-based transport. Because of its wide applicability, this research primarily focuses on diffusion-based morphogen dispersal to analyze the scaling of patterns, and used a similar concept to explain the surface dynamics of BMP dimers in the oligomerization process.

1.3 BMP signaling and the dorsal-ventral pattern formation

Bone Morphogenetic Protein (BMP), a TGF- super family ligand, is a secreted group of molecules that directs a numerous developmental processes, including cell

fate determination, and cell differentiation [7]. BMPs are secreted as dimers (homodimers or het- erodimers), where each dimer is comprised of two covalently-linked BMP monomers [63]. For instance, in Drosophila two copies of the BMP monomers Gbb and Scw form a heterodimer, which patterns the wing imaginal disc [29], whereas in wing vein formation, Dpp and Gbb form heterodimers [64, 65]. In zebrafish development, BMP2 and BMP7 monomers form a covalently-linked BMP2/7 heterodimer that exclusively initiates signaling and specifies distinct cells fates [6, 66].

A BMP dimer forms a complex with a heterotetrameric receptor association of two non-redundant type I receptor kinases and two type II receptor kinases [6]. Upon binding to a/the BMP ligand, type II receptors phosphorylate and thereby activate type I receptors. Once the type I receptor kinase is activated, it activates the recruited Smads within the intracellular domain. Subsequently, two copies of receptor-activated Smads (R-Smad) together with a common-mediator Smad (CoSmad) translocate to the nucleus through neucleo-cytoplasmic shuttling [67]. Inside the nucleus, the trimeric complexes participate in the nucleoprotein complexes along with other factors and execute the BMP-induced activation of different target genes [7].

Drosophila homologues of BMP ligands include Decapentaplegic (Dpp), Screw(Scw) and Glass Bottom Boat (Gbb). Thickveins (Tkv) and Saxophone (Sax) work as the two type I receptors and Punt is a type II receptor through which Dpp can transmit the signaling. More specifically, Dpp and Scw pattern the dorsal region and create the amnioserosa and dorsal ectoderm [43,68] in Drosophila development. Experimental evidence reveals that Dpp mutant embryos become ventralized as development progresses, and, for a Scw mutant, the embryo becomes partially ventralized. For instance, from null mutation experiment it is further seen that absence of Dpp causes ventral fate of the ectoderm [69]. In Drosophila, though, Dpp is initially produced uniformly, its activity becomes concentrated primarily in the dorsal region as time proceeds (less than an hour). Such a sharp gradient of Dpp compared to the initial uniform density illustrates that the gradient is not formed through simple and normal diffusion. Rather, the sharp gradient is the result of Dpp's interaction with other

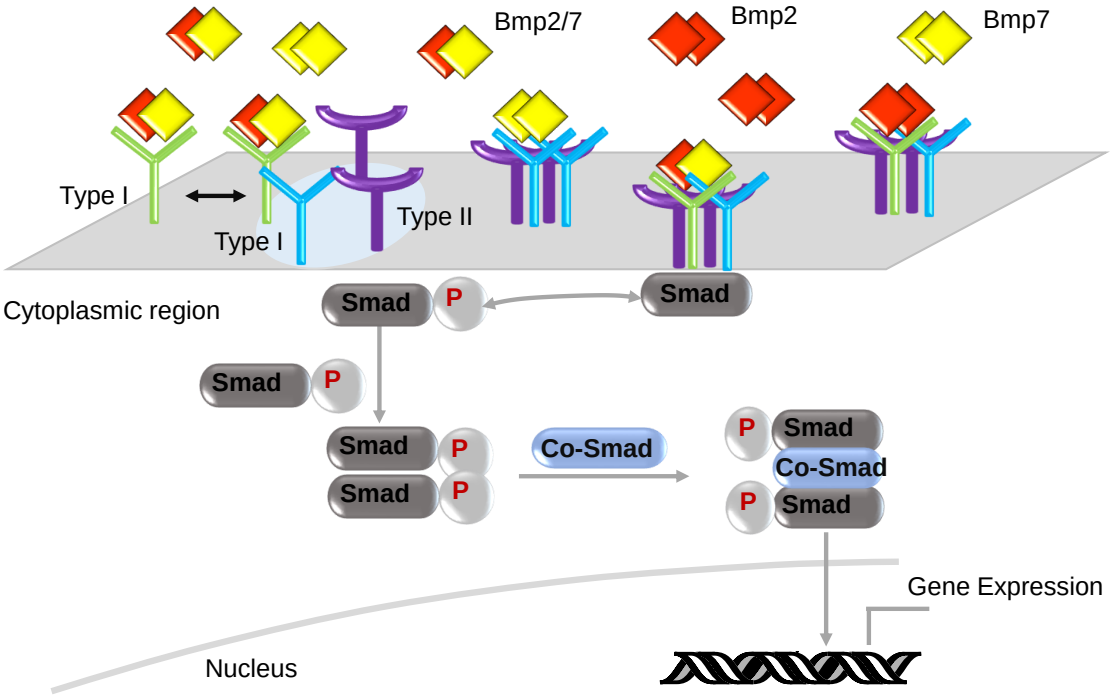

Fig. 1.2. BMP signaling pathway: BMP initially interacts with Type I receptors and forms a dimer-receptor complex. The initial dimer-receptor complex subsequently recruits additional receptors on the cellular surface resulting in a tetrameric receptor association, the process is known as the receptor oligomerization. BMP dimer signals through the heterotetrameric receptor complex consisting of two type I (*Alk3/6, Alk2/8*) and two type II receptors. The tetrameric complex subsequently activates the intracellular phosphorylation of Smad. Phosphorylated Smad (pSmad) forms a trimeric complex with coSmad and translocate into the nucleus through nucleo-cytoplasmic shuttling to initiate dose-dependent gene expression.

factors that regulate reactions through receptors [7]. For instance, a BMP signal that patterns the dorsal ectoderm into different functional tissues transforms from providing ubiquitous levels of signaling to a highly concentrated active domain of signaling due to the regulatory role of secreted factors. Some of these factors may include Short gastrulation (Sog) [70], Tolloid, and Twisted gastrulation (Tsg) [71].

BMP signaling also patterns the D/V axis in vertebrates during the early stages of embryonic development. For instance, BMP patterns the D/V axis in zebrafish [6]. Unlike Drosophila, a BMP signal in zebrafish patterns the ventral region, and it is low in the dorsal region [6]. This is evident from the mutant experiments, where mutations in BMP signaling resulted in dorsalized phenotypes [72]. In xenopus, similar to zebrafish, BMP signaling patterns the ventral fates. Experimentally, it has been shown that the occurrence of dorsal fate in zebrafish and xenopus requires a repression of BMP signaling [72–75]. The role of a BMP graded profile in D/V patterning both in zebrafish and xenopus has been further validated through the gain-of-function experiments (in xenopus), and the lateral cell fate specification of neural crests in zebrafish mutants [76, 77].

BMPs generally function as covalently-linked homodimers or heterodimers. The dimers arise intracellularly when two copies of a similar type BMP monomer are covalently linked, homodimers form, whereas the heterodimers of BMPs form by covalently-linking a pair of monomers of different BMP types. There are two homodimers, and one heterodimer is found in BMP signaling namely, BMP2 homodimers ($B2$), BMP7 homodimers ($B7$) and BMP2/7 heterodimers ($B27$). Among all the dimers, BMP heterodimers are widely observed as the signaling ligands. In Drosophila, Decapentaplegic(Dpp)-Screw (Scw) and Dpp-Gbb heterodimers actively participate in dorsal-ventral patterning, wing disc patterning, and in the wing vein formation. In zebrafish, dorsal-ventral patterning is exclusively mediated by BMP heterodimer BMP2/7, and is verified by the loss of signaling in the BMP2b or BMP7 mutant embryos.

Two distinct type I BMP receptors (Alk 3/6, Alk 2/8 respectively) are required non-redundantly in a complex with two type II receptors in order to initiate BMP signaling during dorsal-ventral patterning both in zebrafish and Drosophila. This has been verified in zebrafish using co-immunoprecipitation experiments. In BMP signaling, the affinity between BMP heterodimers and Alk2/8 has not been confirmed, since the structure of ligand-bound Alk2/8 has not yet been determined [11]. Therefore, based on existing data and our current understanding of dimer-receptor interactions, no obvious conclusion can be drawn on the potential reasons for heterodimer-bound heteromeric receptor complex dominated signaling, and further studies to identify the details of BMP signaling mechanisms and new insights are necessary.

Previous studies show [55, 78] that BMP2 homodimers exhibit higher affinity for type I receptors, as does BMP7 homodimers with Type II receptors [79–81]. Upon binding to $Alk3/6$, $B2$ dimer then recruits type II receptors [55, 78]. The BMP7 homodimer ($B7$) possesses different binding affinities: it exhibits higher affinity for type II receptors and recruits type I with a lower affinity than what a BMP2 homodimer does. It is found that B7 binds a type I $Alk2/8$ receptor with a very low affinity binding [55,80,82], whereas BMP2 homodimer does not have any demonstrable affinity for $Alk2/8$. However, as we do not know the structure of a BMP2/7 heterodimer-bound Alk2/8 yet, the affinity of B27 and Alk2/8 can not be measured precisely. Therefore, how the stipulated signaling complex, that is, the heterodimer-bound quadripartite heteromeric receptor association of two distinct type I receptors (Alk3/6 and Alk2/8) and two type II receptors, is favored cannot be explained with the existing level of molecular data and knowledge [6].

1.4 Scaling of patterns in species

Scaling is the property by which a patterning system retains its proportionate structure and positioning despite the presence of numerous perturbations. Patterning processes may depend differently on system size, hence the underlying mechanisms

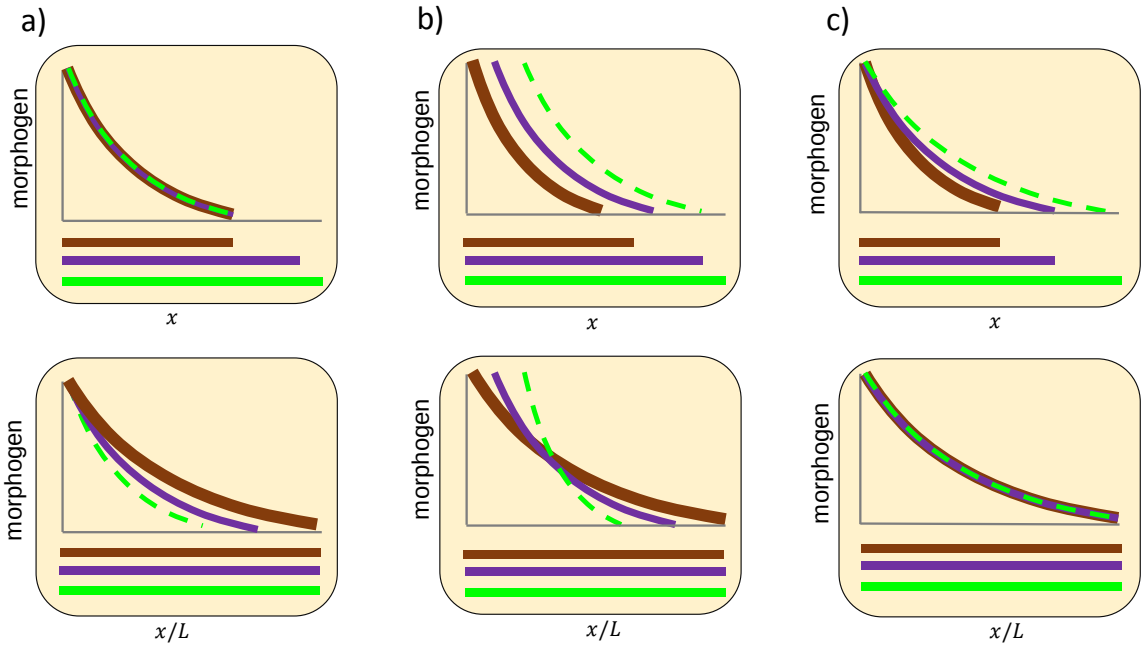

Fig. 1.3. Different types of scale-invariance of morphogen signaling: the upper and lower panels represent absolute and normalized morphogen signaling respectively. **a)** No scaling: the normalized morphogen distributions don't overlap at any position. **b)** Partial scaling: when morphogen distribution is normalized against the corresponding system size, there are overlaps among the normalized distribution. **c)** Morphogen distributions for different system sizes overlap perfectly when normalized against their respective system length.

that help achieve scaling in different patterning systems may vary widely. For instance, when the scaling of pattern formation in species is independent of system size and depends on an intrinsic scale of underlying mechanisms, repetitive skin patterns in fish and animals emerge [83–85], which may extend as the system size increases. Scaling mechanisms seen in these species can be related to Turing mechanisms, initially proposed by Alan Turing in 1952 [4].

Contrary to this, pattern formation in many organisms and tissues often depends on system size. Patterns scale with a change in system length, and appear as scaled versions of a common template. This means that developmental processes can adjust the intrinsic scale of patterns to a variation in system size, a phenomenon defined as scale-invariance. Scale- invariance is observed in morphogen signaling to repetitive patterns that appear frequently in certain fish and animals. For instance, distribution of bicoid in A/P axis patterning scales for different embryo size in Drosophila [44], and skin patterns demonstrate scale-invariance among various fishes [83] (also, reviewed in [9]). Not all systems achieve perfect scaling, and hence, the notion of partial scaling is used to differentiate the degree of scaling achieved by a system. This can be explained schematically as shown in Fig.1.3, where we consider an exponentially distributed morphogen signaling to explain three different scenarios of scaling.

As seen in Fig.1.3, if the system-size change is not compensated during development, the absolute scale of morphogen signaling distribution does not scale and is clearly evident when normalized against its respective system length (Fig.1.3a). If more morphogen is added to the system, the developing system may achieve some scaling, which is subject to partial scaling as shown in Fig.1.3b. Precisely, some positions of the system dont scale perfectly [44,86]. Finally, when a developing system can target the biophysical properties of morphogen signaling, such as the transport rate, the decay rate and the production rate of morphogen and morphogen distribution can achieve perfect scaling as seen from the superimposed normalized distribution. Moreover, patterning formation by morphogens is a dynamic process as observed in

numerous systems [27, 60, 87], hence the scale invariance of morphogen patterning is needed in both a dynamic and steady state [88] for perfect species development.

In vivo evidence of scaling in species development was observed initially in the classical experiment conducted by Hans Spemann as early as 1903 [89]. In an experiment done on amphibian embryos, Spemann found that when bisected into dorsal and ventral halves, the dorsal half of the embryo developed normally, and grew in proportion during subsequent developmental processes giving rise to a smaller, yet healthy tadpole. This indicated the intrinsic ability of developmental process to withstand extreme forms of perturbations, since the dorsal half of the embryo was able to adjust its developmental cues and signals for regular development. Later on, it was shown in Drosophila that, if the embryo is treated under nutrient-deficient conditions, the developmental process can mitigate the perturbations resulting in an appropriately scaled version of a healthy adult [56, 90]. That is, while the mechanisms that achieve scaling can largely vary among species, and are unknown, in order to achieve scaling information related to perturbations must be accommodated in the underlying biophysical mechanisms of signal generation and transduction so that developmental processes can compensate for the intrinsic scale of the active signaling domain. Thus, the ability of a species to scale has been a fact during development, but much of the mechanisms that facilitate such scaling are unknown, and have yet to be determined.

1.5 Biological systems that demonstrate scaling of patterns

According to experimental data, fruit flies have developed proportionately scaled wing and eye pigmentation in starving conditions [90]. Although lack of nutrients affects embryo size, developmental processes can adjust size difference effectively. More specific evidence of scaling in Drosophila can be seen during the formation of wing veins, where Decapentaplegic (Dpp) acts as a morphogen and directs pattern formation in the longitudinal veins along the A-P axis. Recent experimental data shows that the Dpp active domain, which also controls the growth of the wing imaginal

disc and its concentration, scales as the disc size changes during wing development [91, 92], and is evident by the fact that signaling profiles appear size-independent when they are normalized by the peak intensity of the signal.

Size adjustment in Bicoid (Bcd) signaling is another example of scaling that is observed in Drosophila A/P patterning. In Drosophila, Bcd acts as a morphogen, and the Bicoid signaling turns on a family of gap genes (hunchback, Kruppel, knirps etc.) in a concentration-specific manner [44, 93]. Evidence of Bicoid scaling has also been seen experimentally within and between various Drosophila species. But the exact mechanisms of intra-species and inter-species Bicoid scaling vary in details [44,94] and are reviewed in [86]. For example, previous research considered nuclear density as a possible mechanism to obtain Bcd scaling between species [7,12,44]. However, *in vivo* measurements showed that the Bcd gradient remains spatially and temporally invariant during cycles 10-14 of nuclear division, whereas the number of nuclei increases by approximately 16-fold [44, 95, 96]. This conflicts with the idea that Bcd scaling may be mediated by an embryonic environment, possibly by altering some biophysical properties, such as the transport and reaction rates of Bcd. However, the relation between nuclear density and the signaling shape is demonstrated in another context. That is, in dpERK signaling, signaling distribution is guided by the number of nuclei added after each nuclear division cycle [97]. That is, there is a strong correlation between nuclear density and the shape of the signaling distribution, which is further demonstrated using mutant embryos as was done by Coopey et al. However, it also indicates that as the development of species progresses the signaling distribution is tuned accordingly.

Another view of Bcd scaling suggests that it may be achieved through input flux optimization. In other words, as the embryo grows in size input flux increases in order to establish a signaling threshold at the same normalized position. Although this is not perfect scaling, it is adequate in defining the correct boundary between two distinct cell types [9]. Alternative mechanisms of Bcd scaling consider the lifetime of Bcd molecules, since evolution modifies the lifetime of Bcd molecules in each species.

This may lead to a broader range of Bcd distribution in larger systems because of a larger Bcd lifetime, whereas in smaller systems Bcd lifetime is small and causes shorter distribution. However, evidence shows that Bcd lifetime is not a species-specific intrinsic property [98].

Evidence of scaling of patterns is observed during xenopus development as well [11, 37, 99, 100]. Besides the classic experiment of Spemann and Mangold associated with the Siamese twin formation, experimentally it is shown that patterns in xenopus demonstrate size adaptation in the presence of embryo size variation [101]. As observed, when embryos are reduced by removing the ventral cells during pre-gastrula stage, normal proportions are observed in embryos that are about 60% shorter than normal embryos. Moreover, the stage when perturbations occur during development also control the degree of regulation that can be achieved. For instance, while a bisected xenopus embryo from blastula stage is able to adjust size variation perfectly and generate identical twins, perturbations up to the 8-cell stage may or may not produce healthy adults [102, 103]. Together, this data shows that scaling of patterns is common, and is seen at all stages of biological organization.

1.6 Mathematical modeling in morphogen signaling

Research related to pattern formation and in this area is mostly based on molecular level data for multiple developmental processes obtained via in vivo experiments. Many findings for morphogen pattern formation rely on observing changes in phenotypic responses to disturbances in specific networks, either by overexpressing or underexpressing specific morphogens and/or regulators of the morphogens. This has been accomplished through the injection of specific morpholinos and the generation of mutants with a knockdown of genes of interest [6, 29].

Although this grants insights into how morphogen signaling is altered, or regulated, as a result of genetic modification of a species, at times the observed phenomenons are puzzling. For instance, the Bicoid (Bcd) gradient in Anterior-Posterior

(A/P) axis patterning of Drosophila directs the formation of four gap domains with remarkable reproducibility and precision despite the realm of stochastic fluctuations in morphogen activity, and the underlying mechanisms for such remarkable precision require further investigation and analysis [44]. Moreover, as the dynamics of the process often change because of numerous factors (like temperature change, pH variation, lack of nutrients), and it is difficult to determine the kinetics of physiological processes, experimental data may not be always sufficient.

To aid in our understanding on how a biological system such as the BMP signaling pathway functions, to ensure remarkable reproducibility, and to test numerous hypotheses relevant to signaling and biological pattern formation, mechanistic models have been proven extremely useful [12, 51, 104–109]. Quantitative models are capable of equipping us with predictive power, which can subsequently be applied to model-based experiment design techniques [110–114] to design desired experiments.

The ever increasing use of mathematical modeling in the analysis of biological systems has facilitated our understanding in many ways; computational models are now used for a wide variety of reasons ranging from testing hypotheses, generating new hypotheses, designing new experiments, etc. by considering the interactions of components within and between cells. [4,5,8,12,24,27,29,40,51,83,100,104,109,113–123]. For instance, species development involves the interactions of signaling pathways, pattern formations, cell growth, and cell-to-cell interactions, and computational models have been extensively used to analyze numerous processes. One such model is the gradient-based model, which has been used for decades to analyze spatial pattern formation in many species, such as Drosophila, zebrafish, xenopus etc. Moreover, mathematical models are used to devise new hypotheses and mechanisms for understanding problems that have puzzled researchers for decades. For instance, computational models have played an instrumental role in analyzing how different developmental processes scale in the presence of perturbations. [10, 11, 86, 106].

In many patterning systems, the spatial distribution of extracellular morphogen [3, 5, 35] directs the activation of downstream signaling, or the binding of morphogens

to DNA regions, to initiate a dose-dependent gene expression. That is, a pre-pattern of morphogen plays a crucial role in the spatial pattern formation during species development. In a patterning system, morphogens are the secreted group of molecules produced from a tiny region of a tissue. Upon secretion, morphogens transport away from the source creating a gradient that instructs cell-positional information in a concentration-dependent manner. The transport of morphogen from the source region may happen by diffusion, or by other alternative mechanisms (already discussed in Section 1.2) [56]. In this research, we assumed that the transport of morphogen occurs by diffusion and, therefore, the morphogen distribution was modeled using the widely studied and used reaction-diffusion (RD) model.

1.6.1 Reaction-Diffusion (RD) models

The transport process of extracellular molecules often depends on the time and length scale of the underlying system. In an arbitrary volume, concentration $m(x,t)$ of a chemical species at any given time (t) and space (x) can be formulated as:

$$rate\ of\ change\ of\ m(x,t) = -flux\ of\ the\ species\ m + net\ production \tag{1.1}$$

Using divergence theorem as used in [118], we obtain:

$$\frac{\partial m}{\partial t} = -\nabla.\mathbf{m}_{Flux} + R(m) \tag{1.2}$$

where, $\mathbf{m}_{Flux}$ is the net flux of species m and $R(m)$ is the net production of species m within the arbitrary volume considered.

If the morphogen transport happens as a result of a diffusion process, the flux term $\mathbf{m}_{Flux}$ can be represented as using Fick's Law [124]. According to Fick's law, flux of species m is directly proportional to the concentration gradient of m, and is stated as:

$$\mathbf{m}_{Flux} = -D_m \nabla m \tag{1.3}$$

Where D_m, is the diffusion coefficient of species m. By plugging in Eq.1.3 to Eq.1.2:

$$\frac{\partial m}{\partial t} = D_m \nabla^2 m + R(m) \tag{1.4}$$

Here D_m is assumed as constant and positive.The Eq. 1.4 represents a generic reaction-diffusion model with constant diffusion coefficient. For a 1-dimensional diffusion, Eq.1.4 is written as:

$$\frac{\partial m}{\partial t} = D_m \frac{\partial^2 m}{\partial x^2} + R(m) \tag{1.5}$$

However, diffusion coefficient of chemical species m (D_m) can be a spatially varying property, and the Eq. 1.4 for 1-D diffusion is stated as follows:

$$\frac{\partial m}{\partial t} = \frac{\partial}{\partial x}\left(D_m \frac{\partial m}{\partial x}\right) + R(m) \tag{1.6}$$

Eq.1.4, and Eq.1.6, both are derived for a single species 1-D diffusion case.

Reaction-diffusion system can be generalized for an interacting systems of multiple species in a given volume. For a system of multiple species with constant diffusion coefficient, Eq.1.4 generalizes to:

$$\frac{\partial \mathbf{m}}{\partial t} = \mathbf{D_m}\nabla^2 \mathbf{m} + R(\mathbf{m}) \tag{1.7}$$

where $\mathbf{m}$ represents a vector of species concentration, $m = [m_1, m_2, m_3 \ldots, m_n]^T$ and $R(\mathbf{m}) = [R_1(\mathbf{m}), R_2(\mathbf{m}), R_3(\mathbf{m}), \ldots, R_n(\mathbf{m})]$. In this set up, $\mathbf{D_m}$ is $n \times n$ matrix, and when we discard cross-diffusion between species $\mathbf{D_m}$ simplifies to a diagonal matrix with all the off-diagonal elements to be zero. For instance, in a system of two interacting species $\mathbf{D_m}$ becomes:

$$\mathbf{D_m} = \begin{bmatrix} D_{11} & D_{12} \\ D_{21} & D_{22} \end{bmatrix}$$

When cross-diffusion is zero ($D_{12} = D_{21} = 0$), for a two species system $\mathbf{D_m}$ transforms to a diagonal matrix:

$$\mathbf{D_m} = \begin{bmatrix} D_{11} & 0 \\ 0 & D_{22} \end{bmatrix}$$

If we consider a two species system (m and M) with spatially varying diffusion coefficients D_m and D_M respectively, for 1-D diffusion the system can be represented as:

$$\begin{aligned}\frac{\partial m}{\partial t} &= \frac{\partial}{\partial x}\left(D_m \frac{\partial m}{\partial x}\right) + R(m, M) \\ \frac{\partial M}{\partial t} &= \frac{\partial}{\partial x}\left(D_M \frac{\partial M}{\partial x}\right) + R(m, M)\end{aligned} \tag{1.8}$$

The model is accompanied by necessary boundary condition (B.C) and initial condition (I.C), and depending on the systems behavior we can consider non-zero/zero flux boundary condition or fixed boundary conditions [118, 125]. In this dissertation, we primarily used reaction-diffusion model of two interacting species, and considered all parameters such as the diffusion coefficient, net production etc., to be spatially dependent on species concentration. Mostly, analytical solutions of reaction-diffusion models are intractable, and therefore, RD models are often numerically approximated using different schemes such as, Finite Difference Method [126], Finite Element Method [127, 128], Finite Volume Method [129] etc.

1.7 Objectives

In this dissertation, we address morphogen-mediated signaling and pattern formation as observed in different stages of species development. Specifically, this work involves a rigorous interrogation of scaling problems in biological patterns using computational approaches, and it emphasizes signal transductions of underlying patterning signals (e.g BMP signaling) to identify the mechanisms of heterodimer dominance in BMP signaling. This thesis extensively addresses the question: What mechanisms confer scaling of patterns during development? A number of models for scaling mechanisms have been previously proposed, but they were limited in scope [9], and did not consider physiologically relevant alternative mechanisms. To address the scaling problem in biological pattern formation, a theoretical framework namely, the Two Component System (TCS) model, is proposed and extensively analyzed.

The newly proposed TCS model encompasses the previously proposed models of scale- invariance, and includes a wide number of alternative scenarios. Unlike previous models, the proposed TCS considers the spatial dependence of all biophysical coefficients, which poses an immense computational challenge in terms of accuracy and computational costs. To circumvent the computational challenges, this work integrates a reduced-storage solver CVODE [130] with supercomputer clusters to numerically approximate the Partial Differen-tial Equations (PDEs) of TCS. The simulation strategy used here can be applied beyond biological systems where reaction-diffusion paradigms with spatially varying coefficients are considered.

Besides questioning the manner in which scaling of patterns is achieved, this dissertation also focuses on identifying the mechanisms of heterodimer dominance in Bone Morphogenetic Protein (BMP) signaling that actively participates in the D/V patterning of different species. To determine how BMP heterodimers win over BMP homodimers in a competitive environment, we developed a mathematical model of receptor oligomerization commonly seen during tetrameric/trimeric complex formation in various signaling pathways. The model was used to test our hypothesis, and to identify the conditions that favored heterdimer dominance in BMP signaling. The oligomerization model developed here can also be applied beyond the scope of BMP signaling and be used to develop models for surface-associated tetrameric complex formation often seen in other signaling pathways. This dissertation also considers stochastic analysis of ligand-receptor recruitment in BMP signaling to assess the impact of oligomerization steps on the noise profile, which can be further applied to reduce model structure while implementing the stochastic realization of the complete oligomerization process.

The remainder of this thesis is organized as follows: Chapter 2 presents modeling of cell-surface interactions of Bone Morphogenetic Protein (BMP) signaling. This chapter also includes mathematical analysis of BMP surface dynamics, mutant modeling in BMP signaling, and it tests different hypotheses using the oligomerization model developed in this work. In chapter 3, a stochastic analysis is conducted to

identify whether the oligomerization steps of type II recruitment can affect the noise characteristic in BMP signaling. This chapter demonstrates a previously developed (during my masters research) algorithm of steady-state probability approximation and includes some benchmarks. Chapter 4 is comprised of the scaling problem and, in this chapter, we attempted to identify all the possible minimal network motifs that achieve scaling by satisfying a number of performance objectives. Reaction-diffusion systems with spatially varying parameters have been numerically approximated for millions of networks. This chapter also expands on other possible versions of TCS and the identification of minimal regulatory motifs. We also provide a description of ongoing research in scaling, and projects in the final phases of analysis involving the scaling problem. Finally, this thesis concludes the work performed and considers some of the proposed future extensions in Chapter 5.

1.8 Significance

Not only do the members of TGF- superfamily ligand regulate different developmental processes in Drosophila, zebrafish, mouse, xenopus etc., they are known to control cellular processes in humans as well. Cells in human tissues communicate among themselves via signaling mediated by members of the TGF- superfamily of ligands. A disruption of this signaling can lead to lethal consequences, like causing human cancer [131]. For example, Bone Morphogenetic Protein (BMP), a member of TGF- superfamily ligand, significantly contributes to human development [132]. Previous studies have also shown that BMP mediated signals have a critical role in heart, cartilage, and neural development within complex species such as humans [133]. Further work indicates that BMPs have the ability to inhibit the growth of prostate cancer as well [132] and, for that reason, may be useful in a therapeutic sense.

Deregulation of BMP signaling during development in many species may result in severe developmental disorders and other lethal consequences. The loss of TGF-β signaling is known to destabilize the homeostasis [134], and misregulation of TGF-

β signaling can cause tumor development in humans [135] etc. Moreover, TGF-β acts as a tumor-suppressor and tumor-promoter simultaneously, a biphasic role that is also seen during crossvein development in Drosophila; where cellular responses are regulated by Crossveinless-2(Cv-2) in a biphasic manner [7]: low levels of Cv-2 increase BMP signaling while high levels decrease it. Thus, information on how the signaling mediated by the members (BMPs) of the TGF-β superfamily works and maintains high fidelity during development in model organisms such as Drosophila and zebrafish will enhance our understanding on how BMPs work in humans. This will increase our current knowledge on BMP signaling pathways and, eventually, be useful in drug discovery and development.

Moreover, the numerical approaches adopted here to approximate the nonlinear reaction-diffusion system with spatially varying parameters are pertinent for other morphogen systems, such as the coordination of FGF and Shh in limb formation [106, 136], retinoic acid, etc. Also, the dimer-receptor ODE model is applicable to all other systems that require multimerization events at the cellular surface, and One such system would be the epidermal growth factor (EGF) system [137]. The dimer-receptor model is further applicable to computational models that attempt to integrate extracellular regulation of BMP signaling and intracellular events. More precisely, the dimer-receptor model can be used as an interface between the phosphorylation events of intracellular transcription factors (Smad) and the extracellular activation of receptor families in a BMP mediated patterning system.

2. CHAPTER: ANALYSIS OF DIMER-RECEPTOR INTERACTIONS AND RECEPTOR OLIGOMERIZATION IN BONE MORPHOGENETIC PROTEIN SIGNALING

Bone Morphogenetic Proteins (BMPs) pattern the dorso-ventral axes of both vertebrates and invertebrates. Previous work demonstrates that under physiological conditions, BMP heterodimers signal through a receptor complex consisting of two distinct type I receptors and two type II receptors. Intriguingly, homodimers of the BMP ligands are much less effective at initiating signaling and are unable to compensate for a loss of heterodimers. Ascertaining why heterodimer signals are dominant is an important biophysical problem. To determine the control of heterodimer signaling, we developed a quantitative model of dimer-receptor interactions. We used the quantitative model to test different hypotheses regarding receptor binding kinetics, surface reactions, and mutant cases of embryos. The model contains all of the different BMP dimers, namely BMP2 homodimers, BMP7 homodimers, and BMP2/7 heterodimers.

Our simulation predicts how the factors compete in a well-mixed environment. We discovered, by using the mathematical model, that the kinetics of ligand-receptor interactions cannot favor heterodimer dominance. While the computational model based on published kinetic data and equimolar dimer levels doesnt favor a kinetic based hypothesis, it was used to identify a number of scenarios that favor heterodimer dominance. Firstly, a kinetic driven explanation of heterodimer dominance is possible when binding occurs between hetorodimers and a specific class of Type I receptor (Alk 2/8) with a considerably higher affinity. However, available experimental evidence [138] does not support the hypothesis that heterodimer dominance requires tight binding between a heterodimer and its cognate Type I receptor Alk2/8. Secondly, if homodimers are blocked in vivo by BMP antagonists, leaving only BMP2/7 to bind

receptors and making Alk2/8 levels 9 times higher than Alk 3/6 receptors, the model favors formation of the $BMP2/7Alk2/8Alk3/6TypeII-TypeII$ complex over a wide range of ligand concentrations.

A third scenario of heterodimer-heteromeric receptor dominance occurs if complexes with two BmpR1 receptors signal poorly. In this case the next most abundant complex in the majority of simulations is BMP2/7-Acvr1l-BmpR1-(Type II)2, and the last two hypotheses are tested experimentally by our collaborators. To summarize, the computational model was used to demonstrate that in BMP signaling system, the BMP2/7 heterodimer brings two distinct classes of type I receptors together to create a robust sensor capable of responding to a wide range of morphogen concentrations; a fundamental concept necessary for morphogen mediated signaling.

This chapter includes the outcomes of a collaborative project on BMP signaling in zebrafish. It primarily considers computational analysis of the oligomerization of the initial receptor-ligand complex, a process that is seen among a wide variety of signaling pathways. The computational model and its variants were used to test previously proposed hypotheses, and further used to explore other potential mechanisms of heterodimer dominance. Part of the material presented here is adopted directly from a paper that is already submitted for publication and is currently under review. The paper is titled: "BMP Heterodimers Signal via Distinct Type I Receptor Class Functions", *James A. Dutko, Md. Shahriar Karim, Shawn C. Little, David M. Umulis, and Mary C. Mullins* (submitted). Additional completed unpublished data and computational analyses are included in this chapter.

Our work in this chapter extend the previously proposed hypothesis on the heterodimer dominance [6, 29]. In a canonical BMP-signaling pathway, a BMP heterodimer bound heteromeric receptor association consisting of two type I (Alk3/6, Alk2/8) and two type II receptors, initiates signaling. In this collaborative work, the computational analysis considered all possible biochemical reactions between dimer-receptors, and, using mass-action kinetics, it considered a local Ordinary Differential Equation (ODE) model to test different hypotheses. The surface dynamics of the

initial dimer-receptor interactions and subsequent receptor oligomerization were analyzed mathematically, and can be further extended to other systems. The model was tested and validated against a number of mutant conditions for BMP signaling to explain some of the experimental data generated by James A. Dutko, and Mary C. Mullins Over-expression and mutant cases of dimers and receptors are also implemented using com- putational models to assess the impact of those that initiate signaling.

To highlight the focus of the computational analysis, experiments done in this collaborative project to test our proposed hypotheses are mostly excluded. The mathematical analysis of surface dynamics using Partial Differentiation Equations (PDE) is shown in details, and part of the local ODE model of receptor oligomerization is taken from supplementary information within the submitted paper of Dutko et al.

Finally, the chapter is organized as follows: First, the importance of studying BMP signaling is described. Second, we analyze current models of dimer-receptor interactions, specifically discussing kinetics and new insights into receptor oligomerization. Then, we introduce the ordinary differential equations (ODE) model of BMP receptor interactions. Finally, this chapter concludes with an analysis of the mathematical model.

2.1 Background

Bone morphogenetic proteins (BMPs) are signaling proteins that participate in a wide range of cellular processes in both vertebrate and invertebrate systems [6,29,139]. Zebrafish, a vertebrate model organism, secrets BMP2 and BMP7 which have genetically equivalent yet non-redundant roles [66], and pattern the dorsal-ventral (D/V) axis during the early stages of embryonic development [6, 66]. In a canonical BMP pathway, secreted dimeric BMP-ligands (homodimers and heterodimers) interact with a family of receptor tyrosine kinases (RTK), and, presumably, form a quadripartite signaling complex consisting of two non-redundant type I and two type II kinase

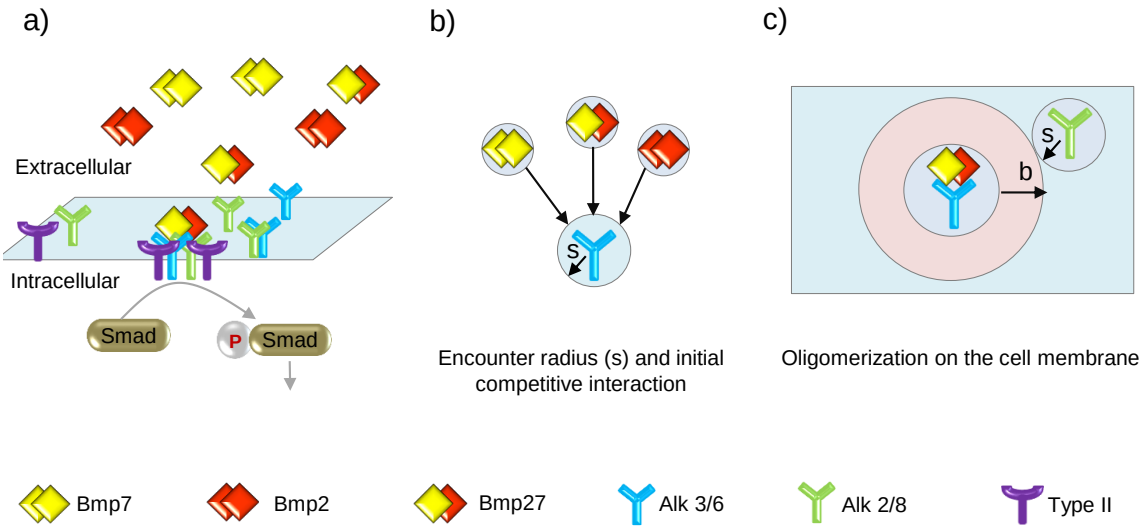

Fig. 2.1. a) BMPs are secreted as dimers, and the three different BMP dimers are shown in red, yellow and red-yellow. Each of the dimers can recruit any of the available type I and type II receptors. By participating in subsequent receptor recruitment steps, a dimer forms a number of putative signaling complex consisting of two distinct type I receptors and two type II receptors. The three different types of receptors that are available for binding are the type I receptor (Alk3/6), another variant of type I receptor (Alk2/8), and type II receptors. However, the affinity of different interactions varies between different dimer-receptor combinations. b) Each dimer competes to bind with a free receptor. If a dimer reaches a proximity equivalent to or less than the encounter radius, s, it binds with the receptor and forms the initial dimer-receptor complex. c) Once the initial ligand-receptor complex (BR) is formed, its movement is restricted on the cell surface and all the subsequent binding happens between species restricted on the cell surface and the family of the membrane receptors.

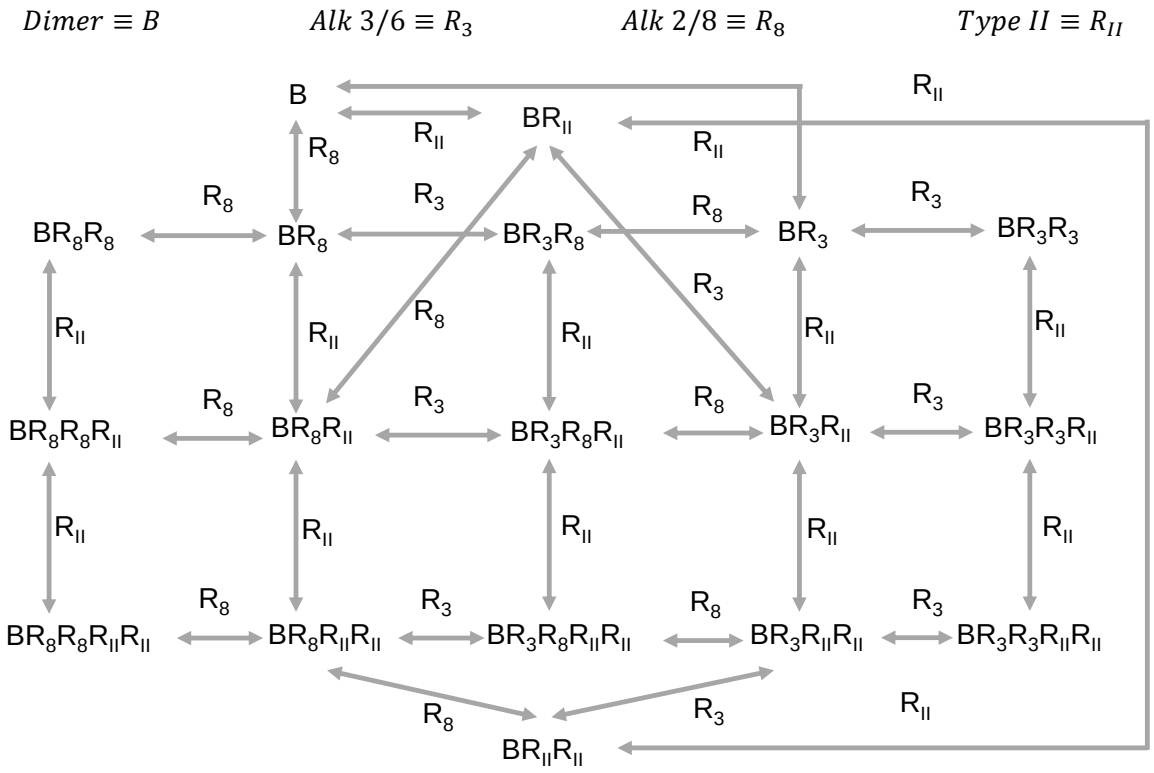

Fig. 2.2. Biochemical interactions between dimers and receptors: All the possible reactions between a dimer (B) and its cognate receptors are shown here. For example, dimer (B) initially interacts with any of the three receptors R_3, R_8, and R_{II}, and, upon initial binding, the dimer-receptor complex continues accumulating more receptors to finally give rise to a tetrameric receptor association. Evidently, the tetrameric association cannot have more than two copies of any specific receptors that is, only $BR_3R_3R_{II}R_{II}$, $BR_3R_8R_{II}R_{II}$, and $BR_8R_8R_{II}R_{II}$ complexes are possible in system. All these reactions are bidirectional and follow mass-action kinetics. In a BMP signaling pathway, the three dimers BMP7, BMP2 and BMP2/7 heterodimers are all theoretically able to participate in these interactions and form tetrameric complexes. However, certain interaction edges of the network might be insignificant for different dimers because of a very low binding affinity for the corresponding interaction, and is shown later.

receptors [6, 29]. This is shown in Fig.2.1a, where the three dimers BMP7, BMP2, and BMP27 interact with a group of RTKs to form putative signaling complexes. These complexes play a crucial role in initiating the intracellular signaling cascade by instigating phosphorylation of BMP-responsive Smad proteins [7, 29, 67]. Finally, the phosphorylated Smad (pSmad) forms complexes with co-Smad and accumulates in the nucleus to regulate gene expression [67].

Much is known about the identity of BMP-signaling complexes that initiate Smad phosphorylation in both vertebrates and invertebrates [6,29]. For example, patterning in vertebrates, such as zebrafish, requires two classes of non-redundant type I receptors (Alk 3/6 and Alk 2/8) with two copies of type II receptors in order to elicit signaling [6, 29]. In Drosophila, BMP homologues, Decapentaplegic (Dpp) and Screw (Scw), signal through two type I receptors (Saxophone and Thickvein) and two type II receptors (Punt), thereby forming a hetero-tetrameric receptor association and transmitting patterning information [29]. However, the true identity of the BMP signaling complex in *Drosophila melanogaster* embryo is still debatable [29, 140].

In numerous contexts BMP heterodimers consistently demonstrate stronger biological activity than BMP homodimers. For instance, in D/V patterning of Drosophila, bone regeneration, axon guidance, and stem cell differentiation BMP heterodimers are more effective in initiating signaling [6, 29–32, 34]. It is demonstrated mathematically that heterodimers are more robust to changes in gene dosage within the context of BMP signaling [29]. In zebrafish patterning, the signal is exclusively mediated by heterodimers [6]. From mutant experiments we found that the loss of BMP2b or BMP7a is sufficient to induce a complete loss of BMP signaling in the embryo [6]. Additionally, knockdown experiments for the two distinct type I receptors (Alk 3/6 and Alk2/8) show that signaling requires both receptors, and that the receptors demonstrate a non-redundant role in BMP signaling [6].

Though previous studies [6, 29, 140] provide key information on the identity of signaling complexes that transmit signaling information downstream, many questions remain, including how a specific combination of receptor association is favored over

other dimer- receptor complexes. A previously proposed hypothesis [6] supports an affinity-based explanation on the dominance of heterodimer-bound heterotetrameric receptor association, but this has not been tested yet as the exact affinity of BMP2/7 heterodimer and Alk2/8 receptor binding is still unknown, and has not been possible to measure [6].

To investigate why BMP heterodimers prevail over BMP homodimers, we developed a new physiologically relevant mathematical model that includes initial receptor binding and subsequent receptor oligomerization. Using the computational model, we identified a number of mechanisms that explain heterodimer dominance, a few of which we tested experimentally. Our research revealed that outcomes of the computational models complied with experimentally observed phenomenon in BMP signaling. The computational model also identified theoretically plausible mechanisms. In this research, our efforts revealed works reveal mechanisms that could explain the increased activity of BMP heterodimers, which has implications for nearly all BMP signaling in other developmental contexts and disease conditions. This will likely increase our understanding on how BMP signaling works in complex species, such as humans, and it could be useful for drug development and BMP therapies.

Furthermore, the mathematical model of receptor oligomerization developed here could have potential applications in other signaling pathways. Dimer-receptor bindings events occur at two levels, namely initial dimer-receptor binding and receptor recruitment by an already formed dimer-receptor complex. In this analysis, we revisited surface dynamics to mathematically show how a dimensionality reduction of a ligands movement from three to two dimensions which resulted because of initial ligand-receptor binding, affects the dynamics of subsequent receptor binding events. Our analysis eventually connects the binding events and the effective density of ligands encountered by a receptor. Together with an ODE model of all possible biochemical interactions shown in Fig.2.2, the computational analysis conducted in this work can be applied to other signaling pathways, where subsequent binding events

generate trimeric/tetrameric complexes in order to activate membrane receptors or downstream pathways [137].

2.2 Mathematical model of dimer-receptor interactions

In a canonical BMP signaling pathway, secreted dimeric BMP-ligands (homodimers and heterodimers) interact with a family of Receptor Tyrosine Kinases (RTKs) and presumably form a quadripartite signaling complex consisting of two non-redundant type I and two type II kinase receptors [6, 29, 117]. Dimer-receptor complexes play a pivotal role in initiating the intracellular signaling cascade by instigating phosphorylation of BMP-responsive intracellular transcription factors [7, 29, 67]. Subsequently, the Phosphorylated Smad (pSmad) forms complexes with co-Smad, and finally accumulates in the nucleus to regulate dose- dependent gene expression [67].In BMP signaling, there are three dimers (BMP2 homodimers, BMP7 homodimers and BMP2/7 heterodimers) that interact with a family of type I and type II receptors and, interestingly, dimers have dissimilar affinities for similar type receptors. Thus, a careful consideration of dimer-receptor binding affinity is required for the computational model.

Measured molecular data revealed that biochemical properties among the dimers vary significantly. More precisely, BMP homodimers have high, low, and very low affinities for the BMP receptor family [24, 33, 55, 79, 81, 82, 141–146]. As reported, unlike a homodimer, a BMP heterodimer contains dissimilar binding domains for similar type receptors [6]. The binding domains of a BMP heterodimer comes from each of the constituent monomers, which cause qualitative dissimilarities between binding domains that bind to similar types of receptors. For instance, in the BMP2/7 heterodimer, binding affinities for the recruitment of two type I receptors must be different, since the affinities of heterodimer and receptor binding are primarily determined by the constituent BMP2 and BMP7 monomers [6, 25, 33].

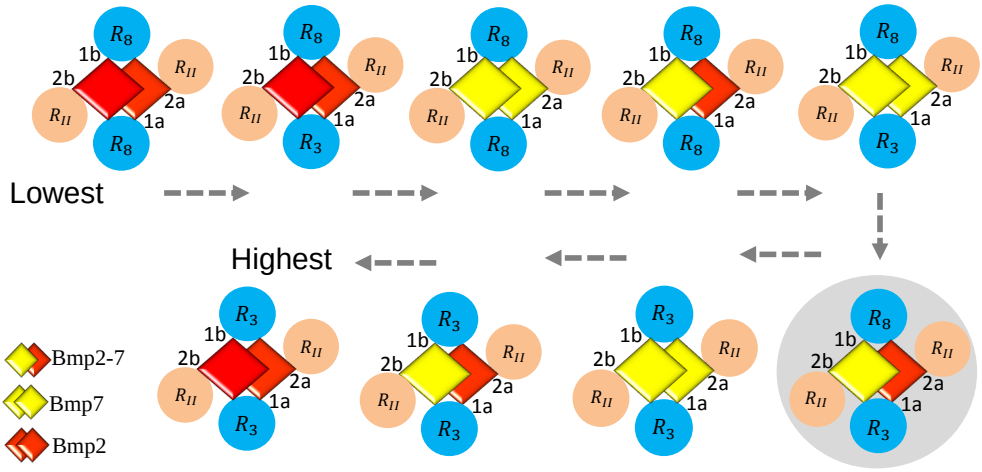

Fig. 2.3. Putative signaling complexes in a dimer-receptor system: through a series of receptor interactions, each dimer (BMP2, BMP7 and BMP2/7) forms three tetrameric receptor associations in a competitive dimer-receptor environment. The relative strength of all the formed complexes depends on the affinity of corresponding binding events. For instance, affinity-based assessment reveals that BMP2 binds with Alk 3/6 with a high affinity and therefore, the complex $BMP2{-}Alk3/6{-}Alk3/6{-}TypeII : TypeII$ is likely to form in larger quantities than other tetrameric complexes. The stipulated signaling complex, as seen in the D/V patterning of the zebrafish, is displayed inside a grey circle, and the arrow directs the concentration hierarchy of all the complexes.

Additionally, current published data demonstrates that not all dimers interact and form complexes with all the receptors. For this reason, there is a critical need to further clarify the kinetic description of receptor oligomerization process and to define the necessary requirements that ensure a physiologically relevant demonstration of BMP signaling.

2.2.1 Kinetics of dimer-receptor interactions

Considering all the theoretically possible interactions between the three dimers and their cognate receptor families, we devised the biochemical network shown in Fig.2.2 which demonstrates the steps of receptor oligomerization through a series of bidirectional biochemical interactions. A complete dimer-receptor system is comprised of 90 bidirectional interactions and 51 species. However, a careful review of all the affinities reveals that a number of dimer- receptor interactions happen with very low binding affinity, which are further elaborated on in later sections.

The kinetics of receptor recruitment depend largely on the type of interacting dimers. Experimentally measured kinetic data shows that the BMP2 homodimer binds Alk 3/6 with high affinity [6,80] with a dissociation constant of $K_D = \frac{k_{off}}{k_{on}} \approx 0.2\ to\ 0.9\ nM$ [80], whereas whereas it binds poorly to the type II receptor with a comparatively large K_D range from 50 *to* 100 nM [24,80]. However, the BMP2 dimer does not interact with the other type I receptor, Alk 2/8 [unpublished data], and a very low affinity ($1024nM$ [80, 82, 147]) of Alk 2/8 and BMP2 binding ensures an almost complete lack of interaction during the oligomerization steps. Therefore, a BMP2 dimer is less likely to form any complex that includes Alk 2/8 in it to form a heterotetrameric receptor association. The effective set of interactions (which were identified by considering the binding affinities) between a BMP2 homodimer and the receptor family include a total of 12 bidirectional interactions as shown by the green edges in Fig. 2.4. In contrast to the selective binding of the BMP2 homodimer, the BMP7 homodimer is known to bind with all the receptors in a system. While both

BMP2 and BMP7 homodimers bind strongly with Alk 3/6 receptors, only the BMP7 homodimer is known to bind to the other class of Type I receptor Alk 2/8. The binding happens, however, with a considerably low affinity $K_D > 500$nM [80]. As BMP7 homodimer binds with both Alk 3/6 and Alk 2/8 receptors, all the possible interactions and species can be obtained by juxtaposing the green, red, and blue edges as shown in Fig.2.4.

BMP homodimers are known to have identical binding domains for type I receptors, but the type I binding domains of BMP2/7 are dissimilar and possess different affinities for the type I receptor class [6]. The recruitment of Alk3/6 to the BMP2/7 heterodimer follows the kinetics of BMP2 homodimers, i.e., high binding affinity, because one of the type I binding sites of BMP2/7 heterodimer has a similarity of 96% to the high affinity binding site of BMP2 homodimer. This domain binds to the Alk 3/6 receptor [6]. However, since the structural resemblance of a ligand-bound second type I binding site is still unknown [6], it is not possible to determine affinity and other biochemical information about the binding event that occurs at the second type I binding site of the BMP2/7 heterodimer. Hence, we considered the binding kinetics between the BMP2/7 heterodimers and Alk 2/8 receptors from a physiologically relevant K_D range, and further observations on the dimer-receptor binding kinetics are as listed below:

1. Interactions with Alk2/8 (also, represented as R_8): The kinetics of BMP2/7 binding to Alk2/8 has not been determined. It is possible that BMP2/7 heterodimers bind to Alk2/8 with higher binding affinity than the BMP7 homodimers ($K_D > 500$ nM, which is very low) and Alk2/8 binding affinity. Thus, in this research, we considered a K_D within the range of 1 to 1000 nM which included both a very tight and weak binding between Alk 2/8 and BMP2/7 heterodimer.

2. As there is no existing evidence of Alk 2/8 and B2 binding, we consider a very high K_D (> 1024 nM), so that the possibility of B2 bound heterotetrameric

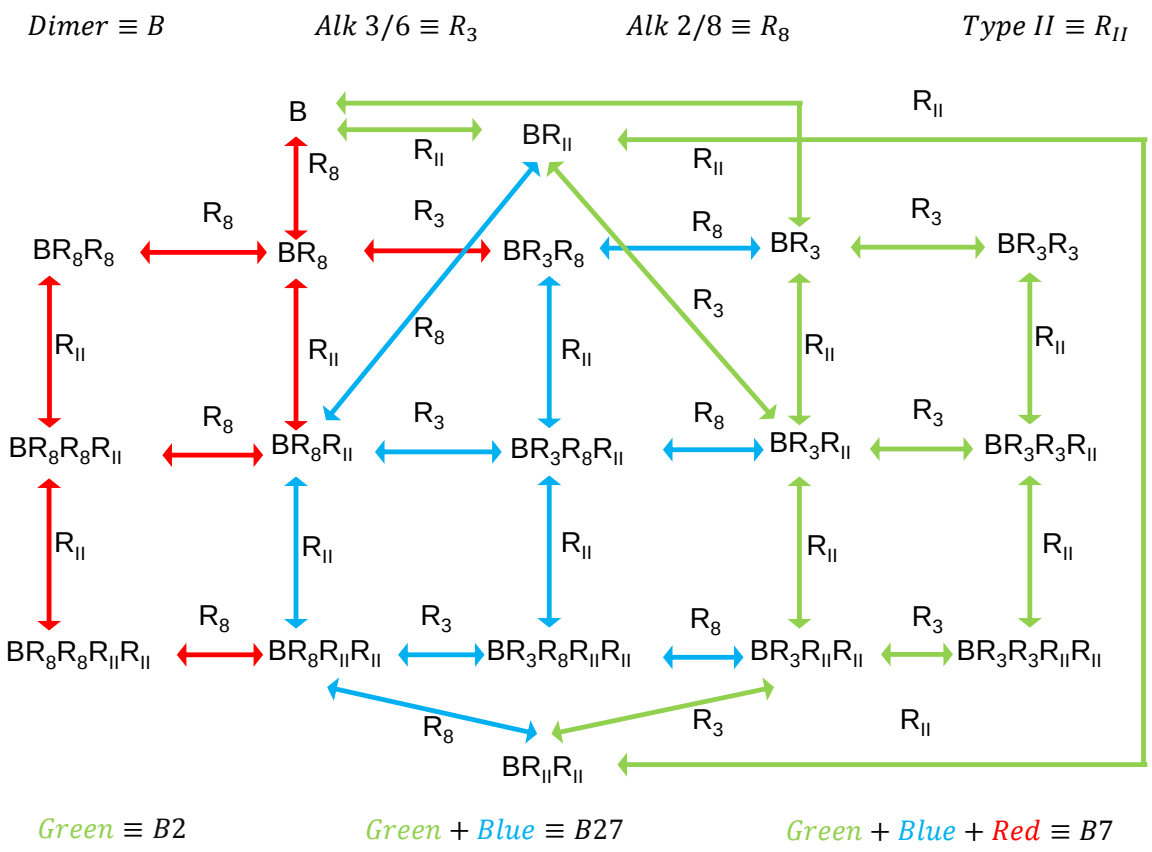

Fig. 2.4. Effective edges of oligomerization network based on dimer-receptor interaction affinity: Based on dimer-receptor binding affinity receptor recruitment to specific dimer types varies. For instance, BMP7 dimers and BMP2 dimers have largely varying affinity for the Alk 2/8 receptor. To be more precise, the BMP2 receptor binds very poorly with Alk 2/8 and, hence, the effective edges of BMP dimer receptor interactions reduce from a complete network as seen in Fig.2.2 to a simpler network of 12 bidirectional interactions, demonstrated here using the green edges. Similarly, after affinity assessment, the effective edges of $BMP2/7$ and receptor interactions are reduced to a sub-network formed by connecting green and blue edges. Since BMP7 interacts with all the receptors through considerable affinity, BMP7-only interactions comprise all the edges (red + blue + green).

complex is small in the system. Moreover, because the K_D is high (> 1024 nM), the chances of a B2 bound Alk 2/8 complex decrease when the dimers compete to bind with free receptors in a well-mixed system.

3. The second recruitment of Alk3/6 to the BMP2/7 heterodimer follows the kinetics of BMP7 homodimers, i.e., lower affinity binding, because the second type I binding site on the BMP2/7 heterodimer has similarities to that of a BMP7 homodimer binding site [6, 33, 80, 142] for a type I receptor.

4. Based on the affinity of the binding of different dimers and receptors, in descending order, the strength (in nM) among all the tetrameric complexes formed by the three dimers (B2, B7, B27). The list of complexes is shown in Fig.2.3.

The interactions between BMP2/7 heterodimer and receptors are shown in Fig.2.2. Although the dimers are subject to all theoretically possible interactions as shown here, in a competitive environment their respective affinities for specific receptor type decides the occurrence of a specific interaction. If the affinity for a binding event is very low, it is more likely that a complex formed via the binding event of low affinity will not be accumulated in a considerable amount. The complete kinetic details for the system are listed in Table 2.1.

2.2.2 New insights of the dynamics of receptor oligomerization

In BMP signaling, the oligomerization steps between receptor subunits begin (shown in Fig.2.3) after the initial binding between a BMP dimer and any of the receptors. Eventually, this dimer-receptor complex assembles three more receptors to finally form a quadripartite receptor association consisting of two type I receptors (Alk 3/6, Alk 2/8) and two type II receptors as shown in Fig.2.2a. Initially, dimers move freely in the extracellular region (a 3D volume) and the receptors are restricted on the cell membrane (a 2D plane). When a dimer and a receptor come within the

minimum distance required for binding to occur, interaction takes place and produces a dimer-receptor complex. This initial event can be represented as follows [107]:

$$r_1 : B + R_i \xrightarrow{k_{on}} BR_i, \quad r_2 : \ BR_i \xrightarrow{k_{off}} B + R_i \tag{2.1}$$

where, k_{on} and k_{off} are the receptor association and dissociation rate constants respectively.

The kinetic details of the chemical reactions shown in 2.1 are well-known, and the binding event is treated as a two-step process [107] : i) the transport of B molecules to bring them within the encounter radius (s, as shown in Fig.2.1) and ii) the intrinsic chemical reaction step once B is already within the encounter radius [107]. In a BMP signaling system (where BMP acts as a morphogen), BMP transport occurs mainly due to molecular diffusion [3], and the transport rate constant is denoted as k_{diff}, where diff≡diffusion. If the chemical reaction step is characterized by the intrinsic association rate constant k_r, the effective reaction rate constant k_{on} for BR_i formation in Eq.2.1 can be written as [107]:

$$k_{on} \ = \ \frac{k_{diff} k_r}{k_{diff} + k_r} \tag{2.2}$$

Eq.2.1 depicts a scenario where a freely moving dimer in a 3D volume interacts with receptors located on a 2D membrane surface, and produces a dimer-receptor complex (BR_i). However, if the dimer-receptor complex recruits more receptor copies to the initially formed receptor-ligand complex (BR_i), and the interaction events are restricted on a 2D surface, a dimensionality reduction from a 3D volume to a 2D surface affects effective ligand concentration during the receptor recruitment events [8, 107]. Thus, we need further assessment of surface dynamics associated with the oligomerization steps in order to quantify the impact of the dimensionality reduction that happens because of initial ligand-receptor binding.

To analyze the oligomerization steps, interactions are divided into two main subclasses: i) initial receptor binding, and ii) secondary receptor binding. Once a dimer (B) binds to a membrane receptor (R_i), the diffusion of the dimer-receptor complex

(BR_i) reduces considerably. Hence, we hypothesize that the subsequent membrane receptor recruitment, defined as the *secondary receptor recruitment*, becomes transport limited [107].

However, since the diffusivity of R_i is negligibly low because of its attachment to the cell membrane, D mainly represents the diffusivity of morphogen (B) only. For a diffusion limited receptor recruitment [107], the rate constant is significantly faster than the rate constant of *initial receptor binding*. To accommodate this in our model, we introduced a surface enhancement factor, denoted as γ, and multiply all the forward reaction rate constants (k_{on}) for each oligomerization step that causes *secondary receptor recruitment*. This is summarized here using sample interactions between a BMP2/7 (alias, B27) heterodimer and Alk 3/6 receptors (R_3), and is shown as below:

$$
\begin{aligned}
&Initial\ \ receptor\ \ binding:\\
&r27_1 : B27 + R_3 \xrightarrow{k27_1} B27R_3 \quad r27_{1r} : B27R_3 \xrightarrow{k27_{-1}} B27 + R_3\\
&Secondary\ \ receptor\ \ binding:\\
&r27_4 : B27R_3 + R_3 \xrightarrow{k27_1\gamma} B27R_3R_3\\
&r27_{4r} : B27R_3R_3 \xrightarrow{k27_{-4}} B27R_3 + R_3
\end{aligned}
$$

Measured kinetic details as reported in research show L.H.S. data of Eq.2.2, where k_{diff} and k_r contributions are generally lumped together. The transport rate constant, k_{diff}, is approximated as $k_{diff} = 4\pi Ds$ with an encounter radius s (Fig.2.1b) that lies in the range of $1 - 10$ nm [107].Estimated receptor length is necessary to approximate the surface enhancement factor (γ). As reported, the Alk receptor family has an extracellular length in the range of 23 aa to 110 aa (aa: amino acid). For an average amino acid length equivalent to 1 nm, the encounter radius (s) for a receptor would be about 100 nm. For the typical range of morphogen diffusion constants

D$\sim$ [0.1 100]$\mu m^2 s^{-1}$ [27] [107], contribution of diffusion to the effective kinetic rate constant $k_{eff} \equiv k_{on}$ can be calculated as follows:

$$\begin{aligned} k_{diff} &= 4\pi Ds \\ &\equiv 4\pi \times 10 \times 10^{-12} \times 100 \times 10^{-9} (\frac{molecule}{m^3})^{-1} s^{-1} \\ &= 4000\pi \times 10^{-12} \times 10^{-9} \frac{molecule}{m^3}^{-1} s^{-1} \times N \\ &= 15.128\ nM^{-1}s^{-1} \end{aligned} \tag{2.3}$$

where $N = 6.022 \times 10^{23}$ is Avogadro's number. Using the measured effective rate constant k_{on} between BMP2 and Alk 3/6 is 0.0005 nM^{-1} s^{-1} and for a $k_{diff} = 1.5128\ nM^{-1}s^{-1}$, we obtain $k_r \approx k_{on} = 0.0005\ nM^{-1}\ s^{-1}$, which is equivalent to the measured k_{on} of the interaction.

In contrast, upon formation, when BR_i subsequently recruits more receptors during the oligomerization steps, binding events occur between two membrane-associated species, and the kinetics of interactions of membrane-associated species follow diffusion-limited kinetics [107]. In a diffusion-limited scenario, k_{diff} is approximated as $k_{diff} = \frac{2\pi D}{ln(b/s)}$, where b is the one-half mean distance between the membrane molecules, s is the encounter radius and D is the total diffusivity of B and R_i [8,107]. The typical value of diffusion-limited bindings between two membrane associated species lie within a range $6 \times 10^4 M^{-1}s^{-1}$ to $2 \times 10^6 M^{-1}s^{-1}$. Thus, the interactions happen significantly faster than the initial interaction where the dimer moves freely in a solution, and we attempted to analytically derive a factor, namely the surface enhancement factor (γ), to account for the faster interactions that took place during the bindings between membrane-associated species.

2.2.3 Membrane-associated dimer-receptor interactions: homogenization of receptor density

To analyze the dynamics of tertiary complex formation, we consider a simplistic model of the receptor oligomerization steps as shown in Fig.2.5. In the model, a

Table 2.1
Kinetic data for dimer-receptor interaction in receptor oligomerization

R_i	Unit	BMP2		BMP7		BMP2-7		Ref.
		Value	K_D	value	K_D	Value	K_D	
$1^{st}R_3$	$k_{on} : nM^{-1}s^{-1}$	0.0005	0.8	0.00014	56.4	0.0005	0.8	[24, 80]
	$k_{off} : s^{-1}$	0.0004		0.0079		0.0004		
$2^{nd}R_3$	$k_{on} : nM^{-1}s^{-1}$	0.0005	0.8	0.00014	56.4	0.00014	56.4	[80]
	$k_{off} : s^{-1}$	0.0004		0.0079		0.0079		
$1^{st}R_8$	$k_{on} : nM^{-1}s^{-1}$	0.0000011694	1024	0:000002338	500	not known	-	[80]
	$k_{off} : s^{-1}$	0.001197		0.0079		0.001197		
$2^{nd}R_3$	$k_{on} : nM^{-1}s^{-1}$	0.0000011694	1024	0:000002338	500	0.0000011694	1024	[80]
	$k_{off} : s^{-1}$	0.001197		0.0079		0.001197		
$1^{st}R_{II}$	$k_{on} : nM^{-1}s^{-1}$	0.0015	46.6	0.0014	6.42	0.0014	6.42	[82]
	$k_{off} : s^{-1}$	0.07		0.009		0.009		
$2^{nd}R_{II}$	$k_{on} : nM^{-1}s^{-1}$	0.0015	46.6	0.0014	6.42	0.0015	46.6	[82]
	$k_{off} : s^{-1}$	0.07		0.009		0.07		

freely moving dimer B initially interacts with receptor R and, upon formation, the BR complex attaches to a secondary receptor S to produce the trimeric/tetrameric complex. Binding events to form tertiary complex are as follows:

$$\begin{aligned} &r_1 : B + R \xrightarrow{k_{on}} BR, \quad r_2 : \ BR \xrightarrow{k_{off}} B + R \\ &r_3 : BR + S \xrightarrow{k_+} BRS, \quad r_4 : \ BRS \xrightarrow{k_-} BR + S \\ &R_{tot} = R + BR + BRS, \quad R_{ST} = S + BRS \end{aligned} \tag{2.4}$$

The Units of all the components of Eq.2.4 are defined as:

$$\begin{aligned} &[Mole/L^3] : B \\ &[Mole/L^2] : BR, BRS, R_T, R_{ST} \end{aligned} \tag{2.5}$$

BMP dynamics, assumed to be in a cubic volume along X, Y, and Z direction with dimension L_x, L_y, L_z, can be described by the 2^{nd} order partial differential equation as follows:

$$\frac{\partial B}{\partial t} \quad = \quad D_B\left(\frac{\partial^2 B}{\partial X^2} + \frac{\partial^2 B}{\partial Y^2} + \frac{\partial^2 B}{\partial Z^2}\right) - k_\delta B \tag{2.6}$$

Defining a set of dimensionless variables $\xi_x = \frac{X}{L_x}, \xi_y = \frac{Y}{L_y}, \xi_z = \frac{Z}{L_z}$ and $\tau = \frac{t}{T}$, and considering $k_\delta = 0$ to simplify, we obtain $\partial x = L_x \partial \xi_x, \partial y = L_y \partial \xi_y, \partial z = L_z \partial \xi_z$, $\partial t = T\partial\tau$, $b = \frac{B}{B_0}$, we obtain:

$$\begin{aligned} \frac{\partial(B_0 b)}{\partial(\tau T)} \ &= \ D_B\left(\frac{\partial^2(B_0 b)}{{L_x}^2 \partial {\xi_x}^2} + \frac{\partial^2(B_0 b)}{{L_y}^2 \partial {\xi_y}^2} + \frac{\partial^2(B_0 b)}{{L_z}^2 \partial {\xi_z}^2}\right) \\ \Rightarrow \frac{\partial b}{T\partial\tau} \ &= \ D_B\left(\frac{\partial^2 b}{{L_x}^2 \partial {\xi_x}^2} + \frac{\partial^2 b}{{L_y}^2 \partial {\xi_y}^2} + \frac{\partial^2 b}{{L_z}^2 \partial {\xi_z}^2}\right) \\ \Rightarrow \frac{\partial b}{\partial\tau} \ &= \ D_B \times T\left(\frac{\partial^2 b}{{L_x}^2 \partial {\xi_x}^2} + \frac{\partial^2 b}{{L_y}^2 \partial {\xi_y}^2} + \frac{\partial^2 b}{{L_z}^2 \partial {\xi_z}^2}\right) \\ \Rightarrow \frac{\partial b}{\partial\tau} \ &= \ D_B \times T \times \frac{1}{{L_x}^2}\left(\frac{\partial^2 b}{\partial {\xi_x}^2} + \frac{{L_x}^2 \partial^2 b}{{L_y}^2 \partial {\xi_y}^2} + \frac{{L_x}^2 \partial^2 b}{{L_z}^2 \partial {\xi_z}^2}\right) \end{aligned} \tag{2.7}$$

At $Z = 0$, the BMP dimer binds with receptor R, and hence the boundary condition can be devised as follows:

$$-D_B \frac{\partial B}{\partial Z}\bigg|_{Z=0} = -k_{on}.B.R + k_{off}.BR$$

By defining two more dimensionless quantities $r = \frac{R}{R_T}$ and $br = \frac{BR}{R_T}$, we obtain:

$$
\begin{aligned}
-D_B \frac{\partial B_0 b}{L_z \partial \xi_z}\bigg|_{\xi_z=0} &= -k_{on}.B_0.b.r.R_T + k_{off}.br.R_T \\
-D_B \frac{\partial B_0 b}{L_z \partial \xi_z}\bigg|_{\xi_z=0} &= B_0.R_T\bigg(- k_{on}.b.r + k_{off}.br.\frac{1}{B_0}\bigg) \\
\frac{\partial b}{\partial \xi_z}\bigg|_{\xi_z=0} &= -\frac{R_T.L_z}{D_B}\bigg(- k_{on}.b.r + k_{off}.br.\frac{1}{B_0}\bigg)
\end{aligned}
$$

In all other boundaries, we have no flux boundary conditions as stated below:

$$
\begin{aligned}
\frac{\partial B}{\partial \xi_x}\bigg|_{\xi_x=0} &= 0 \\
\frac{\partial B}{\partial \xi_x}\bigg|_{\xi_x=1} &= 0 \\
\frac{\partial B}{\partial \xi_y}\bigg|_{\xi_y=0} &= 0 \\
\frac{\partial B}{\partial \xi_x}\bigg|_{\xi_y=1} &= 0 \\
\frac{\partial B}{\partial \xi_z}\bigg|_{\xi_z=0} &= 0
\end{aligned} \tag{2.8}
$$

The transport of BMP (B) in the extracellular surface happens considerably faster than other processes(such as the initial binding between ligand and receptor) and thus, the concentration of BMP can be averaged out along Z-direction as:

$$
\begin{aligned}
&\int_0^1 \frac{\partial b}{\partial \tau} d\xi_z = \int_0^1 D_B \times T \times \frac{1}{{L_x}^2}\bigg(\frac{\partial^2 b}{\partial {\xi_x}^2} + \frac{{L_x}^2 \partial^2 b}{{L_y}^2 \partial {\xi_y}^2} + \frac{{L_x}^2 \partial^2 b}{{L_z}^2 \partial {\xi_z}^2}\bigg) d\xi_z \\
&\Rightarrow \frac{\partial b}{\partial \tau} = \int_0^1 D_B \times T \times \frac{1}{{L_x}^2}\bigg(\frac{\partial^2 b}{\partial {\xi_x}^2} + \frac{{L_x}^2 \partial^2 b}{{L_y}^2 \partial {\xi_y}^2} + \frac{{L_x}^2 \partial^2 b}{{L_z}^2 \partial {\xi_z}^2}\bigg) d\xi_z \\
&\Rightarrow \frac{\partial b}{\partial \tau} = \frac{D_B \times T}{{L_x}^2}\bigg(\frac{\partial^2 b}{\partial {\xi_x}^2} + \frac{{L_x}^2 \partial^2 b}{{L_y}^2 \partial {\xi_y}^2}\bigg) + \frac{D_B \times T}{{L_x}^2}\int_0^1 \bigg(\frac{{L_x}^2 \partial^2 b}{{L_z}^2 \partial {\xi_z}^2}\bigg) d\xi_z
\end{aligned} \tag{2.9}
$$

This simplifies to:

$$\begin{aligned}
\frac{\partial b}{\partial \tau} &= \frac{D_B \times T}{{L_x}^2}\left(\frac{\partial^2 b}{\partial {\xi_x}^2} + \frac{{L_x}^2 \partial^2 b}{{L_y}^2 \partial {\xi_y}^2}\right) + \frac{D_B \times T}{{L_z}^2}\int_0^1 \left(\frac{\partial^2 b}{\partial {\xi_z}^2}\right) d\xi_z \\
&= \frac{D_B \times T}{{L_x}^2}\left(\frac{\partial^2 b}{\partial {\xi_x}^2} + \frac{{L_x}^2 \partial^2 b}{{L_y}^2 \partial {\xi_y}^2}\right) + \frac{D_B \times T}{{L_z}^2}\int_0^1 \left(\frac{\partial}{\partial \xi_z}\left(\frac{\partial b}{\partial \xi_z}\right)\right) d\xi_z \\
&= \frac{D_B \times T}{{L_x}^2}\left(\frac{\partial^2 b}{\partial {\xi_x}^2} + \frac{{L_x}^2 \partial^2 b}{{L_y}^2 \partial {\xi_y}^2}\right) + \frac{D_B \times T}{{L_z}^2}\left[\frac{\partial b}{\partial \xi_z}\right]_0^1 \\
&= \frac{D_B \times T}{{L_x}^2}\left(\frac{\partial^2 b}{\partial {\xi_x}^2} + \frac{{L_x}^2 \partial^2 b}{{L_y}^2 \partial {\xi_y}^2}\right) + D_B T \frac{1}{{L_z}^2}\left(\frac{\partial b}{\partial \xi_z}\right)\Big|_{\xi_z=1} - D_B T \frac{1}{{L_z}^2}\left(\frac{\partial b}{\partial \xi_z}\right)\Big|_{\xi_z=0}
\end{aligned}$$

At $\xi_z = 1$, the term $\frac{\partial b}{\partial \xi_z}$ is zero. Thus, we finally obtain:

$$\begin{aligned}
& -D_B \times T \times \frac{1}{{L_z}^2}\left(\frac{\partial b}{\partial \xi_z}\right)\Big|_{\xi_z=0} \\
&= -D_B \times T \times \frac{1}{{L_z}^2}.\left(-\frac{R_T.L_z}{D_B}\right)\left(-k_{on}.b.r + k_{off}.br.\frac{1}{B_0}\right) \\
&= \left(\frac{R_T \times T}{L_z}\right)\left(-k_{on}.b.r + k_{off}.br.\frac{1}{B_0}\right) \qquad (2.10)
\end{aligned}$$

So, the equation for BMP becomes:

$$\frac{\partial b}{\partial \tau} = D_B.T\left(\frac{\partial^2 b}{{L_x}^2 \partial {\xi_x}^2} + \frac{\partial^2 b}{{L_y}^2 \partial {\xi_y}^2}\right) + \left(\frac{R_T.T}{L_z}\right)\left(-k_{on}.b.r + k_{off}.br.\frac{1}{B_0}\right) \qquad (2.11)$$

The term $\frac{R_T}{L_z}$ in Eq.2.11 demonstrates that receptor density is homogenized over L_z length and the effective unit of receptor density becomes $Mole\ Length^{-3}$ during the initial dimer-receptor binding. Therefore, when a ligand is initially interacting with a free receptor it experiences a receptor density R_T with units different than the R_T unit for recruitment of subsequent receptors by ligand-bound complex (BR_i). So, it is imperative that these two different receptor densities are treated separately.

However, Eq.2.11 does not reveal much about receptor oligimerization step dynamics, and we dont obtain any information on the surface enhancement factor (γ) as defined before. To obtain more information on the surface dynamics, an alternative view of oligomerization dynamics by subdividing the extracellular binding domain is considered further.

2.2.4 Two sub-volume concept of receptor oligomerization dynamics

Let's consider a rectangular geometry Ω in the extracellular region, with L_x, L_y, and L_z as the dimensions along its x, y and z directions as shown in Fig.2.5. Along the z-direction, the extracellular space Ω is subdivided into two sub-volumes: i) a larger volume of height $L_z - l_z$ and ii) a smaller volume adjacent to cell-membrane with height l_z, as shown schematically in Fig.2.5.

Species in subvolume (Ah_2):

$$[Mole/L^3] : BR, BRS \tag{2.12}$$

Species in subvolume (AL_z):

$$[Mole/L^3] : B \tag{2.13}$$

BMP dimer B moves freely in the solution. When a dimer B comes within the smaller sub-volume of height l_z, initial binding takes place to form a BR complex. The 3-dimensional transport of a free dimer B within Ω can be represented as:

$$\frac{\partial B}{\partial t} = D_B\left(\frac{\partial^2 B}{\partial X^2} + \frac{\partial^2 B}{\partial Y^2} + \frac{\partial^2 B}{\partial Z^2}\right) \tag{2.14}$$

We define a set of dimensionless variable:

$$\begin{aligned} &\frac{B}{B_0} = b, \ \ \frac{R}{R_T} = r, \ \ \frac{BR}{R_T} = br, \ \ \frac{BRS}{R_{ST}}, \xi_x = \frac{X}{L_x}, \ \ \xi_y = \frac{Y}{L_y}, \ \ \xi_z = \frac{Y}{L_y} \\ &\xi_z = \frac{Z}{L_z}, \tau = \frac{t}{T} \end{aligned} \tag{2.15}$$

Using the set of dimensionless variable, we can rewrite:

$$\frac{\partial b}{\partial \tau} = D_B \times T\left(\frac{\partial^2 b}{{L_x}^2 \partial {\xi_x}^2} + \frac{\partial^2 b}{{L_y}^2 \partial {\xi_y}^2} + \frac{\partial^2 b}{{L_z}^2 \partial {\xi_z}^2}\right) \tag{2.16}$$

If the transport of a morphogen happens significantly faster than other processes within Ω, we can average the distribution of the morphogen over the whole extracellular domain, which is shown in the previous section. Furthermore, any BMP within

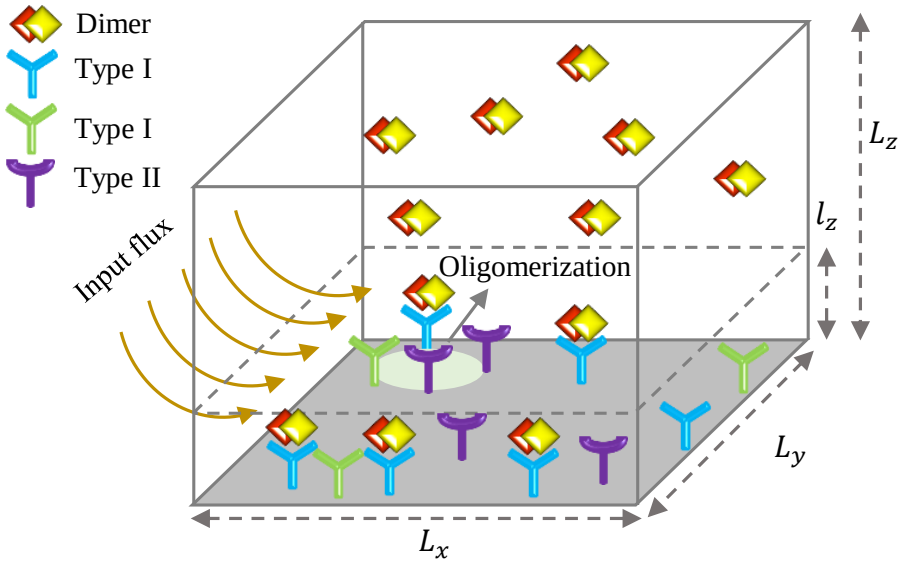

Fig. 2.5. Schematic representation of the two sub-volume concept: When BMP reaches a smaller volume it interacts with the transmembrane receptor and, subsequently, the ligand-bound receptor initiates the oligomerization steps. Oligomerization generates the required tetrameric receptor association to initiate downstream signaling.

l_z interacts with a receptor and hence, at l_z BMPs are captured through initial receptor binding events. Considering that dimer B is captured at l_z (or within l_z), and using the dimensionless variables, we rewrite Eq. 2.16 as follows:

$$\begin{aligned}
\frac{\partial b}{\partial \tau} &= D_B \times T\left(\frac{\partial^2 b}{{L_x}^2 \partial {\xi_x}^2} + \frac{\partial^2 b}{{L_y}^2 \partial {\xi_y}^2} + \frac{\partial^2 b}{{L_z}^2 \partial {\xi_z}^2}\right) \\
&- \left(k_{on} \cdot b \cdot r \cdot R_T - k_{off} \cdot br \cdot \frac{R_T}{C_0}\right)(1 - H(z - l_z)) \\
\frac{\partial b}{\partial \tau} &= \frac{D_B T}{{L_x}^2}\left(\frac{\partial^2 b}{\partial {\xi_x}^2} + \frac{{L_x}^2 \partial^2 b}{{L_y}^2 \partial {\xi_y}^2} + \frac{{L_x}^2 \partial^2 b}{{L_z}^2 \partial {\xi_z}^2}\right) \\
&- \left(k_{on} \cdot b \cdot r \cdot R_T - k_{off} \cdot br \cdot \frac{R_T}{C_0}\right) \\
&\quad (1 - H(z - l_z))
\end{aligned} \tag{2.17}$$

where, $H(n)$ is the Heaviside function and behaves as stated below:

$$H(n) = \begin{cases} 1 & \text{if } n > 0 \\ 0 & \text{if } n < 0 \end{cases}$$

As BMP is captured at, or within, l_z height only, no binding occurs within height $(l_z\ L_z]$ and the term $(1 - H(z - l_z))$ becomes zero when $z > l_z$. Transport of BMP across the gap (between l_z and L_z) is faster than other processes, which averages out the originally defined binding density (within l_z) over the L_z height. This redefines the receptor density to ensure the conservation conditions of the binding site density, and is readjusted as follows:

$$R_T = \frac{N_T}{A l_z} \tag{2.18}$$

$$\begin{aligned}
R_T \frac{l_z}{L_z} &= \frac{N_T}{A \times l_z} \times \frac{l_z}{L_z} \\
\Rightarrow R_T \frac{l_z}{L_z} &= \frac{N_T}{A \times L_z}
\end{aligned} \tag{2.19}$$

Also, the Heaviside function is eliminated and we finally obtain:

$$\begin{aligned}
\frac{\partial b}{\partial \tau} &= D_B \times T\left(\frac{\partial^2 b}{{L_x}^2 \partial {\xi_x}^2} + \frac{\partial^2 b}{{L_y}^2 \partial {\xi_y}^2} + \frac{\partial^2 b}{{L_z}^2 \partial {\xi_z}^2}\right) \\
&- \left(k_{on} \cdot b \cdot r \cdot R_T \cdot \frac{l_z}{L_z} - k_{off} \cdot br \cdot \frac{R_T}{C_0} \cdot \frac{l_z}{L_z}\right) \\
&= D_B \times T\left(\frac{\partial^2 b}{{L_x}^2 \partial {\xi_x}^2} + \frac{\partial^2 b}{{L_x}^2 \partial {\xi_y}^2} + \frac{\partial^2 b}{{L_x}^2 \partial {\xi_z}^2}\right) \\
&- \left(k_{on} \cdot b \cdot r \cdot \frac{R_T}{\frac{L_z}{l_z}} - k_{off} \cdot br \cdot \frac{R_T}{\frac{L_z}{l_z}} \cdot C_0\right) \qquad (2.20)
\end{aligned}$$

Therefore, in Eq.2.20, receptor density R_T is scaled down (from R_T to $R_T \frac{l_z}{L_z}$) by a factor equal to the ratio between the heights of the two sub-volumes. After the initial complex (BR_i) is formed, BR_i and other ligand-bound receptor species do not diffuse enough. Thus, we neglect the terms that account for diffusion, and represent changes in species concentration over time as a set of Ordinary Differential Equations (ODEs). The set of ODEs for receptor oligomerization steps are as follows:

$$\begin{aligned}
\frac{d[BR]}{dt} &= k_{on}[B][R] + k_{-}[BRS] - k_{off}[BR] - k_{+}[BR][S] \\
\frac{d[BRS]}{dt} &= k_{+}[BR][S] - k_{-}[BRS] \qquad (2.21)
\end{aligned}$$

where, free R and S are from a single free receptor pool, and are considered to be the same type of receptor. However, we used different naming in order to differentiate between the initial (R) and secondary receptor (S) recruitment. When R and S are considered similar type of receptors, the conservation condition shown in Eq. 2.4 readjusted as $R_T = R + S + BR + 2BRS$. Here, in Eq. 2.21, k_+ and k_- are the formation and decoupling rate constant for surface interactions. They are equal to k_{on} and k_{off} respectively, but their notations are made different.

Lets assume that the total number of BRS complexes formed on the surface is denoted as N_{BRS}. Then, Eq.2.21 becomes:

$$\frac{dN_{BRS}}{dt} = A \cdot l_z\left(k_{+}[BR][S] - k_{-}[BRS]\right) \qquad (2.22)$$

We consider receptor density $R_T^{l_z} = \frac{N_T}{A.l_z}$ within the small sub-volume of height l_z, where A is the surface area. The total number of receptors is equivalent to $N_T = R_T^{l_z} A.l_z$.

The transport of BMP is significantly faster than other processes during initial dimer-receptor binding and, hence, BMP distribution is averaged out over the sub-volume of height L_z. Because of this, receptor density needs to be adjusted to ensure that the total number of receptors is conserved. The readjusted binding density is:

$$R_T^{LZ} = \frac{N_T}{A.L_z} \tag{2.23}$$

When all the equations are homogenized over same volume of height L_z, we finally obtain the following from Eq.2.22:

$$\frac{dN_{BRS}/A \cdot L_Z}{dt} = \frac{A \cdot l_z}{A \cdot L_Z}\Big(k_+[BR][S] - k_-[BRS]\Big) \tag{2.24}$$

Species BR, BRS, R, and S are all defined in the small subvolume, and when homozenized over the larger volume of height L_z, it should be adjusted in the reaction terms as well.

Let's consider $R_T^{l_z}$ and $R_T^{L_z}$ as the receptor densities in smaller and larger volume respectively. As the total receptor number (N_T) is conserved, we obtain:

$$\begin{aligned} R_T = R_T^{l_z} &= \frac{N_T}{A.l_z} \\ \Rightarrow R_T \cdot \frac{l_z}{L_z} &= \frac{N_T}{A.l_z} \cdot \frac{l_z}{L_z} = \frac{N_T}{A.L_z} \\ \Rightarrow R_T \cdot \frac{l_z}{L_z} &= R_T^{L_z} \\ \Rightarrow R_T &= R_T^{L_z} \cdot \frac{L_z}{l_z} \equiv \mathbb{R}_\mathbb{T} \end{aligned} \tag{2.25}$$

Similarly, for BRS, S, BR we obtain:

$$\begin{aligned} BR &= \mathbb{BR} \cdot \frac{L_z}{l_z} \\ BRS &= \mathbb{BRS} \cdot \frac{L_z}{l_z} \\ S &= \mathbb{S} \cdot \frac{L_z}{l_z} \end{aligned} \tag{2.26}$$

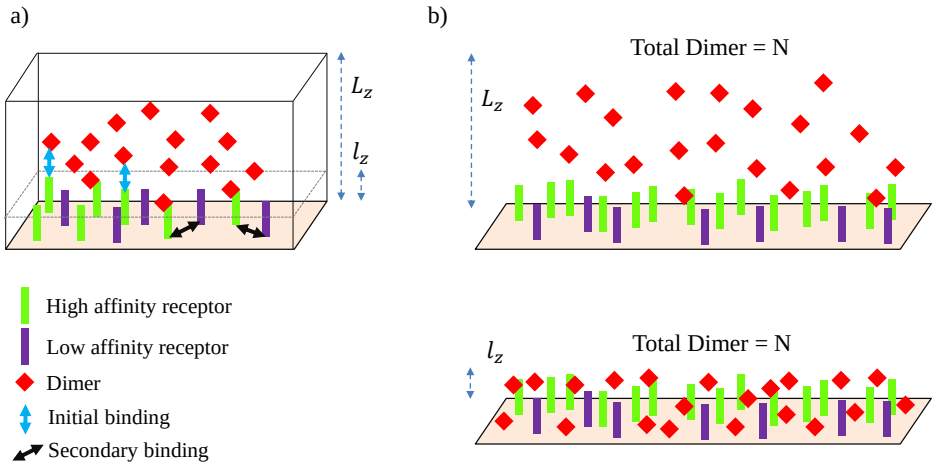

Fig. 2.6. Insights into receptor oligomerization: a) All free dimers reside in a 3D extracellular volume. Free dimers initially interact with receptors that have the highest affinity for dimer binding, as shown by the blue arrows. Upon formation of the dimer-receptor complex, all subsequent receptor recruitments, defined as secondary receptor recruitments (shown by black arrow), happen on the cell surface with a comparatively lower affinity than that of the initial binding. b) During initial binding, the receptor experiences dimers in a 3D volume, whereas during secondary binding it experiences all the dimer-receptor complexes, or free dimers in a 2D domain. This reduction in dimensionality increases the effective concentration (as the amount of Dimer = N is fixed) of dimers, as observed by all those low affinity receptors and is demonstrated here schematically.

By replacing these species in the reaction terms of Eq.2.22, the secondary receptor recruitment homogenized over the volume of height L_z as follows:

$$\begin{aligned} \frac{d\mathbb{BRS}}{dt} &= \frac{A \cdot l_z}{A \cdot L_z}\left(k_+ \cdot \frac{L_z}{l_z} \cdot \frac{L_z}{l_z}[\mathbb{BRS}][\mathbb{S}] - k_-[\mathbb{BRS}] \cdot \frac{L_z}{l_z}\right) \\ \Rightarrow \frac{d\mathbb{BRS}}{dt} &= \left(k_+ \cdot \frac{L_z}{l_z}[\mathbb{BRS}][\mathbb{S}] - k_-[\mathbb{BRS}]\right) \end{aligned} \tag{2.27}$$

The height of the smaller sub-volume can be correlated with the height of the extracellular domain of $TGF-\beta$ receptor, and may be useful to approximate the boost up factor (γ) for all subsequent receptor recruitments.

To summarize, after the formation of the initial dimer-receptor complex (BR_i), all the subsequent forward interactions between ligand-bound complexes (BR_i) and

receptors (S) on the surface happen at a rate that is γ times faster than the rate of initial dimer-receptor binding. The value of γ can be approximated by the ratio of the height of two sub-volumes (which is L_z/l_z), and an appropriate estimate of the surface enhancement factor γ would be within 10 to 100. Alternatively, the impact of the reduction of dimensionality from a 3D to 2D reaction could be demonstrated as shown in Fig. 2.6, where the effective dimer concentration, as observed by the free receptors, increases significantly once the dimer is initially trapped on the cellular surface. To account for the change in this effective concentration, complex formation occurs faster during the oligomerization steps.

2.2.5 Enrichment Criteria: constraints for signaling enrichment

To decide if the complete dimer-receptor system, as demonstrated in Fig.2.2, enriches under a specific physiological set up, we propose an enrichment criteria considering only 7 of the tetrameric receptor associations (shown in Fig.2.3) of the system. We assume in our analysis that all of the intermediate states (nodes other than the tetrameric receptor association), as shown in Fig.2.2, cannot activate signals, but that they instead either assist in dimer movement or may block dimers to assemble the tetrameric receptor association required for signaling. To compare between homodimer and heterodimer activity, a signaling strength ratio between the total concentration of $B27R_3R_8R_{II}R_{II}$ and the concentration of all other tetrameric complexes formed by B2 and B7 homodimers is considered, and is evaluated as follows:

$$\begin{aligned} P &= B27R_3R_8R_{II}R_{II} \\ L &= B2R_3R_3R_{II}R_{II} + B2R_3R_8R_{II}R_{II} + B2R_8R_8R_{II}R_{II} \\ &+ B7R_3R_3R_{II}R_{II} + B7R_3R_8R_{II}R_{II} + B7R_3R_8R_{II}R_{II} \\ \Rightarrow \quad & Signaling\ Strength(\alpha) = \frac{P}{L} \end{aligned}$$

When the signaling strength ratio (α) is greater than 1 ($\alpha > 1$) the system enriches. In another screening set up, an additional constraint (χ) is added to ensure that a

threshold level of $B27R_3R_8R_{II}R_{II}$ is generated in the system. In either case, if the system fails to satisfy the enrichment criteria, it is flagged as a non-enriched system, whereas for any satisfied case, it is marked with a circle on the $R_8 - R_{II}$ plane. The screening is conducted considering two different enrichment criteria– i) both α and χ are used to differentiate between enriched and non-enriched regions (data not shown), and ii) no threshold on the signaling strength requirement, that is, only with α.

2.2.6 Ordinary Differential Equation (ODE) model of receptor oligomerization

All the possible interactions are depicted in Fig.2.1, where each network edge demonstrates a bi-directional interaction between dimers and their cognate receptors. All of the forward interactions between dimer or dimer-bound receptors with free receptors follow a second order reaction rate constant. Receptor decoupling from any bound-state is treated as a first order reaction. We use mass-action kinetics to formulate the Ordinary Differential Equation (ODE) model.

The formulation presented in this work (Appendix A) for the receptor oligomerization process could be followed in other multimerization systems either by extending, or by truncating, the interactions steps. For example, if the multimerization requires fewer than the four receptor units as seen in the dimer-receptor model, interactions that generate tetrameric (and trimeric) receptor association could be omitted based on the final form of the com- plex in the system. For a multimerization system that requires the assembly of more than four receptors or membrane-bound molecules, extra binding event steps between tetrameric complexes and the membrane-attached species should be added. A Sample ODE model for BMP2 homodimer part is shown in Appendix A.

The complete ODE model of all the dimers contains 51 differential equations and more than 100 kinetic parameters. The dimer-receptor oligomerization model is remarkably supported by published kinetic data on receptor binding [82], leaving

only unknowns that include: i) the concentrations of BMP2, BMP7, BMP27, ii) the concentrations of Alk3/6, Alk 2/8, and Type II receptor, iii) the kinetics between BMP27 and Alk 2/8, and iv) the surface enhancement factor (gamma). We created a parameter space consisting of all these unknowns and conducted a screening over the parameter space to identify combinations that enrich the system and demonstrate heterodimer dominance.

2.2.7 Global parameter screen

To identify conditions that maximize the level of heterodimer signaling, we designed a global parameter screen that considers an uncertain parameter space and a set of cost functions (aimed at increasing the production of $B27-Alk3/6-Alk2/8-TypeII-TypeII$ complex). More precisely, the design chose the n best points found from a parameter screen over an uncertain parameter space. The space was formed by the surface enhancement factor γ, the K_D of Alk2/8 and BMP2/7 interactions, and the concentration of all dimers and receptors. Each time a parameter vector is selected, the design starts a gradient search from each. The computational setup for the screening was done using the codes developed in [113,114]. The customized setup details for the oligormerization ODE model is elaborated below.

Let us consider all the complexes formed in the system as c, and the parameters considered to perform the global screening as θ, where $\theta \in \Omega$. These are the set of parameters that are unknown and only a physiologically possible range of each parameter is known. With a given initial condition $c = c_0$, the non-linear ODE model of dimer-receptor interaction can be represented as:

$$\frac{\mathrm{d}\,\mathbf{c}}{\mathrm{d}\,t} = f(\mathbf{c},\theta); \mathbf{c}(t=0) = \mathbf{c}_0 = 0$$
$$y(\mathbf{c},\theta,t) = g(\mathbf{c}) \tag{2.28}$$

where, f is a deterministic smooth function of c, and $c \in \mathbb{R}^{n_c}$. To ease the computational cost, the dynamics of Eq.2.28 is approximated using the sparse grid toolbox for Matlab as described in [148]. The sparse grid offers a computationally efficient

and accurate way to approximate the dynamics concerning the uncertain parameter space (Ω). With sparse grid interpolant, the corresponding model output of the ODE system can be approximated as:

$$\widetilde{y}(\theta, t) = L_{d,q}(t) \times y(\theta, T_s) \tag{2.29}$$

where T_s represents time points where model outputs are approximated, and $L_{d,q}$ is the LaGrange polynomial with degree d. Subscript q represents the exact degree being used to build the polynomial ($0 < q < d$).

Upon initial screening using a sparse-grid, the chosen subset (Ω_s) of uncertain parameter space (Ω) is subsequently used to optimize the desired cost function. We designed a total of 5 objective functions that are minimized using a gradient search strategy, and the cost functions (CF, which is a function of species concentration in the system) are formulated as below:

1. CF1: $f(c) = \frac{Low\ \ signaling}{Productive\ \ Signaling}$
2. CF2: $f(c) = \frac{1}{Productive\ \ Signaling}$
3. CF3: $f(c) = \frac{\sum_{i=1, i \neq c_{hs}}^{N} c_i}{Productive\ \ Signaling}$
4. CF4: $f(c) = |((min(R_3, R_8, R_{II}) - Productive\ \ Signaling)|$

An alternative definition of a high-signaling complex is devised depending on the outcomes demonstrated in *Isaacs et.al*, where a single type I and two type II receptors can also elicit signals when bound with a heterodimer. This alternative definition is considered here to see if outcomes obtained with CF1 to CF4 matches with CF5 or not.

In *Isaacs et al.*, it is reported that B2 interacts with type I (bmpr1a) and type II (ActRIIb) with a K_D equivalent to 1.31 and 38.47 nM, whereas the B6 homodimer interacts with the same receptors with a K_D equivalent to 62.46 (bmpr1a) and 6.68nM. Binding kinetics for the BMP 2/6 heterodimer are 1.02 nM for bmpr1a and 6.52 nM

for ActRIIb, and experimental evidence demonstrated that the binding affinities for heterodimer BMP2/6 were dominated by the higher affinity binding of homodimers. This implies that the binding affinity of the B26 heterodimer and bmpr1a is primarily contributed by the high affinity binding of the B2 homodimer and bmpr1a, whereas the binding affinity of B2/6 and ActRIIb occurs mainly by the affinity of the B6 homodimer and ActRIIb binding.

2.3 Results and Discussion

2.3.1 Simple kinetic explanation is insufficient to demonstrate heterodimer dominance

Earlier studies reported the dominance of heterodimers over homodimers in the pattern- ing of Dorsal-Ventral (D/V) axis of Zebrafish [6]. It was shown through experimentation that a hetero-tetrameric receptor association consisting of two non-redundant type I receptors (Alk3/6, Alk2/8) and two type II receptors, bound by a heterodimer, is capable of eliciting signaling [6]. To explore the possibility that heterodimers prevails because they bind to the receptor complex with the lowest overall K_D, we developed a mathematical model of all the possible ligand-receptor interactions. The model is largely supported by the published kinetic data of dimer-receptor interactions, and was later used to conduct a parameter screen of the network by considering receptors and dimers as parameters. Each parameter was varied over at least two orders of magnitude and is summarized in the table below:

Published kinetic data suggests that BMP2 doesnt bind to Alk 2/8 at all because of an exceedingly high K_D between a BMP2 dimer and Alk 2/8 receptor. Hence, a BMP2/7 dimer is able to recruit an Alk 2/8 receptor only because of the presence of a BMP7 monomer in it. The kinetics of Alk 2/8 recruitment by a BMP2/7 heterodimer is considered equivalent to the kinetics between Alk 2/8 and the BMP7 homodimer. Initially, we used $K_D = 512$ nM for Alk 2/8 and BMP7 interaction interaction to keep it above or equal to 500 nM as mentioned earlier in [80], and we used the same

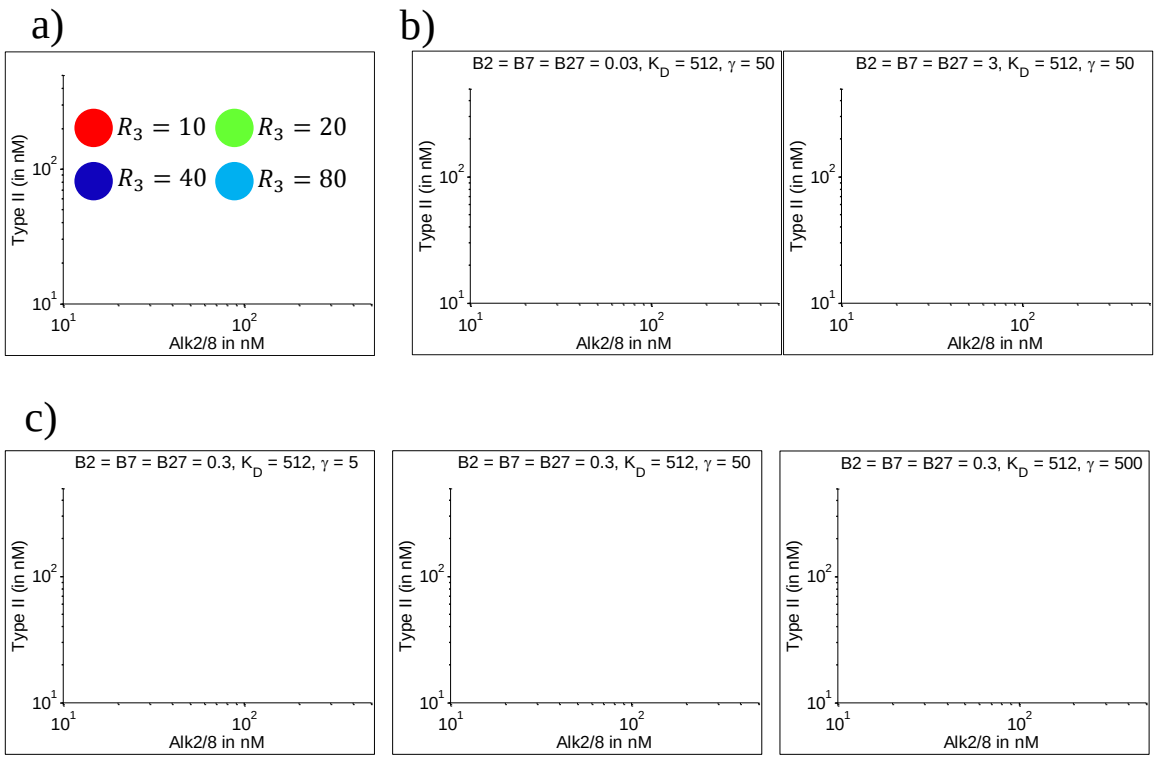

Fig. 2.7. Heterodimer dominance is not assured with a simple kinetics explanation: Dimer-receptor network screening by varying all the parameters reveals that heterodimer dominance is unobtainable with any combination of parameter values. Both X and Y axis are represented in a log-scale. a) The occurrence of heterodimer dominance is manifested here: any colored circle on the $Alk2/8 - TypeII$ plane demonstrates that heterodimer dominance is obtained for a specific combination of parameters. As seen in the plots, colored circles are used to vary the level of $Alk3/6$ (R_3) receptors. b) Dimer concentration varies over two orders of magnitude while fixing the surface enhancement factor to $\gamma = 50$ to obtain heterodimer dominance, but the colored circles are not visible on the $Alk2/8 - TypeII$ plane. c) Here, the dimer level is fixed at 0.3 nM, while the surface enhancement factor γ is varied over two orders of magnitude. Similar to previous screening outcomes, heterodimer dominance is unobtainable, as evident from the absence of colored-circle on the $Alk2/8 - TypeII$.

Table 2.2
Dimer-receptor levels used in the network screen

Parameter Name	Values	Grid Points	Comment
Bmp	$3\times$ $[10^{-2} to 10^{0}]$ nM	4	Bmp2 = Bmp7 = Bmp27
$Alk3/6$	[10 to 150] nM	15	uniformly distributed
$Alk2/8$	[10 to 500] nM	50	uniformly distributed
$TypeII$	[10 to 500]	50	uniformly distributed
γ	[10 100 1000]	3	logarithmic
Total grid points:			$\simeq$ 450000

value for the K_D between BMP2/7 and R_8 interactions ($K_D B27 - R_8$). The signaling strength (α) remained less than 1 for any combination of receptor-dimer concentrations we considered out of about 450,000 possible cases. This was demonstrated by the absence of the colored circles (the variation of Alk 3/6 is shown using different colors as demonstrated in part a) on the Type II-Alk2/8 plane, and, also, the outcomes remain unchanged when the dimer strength was increased by orders of magnitude as evident from Fig.2.7c. Even with enhanced 2^{nd} order reactions, as implemented using the surface enhancement factor ($\gamma = 1$) the signaling strength remained below 1, suggesting that the heterodimer complex contributed less compared to all other signaling complexes formed by homodimers.

2.3.2 A tight binding between heterodimers and Alk2/8 receptors can theoretically achieve heterodimer dominance

From the screening, it is evident that the natural hypothesis on heterodimer dominance based on a simple kinetic explanation does not favor heterodimer dominance (no colored regions appear on the plot shown in Fig.2.7). To obtain heterodimer dominance, we hypothesized that binding between Alk 2/8 and BMP2/7 binding may occur with considerably higher affinity than that of Alk 2/8 and BMP7, a possibility outlined in a previous study as well [6]. To test this hypothesis with the local ODE model of oligomerization dynamics, we varied the K_D between a B27 dimer and an R_8 receptor between 1 to 1000 nM.

In a well-mixed system, where BMP2/7 is free to bind to a pool of free receptors, the affinity of different receptor binding becomes important. In B27 and receptor binding, the two type I binding domains may recruit two Alk 3/6, Alk 3/6, where the 1^{st} Alk 3/6 binds according to BMP2 kinetics ($K_D = 0.8$ nM) and the 2^{nd} Alk 3/6 Alk 3/6 follows the BMP7 kinetics ($K_D = 46.6$) nM. When the K_D of Alk 2/8 of Alk 2/8 recruitment is reduced from 1000 nM to 10 nM in the system, the chances of BMP2/7 and Alk 2/8 interaction at the 2^{nd} type I domain increases, due to a lower $K_D B27-R_8 = 10$ than the $K_D = 46.6$ nM of the 2^{nd} Alk 3/6 recruitment. As a result, while keeping the level of Alk 3/6 fixed at 10 nM and type II at a very high value, an increase in the level of Alk 2/8 results in a considerable rise in concentration of the productive signaling complex $B27R_3R_8R_{II}R_{II}$, and the system elicits signaling (data not shown). Also, our simulation reveals that surface enhancement results in more tetrameric complexes. With these preliminary observations, we designed a global screen of parameter space coupled with a gradient search approach and identified the kinetic conditions that maximize heterodimer signaling in the system.

To identify conditions that maximize heterodimer-dimer signaling, we varied a number of parameters and optimized several cost functions each at a time to see the constraint needed on the K_D of Alk2/8 and the BMP2/7 dimer to maximize the

production of the stipulated signaling complex (B27-Alk3/6-Alk2/8-TypeII-TypeII). In this screening, concentrations of Alk 3/6, Alk2/8, and Type II receptors are 10 nM, 10 nM and 20 nM respectively, and remain unchanged in all other setups of global screening conducted in this study.

The K_D between the Alk 2/8 and B7 interaction is reported to be $>$ 500nM, and and as the K_D range for B27 and Alk 2/8 interaction is uncertain, we treated it as a parameter for the screening. To obtain a different K_D, we defined an upper and lower range for the forward reaction rate constant only. Furthermore, we hypothesized that after the initial binding event takes place on the cellular surface, the subsequent binding events happen at a faster rate due to the dimensionality reduction of the interaction domain. This factor γ is treated as another parameter, where the lowest value 1 manifests that the surface enhancement of kinetics during subsequent recruitment of receptors is not considered. The reverse reaction rate constant for Alk 2/8 and B27 interactions is taken as 0.000997 s^{-1}, and is kept unchanged for different K_D's used in the screening. K_D between Alk 2/8 and B7 interaction is reported to be $>$ 500nM. As the K_D range for B27 and Alk 2/8 interaction is uncertain, we treat it as a parameter for the screening. To obtain different K_D, we define a upper and lower range for the forward reaction rate constant only– that's the lower and higher K_D is obtained by tuning the $k_{on}[nM^{-1}s^{-1}]$.

Initial analysis shows that with the published kinetic data so far it is not possible to achieve heterodimer dominance as proposed. Our previous screen created a coarse grid consisting of all dimer-receptor concentrations as parameters and the binding kinetics of BMP2/7 and Alk2/8 heterodimer dominance was screened considering an enrichment criteria, and if the criteria was satisfied, we believed that the system demonstrated heterodimer dominance. While this screen was sufficient to determine if the published kinetic data was sufficient to explain heterodimer dominance, it did not identify mechanisms that, in theory, can ensure heterodimer dominance.

From the global screening of parameter space it is found that to maximize the production of the stipulated signaling complex $B27R_3R_8R_{II}R_{II}$ recruitment of Alk2/8

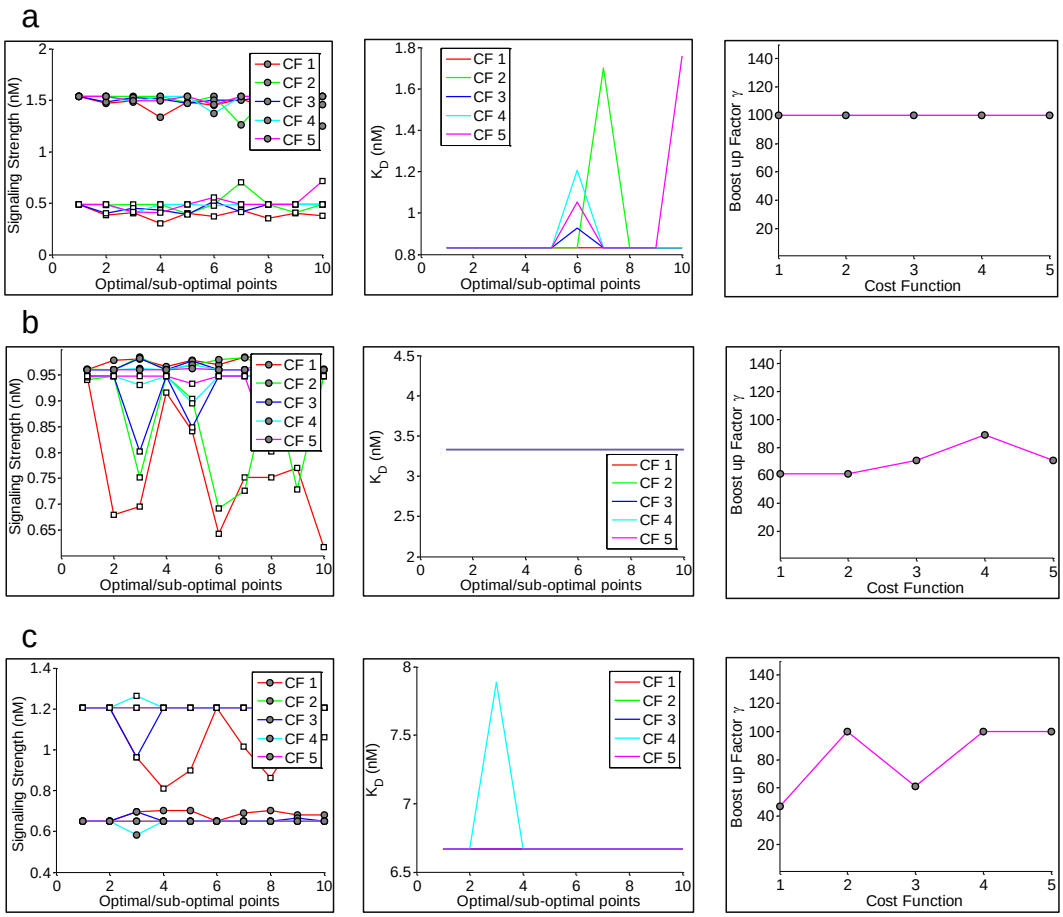

Fig. 2.8. Global screening of parameter space: a) Signaling enrichment is evident when the K_D between Alk 2/8 and B27 is within range 0.833 *to* 1.8 nM, and the range is true for all the CFs we have considered. This is shown in the left-most panel optimized screening gives a total of 10 optimal/sub-optimal parameter sets, and the corresponding low and high signaling strength is plotted along the Y-axis. For all optimal/sub-optimal points K_D for $Alk2/8$ and $B27$, interactions are between 0.833 to 1.2 nM and this is shown in the right panel. b) Similarly to part a, except that the lowest range for K_D was set to be 3.333 nM. An optimized condition for signaling enrichment requires K_D to range from 3 to 3.3 nM. c) The lowest K_D allowed for this global screening is 6.666 nM, and the screening reveals that optimal and sub-optimal points have a clear bias towards the lowest K_D allowed in the global screening process for the system. In all cases, the boost up factor (γ) is significantly greater than 1, which means that the boost up of secondary receptor recruitment on the cell surface is necessary to produce sufficient signaling.

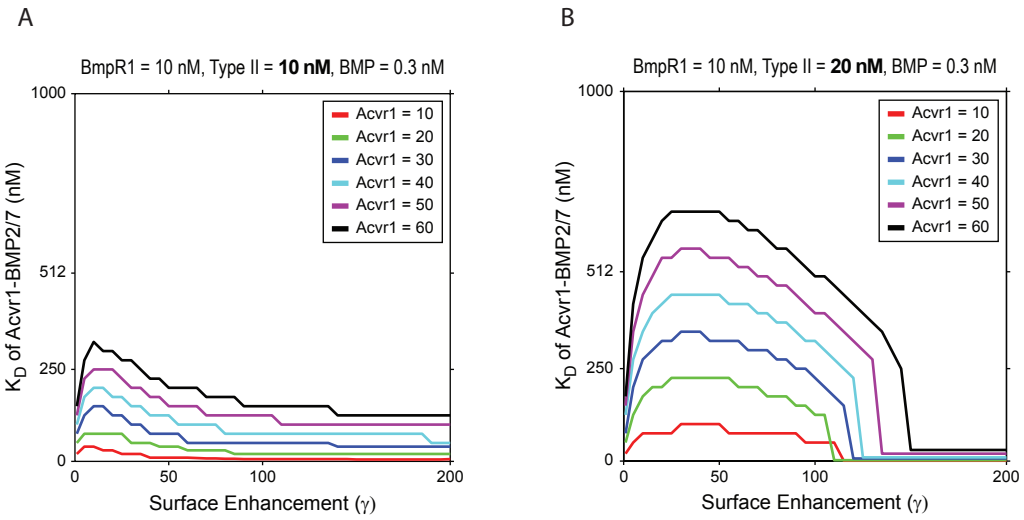

Fig. 2.9. Heterodimer dominance for tight Alk2/8 binding: $BMP2/7 - Acvr1 - BmpR1 - TypeII - TypeII$ dominance over BmpR1 homodimer formation could occur in systems with excess $Acvr1$ and a higher binding affinity between Acvr1 and BMP2/7. The lines on the plot demonstrate the specific requirements for the highest possible dissociation constant before the signaling system favors formation of $BMP2/7 - Acvr1 - BmpR1 - TypeII - TypeII$ at a ligand concentration of 0.3 nM.

Table 2.3
Parameters for the global screen

Parameter	Lower Range	Upper Range	Unit	Comments
K_D B27-Alk2/8	0.833	833.3	nM	$\frac{k_{off}}{k_{on}}$
k_{on} B27-Alk2/8	0.0000011964	0.0011964	$nM^{-1}s^{-1}$	forward rate const.
k_{off} B27-Alk2/8	0.000997	0.000997	s^{-1}	Same upper and l.
Boost up factor	1	100	-	$1 \equiv$ no boost up

by a BMP2/7 heterodimer must occur with a considerably higher affinity than BMP7 and Alk2/8. As seen in Fig.2.8, the minimum range of K_D between Alk2/8 and BMP2/7 dimer was gradually increased from 0.8 nM to 6.6 nM and, in all cases, signaling production was maximized for the lowest K_D allowed during the screening.

These facts, that published kinetic data fails to explain, and the global parameter screen reveal a low K_D requirement to maximize the signaling. The dimer-receptor model is later used to evaluate whether the BMP2/7 heterodimer prevails over the homodimers for low overall K_D interactions, where BMP2/7 heterodimers bind with Alk2/8 under a K_D that is considerably lower than the K_D between Alk 2/8 (such as, Acvr1) and BMP7 homodimers. From a screen of surface enhancement factor (γ = [1 200]) and K_D of Alk 2/8 binding, it is found that for an equimolar dimer level (BMP2/7 = BMP2 = BMP7 = 0.3 nM), and equal strength of each receptor (BmpR1 = Acvr1 = Type II = 10 nM), signaling enrichment can be achieved if the binding between BMP2/7 and Acvr1 is very tight. This means that a corresponding K_D should be very low, and is evident from Fig.2.9A (red line).

However, the requirement of tight binding is gradually relaxed as the level of Alk 2/8 (Acvr1) increases. Its worthwhile to note that not all the values of the sur-

face enhancement factor can produce heterodimer dominance, which could be caused by a quicker receptor saturation attained at the higher values of γ. Similar analysis conducted with an elevated level of Type II (= 20 nM) revealed the same, and is shown in Fig.2.9B. While heterodimer dominance is theoretically possible if the binding affinity between BMP2/7 and Alk2/8 is higher than both BMP7 and BMP2 homodimers, current measurements of kinetic data dont support a higher affinity between the BMP2/6 heterodimer and Acvr1 [138] and the computational model of dimer-receptor is further used to identify scenarios that favor heterodimer dominance in BMP signaling.

2.3.3 The hierarchy of tetrameric complex strength depends on the binding affinity

The three dimers (BMP2, BMP7, BMP2/7) produce a total of nine tetrameric complexes, known as the putative signaling complexes (shown in Fig.2.3), where the strength of all complexes is determined by their respective affinities for BMP receptors. As seen in zebrafish gastrula, this study considers an equimolar strength of all dimers. Steady-state concentrations of tetrameric complexes are collected for a wide range (0.0001 to 10 nM) of of dimer concentrations while keeping all other parameters fixed at a given level, and is repeated for different receptor strengths.

Published kinetic data informs that BMP2 homodimers have a significantly higher affinity for the Alk 3/6 receptor (BmpR1 in Fig.2.10) compared to other dimers. Thus, because BMP2 binding is stronger with Alk 3/6, in a competitive environment a BMP2 dimer recruits more BmpR1, resulting in a larger production of the $BMP2-BmpR1-BmpR1-TypeII-TypeII$ complex, which is more prevalent than other complexes in the system. Similarly, as BMP2/7 inherits one of the BmpR1 binding sites from a BMP2 monomer, the concentration of $BMP2/7-BmpR1-BmpR1-TypeII-TypeII$ is expected to be higher than complex $BMP7-BmpR1-BmpR1-TypeII-TypeII$ formed by the BMP7 homodimer. That is, an affinity based hierar-

chy is maintained among all the putative signaling complexes, and is evident from the simulated data as shown in Fig.2.10a,b. Between the $BMP2/7 - BmpR1 - Acvr1 - TypeII - TypeII$ and $BMP7 - BmpR1 - Acvr1 - TypeII - TypeII$ complexes, the affinity based hierarchy suggests a larger production of the BMP2/7 complex because of the presence of a high affinity binding site for BmpR1, as contributed in a BMP2/7 heterodimer by a BMP2 monomer. More Precisely, the relative strengths of putative signaling complexes with two BmpR1 in a BMP2/7 or BMP7 bound tetrameric complexes are 26% and 17% respectively. Simulated data, as observed here, is in agreement with the affinity-based hierarchy of tetrameric complex formation.

The simulation suggests that a few complexes do not form in considerable amounts because of the weak binding affinity between the dimers and the receptors family. For instance, since the affinity between dimers and $Acvr1(Alk2/8)$ is very low for BMP2 homodimers, and low for $BMP2/7$ and $BMP7$ homodimers, complexes that include two copies of $Acvr1(Alks2/8)$ are less likely to form, and is evident from the simulated data (approximately, 0% strength) as well.

To further analyze the affinity based hierarchy of tetrameric complex formation, a larger screen is performed, where dimer strength is varied over multiple orders of magnitude, imitating a low dimer level to overexpressed dimers. Receptor strengths were varied as well, and the initial concentration of Alk3/6, Alk2/8, and TypeII were chosen as 10 nM, 10 nM, and 10 nM respectively. Our simulated data showed that the common trend of the affinity based hierarchy of tetrameric complex is preserved for a wide range of dimer concentrations, and is summarized in Fig.2.11. Further simulation reveals that the affinity based hierarchy of putative signaling complexes (shown in Fig.2.11) is preserved when all the dimers are modeled as the system variables (Relevant equations and the sample plots of the affinity based hierarchy are available in APPENDIX B).

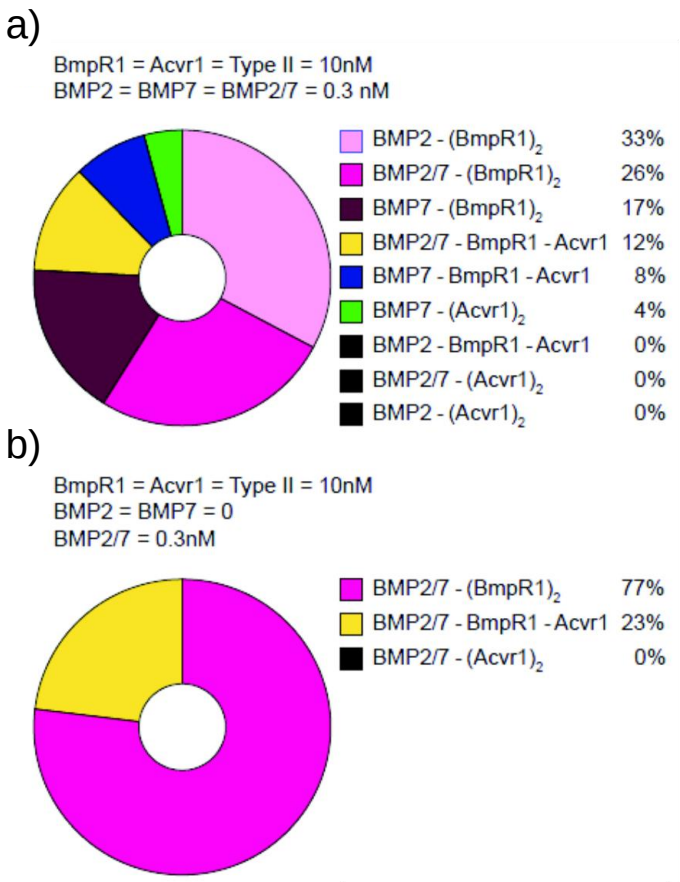

Fig. 2.10. Affinity based putative signaling complexes concentration: a) Based on the concentration magnitude, tetrameric complexes are arranged in descending order. As BMP2 dimer interacts with the $Alk3/6$ (BMPR1) receptor with the highest affinity (lowest K_D), $BMP2 - Alk3 - Alk3 - TypeII - TypeII$ complex is expected to be produced more than any other possible tetrameric complex. As BMP2 binds very poorly with the $Alk2/8(Acvr1)$ receptor family, the complex $BMP2 - Alk8 - Alk8 - TypeII - TypeII$ is expected to be the least produced complex at the given wild-type dimer-receptor strength. Heterodimer (BMP27) bound heterotetrameric receptor association is highlighted by a grey background and it resides at the fourth position in the affinity based hierarchy of putative signaling complexes. b) Affinity based BMP complex assembly for a $BMP2/7$ system, where the concentration of BMP2 and BMP7 were taken as zero. Because a $BMP2/7$ heterodimer possesses a higher affinity for the Alk 3/6 (BMPR1) receptors, the tetrameric complex consisting of two copies of BMPR1 is more prevalent than a heteromeric association (Acvr1-BMPR1) in the system.

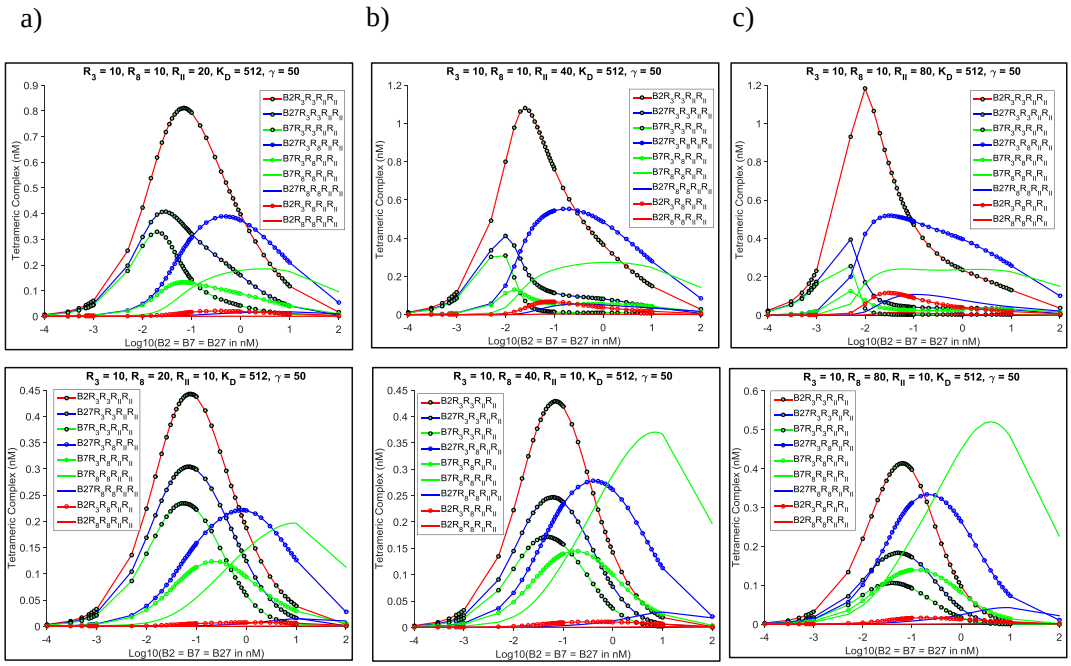

Fig. 2.11. Affinity based hierarchy of tetrameric complexes for different dimer concentrations: Based on the magnitude of concentration, tetrameric complexes are arranged in descending order. Because a BMP2 dimer interacts with the Alk3/6 receptor with the highest affinity (lowest K_D), $BMP2 - Alk3 - Alk3 - TypeII - TypeII$ is expected to be produced more than any other possible tetrameric complex. As BMP2 binds very poorly with the Alk2/8 receptor family, the complex $BMP2 - Alk8 - Alk8 - TypeII - TypeII$ is expected to be the least produced complex at the given Wild-type dimer-receptor strength. Heterodimer ($BMP2/7$) bound heterotetrameric receptor association is highlighted with a grey background, and it resides at the fourth position of the list.

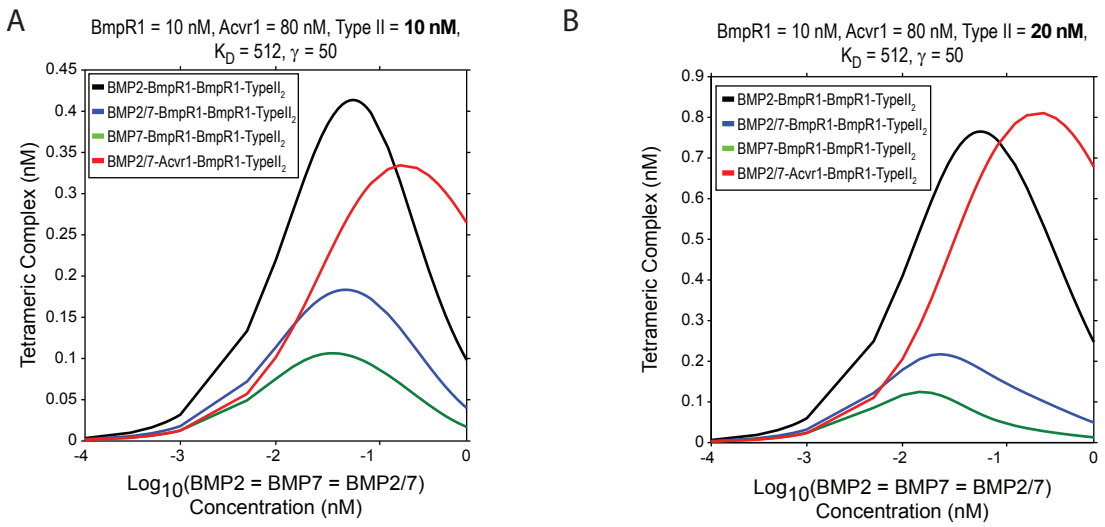

Fig. 2.12. Tetrameric complexes in the presence of an elevated Acvrl level: Distribution of tetrameric complexes is shown here as a function of ligand concentration in the system with an elevated Acvr1 level. As seen here, the level of BmpR1 receptor complexes exceeds the level of $BMP2/7 - Acvr1 - BmpR1 - TypeII - TypeII$ throughout the useful range of ligand. A similar trend is depicted for two different type II receptor strengths (10 and 20 nM in parts A and B respectively).

2.3.4 If homodimers are quelled by BMP antagonists, an elevated level of Alk2/8 as compared to Alk3/6 can initiate signaling

In the affinity based hierarchy of tetrameric complex formation, for equimolar dimer strength and equal amount of Alk 2/8 and Alk 3/6 receptors, stipulated signaling complex with two non-redundant copies of type I receptors ($BMP2/7-BmpR1-Acvr1-TypeII-TypeII$) fails to become the most prevalent complex. Instead, complexes that contain two copies of Alk 3/6 fill the top few positions of the affinity based hierarchy, and is reported in Fig.2.10 and Fig.2.11, for a given set of receptor strengths. However, as the molecular data on the precise quantification of receptor level is unavailable, we investigated whether or not the elevated level of receptor strength could explain heterodimer dominance.

Simulated data demonstrated that the typical predominant complex in the system contains two BmpR1 receptors: $BMP2 - BmpR1 - BmpR1 - TypeII_2$ (subscript 2 denotes two copies of TypeII), followed by $BMP2/7 - BmpR1 - BmpR1 - TypeII_2$, and then $BMP7 - BmpR1 - BmpR1 - TypeII_2$ as shown in Fig.2.10. The fourth most-prevalent complex $BMP2/7 - BmpR1 - BmpR1 - TypeII_2$ is the stipulated signaling complex. Even if the level of Alk 2/8 is a few times higher than the Alk 3/6 level in the system, the concentration of the stipulated signaling complex $BMP2/7 - BmpR1 - Acvr1 - TypeII_2$ fails to exceed the concentration of complexes with two copies of Alk 3/6 receptors and Type II receptors. For instance, the $BMP2 - BmpR1 - BmpR1 - TypeII_2$ complex maintains an overall high concentration when the level of Alk 2/8 (Acvr1) is 9 times higher than Alk 3/6 (BmpR1), and is shown in Fig.2.12.

As the elevated Acvr1 failed to explain heterodimer dominance, we considered the role of BMP antagonists further and investigated whether or not the preferential block of homodimer signals can initiate signaling enrichment both at elevated and normal receptor strengths. Zebrafish embryos express three extracellular BMP antagonists that participate in competitive interactions with BMPs and inhibit BMP signaling. The three antagonists are Chordin (Chd), Noggin1, and Follistatin-like 1b [149]. It is reported that the antagonists have variable affinity for different dimers. For instance, Noggin suppresses BMP homodimer signaling stronger than it does for heterodimers [150]. In vertebrates, Chordin binds similarly to homodimers and heterodimers [151]. However, Drosophila ortholog of Chordin, namely the Sog, demonstrates differential binding affinity for homodimers and heterodimers [29].

To test the hypothesis that BMP antagonists preferentially block BMP homodimers, allowing heterodimers to signal, we used the computational model to imitate a mutant scenario, where zebrafish embryos lack all of the BMP antagonists. That is, the computational model is a BMP2/7-only system and considers interactions between BMP2/7 and receptors only. It was found that when homodimers are preferentially blocked by the BMP antagonists, and the Alk2/8 (Acvr1) level is a couple of times higher than Alk 3/6 (BmpR1), stipulated signaling complex $BMP2/7 - BmpR1 -$

$Acvr1 - TypeII_2$ is favored over the complex with two BmpR1 and two type II receptors. Also, signaling through $BMP2/7 - BmpR1 - Acvr1 - TypeII_2$ is able to respond to a wide range of dimer concentration– a requirement that is necessary for a morphogen mediated patterning system.

2.3.5 BMP heterodimers maximize the dynamic range of signaling

[The following material is partly adopted from the manuscript (Dutko et al.) we have submitted for publishing.]

To further investigate the parameters of BMP2/7 heteromeric receptor signaling, we tested the potential contribution of each of the receptor levels. In model simulations, elevated levels of Acvr1 (Alk2/8) have little impact on BMP2/7 heteromeric receptor signaling, or lead to an initial increase in signaling, depending on the initial levels of Acvr1 and BmpR1 (Fig. 2.14A). For BmpR1 (Alk 3/6), however, an increase in BmpR1 rapidly attenuates signaling complex formation (Fig. 2.14B). In heterodimer-heteromeric receptor signaling, increasing BmpR1 levels lead to $BMP2/7 - (BmpR1)_2$ (subscript 2 means complexes that have two copies of BmpR1) complexes forming for small to moderate increases before Type II becomes limiting (Fig. 2.14C-D). If BMP2/7 signaled appreciably through BmpR1 homomeric complexes, signaling would increase in small to moderate increases in BmpR1. The overexpression of Acvr1 and BmpR1 is tested in vivo as well, and it is found that overexpressing Acvr1l had no effect on the functional signaling assay, whereas even mild increases in BmpR1 caused a loss of signaling.

We investigated whether heterodimer-heteromeric receptor signaling confers a performance advantage over homodimer-homomeric receptor signaling for a wide range of ligand concentrations expected in morphogen patterning systems. To function as optimal sensors for a morphogen, the receptors must mitigate noise and respond to a ligand gradient that sets multiple thresholds over space. We found that BMP2-BmpR1 homomeric complexes form over a BMP2 concentration range of 0.0006 nM up

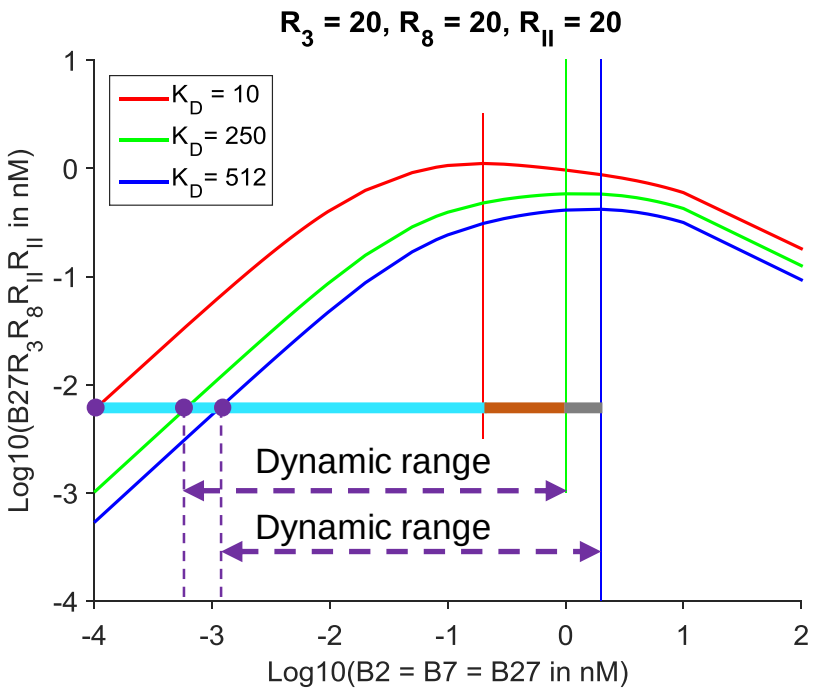

Fig. 2.13. The definition of dynamic range in BMP signaling: For equal dimer strength (B2 = B7 = B27) the signaling data is captured by varying input levels of dimers over several orders of magnitudes. Dynamic ranges of morphogens are defined between the minimum to maximum signaling, given that the signal level gradually increases as input morphogen increases. The dynamic range calculation for multiple distributions requires drawing straight line at the largest value of all the minimum signaling levels seen in each distribution. This line intersects other signaling distributions, identifying the lower end of the corresponding dynamic range, and is shown by drawing a cyan line from the minimum point of the signaling obtained for for $K_D = 10nM$. This line intersects the signaling distribution for $K_D = 250$ and $K_D = 512$ respectively, and provides the lower ends of the dynamic range of morphogen signaling for both K_Ds.

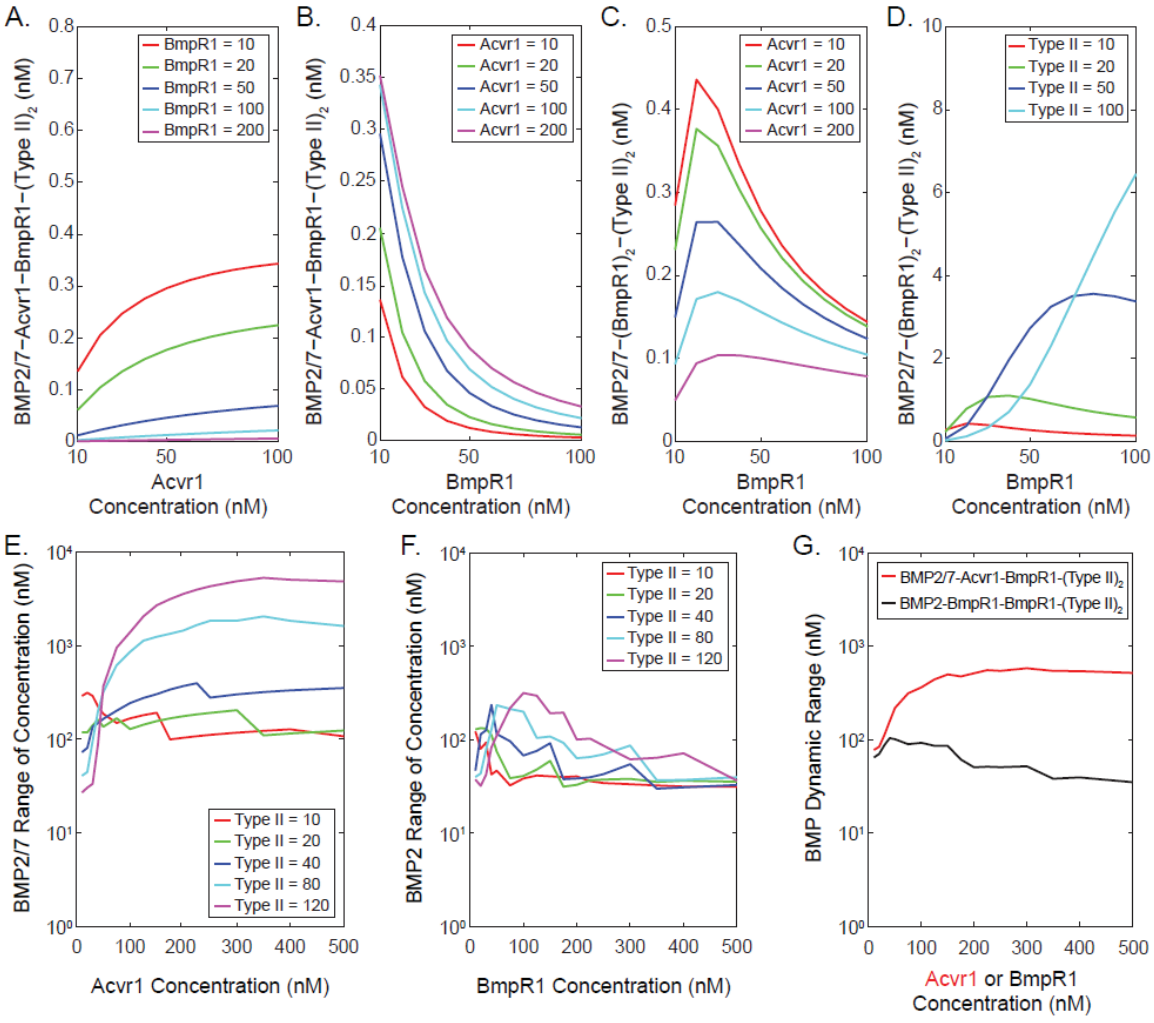

Fig. 2.14. The BMP heterodimer is a better sensor than a homodimer in a morphogen activity. (A-D). BMP2 = BMP7 = BMP2/7 = 0.3 nM; (A-C) Type II = 10 nM; (D) Acvr1 = 10 nM. (A) BMP2/7-heteromeric receptor complex formation (y- axis) exhibits low sensitivity to Acvr1 levels (x-axis), but (B) high sensitivity to increasing BmpR1 levels (x-axis). (C and D) Levels of BMP2/7-BmpR1- BmpR1 signaling complexes (y-axis) versus increasing levels of BmpR1 for different levels of Acvr1 (C) or Type II (D) receptors. (E-G) The dynamic ligand range is greater for (E) BMP2/7-BmpR1-Acvr1 than for (F) BMP2- BmpR1- BmpR1 complex formation at a wide range of receptor concentrations. (G) Shows the average dynamic range from E and F for heterodimer versus homodimer complexes over the range of Acvr1 (red line), or the BmpR1 (black line) receptors used in the model.

to 0.08 nM, where BMP2 saturates receptors in the model. In the model, heterodimer-heteromeric receptor complexes form over a 2.5 times higher BMP2/7 concentration range overall, from 0.003 nM up to 1 nM (Fig.2.15a).

When we consider any combination of receptor levels in the model (2.15a-b), the heterodimer system routinely exhibits better performance (Fig. 2.14E, G) than the BMP2 homodimer system (Fig. 2.14F, G), from a 40% to a 1000% increase in dynamic range (A definition of which is elaborated in Fig. 2.13). In addition to a greater range of ligand responsiveness, these data also show how a heterodimer ligand overcomes a common problem with a tight binding ligand-receptor complex such as BMP2 binding to BmpR1. Tight binding saturates receptors at low ligand concentrations [7, 62], such that the cells in a BMP gradient are saturated at 0.08 nM BMP2, limiting the formation of a spatial activity gradient that directs differential gene expression over space [3, 62]. Indeed, at the lower end of the BMP2 concentration range less than 0.001 nM free ligands approach one molecule or less per cell, which is unrealistically low (estimated for the extracellular volume around a 10 micron diameter cell).

Moreover, the upper and lower ends of the dynamic range are also tracked for a gradual increase of Acvr1 concentration, and the outcomes are presented in Fig. 2.15. The lower end of the dynamic range of $BMP2-BmpR1-BmpR1-TypeII-TypeII$ complex is always smaller than the dynamic range of the $BMP2/7-Acvr1-BmpR1-TypeII-TypeII$ lower end, suggesting a low number of signaling molecule regardless of the receptor strength considered. Also, the higher end of the dynamic range is smaller than the dynamic range of BMP2/7. This is indicative of more noisy dynamics due to a of a low number activity of signaling molecules [26, 152, 153].

To summarize, our in silico analysis revealed that the heteromeric complex, $BMP2/7-Acvr1-BMPR1-TypeII-TypeII$ is the fourth-most prevalent but signals exclusively, whereas BmpR1 homomeric complexes $BMP2-BmpR1-BmpR1-TypeII-TypeII$, $BMP2/7-BmpR1-BmpR1-TypeII-TypeII$, and $BMP7-BmpR1-BmpR1-TypeII-TypeII$ are more prevalent, but dont signal. Moreover, by requiring both BmpR1 and Acvr1, the heterodimer (BMP2/7) offers the best of both

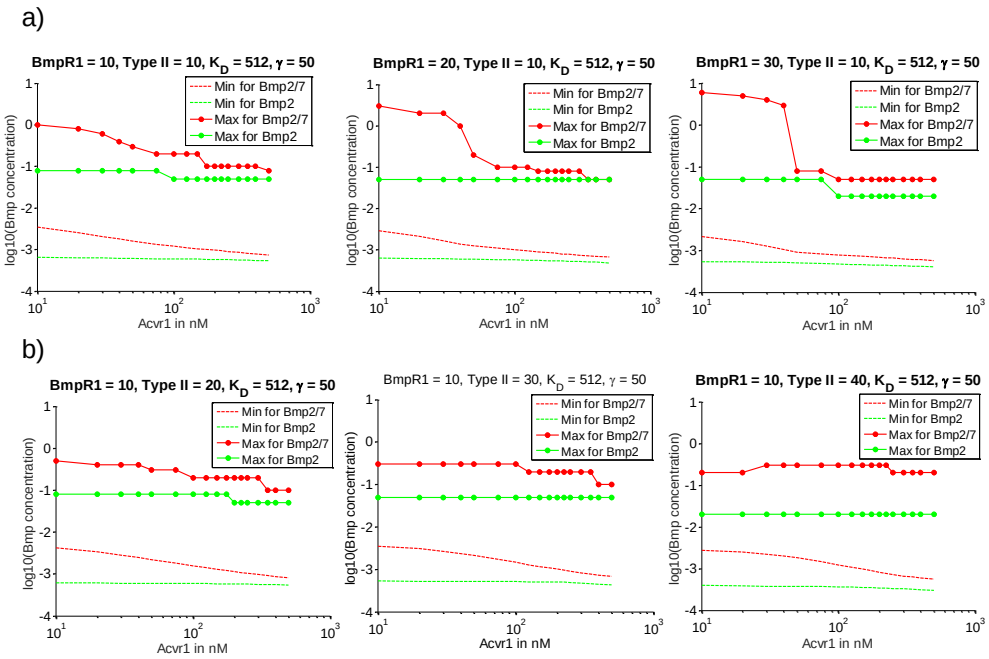

Fig. 2.15. A comparison of the upper and lower ends of the dynamic range. The upper and lower ends of the dynamic range of both $BMP2/7-Alk3-Alk8-TypeII-TypeII$ and $BMP2-Alk3-Alk3-TypeII-TypeII$ are tracked for a gradual increase in Alk 2/8 variation. The common trend, as observed here, is that regardless of receptor type, the upper end of the dynamic range of a B27-bound heterotetrameric receptor complex is always greater than a BMP2-bound homomeric receptor association. This leads into a comparatively larger BMP activity. When considered in an extracellular volume for stipulated BMP activity, the larger BMP activity results in a less noisy dynamics as opposed to the noisy trend of the low copy number BMP signaling demonstrated in [26]. a.) BmpR1 is varied while keeping the concentration of Type II fixed at 10 nM, b.) BmpR1 is fixed at 10nM and TypeII varied from 20 nM to 40 nM. In all these plots, red and green lines are used for $BMP2/7-Alk3-Alk8-TypeII-TypeII$ and $BMP2-Alk3-Alk3-TypeII-TypeII$ respectively.

ligand types. It can be recruited rapidly by its interaction with BmpR1 (Alk 3/6), but it also allows a greater dynamic range by binding to the lower affinity Acvr1 (Alk 2/8) before signaling.

2.3.6 Concluding remarks

In this study, we developed a new mathematical model of the receptor oligomerization process of membrane receptors in BMP signaling. The model disproves the kinetic based explanation, and showed that a simple kinetic based explanation is insufficient to explain the dominance of a BMP heteromeric complex. While the model disproves a kinetically-driven hypothesis, it indicates the possibility of other mechanisms of limited homodimer signaling. The model also proposed and tested alternative hypotheses for heterodimer dominance for the in-silico formation of BMP signaling complexes. Together with experimental measurements, the computational results identified mechanisms of BMP heterodimer dominance in the dorsoventral axis of the zebrafish embryo. Our model is consistent with the ligand and BMP antagonists pattern, and it incorporates the intrinsic binding affinity of BMP ligands with receptors, their levels, and the catalytic activity of the receptors to achieve a high range of signaling to pattern multiple cells types.

BMPs are important growth factors that control various developmental processes both in invertebrates and vertebrates, including humans. Evidences show that disruption of BMP signaling can cause developmental disorders and other diseases. Also, BMPs are very important bio-pharmaceuticals used for the treatment of skeletal conditions and in tissue engineering applications. Studies conducted within this field reveal details of BMP signaling mechanisms, which can be used to develop new biopharmaceuticals and treatments of BMP related dis- orders and diseases. Furthermore, the computational model developed for dimer-receptor interactions and subsequent oligomerization can be used in other systems where signaling requires multi-

merization of membrane receptors, such as the multimerization during the activation of the epidermal growth factor (EGF) receptor [137].

3. CHAPTER: ANALYSIS OF STOCHASTIC RECEPTOR OLIGOMERIZATION IN BMP SIGNALING

A large portion of the content presented in this chapter was published in the BMC Genomics journal [154]:

S Karim, GT Buzzard, DM Umulis. Efficient calculation of steady state probability distribution for stochastic biochemical reaction network. *BMC Genomics* 2012 13(Suppl 6):S10

Many biological networks exhibit stochasticity due to a combinatorial effect of low molecular concentrations and slow system dynamics. One important biological context where stochastic events likely have a large impact is the Bone Morphogenetic Protein (BMP) signaling pathway. BMPs make up the largest subfamily of the Transforming Growth Factor-β superfamily and are involved in numerous processes including growth, differentiation and diseases [7]. Due to their potency at driving development, they are also of great value for stem-cell differentiations in cell culture. BMPs activate near maximal signaling at $1nM$ concentration, have very slow binding kinetics and require oligomerization between multiple receptor subunits [7]. These properties naturally lead to conditions for significant and long-duration stochastic fluctuations in cellular signaling. Interestingly, variability of BMP signaling appears to be very low *in vivo*, while it is very high in stem cell culture studies [155]. What is the underlying causes for the difference between *in vivo* and in vitro signaling, and how do various receptor oligomerization steps alter the signal and noise? To address these important questions, we require stochastic models of receptor oligomerization to test different hypotheses.

In this chapter, a local stochastic model of dimer-receptor interactions was developed to investigate the impact of oligomerization steps on the noise regulation in the system. This work also performs a screen of the network for a number of unknown

kinetics by utilizing a steady state probability approximation approach developed earlier as part of our previous research [26,156]. In addition to the stochastic realization of oligomerization steps, this research also performs the bench-marking of steady state approximation method used in this analysis.

Our analysis revealed that no significant change in stochastic variability is observed with the inclusion of Type II receptors recruitment steps. This result supports a previous assumption made in [26] where the recruitment of Type II receptor was excluded to simplify the modeling steps while characterizing the noise profile of a SBP regulated BMP signaling system.

The rest of this chapter is arranged as follows. First, the importance of studying the stochastic model is described. Second, we provide the details of the stochastic model development and define the alternative ways of dimer-receptor interaction models. Then, we explain the network screen and data generation. Finally, this chapter concludes with results and discussion.

3.1 Background

During embryonic development, positional information is transduced by morphogens to underlying cells that respond to the concentration gradient of morphogen and eventually differentiate into distinct cell types [5]. For example, Decapentaplegic *Dpp*, a drosophila homologue of BMP2/4, forms a spatial profile to pattern dorsal tissues in *Drosophila* development [5]. In a canonical BMP signaling pathway, dimeric ligands bind to receptors and form a heterotetrameric complex that consists of two type I and two type II receptors [6, 29, 117]. The heterotetrameric receptor complex then phosphorylates the intracellular signal transducer Smad and the phosphorylated Smad forms a complex with a co-Smad [7, 29, 67]. Subsequently, the Smad/Co-Smad complex accumulates in the nucleus and regulates gene expressions in a concentration dependent manner [22, 67].

BMPs activate near maximal signaling at 1nM concentration [29], have very slow binding kinetics and require oligomerization between multiple receptor subunits [7,26]. These properties naturally lead to conditions for significant and long-duration stochastic fluctuations in cellular signaling. Interestingly, variability of BMP signaling appears to be very low *in vivo*, while it is very high in stem cell culture studies [155]. Understanding the differences between *in vivo* and in vitro signaling, and to determine how various steps in the receptor oligomerization process might alter the signal and noise, requires developing a stochastic model of the underlying oligomerization process. However, oligomerization steps generate a large number of intermediate states, and the number of states increases further if the interactions between BMP dimers and other antagonists, inhibitors and SBPs are considered [6, 7, 157].

Stochastic regulation can either negatively impact the robustness of the system [26, 109] or, constructively contribute to the phenotypic variation [152, 158, 159] in a species. In stochastic reaction networks, the state of a species traverses different trajectories in a probabilistic manner and the distributions of states can be difficult to predict. As more biological data is available, stochastic modeling is becoming increasingly popular to estimate properties in networks where the time evolution of the system is unpredictable and dependent on unavoidable randomness inherent to the system. The complete solution can be calculated from a Chemical Master Equation (CME) [160–162], that is based on a Markovian approach that captures the inherent randomness of biochemical systems.

Stochastic simulation of biochemical systems has been in place for decades [161, 163–166], but the use of Monte-carlo simulation of Markovian process is often hindered because of the computational costs associated with the tracking of trajectories of all the active species active in the system. Thus, simplifying a biochemical system by reducing interacting species while keeping the stochastic profile unchanged, would also benefit in developing more elaborate network including species of additional interest.

3.2 Model of oligomerization steps in BMP signaling

In the patterning models of BMP signaling pathways, it is often argued that a simplification strategy that omits the recruitment step of a Type II receptor bound to a BMP:Type I receptor complex doesn't affect the outcomes. [22,26,36,54]. While this approach is valid in the deterministic sense, it is not clear how this reduction impacts our estimates for noise in the system. In the BMP signaling pathway, secreted dimeric BMP-ligands (homodimer and heterodimer) interact with Receptor Tyrosine Kinases (RTKs), and presumably, form a quadripartite signaling complex consisting of two non-redundant type I and two type II kinase receptors [6, 29, 117].

In the signaling network shown in Figure 3, recruitment of Type II (= R_1) receptors can happen in two different ways: 1) BMP binds with Type I (=R_1) first and subsequently, recruits Type II receptors to form a tripartite complex BMP:Type I: Type II (BR_1R_2), and 2) BMP directly interacts with Type I and Type II separately, and an intermediate state forms a tripartite BMP:Type I: Type II complex. In both situations, BMP:Type I:Type II complex (BR_1R_2) is the sole signaling complex responsible for the activation of downstream pathways.

All possible biochemical interactions that represent the ligand binding with Type I receptors and further recruitment of Type II receptors are:

$$r_1:\ B + R_1 \xrightarrow{k_1} BR_1 r_2:\ \ BR_1 \xrightarrow{k_{-1}} B + R_1 r_3:\ \ B + R_2 \xrightarrow{k_2} BR_2$$

$$r_4:\ BR_2 \xrightarrow{k_{-2}} B + R_2 r_5:\ BR_1 + R_2 \xrightarrow{k_3} BR_1R_2 r_6:\ BR_1R_2 \xrightarrow{k_{-3}} BR_1 + R_2$$

$$r_7:\ BR_2 + R_1 \xrightarrow{k_4} BR_1R_2 r_8:\ BR_1R_2 \xrightarrow{k_{-4}} BR_2 + R_1$$

The chemical interaction of Case II can easily be obtained from the interactions (r_1 to r_8) of Case III (Figure 3) by equaling the kinetic rate constants $k_{\pm 2}$ and $k_{\pm 4}$ of Case III to zero. For the kinetics, we relied on the published data [7]. The rate at which a Type II receptor is recruited upon formation of a BMP:Type I complex (BR_1) is comparatively faster than the rate of BMPs and Type I receptors interactions [22]. However, exact values of the rates of formulation of (BR_1R_2) complex are not readily available, and hence, parameters were screened over the physiological ranges with

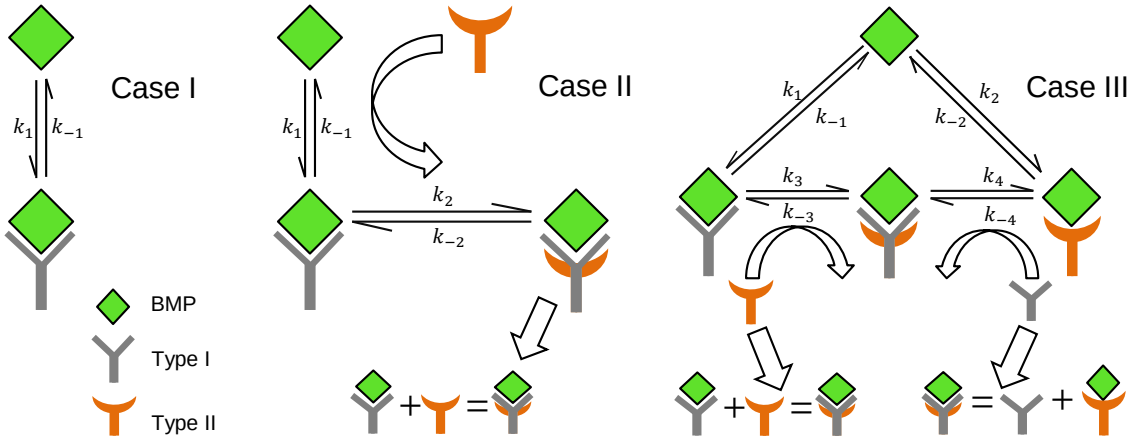

Fig. 3.1. Network cases for Type II recruitment analysis in context of Drosophila melanogaster development: Case I) Recruitment of Type II is overlooked here and it imitates the simplified model used in previous studies. In this type of network, BMP:Type I complex (BR_1) acts as the sole signaling complex. Case II) Upon the forma- tion of a BMP: Type I complex, subsequent recruitment of Type II receptor is considered here. However, a direct interaction between BMP and Type II receptors doesnt happen in the network. Here, a tripartite complex BMP:Type I:Type II (BR_1R_2) activates the downstream pathways. Case III) Similar to Case II, but with the exception that a direct interaction between BMP and Type II receptor is allowed to form a BMP:Type II complex (BR_1). The kinetic equations are equivalent to the SBP system investigated in [26].

values between $[10^{-1} \ to \ 10^{1}]\ nM^{-1}s^{-1}$ for the forward rates and $[10^{-3} \ to \ 10^{0}]\ s^{-1}$ for the reverse reaction rates.

3.3 Stochastic Model Development

The Chemical Master Equation (CME) describes the dynamics of the probability distribution of a species of chemical reactions. Specifically, the CME captures the rate of change of probability that a system will be in state $\mathbf{X}$ at time t for all the species of the system. Solution of the CME is practically intractable due to the curse of dimensionality, as the state-space of the system becomes enormously large with increases in the species number and concentrations (number of states n^N, for $N \rightarrow$ species, $n \rightarrow$ copies of each species). Moreover, the system often involves interactions between different time-scales (slow and fast reactions, frequent and infrequent transitions between states) [167], which add further complexity. Instead, numerical approaches are commonly used [163, 165, 168] to realize the CME of the stochastic system.

The Chemical Master Equation (CME), which is a set of first order differential (ODE) equations, demonstrates loss and gain of probabilities of discrete states of a system [162] and is often applicable to represent the stochasticity of the system. Consider a well-stirred system at thermal equilibrium of N different species $\{S_1, S_2, \ldots, S_N\}$ with $\{X_1, X_2, \ldots, X_N\}$ molecules respectively, participating in a total of M biochemical reactions R_μ, where $\mu = 1, 2, \ldots M$. The state of such a system is represented by the copy number (X_n) molecules of each species (S_n) at any given time t and is represented as $\mathbf{X} = [X_1(t), X_2(t), \ldots, X_N(t)]$. Unless a non-zero initial state is assigned, the default initial species concentrations are always zero $(X_n(t=0) = 0\ ,$ where $1 \leq n \leq N)$.

Two additional other quantities are required to construct the system: 1) a state-change vector ν_μ and 2) propensity functions [160, 163, 168, 169] for the reactions $R_\mu,\ \mu = \{1, 2, \ldots, M\}$. The state-change vector ν_μ for reactions R_μ is defined as

$\nu_\mu = [\nu_{1\mu}, \nu_{2\mu}, \ldots, \nu_{N\mu}]^T$, where $\nu_{n\mu}$ represents the change in concentration of species S_n, caused by the occurrence of R_μ reaction of the underlying biochemical system. These equations fully define the system and the time evolution of the probability function $P(\mathbf{X}, t)$ can be obtained by the solution of the Chemical Master Equation(CME) [160, 163, 169]:

$$\frac{\partial P(\mathbf{X}, t)}{\partial t} = \sum_{\mu=1}^{M} \Big(a_\mu(\mathbf{X} - \nu_\mu) P(\mathbf{X} - \nu_\mu, t) - a_\mu(\mathbf{X}) P(\mathbf{X}, t) \Big) \Big[(\mathbf{X} + \nu_\mu) \in \Omega \Big] \tag{3.1}$$

Here, $[(\mathbf{X} + \nu_\mu) \in \Omega]$ is 1 if $\mathbf{X} + \nu_\mu \in \Omega$ and 0 otherwise. The CME representing the rate of change of probability $P(\mathbf{X}, t)$ in an infinitely large state-space $\mathbf{X} \in \Omega$ is given by taking Ω to be the non-truncated space: $\Omega = \mathbb{N}^N$, $\mathbb{N} = \{0, 1, 2 \ldots\}$

In Eq.3.1, a_μ represents the propensity function to account for transition from a given state X to any other state, and ν_μ indicates the stoichiometry of the reaction μ that results in such a transition. The exact analytical solution of Eq.3.1 is intractable for a large number of species [170], and instead, numerical approximation is used. Approximation of CME can be achieved via Gillespie's SSA [161, 163], and a number of alternative algorithms have also been proposed to speed up the approximation of CME [164].

3.3.1 Steady state probability approximation

In the analysis of stochastic biochemical networks, steady state probability distributions for each species in the system are determined to measure variability about the deterministic steady state. The deviation around the solution contributes to stochastic noise that can be quantified by measuring the coefficient of variation $\Lambda = \frac{\sigma}{\mu}$ (the ratio between the standard deviation σ and the mean level of species concentration μ) obtained by solving the CME [161].

Frequently, Monte-Carlo based simulation approaches [161, 165] are used to solve stochastic problems. But, there are drawbacks to this approach for networks in which the dynamics of the systems' different intermediate states are unknown and continuation of several parameters is necessary to explore the systems' dependency. These networks necessitate screen of parameter values and the Monte-Carlo based approach doesn't prove to be efficient, as it generally takes longer time to numerically simulate the process and satisfy the imposed conditions. Moreover, simulation times increase with increases in the total number of molecules, species and the number of interactions between species.

In order to ameliorate computational cost and complexity, we apply a method developed in our previous research [26, 156] to approximate the steady state probability distribution by 1) reducing the system's state-space to a finite dimension using truncated state-space method [171] and 2) subsequently, translating an eigenvalue problem associated with a CME to a system of linear equations. We illustrate that the eigenvector (for an eigenvalue = 0) that represents the steady state probability distribution can be solved algebraically by approximating it as a system of linear equations.

Eq.3.1 is a linear system of differential equations and may be rewritten as follows:

$$\frac{\mathrm{d}\,P}{\mathrm{d}\,t} \;=\; LP \tag{3.2}$$

where P is the probability distribution $P(\mathbf{X}, t)$ for a vector $\mathbf{X} \;=\; [X_1, X_2, \ldots, X_N]$ and L is the time independent connection operator. For the steady state (SS) distribution, P_{ss}, we have

$$\begin{aligned} i){P_{ss}}^{X} \geq 0;\;\; \forall X \in \Omega \;\; ii) \sum_{\mathbf{X}\in\Omega} P_{ss}(\mathbf{X}) \;\; &= \;\; 1 \\ and \;\; iii) \;\; LP_{ss} \;\; &= \;\; 0, \end{aligned} \tag{3.3}$$

We assume that the deterministic steady state (SS) is unique. The non-truncated state-space Ω can be replaced with a truncated state-space $\hat{\Omega}$ [171,172] to approximate the probability distribution $P(\mathbf{X}, t)$. We define the truncated space as:

$$\hat{\Omega} \;=\; \{\mathbf{X} :\; \alpha_i \leq \;X_i \;\leq \;\beta_i \;, \quad \forall\, i\} \tag{3.4}$$

where α_i and β_i are extendable left and right boundaries of the truncated state-space, and is similar to that in [119], in which it is shown that the approximation based on the truncated space converges to the true steady state distribution as the limits of the truncated state-space converge to the limits of the original space.

The truncated state-space representation implies that given some $\varepsilon > 0$, for a sufficiently large $\beta_i > 0$ and sufficiently small $\alpha_i \geq 0$, the steady state probability distribution $P_{ss}(\mathbf{X})$ is approximated to within ε:

$$\sum_{X \in \hat{\Omega}} P_{ss}(\mathbf{X}) \;=\; 1 - \varepsilon$$

For an optimal SS probability approximation, ε should be made as small as possible. In the truncated state-space, Eq.3.3,(iii) is represented as-

$$\hat{L}\hat{P}_{ss} \;=\; 0 \tag{3.5}$$

where $\hat{L}$ is a matrix of propensities in $\hat{\Omega}$. To get the entries in $\hat{L}$ we use Eq.3.1 modified so that $P(\mathbf{X}, t) \;=\; 0$ if $\mathbf{X} \notin \hat{\Omega}$ and $a_\mu(\mathbf{X}) \;=\; 0$ if $\mathbf{X} + \nu_\mu \notin \hat{\Omega}$. In the truncated state-space $\hat{\Omega}$, Eq.3.5 is an eigenvalue problem for eigenvalue $\lambda \;=\; 0$ and the eigenvector $\hat{P}_{SS}$ can be obtained algebraically, or with an iterative algorithm for a large, sparse matrix $\hat{L}$. Instead of finding the eigenvector, which can be an ill-conditioned problem when there are nonzero eigenvalues close to 0, we translate the problem to a well-conditioned system of linear equations as follows:

We first evaluate the deterministic steady state (Y_0) of the system, and then select state X_0 of the discrete system closest to this deterministic steady state, where $X_0 \;=\; round(Y_0)$. Taking $\hat{P}_{ss}$ to be the solution of Eq. 5 and using the fact that the deterministic steady state solution is unique, we observe that $\hat{P}_{ss}(X_0)$ is among

the largest entries of $\hat{P}_{ss}$. The states in $\hat{\Omega}$ are labeled as $1, 2, \ldots, K$ with state X_0 denoted by j. Then,

$$\begin{aligned} \frac{\hat{P}_{ss}}{\hat{P}_{ss}^{j}} &= [\hat{P}_{ss}^{1} \ldots \hat{P}_{ss}^{j} \ldots \hat{P}_{ss}^{K}]^{T} / \hat{P}_{ss}^{j} \\ &= [\hat{q}_1, \ldots, \hat{q}_{j-1}, 1, \hat{q}_{j+1} \ldots \hat{q}_K]^{T} \end{aligned} \tag{3.6}$$

where $\hat{q}_k = \frac{\hat{P}_{ss}^{k}}{\hat{P}_{ss}^{j}}, k = 1 \ldots K$, $\hat{q}_j = 1$. With $\hat{q} = [\hat{q}_1, \ldots, 1, \ldots \hat{q}_K]$ Eq.3.5 now becomes $\hat{L}\hat{q} = 0$. Let $\hat{L}_k$ be the k^{th} column of $\hat{L}$. Expanding $\hat{L}\hat{q}$ by column and rearranging gives the following well-conditioned problem:

$$\begin{aligned} \sum_{k=1, k\neq j}^{K} \hat{L}_k \hat{q}_k &= -\hat{L}_j \; or, \\ \hat{L}'\hat{q}' &= -\hat{L}_j \end{aligned} \tag{3.7}$$

In Eq.3.7, $\hat{L}'$ is the matrix $\hat{L}$ with column j removed and $\hat{q}'$ is $\hat{q}$ with entry $\hat{q}_j$ removed. The error criterion for the system is checked for the calculation of $\hat{P}_{ss}$ until a satisfactory value is obtained (see algorithm 1 for further details).

A generalized algorithm for simulation according to the steady state approximation as outlined Methods section is given in Algorithm 1.

3.4 Benchmarking of Direct SS probability approximation method

Carrying out large-scale stochastic simulations can be time consuming, but calculation of the approximate solution via a truncated state-space can greatly improve the speed. In order to show the performance improvement in terms of computational cost and time of direct SS approximation in the analysis of stochastic biochemical networks, we benchmarked the method against Gillespie's stochastic simulation algorithm (SSA) method [161] for numerical calculations of stochastic biochemical networks. In the benchmarking, the processing time taken by each method was calculated based on the steps in the blue box as mentioned in the flow chart diagram (Figure 5).

Algorithm 1 Evaluate steady state (SS) distribution: $\hat{L}\hat{P}_{ss} = 0$

Require: Unique deterministic SS solution X_0

1. Reaction Networks with N Reaction $R_1, \ldots, R_N$
2. Choose: $\varepsilon,\ \gamma_0,\ \gamma$
3. Solve: ODE for steady state(SS) $= Y_0$ and find discrete state X_0 closest to Y_0, where $X_0 = round(Y_0)$.
4. Initiate $\alpha_i,\ \beta_i$; where $\alpha_i = (X_0)_i - \gamma_0,\ \beta_i = (X_0)_i + \gamma_0$
5. Determine: Truncated state-space $\hat{\Omega}$ as shown in 3.4 and $\hat{L}$ as described after Eq.3.5
6. Determine: Column j of $\hat{L}$ corresponding to X_0
7. Form $\hat{L}'$ and $\hat{L}_j$ as in Eq.3.7.
8. Solve: $\hat{L}'\hat{q}' = -\hat{L}_j$
9. Find $\hat{P}_{ss} = \frac{[\hat{q}_1,\ldots,\hat{q}_{j-1},1,\hat{q}_{j+1}\ldots\hat{q}_K]^T}{\eta}$, where $\hat{q}' = [\hat{q}_1, \ldots, \hat{q}_{j-1}, \hat{q}_{j+1}, \ldots \hat{q}_K]^T$ and $\eta > 0$ and $\eta = 1 + \sum_{l=1, l\neq j}^{K} \hat{q}_l$ is chosen so that $\sum_{X\in\hat{\Omega}} \hat{P}_{ss}(\mathbf{X}) = 1$
10. Verify:

if $\sum_{\mathbf{X}\in\hat{\Omega}, \mathbf{X}_i = \delta_i} \hat{P}_{ss}(\mathbf{X}) \geq \varepsilon$, for $\delta_i = \alpha_i$, or $\delta_i = \beta_i$ **then**

$\alpha_i \leftarrow \alpha_i - \gamma$

$\beta_i \leftarrow \beta_i + \gamma$

Return to 5

end if

Table 3.1
Benchmarking between Gillespie's SSA and Direct SS approximation for a target $BR_1R_2 = 20$

Method	End Time (ET) in Gillespie's SSA(hrs)	Processing Time (sec)	Λ
Direct SS approximation	Not Applicable	0.4 -0.6	0.1707
Gillespie's SSA	28000	90-95	0.1705
	2800	8-10	0.1878
	1390	4-5	0.2254

The sample problem was calculated for both methods on the same hardware and software configuration: Processor: Intel(R) Xeon (R) CPU E5405, 2.00 GHz (quad-core), *RAM:* 16 GB, SBTOOLBOX2 [173] and Matlab R2010a with SiMBiology 3.0. The processing time and computed Λ values for a target $BR_1R_2 = 20$ for Case II, Figure 3, is provided in Table 2 to show the accuracy and time gain that can be obtained if the proposed direct SS distribution approximation method is used. Gillespie's SSA takes longer to generate an output that contains enough information to calculate the distribution as compared to the time taken by Direct SS approximation method. The problem becomes severe when continuation of multiple parameters are necessary to explore the system's parameter dependency as done previously in [26].

In Table 3.1, the term 'End time (ET) in Gillespie's SSA' corresponds to the amount of time the system dynamics were allowed to evolve. The accuracy of the Gillespie's SSA approach depends on the 'End time in Gillespie's SSA'(directly contributes to the processing time) set in the model simulation, and is shown clearly in Fig.3.3a and Table 3.1. Very low propensities require long simulation times in Gillespie's SSA due to the infrequency of events. Accuracy of Gillespie's method for the sample example increases as the 'End time in Gillespie's SSA' is increased. This large simulation time in turn directly impacts the processing time, resulting in a large computational cost to achieve the desired accuracy (Table 3.1).

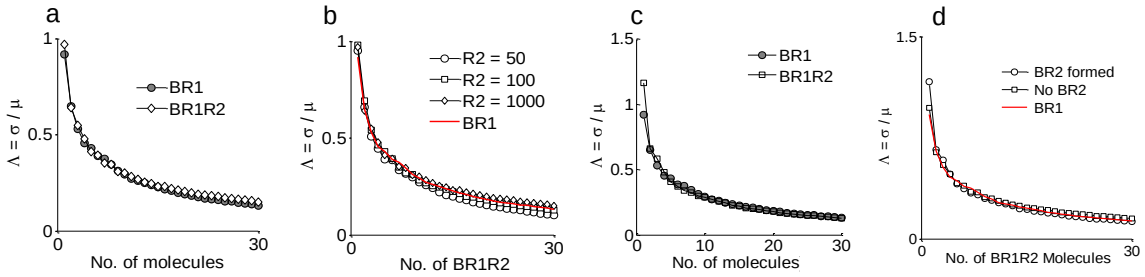

Fig. 3.2. A comparison of coefficient of variation Λ for three network cases: **a)** The coefficient variation of BR_1 (calculated from Case I Figure 3)and BR_1R_2 complexes (calculated from Case II Fig.3.1) is compared. The variability of the system seems to be invariant in the presence of Type II. **b)** The concentration dependency of Λ as a function of R_2. **c)** Same as plot "a", however, direct interaction of BMP and Type II is allowed as in Case III, Fig 3.1. It's clear that the stochasticity of the system does not change over the range of tested values. **d)** Summary of BR_1R_2 formation and its impact on signaling noise.

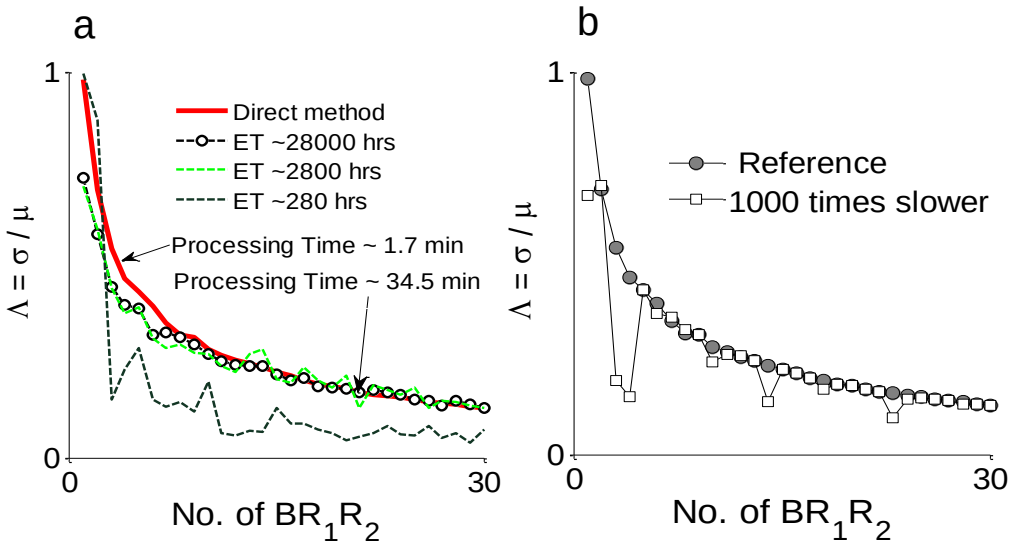

Fig. 3.3. **a)** In Gillespies method, a larger 'End Time' (ET) is required (which translates into a higher processing cost and time) to ensure the accuracy of outcome. Three different ET: 280 *hrs*, 2800 *hrs*, 28000 *hrs* are shown. **b)** The effect of kinetics associated with BR_1 interacting with R_2. The steps of interactions are clearly shown in Case II of Fig.3.1

3.5 Results and discussion

To simulate the networks as shown in Fig.3.1 for the calculation of the coefficient of variation Λ, we applied the truncated state-space approximation. During the simulation, a target of 1 to 30 signaling complexes (BR_1 for Case I and BR_1R_2 for Case II, Case III) in the extracellular region is considered so a direct comparison can be made for the coefficient of variation ($\Lambda = \frac{\sigma}{\mu}$) between B$R_1$ and BR_1R_2.

The coefficient of variation (Λ) for BR_1R_2 remains very close to the coefficient of variation of BR_1 as shown in Fig.3.2a. Proximity in the coefficient of variation between BR_1 and BR_1R_2 as shown in Fig.3.2a demonstrates that the stochastic variability of the system is not affected by the recruitment of the Type II receptor. It is also found that increasing the concentration of R_2 brings the coefficient of variation of BR_1R_2 into very close agreement with the coefficient of variation of BR_1 Fig.3.2ab. A similar outcome is obtained from the simulation of Case III of the Figure 3 and

the result is shown in Fig.3.2c. Finally, all the outcomes are summarized in Fig.3.2d, where it is shown that regardless of the different cases as shown in Figure 3 the coefficient of variation (Λ) of BR_1R_2 is approximately equal to that of BR_1.

Additionally, it is also found from the simulated results that the rate at which the BMP:Type I recruits Type II receptor (Case II in Fig.3.1) also decides the effect of Type II recruitment process on the stochastic variability of the system. With a comparatively slower rate, the coefficient of variation tends to oscillate as observed in Fig.3.3b. When the recruitment rate is slower than the formation rate of BMP:Type I complex, free Type II receptors fail to get frequent access to BMPs via the BMP:Type I:Type II tripartite complex, and can cause heconcentration of BMP:Type I:Type II complex to oscillate more than the case with a comparatively faster dynamics. Thus, mitigating noise is not a natural output of receptor oligomerization and transduction.

3.6 Concluding remarks

In this study, we investigated the binding of Type II receptor in BMP signaling. The results suggest that the recruitment of a type II receptor in BMP signaling doesn't affect the stochasticity of the system over the range of concentration and parameters investigated. Moreover, we also have shown that the larger receptor strength and rate at which Type II receptor is recruited also decides the impact on noise. In this work, we also have done a benchmarking of a steady-state probability approximation method that can be used in stochastic analysis of other biochemical system.

The outcomes of this research may be useful in developing stochastic models for receptor oligomerization steps, and in reducing interacting species without affecting the stochastic profile of the system. This eventually will contribute to reducing model and simulation complexity during the stochastic analysis of extracellular regulation of BMP signaling system.

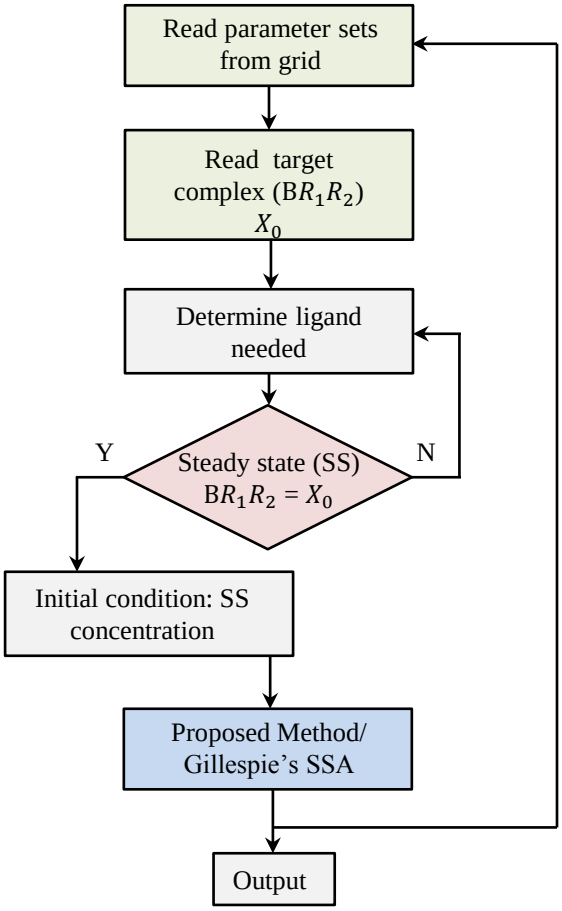

Fig. 3.4. Flowchart of the benchmarking of direct steady state (SS) probability approximation method

4. CHAPTER: SCALING MOTIFS IN MORPHOGEN-MEDIATED PATTERNING

Developmental processes in species require intricate and highly reproducible mechanisms of pattern formation, so the cell fate is assigned at the right time and location. This implies the existence of a developmental blueprint that developing species apply to generate appropriately positioned and proportioned patterns and structures. Through experiments, it is found that developmental processes resolve both inter-species and intra-species size-differences and other forms of perturbations. The intrinsic ability of a species to ensure such proportionate development of its constitutive organs and tissues is known as scaling [9, 86, 106, 174]. However, mechanisms behind the scaling of patterns are still elusive, and further theoretical and experimental studies should be devoted to reveal them.

This work proposed a simple theoretical model, namely the Two Component System (TCS), consisting of a tightly correlated morphogen (m) and a modulator (M). In TCS, The morphogen and the modulator spatially alter each others biophysical properties. Different network motifs involving m and M were considered, and they include positive, negative, and no-regulation cases for the production, diffusion, and degradation of morphogen-modulator dynamics. Later, using the model we identified a number of network motifs that can achieve the required degree of preciseness and resilience for flawless organs and tissue development.

Spatial dependence of all coefficients (such as, diffusivity, production rates, reaction rates) in the proposed TCS posed an enormous computational challenge, as we aimed to screen millions of network motifs to test a number of performance objectives designed for the scaling of patterns. The numerical screening required a fast, accurate, and efficient solver to screen over the millions of networks within a stipulated time. To achieve these goals, this work uses a multi-step method as implemented in

CVODE [175]. The method is based on the Backward Differentiation Formula, and implements a matrix-free [176] method that does not require storage of the Jacobian from the underlying linear system during every iteration step. Also, the solver option with the Krylov subspace method [177] was used to ameliorate the computational cost. To speed up data generation, numerical simulation of TCS using CVODE is coupled with super-computing clusters. In this study, the serial implementation of CVODE is used. The simulation setup and strategy used in this research could have potential usages in other models that frequently require an interrogation of system behavior under the reaction-diffusion and/or advection-diffusion-reaction paradigm.

This chapter is organized as follows. First, we analyze scaling definitions, and then we provide several previous models and mechanisms proposed to explain the scaling of patterns. Second, we propose the TCS model with all its variants and provide a mathematical representation of all versions of the TCS models. Third, regulatory equations for all biophysical properties are provided along with the range of parameters defined for numerical screening. The rationale of the specific forms of regulatory equations is presented using a simple ligand-receptor model. Then, we introduce the simulation details used to generate trustworthy data for further analysis. Finally, this chapter concludes with an analysis of the data generated and proposes a set of viable network motifs to explain the scaling mechanisms in various species.

4.1 Background

An astounding fact of species development that has fascinated the scientific community over many centuries is its remarkable reproducibility and preciseness. Despite the presence of numerous forms of perturbations (e.g. size-differences, varying nutrient, temperature etc.), developmental processes seem to replicate a common body template, where the proportions and positions of organs and tissues are perfectly maintained [8]. For instance, embryo size often varies substantially both within and

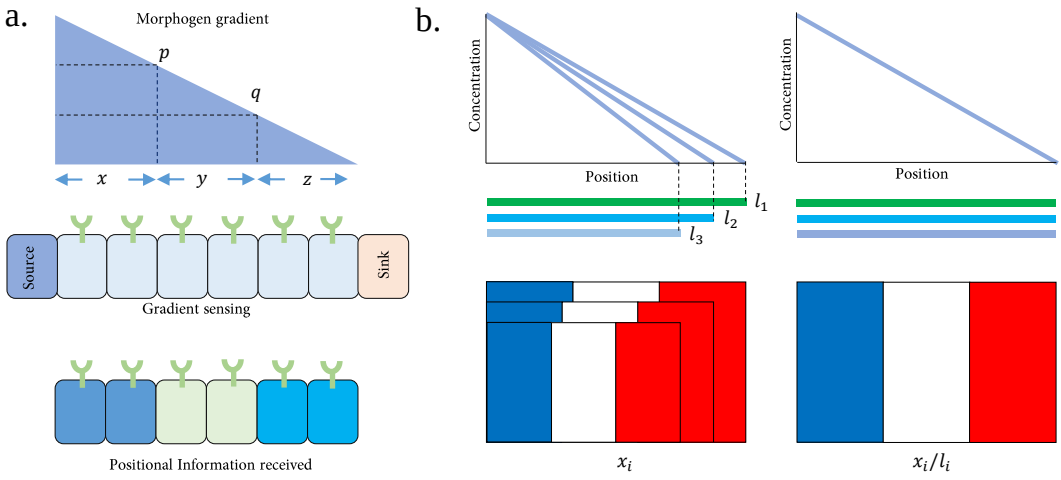

Fig. 4.1. Morphogen gradient and scaling of patterns: a) The Morphogen gradient acts as a patterning signal, and creates patterns among a homogenous field of cells in a concentration dependent manner. Cells sense the extracellular morphogen gradient through transmembrane receptors and discern according to morphogen thresholds (p, q). Therefore, cells between 0 to x length that sense a morphogen level greater than p become a specific cell type, whereas cells that sense a morphogen gradient between p and q assume a different cell fate. b) Scaling of patterns: For different system sizes (l_1, l_2, l_3), if the spatial position is normalized by their respective lengths, normalized distribution is superimposed perfectly a similar concept is explained (lower panel) using the French Flag Model.

between species among closely related dipterans, but the adult organisms maintain a perfect proportion of organs and tissues during development [12, 13]. Thus, developmental processes resolve both inter-species and intra-species size-differences and other forms of perturbations [9, 86, 106, 174].

The concept of scaling can be explained schematically by a non-biological model, namely the French flag model shown in Fig.4.1. According to the model, cells instruct their neigh- boring cells to adopt a specific cell fate in the presence of a signaling field. Cells located in the left-most region act as sources for a secreted group of molecules, such as morphogens, that transport away from the source creating a signaling gradient over a field of cells Fig.4.1b(left panel). Different regions are patterned in blue,

white, and red according to concentration dependent thresholds. In a perfectly scaled scenario, the blue, white, and red sections (in a species, this is similar to a specific field of cells) of different sizes will be superimposed when normalized against their respective flag length (l_i). However, *in vivo* morphogen signaling demonstrates scaling with a certain degree of precision [44], rather than a perfectly scaled scenario. rather than a perfectly scaled scenario. A developing system may also be subject to partial scaling when some positions of the system havent scaled perfectly [86, 174, 178].

The ways in which scaling is achieved within species is a fundamental biological problem that has not been answered with an adequate understanding of the underlying processes. A number of scaling mechanisms have been suggested so far based on mathematical analyses [9, 84, 86, 174, 179, 180]. For instance, in a reaction-diffusion system, the regulation of morphogen diffusion by a molecule secreted from all underlying cells can scale [106]. Another mechanism, namely the expansion-repression mechanism, suggests that scaling is achievable when the characteristic length of morphogen distribution is expanded by a diffusible molecule, and morphogens respond by repressing the production of that molecule [174]. Evidence of these mechanisms is found in the wing imaginal disc of Drosophila, where the Dpp gradient, a Bone Morphogenetic Protein (BMP), is expanded due to the activity of Pent (a regulator of BMP signaling), and the Dpp gradient suppresses Pent expression, completing the expansion-repression motif [10].

In addition, flux optimization provides scaling by adjusting morphogen peak level [9]. All these mechanisms are primarily based on the modulation of one, or more, biophysical quantities of morphogen by the presence of a spatially distributed modulator. In many cases the identity of regulator molecules in morphogen signaling is still unknown. Moreover, the modification of binding density is another proposed mechanism that ensures adjusting morphogen distribution in response to size variation [88]. The ratio based scaling mechanism proposed that if two morphogens emanate from opposing ends of the system, they achieve scaling via the signaling strength ratio

along the domain [179, 180]. Alternative mechanisms of scaling consider the binding site density of morphogens and other geometric factors.

To identify the mechanisms of scaling, we proposed a reaction-diffusion based model, the Two Component System (TCS), consisting of a morphogen (m) and modulators (M), where a morphogen and a modulator interact to spatially alter the biophysical properties of each other. The proposed regulatory machinery is used to identify a number of parsimonious network motifs that are resilient against perturbations. Our simulation reveals that if a morphogen, a gradient based signal inducer active in a large number of species during different developmental stages, and a modulator mutually regulate their respective biophysical properties, scaling of patterns occurs in response to different perturbations, such as, system length variation, input-flux variation of morphogen.

4.1.1 Extracellular Regulation of Morphogen Signaling

Numerous developmental processes directly rely on the local concentration of a secreted group of molecules known as morphogens. A morphogen, upon secretion, transports away from its spatially localized source, creating a spatially non-unform gradient between the source and sink regions [1–5]. For instance, Bone Morphogenetic Proteins (BMPs) act as morphogens in context of the D/V patterning of both vertebrates and invertebrates. BMPs transduce extracellular information to activate downstream signaling pathways by binding to their cognate receptors. Experimental evidence shows that morphogens not only interact with their cognate receptors, but are also known to interact with a number of other extracellular factors [7, 22, 181] that can modulate morphogen distribution and affect the activation of downstream pathways. The secreted regulators of BMPs do not act as BMP inhibitors such as Sog, Chordin, Noggin, and Follistatin [149,150]. Instead, they demonstrate a context-dependent auxiliary function in BMP signaling that can promote or inhibit signaling. A number of BMP regulators have been identified (approximately 20 or more), and

it is reported that the regulators possess cell autonomous effects on BMP signaling. Amongst the regulators, a large portion is attributed with the ability of limiting or promoting BMP signaling [7].

In general, examples of modulators may include activators, inhibitors, and other proteins that interact extracellularly with morphogens and regulate concentration, length, and time-scale of morphogen distribution as well. For instance, in Drosophila melanogaster, Decapentaplegic (Dpp) is a morphogen that actively participates in anterior-posterior (A/P) cell fate determination within the wing imaginal disc [92, 182]. In the early embryo, Dpp levels are highest near the dorsal midline with lower expressions in the lateral domain. However, it has also been shown that during earlier stages, transcription of Dpp is uniform throughout the entire dorsal domain. This suggests that additional secreted extracellular factors are involved in shaping Dpp distribution, which may include inhibitor short-Gastrulation (Sog), Twisted-Gastrulation (Tsg), and metalloprotease Tolloid (Tld) [9,29,71], as well as many other factors [6,42]. Another extracellular factor that regulates Dpp signaling in Drosophila is Dally [181, 183], a heperan sulfate proteoglycans (HSPGs) [184]. Experimentally, Dally is shown to act as a modulator of Dpp by disrupting both receptor-mediated uptake and degradation of Dpp-receptor complex [181, 183, 185].

Moreover, dorsal-ventral (DV) patterning in xenopus also involves a number of potential candidates that can act as modulators for morphogen signaling. In Xenopus, BMP4/7 expression is ventrally high with a positive feedback loop in place to maintain a high level of BMP signaling in the ventral region, whereas BMP2 and antidorsalizing morphogenetic protein (ADMP) levels are repressed ventrally and they maintain high signaling at the dorsal region [186].Chordin (Chd), an inhibitor, is responsible for inhibiting BMP4/7 in the dorsal region to create a low expression level of BMP4/7, whereas BMP2 and ADMP are highly expressed in the dorsal regions. As a result, the opposing gradients of BMPs and Chordin are active during pattern formation. Due to this interplay between varying BMP ligands and ADMP, and because the total BMP signaling is defined as the sum of all BMP activities in the D/V patterning

of xenopus, the loss of all four BMP ligands involved in DV patterning is needed to cause dorsalization [187]. While in Drosophila, the depletion of a single BMP ligand is sufficient to ventralize the embryo.

In xenopus D/V pattenring, ADMP exhibits a dual role of both morphogen and expander- it expands the BMP signal to the ventral region and is eventually repressed by the BMP signal. This results in closing the feedback loop of expander-repression mechanisms [10,174]. D/V patterning in Xenopus can thus be considered an example of a TCS system composed of morphogen and modulator.

4.1.2 Scaling in reaction-diffusion model of morphogen signaling

The notion of scaling of morphogen mediated pattern formation can be explained by considering a simple model of morphogen dispersal, where the dispersal of morphogens happens through a diffusion-decay mechanism. As stated mathematically, upon secretion from a source located at $X = 0$, morphogen transports away from the source by a diffusion-decay mechanism. With necessary initial (I.C) and boundary conditions (B.C), the morphogen dispersal model is represented as follows:

$$\begin{aligned} \frac{\partial m}{\partial t} &= D_{m0}\frac{\partial^2 m}{\partial x^2} - k_m[m] \\ B.C &: -D_{m0}\frac{\partial m}{\partial x}\bigg|_{x=0} = j, \frac{\partial m}{\partial x}\bigg|_{x=L} = 0 \\ I.C &: m(x, t=0) = 0 \end{aligned} \tag{4.1}$$

Units of D_{m0}, k_m is $(length)^2$ $time^{-1}$ and $time^{-1}$ respectively. The dimensionless form of Eq.4.1 is obtained by defining two dimensionless variable $\tau = \frac{t}{T}$ and $\xi = \frac{x}{L}$, and the dimensionless form is as follows:

$$\begin{aligned} \frac{1}{T}\frac{\partial m}{\partial \tau} &= \frac{D_{m0}}{L^2}\frac{\partial^2 m}{\partial \xi^2} - k_m[m] \\ B.C &: \frac{\partial m}{\partial \xi}\bigg|_{\xi=0} = -\frac{jL}{D_{m0}}, \frac{\partial m}{\partial \xi}\bigg|_{\xi=1} = 0 \\ I.C &: m(\xi, \tau=0) = 0 \end{aligned} \tag{4.2}$$

Rearrangement of Eq.4.2 gives us three dimensionless quantities, all of which should be length or flux-independent in order to achieve scaling. The dimensionless terms are: $\frac{1}{Tk_m}$, $\frac{D_{m0}}{k_m L^2}$, and $\frac{jL}{D_{m0}}$.

By defining $J = \frac{jL}{D_{m0}}$ and $\lambda^2 = \frac{k_m L^2}{D_{m0}}$, and considering steady state analysis of morphogen dispersal system we obtain the Sturm-Liouville form of equation with a generalized solution as given below:

$$m_{ss}(x) = A \times e^{(\lambda x)} + B \times e^{(-\lambda x)} \tag{4.3}$$

Here, A and B are integral constants and can be calculated using the two boundary conditions (B.C)– $A = Be^{-2\lambda}$ and $B = \frac{-J}{\lambda((e^{-2\lambda})-1)}$. By plugging in the values of A and B, we obtain:

$$m(\xi) = \frac{J}{\lambda}\left[\frac{e^{(\lambda(2-\xi))} + e^{(\lambda\xi)}}{e^{2\lambda} - 1}\right] \tag{4.4}$$

where, $A = Be^{-2\lambda} = \frac{-J}{\lambda((e^{-2\lambda})-1)}e^{-2\lambda}$ and for a large λ, $A \to 0$ and the steady-state profile of morphogen becomes:

$$m(\xi) = \frac{J}{\lambda}B \times e^{(-\lambda\xi)}$$

$$m(\xi) = \frac{j}{\sqrt{k_m D_{m0}}}B \times e^{-\left(\sqrt{\frac{k_m L^2}{D_m}}\xi\right)} \tag{4.5}$$

The system scales if the morphogen distribution m in Eq.4.5 becomes independent of system length L (scale-invariance) and production (robustness) of morphogen j.

Morphogen spreading is controlled by the rate of diffusion (D_{m0}) and the rate (k_m) at which morphogen degrades while spreading. That is, the decay length of (ψ) morphogen distribution is directly dependent on the diffusion and degradation dynamics of morphogen, and morphogen distribution must adjust its decay length to accommodate the system size variation (shown in supplemental information). The decay length (ψ) of morphogen can be defined as:

$$\psi = \sqrt{\frac{D_{m0}}{k_m}} \tag{4.6}$$

Inspection of Eq.4.6 demonstrates that to achieve scaling when system length L increases, morphogen must diffuse faster, or either the degradation of morphogen happens at a slower rate, or both the degradation and diffusion of morphogen must change together to ensure scaling. This suggests the notion of modulation of biophysical properties of morphogens, and indicates the potential existence of modulators capable of altering transport and reaction dynamics of morphogen to achieve scaling.

For a perfect scaling, the ratio $(\frac{\psi}{L})$ should remain constant along the process. Furthermore, we can define two more quantities: diffusion time (τ_D) and reaction time (τ_R) (preferably the slowest one). The diffusion time τ_D demonstrates the time on average taken by a molecule to diffuse through distance L, shortly known as the transport time scale as well.

$$\tau_D = \frac{L^2}{D_{m0}} \tag{4.7}$$

$$\tau_R = \frac{1}{k_m} \tag{4.8}$$

We define another dimensionless parameter (χ) to measure the scaling of morphogen distribution, which is as follows:

$$\chi = \frac{D_{m0}}{k_m L^2} \tag{4.9}$$

Our performance objectives could be correlating these quantities with systems that scale and exhibit robustness, given that morphogens and modulators regulate each others biophysical properties.

4.1.3 Modulation of biophysical properties: transport modulation

Regulation of biophysical properties is at the center of the TCS model. It also identifies the form of the modulation equation between morphogen and modulator. A simple model of morphogen and regulator binding (similar models can be formed using interactions between BMP and SBP [26], or inhibitors [7,86] etc.) is considered here to study the form of regulatory equations that can arise because of the mutual

regulation between morphogens and modulators. In the model, a diffusing morphogen (m) interacts with a signaling regulator (R) and forms a complex, denoted as mR. Mathematically, the model can described as:

$$\begin{aligned} \frac{\partial[m]}{\partial t} &= D_{m0}\frac{\partial^2[m]}{\partial x^2} - k_1[m][R] + k_{-1}[mR] \\ \frac{\partial[mR]}{\partial t} &= D_{mR0}\frac{\partial^2[mR]}{\partial x^2} + k_1[m][R] - k_{-1}[mR] - k_{end}[mR] \\ & R_T = R + mR \end{aligned} \tag{4.10}$$

Where k_1, k_{-1} are the association and dissociation rate constants respectively, and the last term, R_T, is the conservation condition. If morphogen diffuses significantly faster than regulator (R), that is $D_{m0} >> D_{mR0}$, the model can represent a simple ligand-receptor interactions, and simplifies further to:

$$\begin{aligned} \frac{\partial[m]}{\partial t} &= D_{m0}\frac{\partial^2[m]}{\partial x^2} - k_1[m][R] + k_{-1}[mR] \\ \frac{\partial[mR]}{\partial t} &= k_1[m][R] - k_{-1}[mR] - k_{end}[mR] \\ & R_T = R + [mR] \end{aligned} \tag{4.11}$$

If binding reactions of between morphogen (m) and regulator (R) occur very fast, the term $\frac{\partial mR}{\partial t} = 0$ is a good approximation of morphogen complex ($[mR]$) dynamics. So, we obtain:

$$\begin{aligned} & \frac{\partial[mR]}{\partial t} = 0 \\ & \Rightarrow k_1[m][R] - k_{-1}[mR] - k_{end}[mR] = 0 \\ & \Rightarrow k_1[m][R] - [mR]\,(k_{-1} + k_{end}) = 0 \\ & \Rightarrow k_1[m](R_T - [mR]) - [mR]\,(k_{-1} + k_{end}) = 0 \\ & \Rightarrow k_1[m](R_T - [mR]) = [mR]\,(k_{-1} + k_{end}) \\ & \Rightarrow [mR] = \frac{[m][R_T]}{m + \frac{k_{-1}+k_{end}}{k_1}} \end{aligned} \tag{4.12}$$

The term $\frac{k_{-1}+k_{end}}{k_1}$ is the dissociation constant K_D, which is considerably larger than $[m]$. At the cellular surface $K_D = \frac{k_{-1}+k_{end}}{k_1} >> [m]$, which implies that binding

sites available for the morphogen are significantly large enough to keep it away from saturation. Thus, the Eq. 4.12 can be simplified as:

$$[mR] = \frac{[m]R_T}{K_D} \tag{4.13}$$

By adding $\frac{\partial[m]}{\partial t}$ and $\frac{\partial[mR]}{\partial t}$ from Eq. 4.11:

$$\begin{aligned}
&\frac{\partial[m]}{\partial t} + \frac{\partial[mR]}{\partial t} = D_{m0}\frac{\partial^2[m]}{\partial x^2} - k_{end}[mR] \\
&\Rightarrow \frac{\partial[m]}{\partial t} + \frac{\partial[mR]}{\partial t} = D_{m0}\frac{\partial^2[m]}{\partial x^2} - k_{end}\frac{[m]R_T}{K_D} \\
&\Rightarrow \frac{\partial[m]}{\partial t}\left(1 + \frac{R_T}{K_D}\right) = D_{m0}\frac{\partial^2[m]}{\partial x^2} - k_{end}\frac{[m]R_T}{K_D} \\
&\Rightarrow \frac{\partial[m]}{\partial t} = \frac{D_{m0}}{\left(1 + \frac{R_T}{K_D}\right)}\frac{\partial^2[m]}{\partial x^2} - \frac{k_{end}}{\left(1 + \frac{R_T}{K_D}\right)}\frac{[m]R_T}{K_D}
\end{aligned} \tag{4.14}$$

A careful observation of Eq.4.14 shows that the diffusion coefficient (D_{m0}) and the rate of removal (k_{end}) of morphogen are both scaled by a term of the form $(1 + \alpha R)$, which is rearranged as $(1 + \alpha R)^{\nu}$ and is used in the TCS model for the regulation of biophysical properties. By varying the value of ν, we obtained positive, negative, and no regulation of transport properties. Similar forms of equations are used for reaction rate modulation, and all the exact regulatory equations of TCS model are listed later.

In summary, to identify the mechanisms for scaling and preciseness in patterning, we consider regulation of all biophysical properties of morphogen dynamics: the modification of transport properties, the production or the influx of morphogen and modulators, and the reaction rates of extracellular morphogen and modulator dynamics. We hypothesize that regulations of transport, production, and reaction properties, either separately or in combination, can explain a number of the performance objectives, such as scale-invariance, robustness, etc. Depending on the location of the modulator source, TCS models are subdivided into three main categories– i) modulator source is at $X = 0$, ii) modulator source is at $X = L$, iii) spatially distributed modulator source. All these model variations are elaborated in subsequent sections.

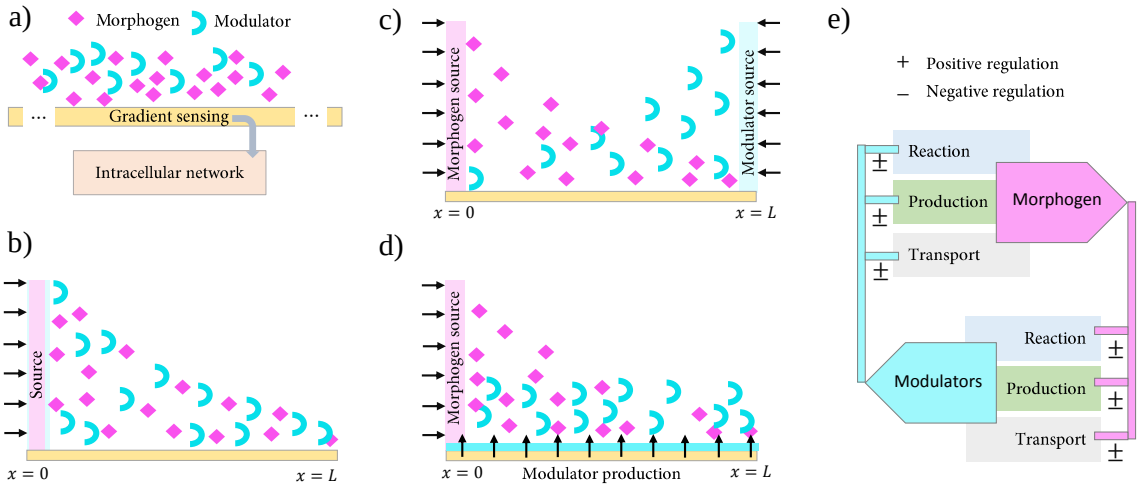

Fig. 4.2. Two Component system (TCS) for scaling: In the cellular environment, free morphogen movement is often hindered by the presence of interacting molecules (cyan). Besides cognate receptor binding, a morphogen (magenta) also interacts with numerous other extracellular binding proteins (cyan), defined as modulators. These extracellular interactions can change the biophysical profile of the morphogen and thus, diffusivity and other kinetics may no longer be constant in the cellular environment. b,c,d) Based on the location of the modulator source, the proposed TCS is subdivided into three main subclasses i) modulator flux source at $x = 0$, ii) modulator flux source at $X = L$, and iii) spatially non- uniform production of morphogen. In all these TCS versions, the morphogen flux source is always located at $x = 0$.

4.2 Two Component System Model (TCS) and its variants

As stated earlier, based on the location of the modulator source, we consider three different model variants of TCS, and the details of the source location of both morphogen and modulator are: i) Both the morphogen and modulator sources are co-located at $X = 0$, ii) The morphogen and modulator sources are in opposite directions, that is, the morphogen source is at $X = 0$ and modulator source is at $X = L$, and iii) The modulator source is spatially distributed and the production is regulated spatially by the morphogen, and the morphogen source is located at $X = 0$. The exact equations of all the TCS variants are as follows:

4.2.1 Modulator source is at X = 0

$$\frac{\partial m}{\partial t} = \frac{\partial}{\partial x}\left(D_m(M)\frac{\partial m}{\partial x}\right) + K_m(M,m) \tag{4.15}$$

$$-D_m(M)\frac{\partial m}{\partial x}\bigg|_{x=0} = j_m(M), \frac{\partial m}{\partial x}\bigg|_{x=L} = 0 \tag{4.16}$$

$$\frac{\partial M}{\partial t} = \frac{\partial}{\partial x}\left(D_M(m)\frac{\partial M}{\partial x}\right) + K_M(M,m) \tag{4.17}$$

$$-D_M(m)\frac{\partial M}{\partial x}\bigg|_{x=0} = j_M(m), \frac{\partial M}{\partial x}\bigg|_{x=L} = 0 \tag{4.18}$$

where, $K_m(M,m)$ and $K_M(M,m)$ depend both on the spatial concentration of morphogen and modulator, and account for the removal of morphogen and modulator form the cell surface. The exact equations of $K_m(M,m)$ and $K_M(M,m)$ are as follows:

$$K_m(M,m) = -k_{\delta m}(\zeta_m + \beta_m M)^{\nu_m^R}[m]$$

$$K_M(M,m) = -k_{\delta M}(\zeta_M + \beta_M m)^{\nu_M^R}[M]$$

Here, k_δ is the rate of removal (s^{-1}) of a species from the system, and the removal could be a form of the decay of species, or annihilation by the presence of other species.

The modulation of transport properties, which is the diffusivity of morphogen and modulator, is considered as:

$$D_m(M) = D_{m0}(1 + \alpha_m M)^{\nu_m^D} \tag{4.19}$$

Using Eq.4.19, we obtain the PDE equation below:

$$\begin{aligned}
\frac{\partial m}{\partial t} &= \frac{\partial}{\partial x}\left(D_m(M)\frac{\partial m}{\partial x}\right) + K_m(M,m) \\
&= D_m(M)\frac{\partial}{\partial x}\left(\frac{\partial m}{\partial x}\right) + \frac{\partial m}{\partial x}\frac{\partial}{\partial x}\left(D_m(M)\right) + K_m(M,m) \\
&= D_m(M)\frac{\partial^2 m}{\partial x^2} + \frac{\partial m}{\partial x}\frac{\partial}{\partial x}\left(D_{m0}(1+\alpha_m M)^{\nu_m^D}\right) + K_m(M,m) \\
&= D_m(M)\frac{\partial^2 m}{\partial x^2} + \frac{\partial m}{\partial x}\left(D_{m0}\nu_m^D(1+\alpha_m M)^{\nu_m^D-1}\right)\frac{\partial}{\partial x}(1+\alpha_m M) + K_m(M,m) \\
&= D_m(M)\frac{\partial^2 m}{\partial x^2} + \frac{\partial m}{\partial x}\left(D_{m0}\nu_m^D\alpha_m(1+\alpha_m M)^{\nu_m^D-1}\right)\frac{\partial M}{\partial x} + K_m(M,m) \\
&= D_m(M)\frac{\partial^2 m}{\partial x^2} + \left(\nu_m^D\alpha_m D_{m0}(1+\alpha_m M)^{\nu_m^D-1}\right)\frac{\partial m}{\partial x}\frac{\partial M}{\partial x} + K_m(M,m)
\end{aligned} \tag{4.20}$$

Eq.4.20 is known as the non-divergence form of TCS, and it is obtained by expanding the chain rule of the derivative. The modulation of the influx rate of morphogen is considered as:

$$j_m(M) = j_{m0}\frac{(\gamma_m K_H^n + (1-\gamma_m)M^n)}{K_H^n + M^n} \tag{4.21}$$

In the parameter space, α, γ and β, used in different regulatory equations, are treated as different parameters for m and M. We obtain a total of 6 parameters for the modulation of the biophysical properties of morphogen and modulators, and the combination gives a total of 729 candidate network topologies consisting of different types of modulations of biophysical properties. If only the regulation of transport and reaction properties of morphogen and modulators are considered, we obtain a total of 81 regulatory motifs, and the PDEs for all the 81 motifs are demonstrated in APPENDIX C.

By defining the dimensionless variable $\xi = \frac{x}{L}$, where L is the length of the field of cells, or simply the embryo length, we obtain:

$$\begin{aligned} \xi &= \frac{x}{L} \\ \Rightarrow \quad \partial x &= L\partial\xi \\ \Rightarrow \quad \partial x^2 &= L^2\partial\xi^2 \end{aligned}$$

Using the dimensionless quantity ξ, we obtain the dimensionless form of Eq.4.20 is as given below:

$$\frac{\partial m}{\partial t} = D_m(M)\frac{1}{L^2}\frac{\partial^2 m}{\partial \xi^2} + \left(\nu_m^D \alpha_m D_{m0}(1+\alpha_m M)^{\nu_m^D - 1}\right)\frac{\partial m}{\partial \xi}\frac{\partial M}{\partial \xi} + K_m(M,m)$$

The dimensionless forms of the boundary conditions are as follows:

$$-D_m(M)\frac{1}{L}\frac{\partial m}{\partial \xi}\bigg|_{\xi=0} = j_m(M), \frac{\partial m}{\partial \xi}\bigg|_{\xi=1} = 0$$

Since the biophysical properties of modulators are regulated spatially by the morphogen, we obtain a similar set of equations for modulators:

$$\begin{aligned} \tfrac{\partial M}{\partial t} &= D_M(m)\tfrac{1}{L^2}\tfrac{\partial^2 M}{\partial \xi^2} + \left(\nu_M^D \alpha_M D_{M0}(1+\alpha_M m)^{\nu_M^D - 1}\right)\tfrac{1}{L^2}\tfrac{\partial m}{\partial \xi}\tfrac{\partial M}{\partial \xi} + K_M(M,m) \\ B.C &: -D_M(m)\tfrac{1}{L}\tfrac{\partial M}{\partial \xi}\Big|_{\xi=0} = j_M(m), \tfrac{\partial M}{\partial \xi}\Big|_{\xi=1} = 0 \end{aligned} \tag{4.22}$$

where α, β, γ and ν are modulating parameters and can be tuned to specify the intensity and the types of regulation.

Initially, we consider linear modulation of reaction rates and transport properties with $\nu = [-1\ 0\ 1]$. Different types of modulation along with the parameters to achieve that are summarized below: positive, negative, and no regulation cases of input flux can easily be obtained by choosing the appropriate value of hill coefficient n and γ_m in Eq. 4.21. For example,

- Positive Regulation: $n > 0$ and $\gamma_m = 0$
- Negative Regulation: $n > 0$ and $\gamma_m = 1$
- No Regulation: $n = 0$ and $\gamma_m \geq 0$

Table 4.1
Regulatory parameters and their units and ranges

Parameter Name	Ranges	Units
ν_m^D	$\nu_m^D \in [-1\ 0\ 1]$	-
ν_m^R	$\nu_m^D \in [-1\ 0\ 1]$	-
α_m	$\alpha_m \in (0, \infty]$	1/Concentration
ζ_m	$\zeta_m = \begin{cases} 1 & \text{if } \nu_m^R = 0 \\ 1 & \text{if } \nu_m^R = -1 \\ 0 & \text{if } \nu_m^R = 1 \end{cases}$	-
β_m	$\beta_m \in (0, \infty]$	1/Concentration
γ_m	$\gamma_m \in [\ 0\ 1]$	-
ν_M^D	$\nu_m^D \in [-1\ 0\ 1]$	-
ν_M^R	$\nu_m^D \in [-1\ 0\ 1]$	-
α_M	$\alpha_M \in (0, \infty]$	1/Concentration
ζ_M	$\zeta_M = \begin{cases} 1 & \text{if } \nu_M^R = 0 \\ 1 & \text{if } \nu_M^R = -1 \\ 0 & \text{if } \nu_M^R = 1 \end{cases}$	-
β_M	$\beta_m \in (0, \infty]$	1/Concentration
γ_M	$\gamma_M \in [\ 0\ 1]$	-

4.2.2 Modulator source is at X = L

While all the regulation types and equations of transport, reaction, and flux modulations are similar to the previous model, the difference introduced here is the location of the modulator source. More precisely, the modulator source is located at $X = L$,

Table 4.2
Regulation: positive, negative and no-regulation

ν_m^D	ν_m^R	α_m	ζ_m	β_m	$D_{m0}(1+\alpha_m M)^{\nu_m^D}$	$-k_{\delta m}[m](\zeta_m+\beta_m M)^{\nu_m^R}$	Reg.
$+1$	$+1$	>0	0	>0	$D_{m0}(1+\alpha_m M)$	$-k_{\delta m}(\beta_m M)[m]$	$+\nu$e
-1	-1	>0	1	>0	$D_{m0}(1+\alpha_m M)^{-1}$	$-k_{\delta m}(1+\beta_m M)^{-1}[m]$	Negative
0	0	≥ 0	1	$-$	D_{m0}	$-k_{\delta m}[m]$	No
ν_M^D	ν_M^R	α_M	ζ_m	β_M	$D_{M0}(1+\alpha_M m)^{\nu_M^D}$	$-k_{\delta M}[M](\zeta_M+\beta_M m)^{\nu_M^R}$	Regulation
$+1$	$+1$	>0	0	>0	$D_{M0}(1+\alpha_M m)$	$-k_{\delta M}(\beta_M m)[M]$	Positive
-1	-1	>0	1	>0	$D_{M0}(1+\alpha_M m)^{-1}$	$-k_{\delta M}(1+\beta_M m)^{-1}[M]$	Negative
0	0	≥ 0	1	$-$	D_{M0}	$-k_{\delta M}[M]$	No

whereas the location of the morphogen source is kept unchanged at $X = 0$ as seen in the previous model.

$$\frac{\partial m}{\partial t} = \frac{\partial}{\partial x}\left(D_m(M)\frac{\partial m}{\partial x}\right) + K_m(M,m) \tag{4.23}$$

$$-D_m(M)\frac{\partial m}{\partial x}\bigg|_{x=0} = j_m(M), \frac{\partial m}{\partial x}\bigg|_{x=L} = 0 \tag{4.24}$$

$$\frac{\partial M}{\partial t} = \frac{\partial}{\partial x}\left(D_M(m)\frac{\partial M}{\partial x}\right) + K_M(M,m) \tag{4.25}$$

$$\frac{\partial M}{\partial x}\bigg|_{x=0} = 0, D_M(m)\frac{\partial M}{\partial x}\bigg|_{x=L} = j_M(m), \tag{4.26}$$

4.2.3 Modulator source is spatially distributed, and dependent on morphogen concentration

In this category of the TCS model, we consider both a reflected boundary for the modulators, and a spatially distributed source of modulators. The Production of modulators from the source in any position along the spatial domain is modulated by

the level of morphogen present at that location. We consider the positive, negative, and no-regulation cases for the production of modulators:

$$\frac{\partial m}{\partial t} = \frac{\partial}{\partial x}\left(D_m(M)\frac{\partial m}{\partial x}\right) + K_m(M,m) \tag{4.27}$$

$$-D_m(M)\frac{\partial m}{\partial x}\bigg|_{x=0} = j_m(M), \frac{\partial m}{\partial x}\bigg|_{x=L} = 0 \tag{4.28}$$

$$\frac{\partial M}{\partial t} = \frac{\partial}{\partial x}\left(D_M(m)\frac{\partial M}{\partial x}\right) + K_M(M,m) + \phi_M(m(x)) \tag{4.29}$$

$$\frac{\partial M}{\partial x}\bigg|_{x=0} = 0, \frac{\partial M}{\partial x}\bigg|_{x=L} = 0, \tag{4.30}$$

where $\phi_M(m(X))$ is the source term of the modulator, and depends on the concentration of morphogen present in that location. Regulation of production is implemented as follows:

$$\phi_M(m(X)) = \phi_{M0}\frac{(\gamma_m K_H^n + (1-\gamma_m)m^n)}{K_H^n + m^n} \tag{4.31}$$

4.3 Methods

4.3.1 Numerical Challenges

The numerical approximation of TCS involves a number of challenges to resolve. First, stiffness becomes a major challenge that potentially arises through spatial modulation of the time scale, and widely varying eigenvalues of the Jacobian Matrix. Secondly, the amount of data to be generated, and the time required to generate that data, are major issues that need to be taken care of. Another major challenge is the accuracy of the numerically approximated value. Further explanation of all these challenges are provided below.

Stiffness

The stiffness of Ordinary Differential Equation (ODE) System is not precisely defined. Instead, a number of different observations have been proposed to differentiate

between a stiff and non-stiff system. Even a stable and well-posed system may behave stiff when the system is approximated using a discrete approach [188]. From a computational point of view, in [189], stiffness is defined as "Stiff equations are problems for which explicit methods don't work". Mathematically, the aforesaid definition doesnt identify any standard notion of stiffness for the system. In another effort [190], the non-normality of the coefficient matrix is attributed to the stiffness of the system. However, there are systems where the coefficient matrix is symmetric and, hence, falls under the notion of normality of matrix [188]. A few of the observations that are widely used to differentiate stiff and non-tiff systems are as follows:

1. A system could be stiff because of the presence of widely varying time-scales in the system.

2. A stiff system should have no unstable component (that is, all eigenvalues have negative real parts), and one of the stable components should be largely stable (meaning, a very large negative real part). Also, the solution will vary slowly with respect to the most negative real part of eigenvalues [191].

3. The stiffness of the system can be quantified using the stiffness ratio (S), where S is defined as the ratio between the magnitude of largest and smallest negative real part of eigenvalues.

In a TCS simulation, both the varying time-scales and separation of eigenvalues can be used to quantify the stiffness, as the spatial regulation results in widely varying time-scales and system dynamics of TCS.

Time constraints on data generation

TCS considers screening millions of networks for each of the of performance objectives, and in this research we considered scale-invariance and robustness as our objectives of interest. Scale-invariance requires at least two length scales to be considered, and the robustness analysis requires two different production rates of morphogens to

be considered and studied. The parameter grid we used consists of about 15 million parameter vectors, where each vector contains a total of 18 different parameters. So, for each TCS model type there are about 50 million simulations needed, and simulations for all the three versions of TCS model sum up to about 200 millions of realizations of the model. Furthermore, as we also considered other parameter space by fixing the morphogen removal rate to a fixed value and expand on other regulator parameters, we obtain another parameter space of about 13 million points.

This requires enormous computational resources which can be very costly due to licensing issues, and also because of simulation failures often encountered due to the solvers limitation in treating a highly stiff system.

4.3.2 Discretization of TCS

Divergence form

In the divergence or conservative form of PDE systems, the derivative of spatially varying parameters does not appear in the equation [115]. In accordance with this definition, the divergence form of TCS could be written for morphogen dynamics as follows:

$$\frac{\partial m}{\partial t} = \frac{\partial}{\partial x}\left(D_m(M)\frac{\partial m}{\partial x}\right) + K_m(M, m) \tag{4.32}$$

As seen here, the coefficient $D_m(M)$ is spatially varying and its derivative doesnt appear in Eq.4.32. This form of PDE is also termed as the conservative-law form of

the system. In the divergence form, central differencing scheme [125] is applied as follows:

$$\begin{aligned}
\frac{\partial m}{\partial t} &= \frac{\partial}{\partial x}\left(D_m(M)\frac{\partial m}{\partial x}\right) + K_m(M,m) \\
&= \frac{1}{\Delta x}\left[\left(D_m(M)\frac{\partial m}{\partial x}\right)_{i+1/2} - \left(D_m(M)\frac{\partial m}{\partial x}\right)_{i-1/2}\right] + K_m(M_i,m_i) \\
&= \frac{1}{\Delta x}\left[\left(D_m(M)_{i+1/2}\right)(\frac{\partial m}{\partial x})_{i+1/2} - \left(D_m(M)_{i-1/2}\right)(\frac{\partial m}{\partial x})_{i-1/2}\right] + K_m(M_i,m_i) \\
&= \frac{1}{\Delta x}\left[\left(D_m(M)_{i+1/2}\right)\frac{1}{\Delta x}(m_{i+1}-m_1) - \left(D_m(M)_{i-1/2}\right)\frac{1}{\Delta x}(m_i - m_{i-1})\right] \\
&+ K_m(M_i,m_i) \\
&= \frac{1}{\Delta x^2}\left[\left(D_m(M)_{i+1/2}\right)(m_{i+1}-m_1) - \left(D_m(M)_{i-1/2}\right)(m_i - m_{i-1})\right] + K_m(M_i,m_i)
\end{aligned}$$

where $D(M)_{i+1/2}$ and $D(M)_{i-1/2}$ are the diffusion coefficients approximated at the mid point of $(i+1,i)$ and the midpoint of $(i,i-1)$, respectively, according to the formula given below:

$$\begin{aligned}
D(M)_{i+1/2} &= \frac{D(M_{i+1}) + D(M_i)}{2} \\
D(M)_{i-1/2} &= \frac{D(M_i) + D(M_{i-1})}{2}
\end{aligned}$$

At the left boundary ($\xi = 0$, meshpoint 1), influx of morphogen is discretized as follows:

$$\begin{aligned}
&- D_m(M)\frac{\partial m}{\partial x}\bigg|_{x=0} = j_m(M) \\
&\Rightarrow \frac{\partial m}{\partial x} = -L\frac{j_n(M)}{D_m(M)} \\
&\Rightarrow \frac{1}{2\Delta\xi}(m_{i+1} - m_{i-1}) = -L\frac{j_n(M)}{D_m(M)}
\end{aligned}$$

Non-divergence form

In the non-divergence form, the chain rule is applied to expand the derivative as shown in Eq. 4.20. More precisely, derivative is applied on the spatially dependent

parameters [115]. The PDEs obtained using non-divergence method are again discretized with standard central difference scheme along X direction on a mesh of N grid points, and the resulting discretized PDE for morphogen becomes:

$$\frac{\partial m}{\partial t} = D_m(M)\frac{1}{L^2}\frac{\partial^2 m}{\partial \xi^2} + \left(\nu\alpha D_{m0}(1+\alpha M)^{\nu-1}\right)\frac{1}{L^2}\frac{\partial m}{\partial \xi}\frac{\partial M}{\partial \xi} + K_m(M,m) \quad (4.33)$$

After discretization of Eq. 4.33 using central difference scheme, we obtain:

$$\begin{aligned} f_i &= \frac{\partial m_i}{\partial t} = \frac{D_m(M_i)}{L^2}\left(\frac{m_{i+1}-2m_i+m_{i-1}}{(\Delta\xi)^2}\right) \\ &+ \left(\frac{\nu\alpha D_{m0}(1+\alpha M_i)^{\nu-1}}{L^2}\right)\left(\frac{m_{i+1}-m_{i-1}}{2\Delta\xi}\right)\left(\frac{M_{i+1}-M_{i-1}}{2\Delta\xi}\right) \\ &+ K_m(M_i,m_i) \end{aligned} \quad (4.34)$$

where $0 \leq i \leq N$, $\Delta\xi = \frac{1}{N}$. Boundary conditions are imposed at $i = 0$ and $i = N-1$. At left boundary ($i = 0$), Eq.4.34 becomes:

$$\begin{aligned} f_0 &= \frac{D_m(M_0)}{L^2}\left(\frac{m_1-2m_0+m_{-1}}{(\Delta\xi)^2}\right) \\ &+ \left(\frac{\nu\alpha D_{m0}(1+\alpha M_0)^{\nu-1}}{L^2}\right)\left(\frac{m_1-m_{-1}}{2\Delta\xi}\right)\left(\frac{M_1-M_{-1}}{2\Delta\xi}\right) \\ &+ K_m(M_0,m_0) \end{aligned} \quad (4.35)$$

where m_{-1} is the fictitious node, and needs to be replaced by nodes within the grid. To remove the fictitious node, boundary conditions is used, and by discretizing the boundary conditions at the left boundary $\xi = 0$, we obtain:

$$\begin{aligned} -D_m(M_0)\frac{1}{L}\left(\frac{m_1-m_{-1}}{2\Delta\xi}\right) &= j_m(M_0) \\ \Rightarrow m_{-1} &= m_1 + 2\Delta\xi L\frac{j_m(M_0)}{D_m(M_0)} \end{aligned} \quad (4.36)$$

By plugging in the value of fictitious node m_{-1}, final form of f_0 comes out as:

$$\begin{aligned} f_0 &= \frac{D_m(M_0)}{(\Delta\xi)^2L^2}(2m_1-2m_0) + \frac{2}{L(\Delta\xi)}j_m(M) \\ &+ \nu\alpha D_{m0}(1+\alpha M_0)^{\nu-1}\frac{j_m(M_0)}{D_m(M_0)}\frac{j_M(m_0)}{D_M(m_0)} \\ &+ K_m(M_0,m_0) \end{aligned} \quad (4.37)$$

At the other boundary at $\xi = 1$, the equation becomes:

$$f_N = \frac{D_m(M_N)}{(\Delta\xi)^2 L^2}(2m_{N-1} - 2m_N) + K_m(M_N, m_N) \tag{4.38}$$

Similarly, we can obtain the discretized version of modulator equation by applying central difference scheme [125] as elaborated here in Eq.4.34 for morphogen.

Since the exact analytical solution of TCS is intractable because of nonlinear coupling between species, we rely primarily on the numerical method. To numerically approximate TCS, we used CVODE [175], a solver for the initial value ODEproblem available under the SUNDIAL package [192]. CVODE is suitable for both stiff and non-stiff problems of the explicit form $\frac{dm}{dt} = f(t, m)$.

4.3.3 TCS implementation using CVODE

CVODE [175] is a multistep and variable order solver, which has a wide range of formulas available for different types of problems. For example for non-stiff formula, CVODE includes the Adams-Moultan method, whereas for stiff problems, CVODE provides the Backward Differentiation Formula (BDF). In addition, CVODE also provides different orders for each of its solver methods. The CVODE package is written in C language, and a comprehensive overview of CVODE is available in [192].

The PDE form of TCS is discretized using the Finite Difference Scheme (FDM), which translates the problem from a boundary value elliptical PDE system to an initial value problem of Ordinary Differential Equations (ODEs) of the form:

$$m^{'}(\xi(t)) = f(t, m(\xi(t))), m(\xi(t_0)) = m_0 \tag{4.39}$$

where ξ represents the spatial position of the domain.

$$m^{'}(t) = f(t, m(t)), m(t_0) = m_0 \tag{4.40}$$

A general form of the one-step method of Eq.4.40 is as follows:

$$\frac{m_{i+1} - m_i}{\Delta t} = Z(f, t_i, m_i, m_{i+1}, \Delta t)$$
$$m_{i+1} = m_i + \Delta t Z(f, t_i, m_i, m_{i+1}, \Delta t)$$

where $\Delta t = t_{i+1} - t_i$. Any numerical method that involves the update terms on the left side and the function evaluation on the right is treated as implicit, and to numerically solve such an implicit method, Newton's method [193] is often applied to determine the value at m_{i+1}. The Backward Differentiation Formula [194] is further elaborated in subsequent section of this chapter.

Backward Differentiation Formula

The Backward Differentiation Formula (BDF) is an implicit, multistep solver, and is one of the most frequently used numerical approaches to approximate the solution of stiff ODEs [195]. In BDF, the evaluation of Z depends on both m_i and previous values such as m_{i-1}; a nonlinear equation is solved to determine m_{i+1}. The BDF formula of order p has a general form [125, 130, 175, 195]:

$$\begin{aligned} m_n &= \sum_{i=1}^{p} \alpha_{n,i} m_{n-i} + h\beta_{n,0} m_n{}' \\ &= \sum_{i=1}^{p} \alpha_{n,i} m_{n-i} + h\beta_{n,0} f(t_n, m_n), \quad m_n{}' = f(t_n, y_n) \end{aligned} \tag{4.41}$$

where α and β are the coefficients, and they solely depend on the order q of BDF method. Here, h is the stepsize and $h = t_n - t_{n-1}$, and $m_n = m(t_n)$ is the solution.

Depending on how the stepsize h is chosen, BDF methods are subdivided into different categories: i) fixed-step BDF, ii) variable-step BDF, iii) fixed-leading coefficient (FLC) BDF. In CVODE [130], the fixed-leading coefficient (FLC) form of BDF is implemented. In this approach, coefficients α and β are no longer dependent only on the order p of BDF method. Instead, they rely on the stepsize h as well. The FLC form of BDF considers both fixed-step and variable-step version of BDF while evaluating the coefficients α, β. It introduces the fixed-step value of $\beta_{n,0} \equiv \beta_0$ as follows:

$$\beta_0 = \frac{1}{\sum_{j=1}^{p} j^{-1}}$$

FLC also requires an additional term, and the Eq.4.41 for FLC form becomes:

$$\begin{aligned} m_n &= \sum_{i=1}^{p} \alpha_{n,i} m_{n-i} + h\beta_0 m_n{}' + h\beta_{n,1} m_{n-1}{}' \\ &= \sum_{i=1}^{p} \alpha_{n,i} m_{n-i} + h\beta_{n,0} f(t_n, m_n), \quad m_n{}' = f(t_n, y_n) \end{aligned} \tag{4.42}$$

The FLC form BDF as shown in Eq. 4.42 is more stable than the fixed-step BDF, and it is more efficient than variable-step BDF due its ability to reuse the Newton iteration matrix [125, 130, 175]. The FLC version of BDF is at the core of CVODE solver, making CVODE a very stable solver for stiff-system analysis [130, 175, 192].

4.3.4 Comparison of the different mumerical approximation methods

The accuracy of CVODE TCS implementation is compared with COMSOL data. Here, two versions of CVODE code are used–i) Expanded chain-rule (EC), or the non-divergence form, and ii) The Divergence (DIV) form of TCS implementation. For comparison, three different regulation types are considered: i) Positive regulation of reaction and diffusion properties, ii) Negative regulation of reaction and diffusion properties, iii) No regulation.

To simplify further, only the diffusivity of morphogens and modulators are different during the comparison, whereas the other regulatory parameters are similar. The intrinsic diffusion coefficient of morphogen and modulator (D_{mo}, D_{M0} respectively) is varied as 0.01, 0.1, 1 $\mu m^2 s^{-1}$. So, a total of 9 different combinations simulated using CVODE is compared against COMSOL Multiphysics implementation of TCS.

For the positive regulation of diffusivity, both the divergence form and the non-divergence form are in good agreement in terms of accuracy. However, in a few cases, the divergence form exhibits better proximity towards COMSOL data. For the negative regulation, it is found that the species distribution looks similar except near the origin, where the CVODE-based approach fails to attain the value obtained using COMSOL. This scenario is found mainly in cases where the distribution experiences an abrupt decay in regions right next to the morphogen source and all the concentra-

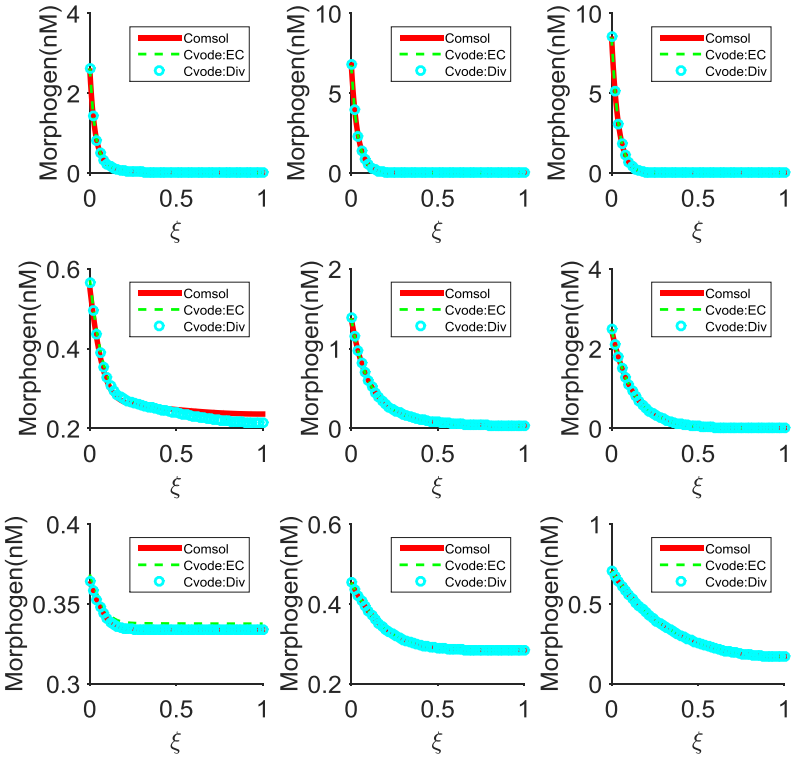

Fig. 4.3. A comparison of different positive regulation methods: Here, D_{m0} is varied in different rows, and D_{M0} is varied in columns. For example, in Row1: $D_{m0} = [0.01]$ and $D_{M0} = [0.01\ 0.1\ 1]$. In most cases, the concentration profile obtained by different numerical approaches matches almost perfectly with comsol data. But, in a few cases, the concentration profile has significant differences as seen in the modulator data for $D_{m0} = 0.01$ and $D_{M0} = 0.1, 1$. For the morphogen data, dissimilarity is visible for $D_{m0} = 0.1, 1$ and $D_{M0} = 0.01$.

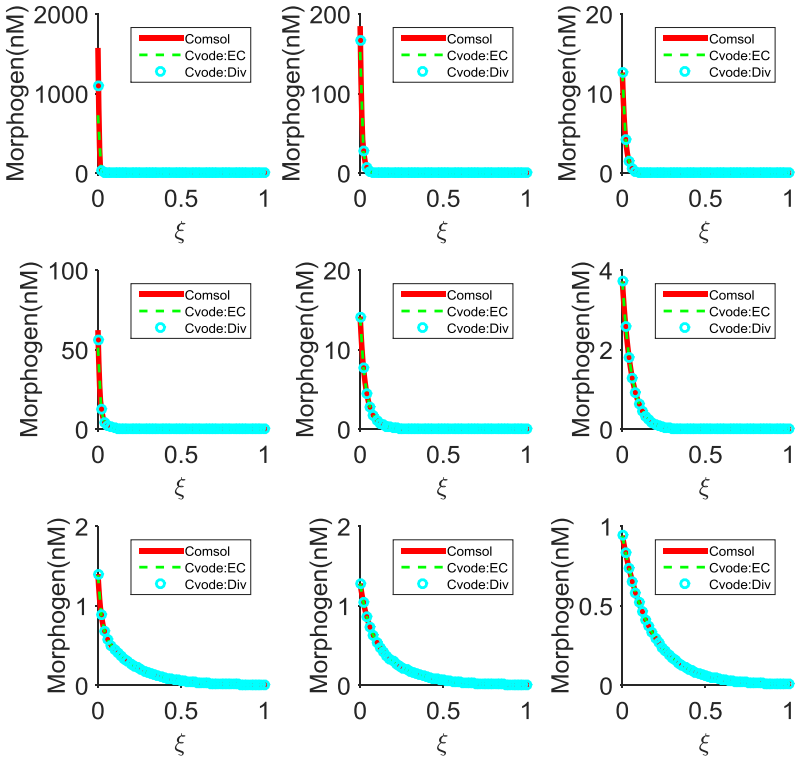

Fig. 4.4. A comparison of different negative regulation methods: For negative regulation of biophysical properties (diffusion, reaction), simulated data looks similar in most cases except where the concentration value varies near the origin. As seen here, if concentration is high near the origin, but close to zero at other spatial locations, dissimilarities arise in different numerical approaches. However, if the species concentration falls gradually, morphogen and modulator distribution look identical. Here, D_{m0} is varied in different rows and D_{M0} is varied in columns. For example, in Row1: $D_{m0} = [0.01]$ and $D_{M0} = [0.01\ 0.1\ 1]$.

tion is concentrated near the source. One possible reason for this dissimilarity could be the number of mesh points (500) used in this comparison. Later, we used a mesh size of 10,000 points and found that the CVODE implementation reaches 1300 nM near the origin ($X = 0$), which still falls behind the 2000 nM achieved by COMSOL (data not shown). From the patterning point of view, any concentration that is concentrated near the origin is not biologically relevant for the patterning system and has been filtered out during post-processing. For other distributions, such as the last row of Fig.4.4, the CVODE methods are in agreement with COMSOL implementation.

One of the challenges that the screening of TCS imposes is the time required to screen all possible parameter sets. For the screening strategy to be efficient, it should be able to produce accurate outcomes while reducing the cost of implementation. To optimize between accuracy and simulation time, we screened different mesh sizes and observed how the Root Mean-Square Error (RMSE) relates with a different mesh size. It is worthwhile to note that discretization size directly decides the number of ODEs to be solved at every iteration, a requirement that often burdens the solver speed [192]. It is found from analysis that a mesh size of 300 intervals would be a good number to better approximate the TCS while reducing computational time, and the details are elaborated later and is shown in Fig.4.5

Mesh variation and error comparison

To identify an efficient and accurate approach for TCS implementation, the mesh size is varied to measure the accuracy and the time needed to simulate the system. Accuracy measures consider two different forms of errors i) the absolute error, and ii) the Root Means- Square Error(RMSE).

The absolute error is the absolute difference of the reference and sample data, and only the maximum difference is considered to quantify the error:

$$E_{ABS} = \max_{m_i \in M, i \in 1 \ldots N} |m_i - m_i^s|$$

Table 4.3
Simulation Time and Failures for mesh size 301

Regulation	Grid Pts	Time		SIV Failures				RBST Failures			
				L_1		L_2		ϕ_1		ϕ_2	
		EC	D	EC	D	EC	D	EC	D	EC	D
POS	1000	22m47s	26m27s	0	4	0	0	0	4	2	5
NEG	1000	4m14s	3m54s	0	0	13 (NaN)	0	0	0	0	0
NO	1000	2m48s	3m10s	0	0	0	0	0	0	0	0

where m_i is the simulated value at spatial point i,and m_i^s is the reference value at i^{th} spatial point. Out of all the values, only the absolute value of the maximum difference is considered. As mentioned earlier, TCS implementation by COMSOL Multiphysics is used as the reference to calculate the maximum absolute error of the CVODE implementation of TCS.

The Root mean square error definition is as follows:

$$E_{RMSE} = \sqrt{\frac{1}{N}\sum_{i=1}^{N}(m_i - m_i^s)}$$

where, N is the total number of mesh points, and is varied over a wide range. Specifically, to compare the accuracy and computational cost, N is varied from 51 to 1001 mesh points.

We consider only positive regulation cases of transport and reaction properties of the morphogen and modulator to evaluate the relation between the errors and mesh size variation. A total of nine different combinations of intrinsic diffusivity of morphogen (D_{m0}) and modulator (D_{M0})) is used to generate the simulated data. In Fig.4.5, the intrinsic diffusion coefficients of the morphogen and modulator are taken as 0.1 and 0.01 $\frac{\mu m^2}{s}$ respectively. All other regulatory parameters were equal for the morphogen and modulator in Fig.4.5.

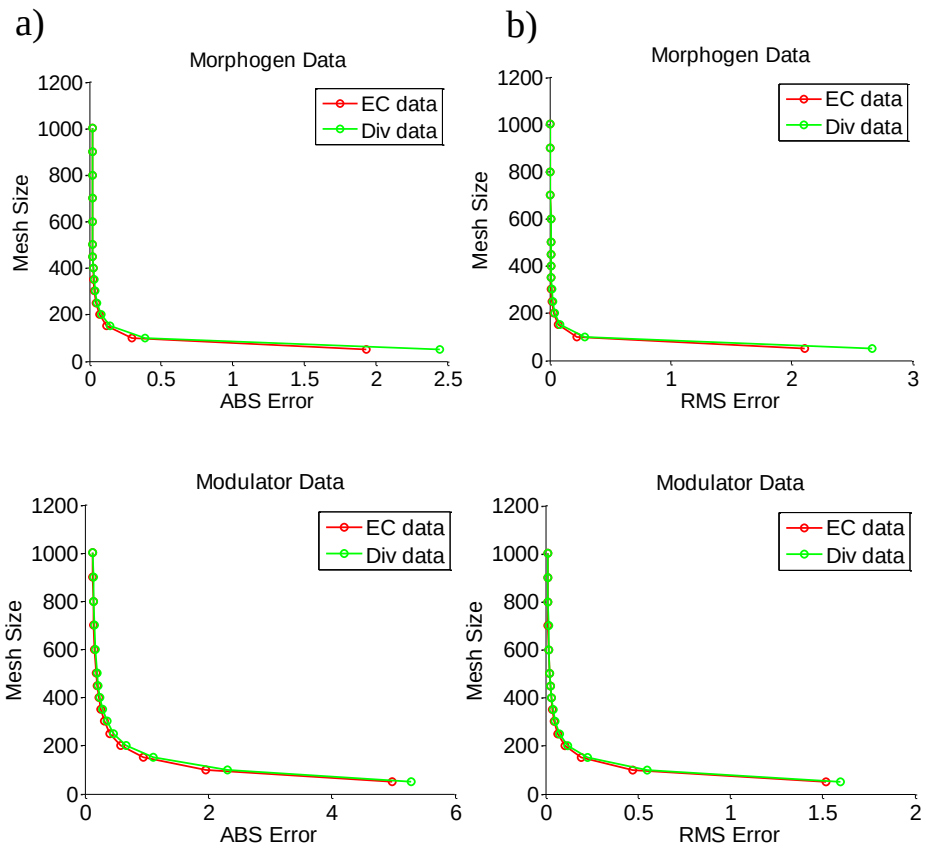

Fig. 4.5. The quantification of absolute and root means square error for different mesh size: Both errors are high when mesh resolution is coarse, which is expected due to the discretization effect. As the number of mesh points (N) increase, the error reduces drastically and, finally, reaches a value that remains steady even at larger mesh point increases. Expanded chain (EC) and divergence (DIV) forms demonstrate similar mesh size vs error plots. However, close comparison of red and green lines reveals that for a number of mesh sizes (smaller mesh size),the expanded chain rule (red) demonstrates better accuracy than the divergence (green line) form of TCS implementation

Comparisons of the accuracy and errors using different approaches (EC and DIV) show that they perform almost equally well. It is shown by comparing both the absolute error and root mean square error against the different mesh size that the DIV and EC forms of implementation demonstrate similar trends of their respective error curves. However, the approaches differ in simulation time and simulation failures. For instance, the EC version performs better when the entire regulation is positive, whereas the DIV version works better for negative regulation (mesh 301 case). The EC form of implementation experiences more simulation failures for mesh size 301. As discovered after a number of trials, the DIV version generates fewer failures for a given simulation setup than the EC implementation. Furthermore, if the two approaches are compared against the time taken to simulate 1000 grid points, it becomes evident that the EC version requires less time than the DIV version. A detailed comparison between the performance of EC and DIV is added in APPENDIX D.

To select the TCS implementation approach between EC and DIV, we assigned more importance to the number of simulations failures. Because the DIV version tends to generate fewer failures, we prefer to use it to reduce simulation failures. Therefore, we chose the DIV version in our research to generate data for the analysis of different versions of TCS.

4.4 Data analysis

4.4.1 Criteria for steady state

A multiple point based definition of steady state is considered to differentiate between steady state and transient values along the spatial domain. The steady state concentration of morphogens and modulators is collected after TCS has been simulated long enough. From trial data, it was found that the maximum TSS equivalent to 380 hours is a good approximation for obtaining steady state data. In order to investigate whether the system dynamics reach steady state within the first few hours of simulation, we selected spatial positions $\xi = 0, 0.2, 0.4, 0.6, 0.8, 1$, which were later

used to check if steady state could be reached within the first 10 hrs of T_{SS} in all those spatial locations. Specifically, the data collected at around 10 hours (m_{T10}) and compared with the last time point (380 hrs) data (m_{T380}) to see if the data m_{T10} is within the 5% tolerance of m_{T380} data.

Such a multiple-point based steady state definition is used in the expansion-repression model of scale invariance [174]. In this work, spatial positions to evaluate steady state at 10hrs are subdivided into two groups: i) boundary points, and ii) internal points. For steady state within the first 10 hours, at least one point from each group, or any point among the internal points, should reach 95% of the steady state concentration, a threshold we set considering the timing of embryonic development both in vertebrates and invertebrates. In vertebrates, such as Zebrafish and Xenopus, gastrulation begins at about 4.5 hpf and 10 hpf, and the limit of 10 hrs here is chosen considering these developmental time windows.

4.4.2 Physiologically relevant morphogen distribution

Not all morphogen distributions appear appropriate, and the pools of inappropriate Morphogen distributions are separated by assigning several screening criteria on the normalized morphogen distribution. Normalization of morphogen distribution is done using the reference case ($L_{ref} = 300\mu m$ for scale-invariance). Distributions of morphogen for the perturbed case (for scale-invariance, length is changed, and for robustness, flux is changed) is normalized considering the maximum morphogen concentration of the reference case. Normalized distribution is later used to investigate whether the network motif is able to achieve a specific performance objective.

A number of criteria are used to identify the appropriate morphogen distribution:

1. Normalized concentration at the midpoint ($\xi = 0.5$) should be $\geq 10\%$ of the maximum normalized morphogen concentration of the respective system. This removes cases where the morphogen distribution falls sharply near the morphogen source.

2. In general, morphogen concentration should be greater than 50 pM any concentration less than that is treated as insignificant strength, or the noise of the system.

3. For a morphogen distribution to be appropriate, it is imperative that the strength of the morphogen be gradually reduced as it moves away from source. To apply this, the normalized $m_{\xi=1}$ value is constrained as $m_{\xi=1} < m_{\xi=0.5}$, and, also, it is ensured that $m_{\xi=1} < 0.25 m_{\xi=1}$. This criterion also ensures the removal of uniform morphogen distributions, as well as the cases with high morphogen levels near the sink region.

4. The system should be at steady state as per the definition considered for the system.

The data generation steps and post-processing of the TCS model analysis is summarized in Fig.4.6. Data generation was done using CVODE [130, 192], whereas the post-processing is done using Matlab R14 and statistical software package R [196].

After the initial screening, we obtain a set of networks that can satisfy the scale invariance or robustness criteria as defined. A new parameter grid is generated by changing the non-zero values values of regulatory parameters to zeros a change that represents the removal of an edge from the original regulatory motif as demonstrated in Fig.4.7.

4.5 Results and Discussion

Not all simulated data is biologically relevant, since morphogen distribution may be concentrated near the source, or the concentration may appear ubiquitous and doesnt ensure an adequate difference among neighboring regions. Such distributions are inappropriate for a gradient based mechanism [174]. To differentiate between good and bad data, we designed a set of criteria and examined each of the candidate distributions to test their biological relevance. Our analysis found that regardless of

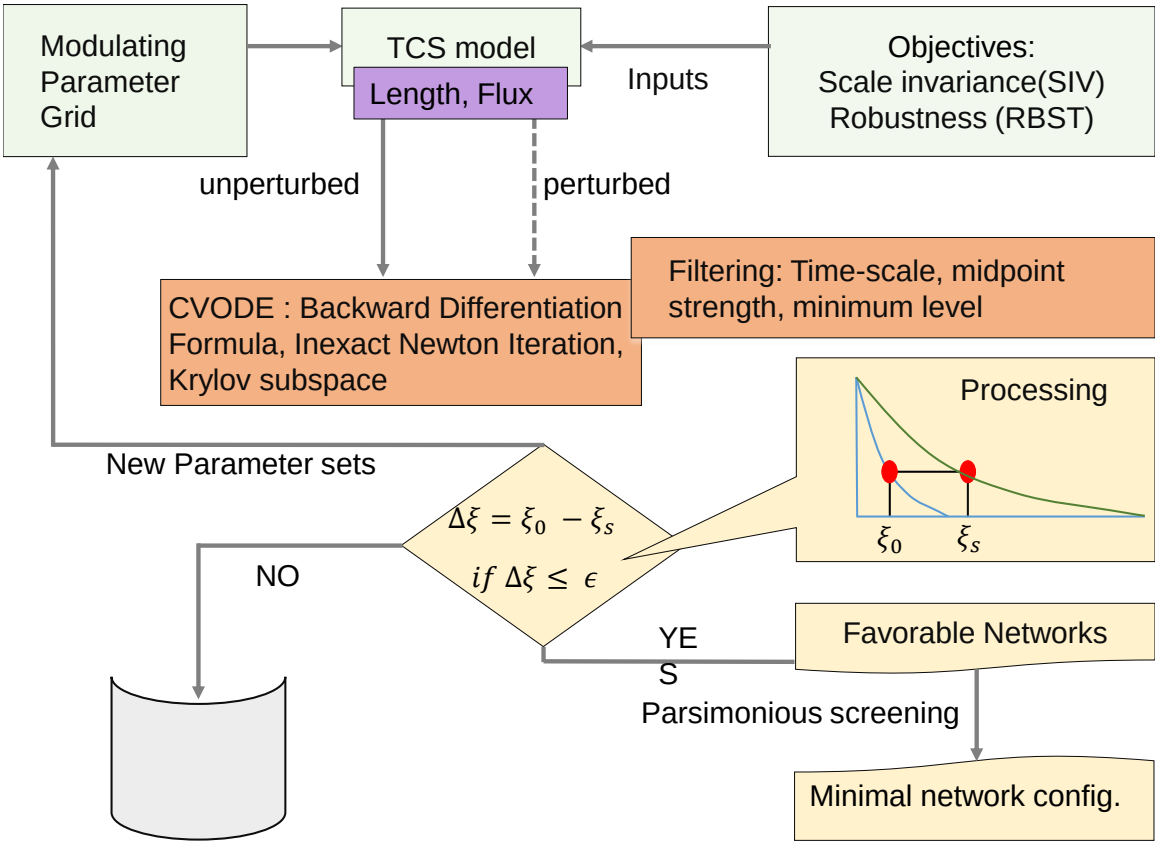

Fig. 4.6. Data generation and post-processing in TCS: All the steps to generate concentration data for the morphogens and modulators, and subsequent steps to differentiate between favorable networks and unfavorable networks are shown here. The unperturbed and perturbed lengths of the system were considered at $300\mu m$ and $600\mu m$ respectively, and for morphogen flux this is 0.01 and 0.02 respectively. The favorable networks were further considered as the input data sets for parsimonious screening.

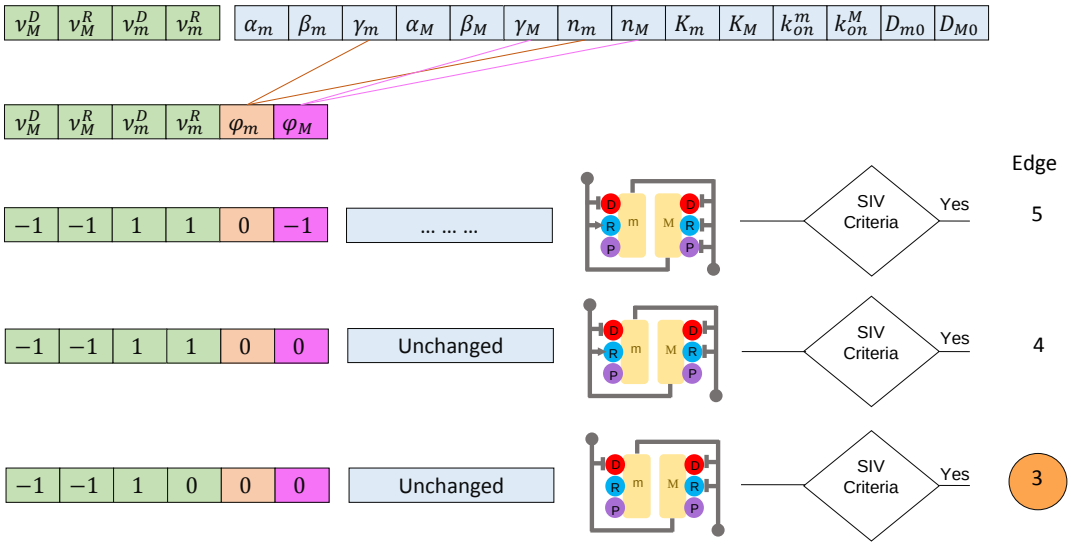

Fig. 4.7. Screening for parsimonious regulatory motifs: Parameters related to transport, reaction, and production regulation were used to generate a new parameter grid for parsimonious screening. In this new grid, parameters in blue remain the same for all the combinations considered. Each parameter grid differs only with the values of regulatory parameters associated with diffusion, reaction, and production modulation. After simulating the system using CVODE, it is filtered again with scale-invariance (SIV) / robustness (RBST) criteria. Finally, the successful candidate network with minimal edges (edge 3 as shown here) is finally chosen.

Table 4.4
Successful network motifs for different versions of TCS model: In this table, we captured the statistics of TCS model 1 and TCS model 2.

TCS	Scale-invariance			Robustness		
	$\leq T_{ss}$	$> T_{ss}$	Total	$\leq T_{ss}$	$> T_{ss}$	Total
Modulator source at X = L	0	2037	2037	2	80	82
Modulator source at X = 0	73	21	94	327	14	351

Table 4.5
Successful network motifs for two versions of TCS model: In this table, we capture the statistics of the two model versions of TCS we consider– i) Modulator source is at X = 0, ii) Modulator source is at X = L

TCS	Scale-invariance			Robustness		
	$\leq T_{ss}$	$> T_{ss}$	Total	$\leq T_{ss}$	$> T_{ss}$	Total
X = L	0	2037	2037	2	80	82
X = 0	73	21	94	327	24	351

the TCS model variants, only a small pool of of data (about 2%) pass the filter test designed to identify biologically acceptable distributions. A similarly low percentage of biologically acceptable distribution was observed in previous screenings conducted for scale-invariance [174].

4.5.1 Comparison of screening statistics between model 1 and model 2

Analysis shows that when modulator source is at $X = L$, TCS works well to satisfy the SIV criteria. This is evident from the comparison of Fig.4.8 and Fig.4.9. As seen from the screening statistics shown in Table 4.5 out of 11.9 million possible network motifs screened, model 1 (Modulator source at $X = 0$) achieved robustness for about 351 parameter sets, whereas only 82 sets are acceptable for model 2 of

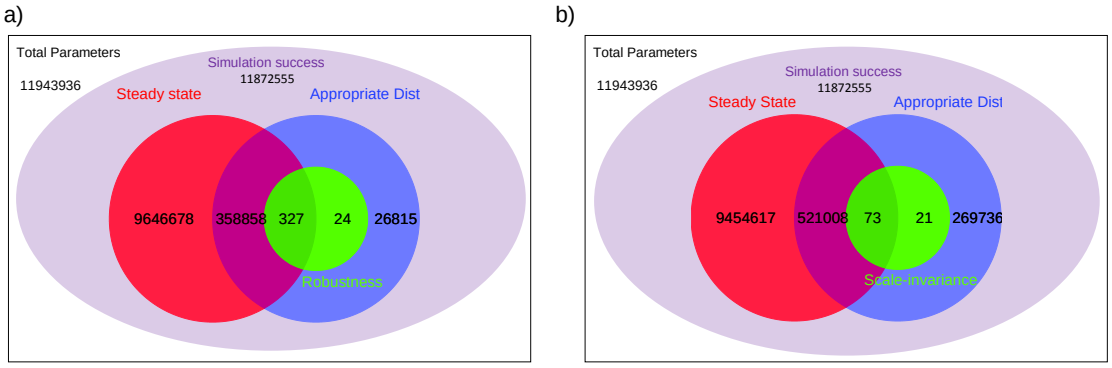

Fig. 4.8. A Venn Diagram for screening statistics of TCS with modulator source at X = 0. Only a small portion of the total parameter vectors generate biologically acceptable morphogen distributions for both the perturbed and unperturbed cases. a) Screening statistics for robustness shows that only 351 data sets out of 11.9 million possible cases satisfy the robustness (RBST) criteria as designed. As seen from the Venn Diagram, 24 sets fail to reach steady state within the first 6 hours of the dynamics. It is worthwhile to note that simulation failures due to CVODE convergence issues were very low. b) Similar to part a, however, the data shown here is designed for scale-invariance (SIV) screening. Compared to the robustness screening data, SIV data has a lower number of successful parameter sets that satisfy the SIV performance objective. However, SIV screening shows more biologically acceptable distributions than the RBST case. Both the RBST and SIV analysis are conducted on 3 points ($\xi = 0.2$, $\xi = 0.4$, $\xi = 0.6$,) along the spatial domain.

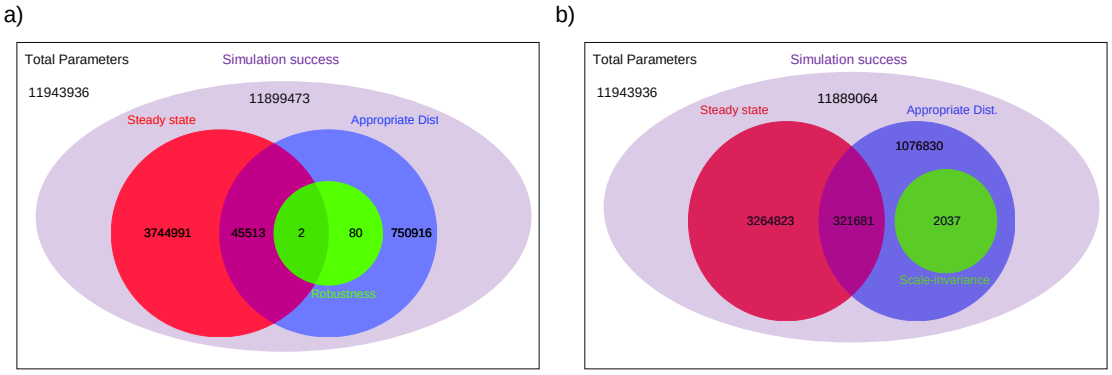

Fig. 4.9. A Venn Diagram for screening statistics of TCS with modulator source at $X = L$. The simulation had a limited number of CVODE failures. For SIV analysis, the data was generated for two different length scales: $L = 300\mu m$ and $L = 600\mu m$. a) Screening statistics for robustness data shows that only 82 data sets satisfy the robustness (RBST) criteria. Most of the successful cases dont reach steady state within the first 6 hours. b) Similar to part a, however the data shown here is for SIV screening. As seen here, a number of cases demonstrate SIV, but none reach steady state within the first 6 hours. Here, RBST and SIV analysis are conducted on a 3 points ($\xi = 0.2$, $\xi = 0.4$, $\xi = 0.6$,) criteria along the spatial domain.

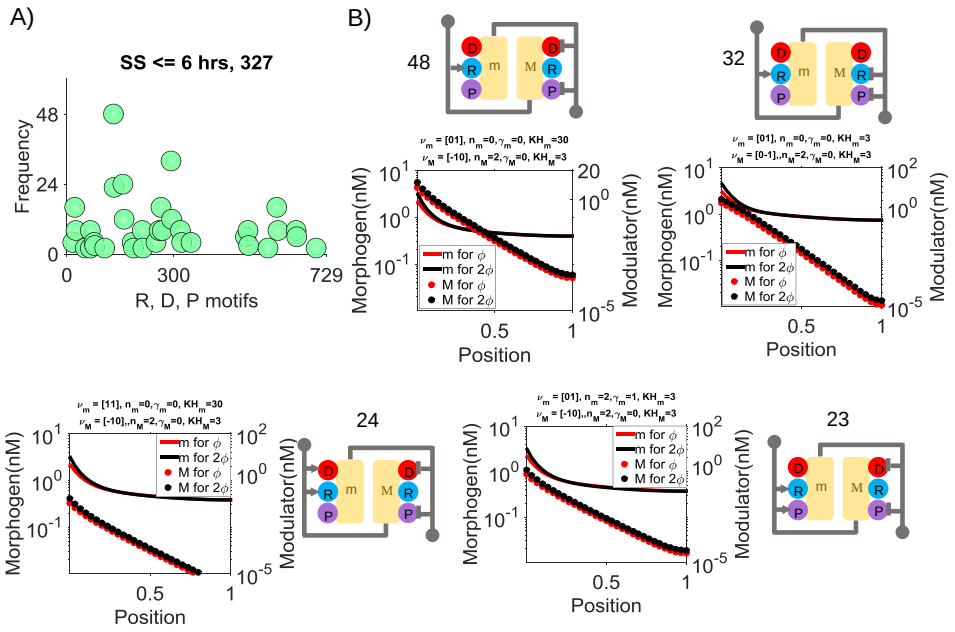

Fig. 4.10. Regulatory motifs for successful RBST cases with modulator source at $X = 0$. Diffusion, reaction, and production of morphogen and modulator can be regulated positively, negatively, or there may be no regulation as well. This generates a total of 729 theoretically possible regulatory motifs for each TCS variant. a) Histogram analysis of successful cases that reach steady state within first 6 hrs show that most motifs fail to satisfy SIV criteria. As seen from the frequency of occurrence data, a few of the acceptable motifs appear more frequently than others. b) The most frequently occurring motifs that achieve SIV are shown here with their corresponding morphogen and modulator distribution. For all plots, logarithmic concentrations of morphogens and modulators are plotted in the left and right sides of the Y-axis respectively. The distribution for the unperturbed system is in red, and circular markers and unbroken lines are used for morphogen and modulators respectively. System length was $L = 300\mu m$ for this analysis.

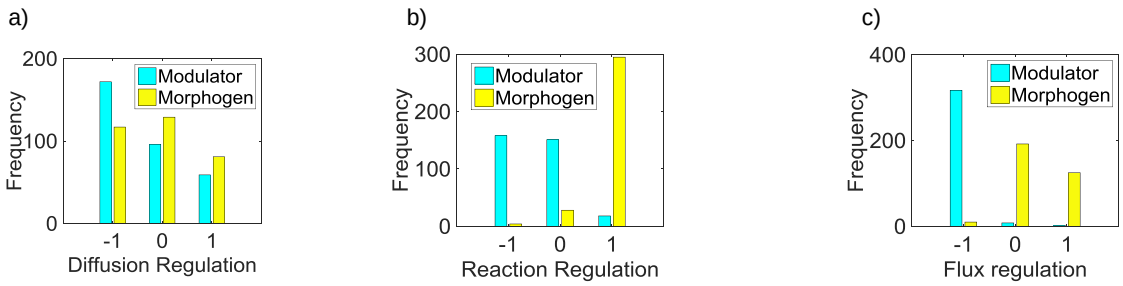

Fig. 4.11. Parameter distribution for scaling robustness when the modulator and morphogen sources are both at the left boundary ($X = 0$): Each morphogen and modulator regulatory parameter is compared here, and it is found that in most cases, the system requires positive morphogen regulation removal (part b, 1 stands for positive regulation). This phenomenon is later observed for scale-invariance cases of TCS when the modulator source is at $X = L$. Modulator production rate is primarily suppressed by morphogen among all the successful cases.

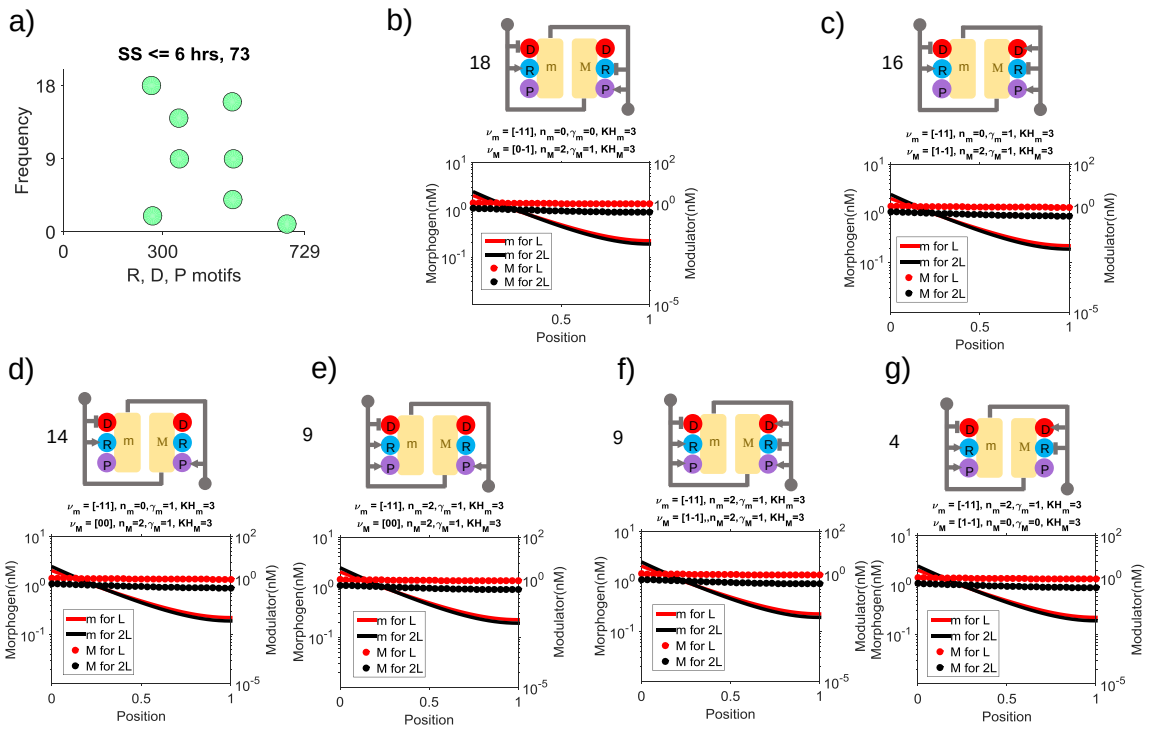

Fig. 4.12. Regulatory motifs for successful SIV cases for modulator source at $X = 0$: Figure details and colors codes are similar to Fig.4.10. For SIV, $L = 300\mu m$ was used for the unperturbed system, whereas for the perturbed system, the system length was doubled ($2L$).

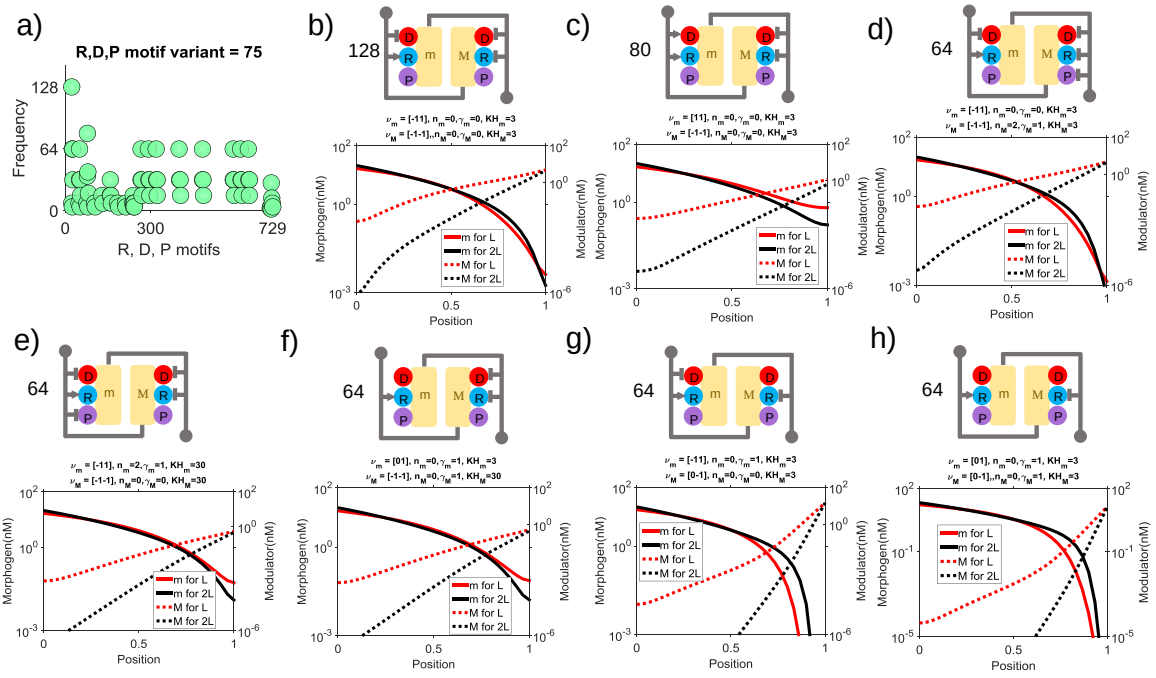

Fig. 4.13. Regulatory motifs for successful SIV cases for modulator source at $X = L$: D,R,P represents the diffusion, reaction and production of each species. a) Each green circle denotes the occurrence of a specific motif. As we clearly see here, several motifs appear with an equal number of occurrences, whereas others have few appearances. Out of 75 regulatory motifs we only considered motifs that have more than 2% appearance. b) Regulatory motifs appearing at least 64 (2%) times have been plotted here together with morphogen and modulator concentrations. Concentration plots are all drawn in log scale, and corresponding regulatory motifs are shown on top of each concentration plot. Positive, negative, and no regulation of biophysical properties are represented using arrow-head, flat head, and no-line respectively. The Y- axis at the left is for morphogen concentration and modulator concentration is plotted in the left Y-axis with a range of $[10^1\ 10^{-5}]$nM. In most of the motifs, modulator concentration is primarily restricted near the source at $X = L$. Moreover, in all these plots, modulator concentration and the active domain for modulation decrease as the system length is increased from L to $2L$.

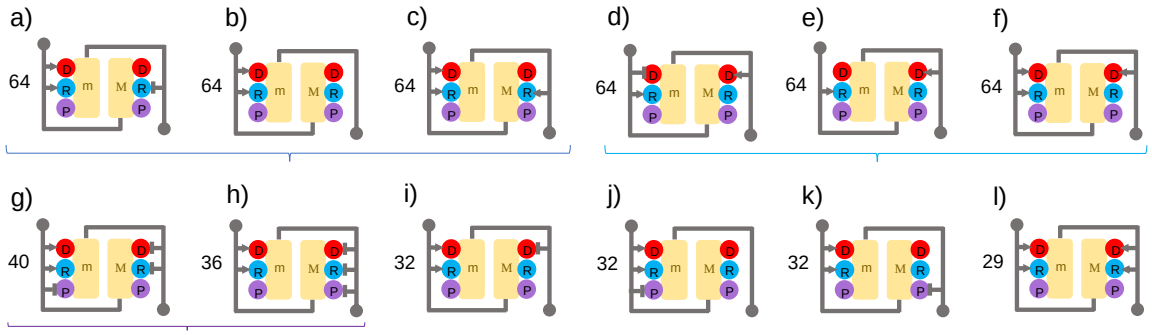

Fig. 4.14. Network motifs that scale when the modulator source is at $X = L$: This is a continuation Fig.4.13. Each motif is presented with its frequency of occurrence in the list of all successful cases.

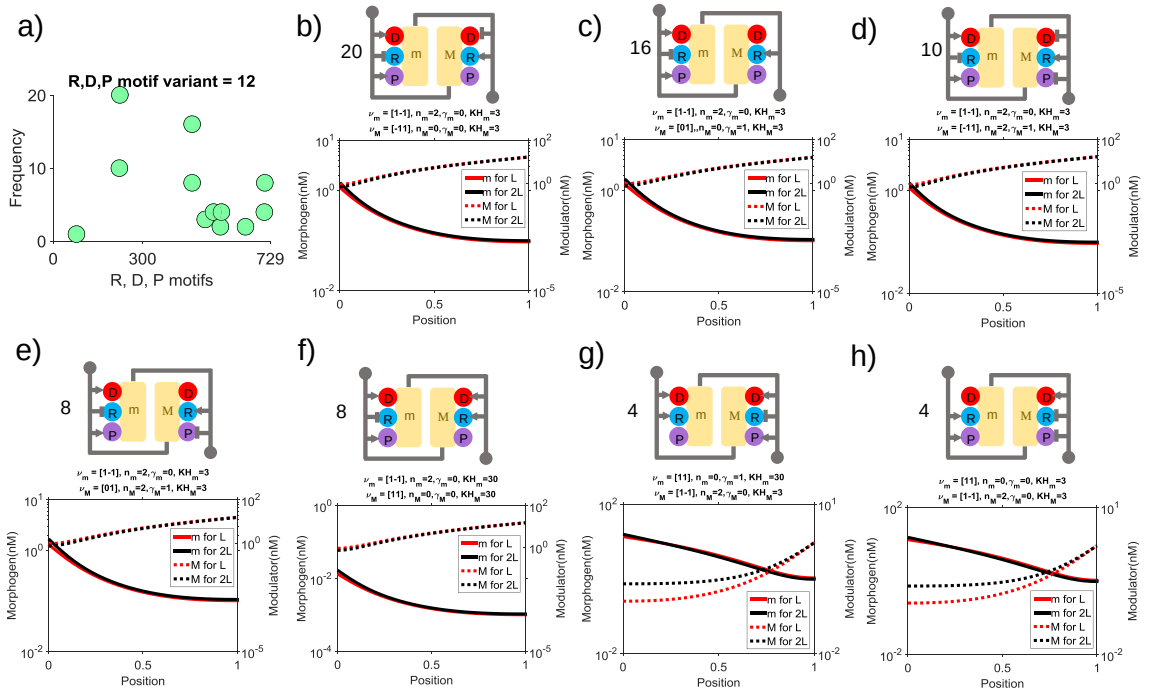

Fig. 4.15. Regulatory motifs for successful RBST cases for modulator sources at X = L. Color codes are similar to the codes in Fig.4.13. However, in the RBST analysis flux ϕ is the unperturbed case and 2ϕ is the perturbed case. In both cases, system length was $L = 300\mu m$.

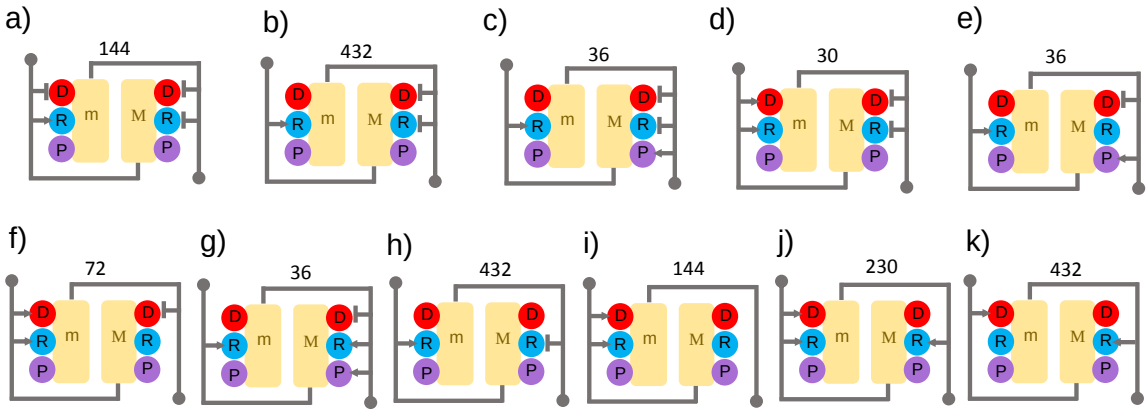

Fig. 4.16. Parsimonious analysis of motifs for morphogen source at $X = L$. Parsimonious screening generates 16 regulatory motifs from the 75 motifs we previously obtained. Details of the parsimonious screening are outlined in Fig. 4.7. There are 3 regulatory motifs that are most frequent out of all 2037 successful cases. Here, flat-head means a negative regulation, no-edge refers to no regulation, and an arrow-head demonstrates positive regulation.

TCS implementation. However, we considered two more data sets with 9.3 and 13.6 million parameters respectively, and it was found in both cases that model 1 does not perform better than model 2 in mitigating the fluctuation of morphogen production. This is evident from Table 4.6 and Table 4.7 where it is seen that successful cases for robustness in TCS model 1 is less than that of TCS 2. However, among all the models, TCS model 3 works best to achieve robustness, and is evident from the fact that the number of successful cases in TCS model 3 is significantly higher than the other two versions of TCS.

For scale-invariance, however, we find a totally different outcome– the TCS version 2 model (modulator is located at $X = L$) works considerably well in satisfying the scale-invariance criteria than the other TCS version (modulator source is at $X = 0$). As the table data shows, only 94 network motifs satisfy the SIV criteria we defined, whereas about 2037 network motifs are acceptable for TCS model version 2. In another simulation of 9.3 million parameter vectors, the ability of model 2 to perform well in achieving scale-invariance is reiterated, and is seen from Table 4.6. However, in the third data set that contains 13.6 million parameter vectors, TCS model 2 does not perform well for scale-invariance when screened using a three point criteria. However, in the third parameter space the intrinsic decay rate constant of both morphogen and modulator were not varied over a wider range as compared to the other two data sets, and hence, a number of physiologically relevant values of the intrinsic decay coefficient may have been omitted in the third data set.

In the screen, we did not obtain many cases where the steady state is achieved within the first ten hours (or, 6 hours as used in one parameter space) of the dynamics, and this is captured in the column titled as SS_{10}. For instance, TCS model 1 and TCS model 2 do not have many successful cases both for robustness and scale-invariance that reach steady state within first 10 hours, as evident from Table 4.5. The three data sets we considered here vary in regards to the intrinsic value of kinetic rate constant, and a few other regulatory parameters that affect the dynamics also differ within these data sets. So, steady state statistics within SS_{10} may vary. However, in

general, TCS not reaching steady state within the first 10 hours does not affect our conclusion much, since a faster dynamic that reaches steady state within 10 hours is obtainable by increasing the parameter values.

Furthermore, our screening of the two parameter spaces with a size of 9.3 and 13.6 million parameter vectors reveals that TCS model 3 is by far the best model to achieve robustness. In TCS model 3, the modulators produce from a spatially distributed source, and the source of morphogen is located at $X = 0$. Besides all the possible topologies of mutual regulation between morphogen and modulator, TCS model 3 also implements the previously proposed expander-repressor [10] mechanism. As seen from Table 4.6 and 4.6, we obtained a large number of cases that satisfied robustness, and among all the successful cases, a large portion achieved steady state value within the stipulated first 10 hours (SS_{10}) of dynamics. However, Model 3 performs poorly for scale-invariance objectives, as evident from the screened data. This is unexpected, as TCS model 3 also includes previously established expansion-repressor mechanisms known for achieving scale-invariance [10, 11, 37], and it is elaborated further in later sections.

The different regulation types for all biophysical properties generates a total of 729 possible network motifs and our simulated data demonstrates that most of the motifs failed to satisfy the robustness defined by the criteria. A few sample motifs, along with their corresponding frequency, is shown in Fig. 4.10B. As observed here, if the production and transport rate of the modulator is negatively regulated, positive regulation of the clearance rate of modulators, together with a positive regulation of either the production or diffusivity of modulators, ensures robust signaling. This is seen from Fig. 4.10B, and in other example networks with lower frequencies of appearance (data not shown). Out of 327 successful motifs, about 107 motifs fall among these classes of networks, and all are examples of active modulation where morphogen and modulators are directly linked to each other. Interestingly, among the acceptable network motifs with higher frequencies, the production of modulators

is always negatively regulated by morphogens. So, near the source where morphogen signaling is high, modulator production is downregulated.

As seen in Fig. 4.10B, the clearance of morphogens is upregulated by the modulators, and this ensures rapid removal of morphogens from the surface once the production of morphogen is doubled in the system. In response to such modulation on morphogen activity, morphogens negatively regulate modulator production, and also, morphogens either slows down the transport of modulators, or the clearance of modulator is slowed down. Once the transports are slowed down, the modulator travels slow and maintains stronger presence near the source region of morphogens, which eventually counter the increased level of morphogens in perturbed case (intrinsic value of morphogen flux becomes 2ϕ) by positively regulating the clearance rate of morphogen. For the negative regulation of modulator clearance, the TCS model may work differently. That is, the diffusivity of modulators remains unchanged, but as their rate of clearance is slowed down, more modulators are available on the surface at any given time to counter the larger production of morphogens (in perturbed case, flux becomes 2ϕ) by enhancing the clearance of morphogens form the surface.

Furthermore, we conducted a histogram analysis to see if morphogens or modulators have any bias towards a specific regulation type for any of their biophysical properties. To our surprise, we observed bias among specific regulation types. More specifically, it was found that among all the network motifs that satisfy the robustness criteria negatively regulated clearance of morphogen is the most prevalent, and is clearly seen from Fig. 4.11b. For modulators, the negative regulation of production rate is significantly prevalent as evident from Fig.4.11c. The regulation of diffusivity of both morphogens and modulators incorporates all types of modulations as evident from Fig. 4.11a.

4.5.2 Network motifs that achieve scale-invariance in TCS model 2

In the first few network motifs, as shown in Fig.4.13, the transport and reaction properties of modulators are all regulated negatively (specifically, Fig.4.13 b,c,d,e,f), and any combination of morphogen biophysical property regulation could achieve scale-invariance. For example, given that the transport and reaction properties of modulators are negatively regulated, a positive regulation of transport and reaction properties can achieve scale-invariance, and is evident in Fig.4.13. Also, we observe a very high frequency appearance of such regulatory motifs. This means that when the system length is increased, the removal rate of modulators from the cellular surface and the diffusivity of modulators should be slowed down. Because the diffusivity of morphogen is slowed down, modulators diffuse slowly once it is secreted from its source at $X = L$. As a result, upon secretion morphogens encounter fewer of modulators near its source region, and positive regulation by the low modulators increases the diffusivity of morphogens, allowing morphogens to travel a longer distance. As the modulator increases the clearance rate of morphogens, more morphogens may be cleared out near the morphogen source regions, imitating an enhanced clearance of morphogen near the source. This can potentially contribute to stabilizing the morphogen gradient near the source region, and may be stabilizing the morphogen amplitude to achieve scaling near the source region.

A more simplified motif involves negative regulation of the removal rate of modulators and positive regulation of the removal rate of morphogens. As the removal rate of the modulator is slowed down, it is expected that more modulators will be on the surface to positively upregulate the clearance of morphogens. That is, to achieve scale-invariance, higher numbers of modulators are expected on the cellular surface for a faster clearance of morphogens from the surface. More candidate network motifs require different strategies to scale the length variation, and a few of those cases are listed in Fig. 4.14. For instance, in a number of candidate cases, both diffusivity and the clearance of morphogens should happen faster because of the modulation and,

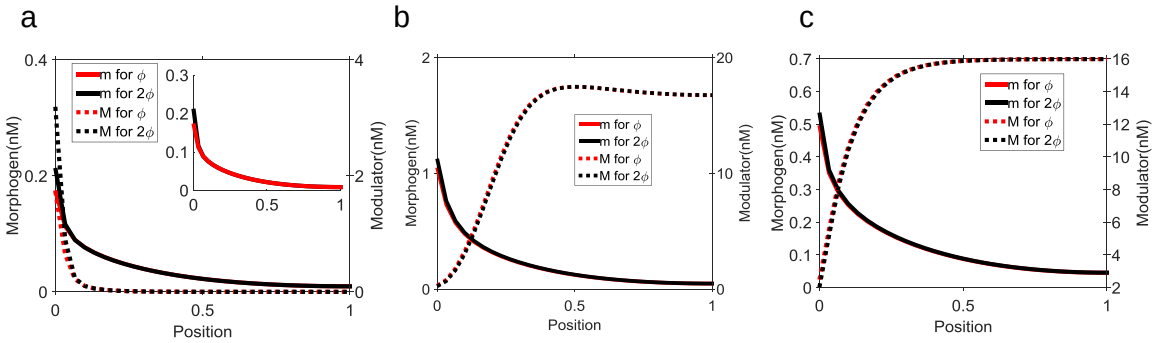

Fig. 4.17. Sample distribution of robustness analysis for TCS model 3: In this model, modulators are secreted from a spatially distributed source and the rate of secretion is regulatedby morphogen spatially. In all the plots, morphogen distributions are presented as continuous lines, whereas the broken lines were used to denote modulator concentrations. The color code was used to differentiate between perturbed (black) and unperturbed (red) cases. a) A high concentration of modulators near the source of morphogen could cause a robust morphogen distribution. b, c) Non-uniform distribution of modulators was able to form a robust morphogen signaling despite the presence of flux variation of morphogen.

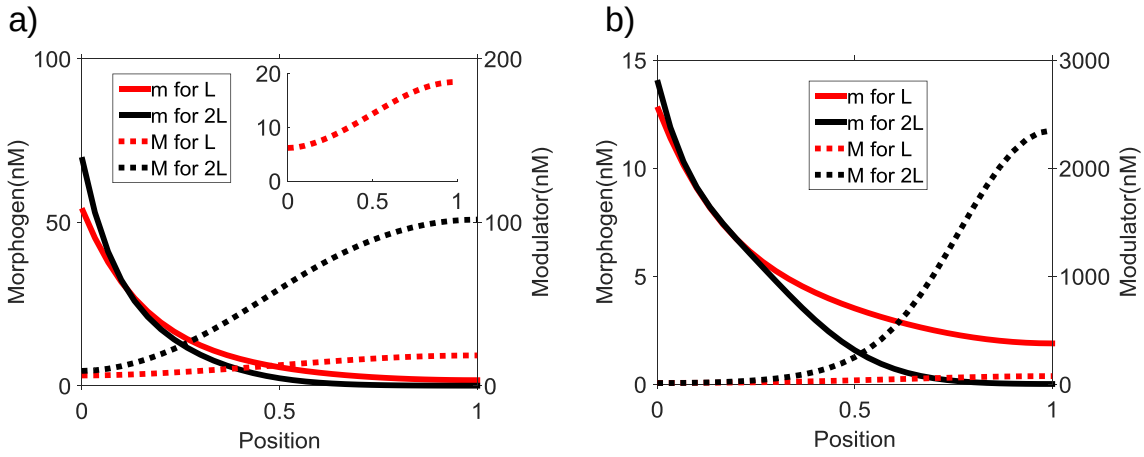

Fig. 4.18. Sample distribution of scale-invariance analysis for TCS model 3: In general, this model didn't work well for scale-invariance, despite the fact that this model included network motifs that represent an explansion-repression (ER) mechanisms proposed previously [10]. We obtained a very few cases that satisfy scale-invariance, and a few sample distributions are shown here. In all the plots, morphogen distributions are presented as continuous lines, whereas the broken lines were used to denote modulator concentrations. The color code was used to differentiate between perturbed (black) and unperturbed (red) cases. a) Scale-invariance was achieved for non-uniformly distributed modulator concentration, which is very interesting as the previous research suggested an uniform distribution of modulators to demonstrate scale-invariance. b. scale-invariance is achieved within the first 30% of the system length for non-uniform modulator distribution.

in response, if a modulator's clearance is positively or negatively regulated, the system exhibits demonstrate scale invariance. These types of motifs are seen in Fig.4.14 a,b,c. In another motif, it is suggested that if modulators can positively upregulate both the transport and reaction properties of morphogens and morphogen signaling downregulates the production of modulators, TCS can adjust the decay length of morphogen to accommodate length variation. In order to identify if these candidate motifs have a minimal number of edges, we conducted a parsimonious screen, and the details are elaborated on later.

4.5.3 The TCS Model with a spatially distributed source fails to demonstrate 3-point scale-invariance

In the third TCS model, modulators of morphogen signaling are spatially distributed. As explained earlier, this version of TCS works remarkably well to achieve robustness. A few sample sets of concentration plots, as shown in Fig. 4.17, reveal that two concentrations of morphogens obtained for two different intrinsic production rate of morphogens superimpose well. This is achieved even though theres a qualitative difference in the shape of modulator distribution in those three sample cases. However, TCS model 3 fails to satisfy the scale-invariance criteria, despite the fact that it imitates the previously proposed expander-repressor (ER) mechanism [10, 11, 174] in its implementation. Sample concentration-plots, as obtained by using a two point scale-invariance criteria, are shown in Fig. 4.18. As seen here, signaling distribution perfectly scales in the presence of system size perturbations in regions near the source of morphogen. More precisely, scale-invariance is demonstrated only in 30% of the system length, and regions away from the source of morphogen fail to satisfy the scale-invariance criteria.

A close comparison of the proposed TCS and previous ER mechanism reveals that the ER mechanism considered a quadratic decay of morphogen, where the intrinsic decay constant for the quadratic degradation of morphogen was regulated by the

modulators. In one of the previous works [197] showed that if morphogen degrades faster near the source of morphogen, and a slow degradation happens regions away from the source, morphogen distribution becomes robust against perturbation. This self-enhanced degradation of morphogen is later modeled as a non-linear degradation of morphogen, and is extensively used in ER mechanism [10] to study the ability of ER mechanisms to demonstrate scale-invariance. In the TCS, we didnt consider any quadratic decay of morphogen, which may be a potential reason that the TCS model 3 didnt demonstrate scale-invariance considerably. Thus, an immediate next step to our TCS model would be to incorporate the quadratic decay of morphogens to see whether the TCS model 3 demonstrates scale-invariance as well.

However, robustness and scale-invariance both are achieved for non-uniform distribution of modulators using the TCS model, whereas in previous research only uniformly distributed spatial modulators topologies demonstrated scale-invaraince. Thus, screening of alternative topologies using TCS model 3 reveals a set of potential network motifs that are able to demonstrate scaling of morphogen signaling for a non-uniformly distributed modulator activity.

4.5.4 Parsimonous motif reveal a set of candidate regulatory motifs with minimal edges

A number of regulatory motifs appear to generate almost identical distribution and signaling. Its likely that the motifs with minimal edges serve as the core for all those motifs that generate characteristically similar signaling. For instance, in Fig.4.13, each pair (b,d), (e,f), (g,h) has similar distribution of morphogens, and the corresponding regulatory motifs also have a common set of edges. In Fig.Fig.4.13 g,h, there is a minimal core network between the two regulatory motifs, which involves the negative regulation of the modular reaction property and a positive regulation on the morphogen reaction property. The existence of such networks could be ensured if

Table 4.6
Scale-invariance and Robustness using a 3-point criteria: We considered three spatial points here to different between acceptable and unacceptable cases. The two data sets considered here have 9.3 and 13.6 millions points respectively.

Mod	Pts.	ξ	SIV	SS_{10}	$SIV \cap SS_{10}$	RBST	SS_{10}	$RBST \cap SS_{10}$
X = 0	9.3	0.25, 0.4, 0.6	184	1146888	0	2948	1331167	0
	13.6	0.25, 0.4, 0.6	137	3082868	0	5511	3329181	13
X = L	9.3	0.25, 0.4, 0.6	480	1438152	0	3113	1629601	0
	13.6	0.25, 0.4, 0.6(5)	12 (36)	2837213	0	6558	3111367	1009
X=[0 L]	9.3	0.25, 0.4, 0.6	0	955591	0	24089	1186499	2452
	13.6	0.25, 0.4, 0.6	0	2424229	0	60204	2941194	2567

one of the edges from regulatory motifs, shown in Fig.4.7 g is removed and the newly formed network retains the scale-invariance property.

Parsimonious screening, as outlined in Fig.4.7, shows that such core minimal motifs exist that involve only the connectivity equivalent of Fig.4.13h. Specifically, 21% out of 2037 motifs show this core element, as shown in Fig.4.16. There are other minimal network motifs where the diffusion and reaction properties of modulators are positively regulated for morphogens and negatively regulated for modulators, and is shown in Fig.4.16d. Moreover, parsimonious screening reveals that both active and passive modulations are able to achieve scale-invariance. Passive modulation is shown in Fig.4.16i, which is about 7% of all the acceptable regulatory motifs. All these acceptable cases took longer than 6 hours to reach steady state, and hence, may be more pertinent for dynamic scale-invariance as explained in [9]. However, an increase in parameter values may help achieve steady state within the stipulated time. Moreover, motifs that require more time to reach steady state may be more pertinent for dynamic scale-invariance as explained in [9].

Table 4.7
Scale-invariance and Robustness analysis for two point criteria: $\xi = 0.25, 5$

Mod	Pts.	ξ	SIV	SS_{10}	$SIV \cap SS_{10}$	RBST	SS_{10}	$RBST \cap SS_{10}$
X = 0	9.3	0.25, 0.5	266	1146888	0	3366	1331167	0
	13.6	0.25, 0.5	176	3082868	0	5707	3329181	13
X = L	9.3	0.25, 0.5(4)	1026 (7460)	1438152	0(0)	3977	1629601	0
	13.6	0.25, 0.5(4)	36 (3344)	2837213	0(0)	6558	3111367	1057
X=[0, L]	9.3	0.25, 0.5	0, 2 [0.1, 0.3]	955591	0	27927	1186499	2696
	13.6	0.25, 0.5	0, 9 [0.2, 0.3]	2424229	0	60651	2941194	2780

4.6 Concluding remarks

In this chapter, we proposed a morphogen and a modulator based system; namely, the Two Component System (TCS), to explain the scaling of patterns in developmental process. The model developed here included all the possible regulatory motifs between the biophysical properties of a morphogen and modulator. More precisely, we developed three different cases of TCS models (TCS model 1, TCS model 2, TCS model 3), and in each case, there were 729 different regulatory motifs between different biophysical properties. The previously developed ER mechanism [10] was a special case under the TCS model 3 that we considered. Here, we attempted to screen all the possible regulatory relations between morphogens and modulators, a large parameter space ranging several order magnitudes of the system parameters, and these were successfully implemented by adapting a strategy that combined the reduced storage solver CVODE and the supercomputing clusters at Purdue University.

Our analysis revealed that scaling of patterns can be explained using the TCS paradigm, and a number of motifs were identified through numerical screens that indicated the role of both active and passive modulation of morphogen activity. In this research, we considered two different forms of perturbations while analyzing the scaling of patternsscaling in the presence of system length variation (known as scale-invariance) and scaling in response to perturbations in morphogen production (known as robustness). We found that TCS models achieved scaling in both scenarios; however the performance of TCS was model specific. Our simulation demonstrated that TCS with spatially distributed modulators works better than the other two versions of TCS models in achieving robustness. One of the interesting outcomes of this research was the scaling of patterns for a non-uniform distribution of modulators as obtained from the screening of TCS model 3. This is important in identifying the candidate modulator, as previous ER mechanisms demonstrated scaling only in the presence of a uniformly distributed modulators role in the regulation of morphogen activity.

Further comparison between the two TCS models with sources of modulators in different boundaries (i.e. TCS model 1 and TCS model 2) showed that when morphogen and modulator sources were located at the opposite ends (this formed TCS model 2) of spatial domain, TCS demonstrated better performance for scale-invariance. For robustness, TCS model 1 performed well compared to TCS model 2. Out of all the successful scenarios that demonstrated scaling of patterns for TCS model 1 and TCS model 2, we conducted a parsimonious screening to identify the regulatory motifs with minimal connectivity.

Moreover, as all the biophysical properties such as diffusivity, reaction rates and production of both morphogen and modulators are varying spatially, TCS becomes computationally challenging. Further complicating the matter, hundreds of millions of parameter vectors were considered to screen over a few order of magnitudes of the system parameters. This research implemented a strategy by coupling a reduced storage solver, namely, the COVDE and supercomputing clusters to generate data within a few days. In order to obtain trustworthy data, COMSOL Multiphysics was used to compare against our different versions of CVODE implementations, and several error comparisons were done to optimize the simulation time and discretization points of spatial domain as well. Approaches used in this research to implement a reaction-diffusion system may be used in all other systems that require an exhaustive screening of parameter space with topological variety.

Finally, the candidate minimal motifs, so far obtained, may help identifying the in vivo candidate molecules that can act as modulators. Our current work on TCS models considers performing sensitivity analysis of the most-frequent regulatory motifs, and the inclusion of quadratic decay in morphogen dynamics.

5. FUTURE WORK

While our analysis of scaling of patterns and the signal transduction of patterning process, provides new insights on morphogen mediated patterning and signaling, there are a number of important questions that can be addressed further. These are the works that we reason to be the immediate next steps to continue what we achieved in this thesis. For instance, one possible extension of our work on heterodimer dominance would be to conduct a global sensitivity analysis to evaluate any correlation between system parameters and the phenotypic outcomes of the system. Our work on scaling can be extended further, and a few of the immediate extensions of TCS are also enumerated in this chapter.

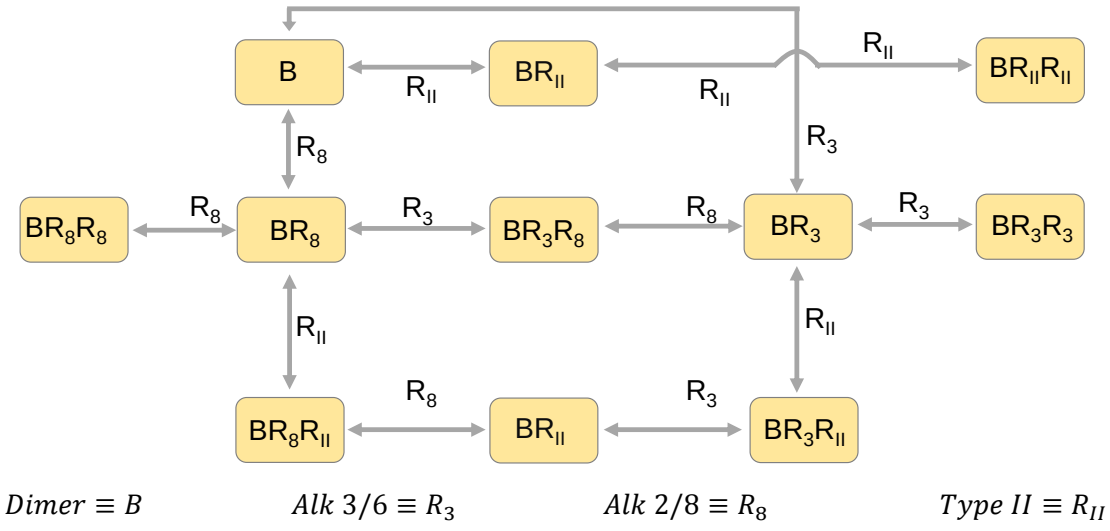

Fig. 5.1. A proposed network for stochastic analysis of the receptor oligomerization process: In this reduced version, after initial binding all the subsequent recruitments of Type II are omitted. However, initial interactions between a dimer and Type II receptor are considered and the resulting receptor complex further recruits an $Alk3/6$ or $Alk2/8$ receptor.

5.1 Analysis of dimer-receptor signaling and receptor oligomerization

Numerous extracellular steps, including receptor oligomerization and interactions with secreted regulators, are required by morphogens to initiate signaling [6, 9, 24, 26, 29, 198]. To determine if receptor oligomerization and other regulatory steps by regulators work together to mitigate stochastic noise, further investigation and new discoveries are needed. We assume this as an immediate next step, and aim to extend our current research to identify the mechanisms behind the preciseness in BMP signaling by developing a stochastic model of the dimer-receptor network considered in this work.

5.1.1 Identify the role of BMP-antagonists on the dynamic range of morphogen activity

Besides their cognate receptors, BMP dimers are also known to interact with a wide variety of extracellular factors [6, 7, 26]. For instance, in the D/V patterning of xenopus, BMP homodimers and heterodimers bind with Chordin (Chd) with almost equal affinity [151]. However, molecular data also revealed that BMP homodimers and BMP heterodimers bind differently with BMP-antagonists [199]. For instance, BMP heterodimers (Dpp-Scw) in Drosophila demonstrate higher affinity for BMP homodimers [199], and our future aims our future aims might also incorporate the role of BMP-antagonists, such as Sog, and the role of metalloprotease Tolloid (Tld), to investigate if the dynamic range of morphogen activity, as evaluated in this thesis, is regulated by the role of BMP antagonists.

5.1.2 Develop a complete stochastic model of the receptor oligomerization process to discover whether heterodimer dominance provides a more robust signaling

Developmental processes are highly robust despite the presence of numerous forms of stochastic fluctuations. For instance, molecular data shows that both transcription and translation are inherently noisy, but developmental processes generate precise patterns that are remarkably robust and reproducible. Thus, species development mitigates noise at different levels to give rise to precise patterns out of a noisy environment, and the mechanisms behind noise suppression are still elusive. In BMP signaling pathways, BMP heterodimers outperform homodimers in eliciting signaling. However, whether or not signaling through heterodimer dominance provides a less noisy pattern is not known, and an interesting immediate next step of our research on receptor complex oligomerization would be to conduct a stochastic analysis of the signaling events.

One of the possible extensions of our current research on dimer-receptor interactions and heterodimer dominance would be to develop a stochastic model of the receptor oligomerization process. The model could be used to analyze whether heterodimer provides more robust signaling by initiating a less noisy signal from the oligomerization steps. Also, the kinetics advantage of heterodimers over homodimers could be investigated as well. To overcome the numerical challenge to quantify the noise using the coefficient of variation as a parameter, this work can be accomplished using a previously developed method for steady-state probability approximation [156].

5.1.3 Investigate whether dissimilar affinities of homodimer-heterodimer towards BMP antagonists are advantageous for heterodimer dominance in BMP signaling

Molecular data reveals that dimers have different affinities for some BMP antagonists [29, 149–151], and as previously stated, we believe an immediate next step for

our dimer-receptor network would be to incorporate BMP antagonists to the model. However, the inclusion of antagonists to the existing model will increase the number of interacting species significantly, causing tremendous computational costs on propensity updates during numerical approximation of the chemical master equations. To circumvent this problem, by referring to our outcomes on the stochastic analysis of the type II receptor recruitment process, we propose that the number of interactions between dimers, receptors, and antagonists could be further simplified.

The complete set of interactions between a dimer and its receptor family involve 17 intermediate states and 30 second-order reactions (shown earlier in Chapter 2), and, for all dimers, the system consists of 51 species. If antagonists are incorporated in this model, the number of species will increase significantly, making the stochastic simulation computationally intractable due to the large number of propensity updates [164, 165, 168]. Since it is known that recruitment of type II receptors doesnt change the stochastic profile of the system significantly, the dimer-receptor network could be simplified further as shown in Fig.5.1, and so the total number of species could be reduced from a system of 51 species to 24 species.

Besides the issue of determining whether heterodimer dominance can reach an advantage by mitigating the noise of the system, the developed stochastic model can further be used to determine the impact of other signaling factors, such as the role of SBPs [6, 7, 26, 198] as studied previously.

5.1.4 Extension of TCS to identify mechanisms of scaling in response to environmental perturbations

Not only can the variation in intrinsic factors affect pattern scaling, extrinsic factors are also capable of altering the biophysical properties of a system. So, to ensure robustness and reproducibility of biological patterns, developing system and process must accommodate for environmental changes, which can impinge the intrinsic biochemical process significantly. For example, developmental processes may experience

detrimental consequences because of the loss of vitamins or amino acids during the early stages of development [200, 201]. Therefore, exposure to adequate nutrition or energy is important to ensure a proper growth for the species. Nutrition variation for the embryo can cause a coordinated modification of the production of signaling factors. Hence, we intend to identify if the proposed TCS can resolve systematic reduction of input flux due to nutrition variation, ensuring a robust and reproducible pattern.

5.1.5 Determine whether the TCS model can explain scaling in the presence of temperature variation

Temperature variation is known to affect biochemical processes. For example, the synthesis rate of a class of protein, known as heat-shock protein, in Drosophila increases significantly with an increase in temperature. Therefore, there is biophysical evidence of the dependence of developmental processes on temperature, which can affect the biochemical processes that occur in the cellular environment. The temperature dependence of the kinetic rate constant (k) is demonstrated using Arrheniuss equation, and is given as below:

$$k(T) = A \times e^{-\frac{E_1}{RT}} \tag{5.1}$$

where, E_a is the activation energy required for the reaction to occur, T is temperature in Kelvin and R is the universal gas constant.

5.1.6 Determine whether TCS can buffer out noise to achieve signaling refinement

Cellular and subcellular processes generally take place in very small spatial scales and the movements of participant molecules are random. Hence, a deterministic analysis of interactions between species may not hold for low concentration biochemical activity. Instead, a stochastic approach in the form of Brownian dynamics [202] seems

to be more appropriate. The randomness in the spatio-temporal distribution of signals is increased further due to a combined effect of tight ligand-receptor binding and the slow kinetics of the processes [26]. Moreover, a deterministic approach often fails to capture the exact qualitative behaviors of a noisy biochemical system [170]. For instance, deterministic approaches fail to produce the random switch between states in gene regulatory networks [203] and demonstrate different qualitative system behaviors. Therefore, considering the variability and stochastic fluctuations involved in BMP-mediated signaling systems, a modeling paradigm shift from deterministic to stochastic, becomes evident based on our study

A previous study [26] used a series of local stochastic models to identify the mechanisms behind robust BMP-signaling, but didnt consider the spatio-temporal correlations between species. We believe TCS is the model to study in order to identify the mechanisms that suppress noise to confer the fidelity of spatial patterning in species development.

LIST OF REFERENCES

LIST OF REFERENCES

[1] J. Gurdon, P. Bourillot, *et al.*, "Morphogen gradient interpretation," *NATURE-LONDON-*, pp. 797–803, 2001.

[2] G. Reeves, C. Muratov, T. Sch?pbach, and S. Shvartsman, "Quantitative models of developmental pattern formation," *Dev. Cell*, vol. 11, pp. 289–300, Sep 2006.

[3] A. Lander, Q. Nie, and F. Wan, "Do morphogen gradients arise by diffusion?," *Developmental Cell*, vol. 2, no. 6, pp. 785–796, 2002.

[4] A. Turing, "The chemical basis of morphogenesis," *Philosophical Transactions of the Royal Society of London. Series B, Biological Sciences*, vol. 237, no. 641, pp. 37–72, 1952.

[5] L. Wolpert, *Princiles of Development*. UK: Oxford University Press, 2006.

[6] S. Little and M. Mullins, "BMP heterodimers assemble hetero-type I receptor complexes that pattern the DV axis," *Nature cell biology*, vol. 11, no. 5, p. 637, 2009.

[7] D. Umulis, M. O'Connor, and S. Blair, "The extracellular regulation of bone morphogenetic protein signaling," *Development*, vol. 136, no. 22, p. 3715, 2009.

[8] D. Umulis, O. Shimmi, M. O'Connor, and H. Othmer, "Organism-scale modeling of early drosophila patterning via bone morphogenetic proteins," *Developmental cell*, vol. 18, no. 2, pp. 260–274, 2010.

[9] D. M. Umulis and H. G. Othmer, "Scale invariance of morphogen-mediated patterning by flux optimization," in *Biomedical Engineering and Informatics (BMEI), 2012 5th International Conference on*, pp. 1030–1034, IEEE, 2012.

[10] D. Ben-Zvi, G. Pyrowolakis, N. Barkai, and B.-Z. Shilo, "Expansion-repression mechanism for scaling the dpp activation gradient in drosophila wing imaginal discs," *Current biology*, vol. 21, no. 16, pp. 1391–1396, 2011.

[11] D. Ben-Zvi, A. Fainsod, B.-Z. Shilo, and N. Barkai, "Scaling of dorsal-ventral patterning in the xenopus laevis embryo," *BioEssays*, vol. 36, no. 2, pp. 151–156, 2014.

[12] T. Gregor, W. Bialek, R. R. de Ruyter van Steveninck, D. W. Tank, and E. F. Wieschaus, "Diffusion and scaling during early embryonic pattern formation," *Proc Natl Acad Sci U S A*, vol. 102, pp. 18403–18407, Dec 2005.

[13] D. Umulis, M. O'Connor, and H. Othmer, "Robustness of embryonic spatial patterning in Drosophila melanogaster," *Curr. Top. Dev. Biol.*, vol. 81, pp. 65–111, 2008.

[14] J. E. Ming, E. Roessler, and M. Muenke, "Human developmental disorders and the sonic hedgehog pathway," *Molecular medicine today*, vol. 4, no. 8, pp. 343–349, 1998.

[15] K. A. Waite and C. Eng, "From developmental disorder to heritable cancer: it's all in the bmp/tgf-β family," *Nature Reviews Genetics*, vol. 4, no. 10, pp. 763–773, 2003.

[16] B. D. Harfe, P. J. Scherz, S. Nissim, H. Tian, A. P. McMahon, and C. J. Tabin, "Evidence for an expansion-based temporal shh gradient in specifying vertebrate digit identities," *Cell*, vol. 118, no. 4, pp. 517–528, 2004.

[17] M. Towers, L. Wolpert, and C. Tickle, "Gradients of signalling in the developing limb," *Current opinion in cell biology*, vol. 24, no. 2, pp. 181–187, 2012.

[18] H. Min, D. M. Danilenko, S. A. Scully, B. Bolon, B. D. Ring, J. E. Tarpley, M. DeRose, and W. S. Simonet, "Fgf-10 is required for both limb and lung development and exhibits striking functional similarity to drosophila branchless," *Genes & development*, vol. 12, no. 20, pp. 3156–3161, 1998.

[19] K. Sekine, H. Ohuchi, M. Fujiwara, M. Yamasaki, T. Yoshizawa, T. Sato, N. Yagishita, D. Matsui, Y. Koga, N. Itoh, *et al.*, "Fgf10 is essential for limb and lung formation," *Nature genetics*, vol. 21, no. 1, pp. 138–141, 1999.

[20] C. V. Pepicelli, P. M. Lewis, and A. P. McMahon, "Sonic hedgehog regulates branching morphogenesis in the mammalian lung," *Current biology*, vol. 8, no. 19, pp. 1083–1086, 1998.

[21] A. Badugu, C. Kraemer, P. Germann, D. Menshykau, and D. Iber, "Digit patterning during limb development as a result of the bmp-receptor interaction," *Scientific reports*, vol. 2, 2012.

[22] M. Serpe, D. Umulis, A. Ralston, J. Chen, D. Olson, A. Avanesov, H. Othmer, M. O'Connor, and S. Blair, "The BMP-binding protein Crossveinless 2 is a short-range, concentration-dependent, biphasic modulator of BMP signaling in Drosophila," *Developmental cell*, vol. 14, no. 6, pp. 940–953, 2008.

[23] O. Shimmi and M. B. O'Connor, "Physical properties of Tld, Sog, Tsg and Dpp protein interactions are predicted to help create a sharp boundary in Bmp signals during dorsoventral patterning of the Drosophila embryo," *Development*, vol. 130, no. 19, pp. 4673–82, 2003.

[24] T. Kirsch, J. Nickel, and W. Sebald, "Bmp-2 antagonists emerge from alterations in the low-affinity binding epitope for receptor bmpr-ii," *The EMBO journal*, vol. 19, no. 13, pp. 3314–3324, 2000.

[25] W. Sebald, J. Nickel, J. Zhang, T. Mueller, *et al.*, "Molecular recognition in bone morphogenetic protein (bmp)/receptor interaction.," *Biological chemistry*, vol. 385, no. 8, p. 697, 2004.

[26] M. Karim, G. Buzzard, and D. Umulis, "Secreted, receptor-associated bone morphogenetic protein regulators reduce stochastic noise intrinsic to many extracellular morphogen distributions," *Journal of The Royal Society Interface*, 2011.

[27] D. Umulis, M. Serpe, M. O?Connor, and H. Othmer, "Robust, bistable patterning of the dorsal surface of the Drosophila embryo," *Proceedings of the National Academy of Sciences*, vol. 103, no. 31, p. 11613, 2006.

[28] D. R. Eldar, A., D. Weiss, H. Ashe, B. Shilo, and N. Barkai, "Robustness of the BMP morphogen gradient in Drosophila embryonic patterning," *Nature*, vol. 419, no. 6904, pp. 304–308, 2002.

[29] O. Shimmi, D. Umulis, H. Othmer, and M. O?Connor, "Facilitated transport of a dpp/scw heterodimer by sog/tsg leads to robust patterning of the¡ i¿ drosophila¡/i¿ blastoderm embryo," *Cell*, vol. 120, no. 6, pp. 873–886, 2005.

[30] S. J. Butler and J. Dodd, "A role for bmp heterodimers in roof plate-mediated repulsion of commissural axons," *Neuron*, vol. 38, no. 3, pp. 389–401, 2003.

[31] E. Valera, M. J. Isaacs, Y. Kawakami, J. C. I. Belmonte, and S. Choe, "Bmp-2/6 heterodimer is more effective than bmp-2 or bmp-6 homodimers as inductor of differentiation of human embryonic stem cells," *PLoS One*, vol. 5, no. 6, p. e11167, 2010.

[32] T. Morimoto, T. Kaito, Y. Matsuo, T. Sugiura, M. Kashii, T. Makino, M. Iwasaki, and H. Yoshikawa, "The bone morphogenetic protein-2/7 heterodimer is a stronger inducer of bone regeneration than the individual homodimers in a rat spinal fusion model," *The Spine Journal*, vol. 15, no. 6, pp. 1379–1390, 2015.

[33] M. Isaacs, Y. Kawakami, G. Allendorph, B. Yoon, J. Belmonte, and S. Choe, "Bone morphogenetic protein-2 and-6 heterodimer illustrates the nature of ligand-receptor assembly," *Molecular Endocrinology*, vol. 24, no. 7, pp. 1469–1477, 2010.

[34] J. Buijs, G. Van Der Horst, C. Van Den Hoogen, H. Cheung, B. De Rooij, J. Kroon, M. Petersen, P. Van Overveld, R. Pelger, and G. Van Der Pluijm, "The bmp2/7 heterodimer inhibits the human breast cancer stem cell subpopulation and bone metastases formation," *Oncogene*, vol. 31, no. 17, pp. 2164–2174, 2012.

[35] A. D. Lander, "Morpheus unbound: reimagining the morphogen gradient," *Cell*, vol. 128, no. 2, pp. 245–256, 2007.

[36] C. M. Mizutani, Q. Nie, F. Y. Wan, Y. T. Zhang, P. Vilmos, R. Sousa-Neves, E. Bier, J. L. Marsh, and A. D. Lander, "Formation of the BMP activity gradient in the Drosophila embryo," *Dev. Cell*, vol. 8, no. 6, pp. 915–24, 2005.

[37] D. Ben-Zvi, B.-Z. Shilo, A. Fainsod, and N. Barkai, "Scaling of the bmp activation gradient in xenopus embryos," *Nature*, vol. 453, no. 7199, pp. 1205–1211, 2008.

[38] E. L. Ferguson and K. V. Anderson, "Decapentaplegic acts as a morphogen to organize dorsal-ventral pattern in the drosophila embryo," *Cell*, vol. 71, no. 3, pp. 451–461, 1992.

[39] L. Wolpert, "Positional information and the spatial pattern of cellular differentiation," *J Theor Biol*, vol. 25, pp. 1–47, Oct 1969.

[40] F. Crick, "Diffusion in embryogenesis," 1970.

[41] D. Nellen, R. Burke, G. Struhl, and K. Basler, "Direct and long-range action of a dpp morphogen gradient," *Cell*, vol. 85, no. 3, pp. 357–368, 1996.

[42] M. B. O'Connor, D. M. Umulis, H. G. Othmer, and S. S. Blair, "Shaping BMP morphogen gradients in the Drosophila embryo and pupal wing," *Development*, vol. 133, pp. 183–93, 2006.

[43] E. L. Ferguson and K. V. Anderson, "Decapentaplegic acts as a morphogen to organize dorsal-ventral pattern in the Drosophila embryo," *Cell*, vol. 71, no. 3, pp. 451–61, 1992.

[44] T. Gregor, E. F. Wieschaus, A. P. McGregor, W. Bialek, and D. W. Tank, "Stability and nuclear dynamics of the bicoid morphogen gradient," *Cell*, vol. 130, pp. 141–152, Jul 2007.

[45] G. Thomsen, T. Woolf, M. Whitman, S. Sokol, J. Vaughan, W. Vale, and D. Melton, "Activins are expressed early in xenopus embryogenesis and can induce axial mesoderm and anterior structures," *Cell*, vol. 63, no. 3, pp. 485–493, 1990.

[46] N. McDowell and J. Gurdon, "Activin as a morphogen in xenopus mesoderm induction," in *Seminars in cell & developmental biology*, vol. 10, pp. 311–317, Elsevier, 1999.

[47] V. Giguere, E. S. Ong, P. Segui, and R. M. Evans, "Identification of a receptor for the morphogen retinoic acid," *Nature*, vol. 330, no. 6149, pp. 624–629, 1987.

[48] G. Drossopoulou, K. Lewis, J. Sanz-Ezquerro, N. Nikbakht, A. McMahon, C. Hofmann, and C. Tickle, "A model for anteroposterior patterning of the vertebrate limb based on sequential long-and short-range shh signalling and bmp signalling," *Development*, vol. 127, no. 7, pp. 1337–1348, 2000.

[49] M. Zecca, K. Basler, and G. Struhl, "Direct and long-range action of a wingless morphogen gradient," *Cell*, vol. 87, no. 5, pp. 833–844, 1996.

[50] C. Neumann and S. Cohen, "Problems and paradigms: morphogens and pattern formation," *Bioessays*, vol. 19, no. 8, pp. 721–729, 1997.

[51] A. Lander, Q. Nie, and F. Y. M. Wan, "Do morphogen gradients arise by diffusion?," *Dev. Cell*, vol. 2, pp. 785–96, 2002.

[52] M. Coppey, A. Berezhkovskii, Y. Kim, A. Boettiger, and S. Shvartsman, "Modeling the bicoid gradient: diffusion and reversible nuclear trapping of a stable protein," *Dev. Biol.*, vol. 312, pp. 623–630, Dec 2007.

[53] M. Coppey, A. Boettiger, A. Berezhkovskii, and S. Shvartsman, "Nuclear trapping shapes the terminal gradient in the Drosophila embryo," *Curr. Biol.*, vol. 18, pp. 915–919, Jun 2008.

[54] D. Ben-Zvi, B. Shilo, A. Fainsod, and N. Barkai, "Scaling of the BMP activation gradient in Xenopus embryos," *Nature*, vol. 453, pp. 1205–1211, Jun 2008.

[55] J. Greenwald, J. Grope, P. Gray, E. Wiater, W. Kwiatkowski, W. Vale, and S. Choe, "The BMP7/ActRii extracellular domain comples provides new insights into the cooperative nature of receptor assembly," *Mol. Cell*, vol. 11, pp. 605–617, 2003.

[56] S. Restrepo, J. J. Zartman, and K. Basler, "Coordination of patterning and growth by the morphogen dpp," *Current Biology*, vol. 24, no. 6, pp. R245–R255, 2014.

[57] P. Müller, K. W. Rogers, R. Y. Shuizi, M. Brand, and A. F. Schier, "Morphogen transport," *Development*, vol. 140, no. 8, pp. 1621–1638, 2013.

[58] E. Bier and E. M. De Robertis, "Bmp gradients: A paradigm for morphogen-mediated developmental patterning," *Science*, vol. 348, no. 6242, p. aaa5838, 2015.

[59] S. C. Little and M. C. Mullins, "Extracellular modulation of bmp activity in patterning the dorsoventral axis," *Birth Defects Research Part C: Embryo Today: Reviews*, vol. 78, no. 3, pp. 224–242, 2006.

[60] A. Kicheva, P. Pantazis, T. Bollenbach, Y. Kalaidzidis, T. Bittig, F. Julicher, and M. Gonzalez-Gaitan, "Kinetics of morphogen gradient formation," *Science*, vol. 315, pp. 521–525, Jan 2007.

[61] K. Kruse, P. Pantazis, T. Bollenbach, F. Julicher, and M. Gonzalez-Gaitan, "Dpp gradient formation by dynamin-dependent endocytosis: receptor trafficking and the diffusion model," *Development*, vol. 131, pp. 4843–4856, Oct 2004.

[62] M. Kerszberg and L. Wolpert, "Mechanisms for positional signalling by morphogen transport: a theoretical study," *Journal of theoretical biology*, vol. 191, no. 1, pp. 103–114, 1998.

[63] J. A. Dutko and M. C. Mullins, "Snapshot: Bmp signaling in development," *Cell*, vol. 145, no. 4, pp. 636–636, 2011.

[64] E. Bangi and K. Wharton, "Dual function of the Drosophila Alk1/Alk2 ortholog Saxophone shapes the Bmp activity gradient in the wing imaginal disc," *Development*, vol. 133, pp. 3295–3303, Sep 2006.

[65] S. Matsuda and O. Shimmi, "Directional transport and active retention of dpp/bmp create wing vein patterns in drosophila," *Developmental biology*, vol. 366, no. 2, pp. 153–162, 2012.

[66] B. Schmid, M. Furthauer, S. A. Connors, J. Trout, B. Thisse, C. Thisse, and M. C. Mullins, "Equivalent genetic roles for bmp7/snailhouse and bmp2b/swirl in dorsoventral pattern formation," *Development*, vol. 127, no. 5, pp. 957–967, 2000.

[67] B. Schmierer, A. Tournier, P. Bates, and C. Hill, "Mathematical modeling identifies Smad nucleocytoplasmic shuttling as a dynamic signal-interpreting system," *Proceedings of the National Academy of Sciences*, vol. 105, no. 18, p. 6608, 2008.

[68] H. L. Ashe, M. Mannervik, and M. Levine, "Dpp signaling thresholds in the dorsal ectoderm of the drosophila embryo," *Development*, vol. 127, no. 15, pp. 3305–12, 2000.

[69] K. Arora and C. Nusslein-Volhard, "Altered mitotic domains reveal fate map changes in Drosophila embryos mutant for zygotic dorsoventral patterning genes," *Development*, vol. 114, pp. 1003–1024, Apr 1992.

[70] V. Francois, M. Solloway, J. W. O'Neill, J. Emery, and E. Bier, "Dorsal-ventral patterning of the drosophila embryo depends on a putative negative growth factor encoded by the short gastrulation gene," *Genes Dev*, vol. 8, no. 21, pp. 2602–16, 1994.

[71] S. C. Little and M. C. Mullins, "Twisted gastrulation promotes bmp signaling in zebrafish dorsal-ventral axial patterning," *Development*, vol. 131, no. 23, pp. 5825–5835, 2004.

[72] M. C. Mullins, M. Hammerschmidt, D. A. Kane, J. Odenthal, M. Brand, F. Van Eeden, M. Furutani-Seiki, M. Granato, P. Haffter, C.-P. Heisenberg, *et al.*, "Genes establishing dorsoventral pattern formation in the zebrafish embryo: the ventral specifying genes," *Development*, vol. 123, no. 1, pp. 81–93, 1996.

[73] A. von Bubnoff and K. W. Cho, "Intracellular bmp signaling regulation in vertebrates: pathway or network?," *Developmental biology*, vol. 239, no. 1, pp. 1–14, 2001.

[74] Y. Sasai, B. Lu, H. Steinbeisser, and E. M. De Robertis, "Regulation of neural induction by the chd and bmp-4 antagonistic patterning signals in xenopus," *Nature*, vol. 376, no. 6538, pp. 333–336, 1995.

[75] A. Suzuki, R. S. Thies, N. Yamaji, J. J. Song, J. M. Wozney, K. Murakami, and N. Ueno, "A truncated bone morphogenetic protein receptor affects dorsal-ventral patterning in the early xenopus embryo," *Proceedings of the National Academy of Sciences*, vol. 91, no. 22, pp. 10255–10259, 1994.

[76] M. Nguyen, S. Park, G. Marques, and K. Arora, "Interpretation of a BMP activity gradient in Drosophila embryos depends on synergistic signaling by two type I receptors, SAX and TKV," *Cell*, vol. 95, no. 4, pp. 495–506, 1998.

[77] L. Marchant, C. Linker, P. Ruiz, N. Guerrero, and R. Mayor, "The inductive properties of mesoderm suggest that the neural crest cells are specified by a bmp gradient," *Developmental biology*, vol. 198, no. 2, pp. 319–329, 1998.

[78] P. Knaus and W. Sebald, "Cooperativity of binding epitopes and receptor chains in the bmp/tgfß superfamily," *Biological chemistry*, vol. 382, no. 8, pp. 1189–1195, 2005.

[79] S. Keller, J. Nickel, J. L. Zhang, W. Sebald, and T. D. Mueller, "Molecular recognition of BMP-2 and BMP receptor IA," *Nat. Struct. Biol.*, vol. 11, no. 5, pp. 481–88, 2004.

[80] K. Heinecke, A. Seher, W. Schmitz, T. Mueller, W. Sebald, and J. Nickel, "Receptor oligomerization and beyond: a case study in bone morphogenetic proteins," *BMC biology*, vol. 7, no. 1, p. 59, 2009.

[81] A. Kotzsch, J. Nickel, A. Seher, K. Heinecke, L. van Geersdaele, T. Herrmann, W. Sebald, and T. D. Mueller, "Structure analysis of bone morphogenetic protein-2 type i receptor complexes reveals a mechanism of receptor inactivation in juvenile polyposis syndrome," *Journal of Biological Chemistry*, vol. 283, no. 9, pp. 5876–5887, 2008.

[82] S. Saremba, J. Nickel, A. Seher, A. Kotzsch, W. Sebald, and T. Mueller, "Type I receptor binding of bone morphogenetic protein 6 is dependent on N-glycosylation of the ligand," *FEBS journal*, vol. 275, no. 1, pp. 172–183, 2008.

[83] S. Kondo, "How animals get their skin patterns: fish pigment pattern as a live turing wave," in *Systems Biology*, pp. 37–46, Springer, 2009.

[84] S. Ishihara and K. Kaneko, "Turing pattern with proportion preservation," *Journal of theoretical biology*, vol. 238, no. 3, pp. 683–693, 2006.

[85] P. Ball and N. R. Borley, *The self-made tapestry: pattern formation in nature*, vol. 198. Oxford University Press Oxford, 1999.

[86] D. M. Umulis and H. G. Othmer, "Mechanisms of scaling in pattern formation," *Development*, vol. 140, no. 24, pp. 4830–4843, 2013.

[87] S. Bergmann, O. Sandler, H. Sberro, S. Shnider, E. Schejter, B. Z. Shilo, and N. Barkai, "Pre-steady-state decoding of the Bicoid morphogen gradient," *PLoS Biol.*, vol. 5, p. e46, Feb 2007.

[88] D. Umulis, "Analysis of dynamic morphogen scale-invariance," *J. Roy. Soc. Interface*, vol. Accepted, p. TBD, 2009.

[89] H. Spemann and H. Mangold, "Induction of embryonic primordia by implantation of organizers from a different species. 1923.," *International Journal of Developmental Biology*, vol. 45, no. 1, pp. 13–38, 2003.

[90] G. Beadle, E. L. Tatum, and C. Clancy, "Food level in relation to rate of development and eye pigmentation in drosophila melanogaster," *The Biological Bulletin*, vol. 75, no. 3, pp. 447–462, 1938.

[91] O. Wartlick, P. Mumcu, A. Kicheva, T. Bittig, C. Seum, F. Jülicher, and M. Gonzalez-Gaitan, "Dynamics of dpp signaling and proliferation control," *Science*, vol. 331, no. 6021, pp. 1154–1159, 2011.

[92] A. Teleman and S. Cohen, "Dpp gradient formation in the Drosophila wing imaginal disc," *Cell*, vol. 103, no. 6, pp. 971–980, 2000.

[93] W. Driever and C. Nusslein-Volhard, "The bicoid protein determines position in the Drosophila embryo in a concentration-dependent manner," *Cell*, vol. 54, pp. 95–104, Jul 1988.

[94] D. Cheung, C. Miles, M. Kreitman, and J. Ma, "Scaling of the bicoid morphogen gradient by a volume-dependent production rate," *Development*, vol. 138, no. 13, pp. 2741–2749, 2011.

[95] O. Grimm, M. Coppey, and E. Wieschaus, "Modelling the bicoid gradient," *Development*, vol. 137, no. 14, pp. 2253–2264, 2010.

[96] M. Coppey, A. M. Berezhkovskii, Y. Kim, A. N. Boettiger, and S. Y. Shvartsman, "Modeling the bicoid gradient: diffusion and reversible nuclear trapping of a stable protein," *Developmental biology*, vol. 312, no. 2, pp. 623–630, 2007.

[97] M. Coppey, A. N. Boettiger, A. M. Berezhkovskii, and S. Y. Shvartsman, "Nuclear trapping shapes the terminal gradient in the drosophila embryo," *Current Biology*, vol. 18, no. 12, pp. 915–919, 2008.

[98] T. Gregor, A. P. McGregor, and E. F. Wieschaus, "Shape and function of the bicoid morphogen gradient in dipteran species with different sized embryos," *Developmental biology*, vol. 316, no. 2, pp. 350–358, 2008.

[99] P. Francois, A. Vonica, A. H. Brivanlou, and E. D. Siggia, "Scaling of bmp gradients in xenopus embryos," *Nature*, vol. 461, no. 7260, pp. E1–E1, 2009.

[100] H. Inomata, T. Shibata, T. Haraguchi, and Y. Sasai, "Scaling of dorsal-ventral patterning by embryo size-dependent degradation of spemanns organizer signals," *Cell*, vol. 153, no. 6, pp. 1296–1311, 2013.

[101] J. Cooke, "Scale of body pattern adjusts to available cell number in amphibian embryos," 1981.

[102] H. Kageura and K. Yamana, "Pattern regulation in isolated halves and blastomeres of early xenopus laevis," *Development*, vol. 74, no. 1, pp. 221–234, 1983.

[103] H. Kageura and K. Yamana, "Pattern regulation in defect embryos of xenopus laevis," *Developmental biology*, vol. 101, no. 2, pp. 410–415, 1984.

[104] D. M. Umulis and H. G. Othmer, "The role of mathematical models in understanding pattern formation in developmental biology," *Bulletin of mathematical biology*, vol. 77, no. 5, pp. 817–845, 2015.

[105] L. G. Morelli, K. Uriu, S. Ares, and A. C. Oates, "Computational approaches to developmental patterning," *Science*, vol. 336, no. 6078, pp. 187–191, 2012.

[106] H. G. Othmer and E. Pate, "Scale-invariance in reaction-diffusion models of spatial pattern formation," *Proc Natl Acad Sci U S A*, vol. 77, pp. 4180–4184, Jul 1980.

[107] D. Lauffenburger and J. Linderman, *Receptors: models for binding, trafficking, and signaling*. Oxford University Press, USA, 1996.

[108] B. Houchmandzadeh, E. Wieschaus, and S. Leibler, "Precise domain specification in the developing drosophila embryo," *Physical Review E*, vol. 72, no. 6, p. 061920, 2005.

[109] A. Lander, W. Lo, Q. Nie, and F. Wan, "The measure of success: constraints, objectives, and tradeoffs in morphogen-mediated patterning," *Cold Spring Harbor Perspectives in Biology*, vol. 1, no. 1, 2009.

[110] T. Mdluli, M. Pargett, G. T. Buzzard, and A. E. Rundell, "Specifying informative experiment stimulation conditions for resolving dynamical uncertainty in biological systems," in *2014 36th Annual International Conference of the IEEE Engineering in Medicine and Biology Society*, pp. 298–301, IEEE, 2014.

[111] T. Mdluli, G. T. Buzzard, and A. E. Rundell, "Efficient optimization of stimuli for model-based design of experiments to resolve dynamical uncertainty," *PLoS Comput Biol*, vol. 11, no. 9, p. e1004488, 2015.

[112] M. Pargett and D. M. Umulis, "Quantitative model analysis with diverse biological data: applications in developmental pattern formation," *Methods*, vol. 62, no. 1, pp. 56–67, 2013.

[113] M. Pargett, A. E. Rundell, G. T. Buzzard, and D. M. Umulis, "Model-based analysis for qualitative data: an application in drosophila germline stem cell regulation," *PLoS Comput Biol*, vol. 10, no. 3, p. e1003498, 2014.

[114] M. Donahue, G. Buzzard, and A. Rundell, "Experiment design through dynamical characterisation of non-linear systems biology models utilising sparse grids," *IET systems biology*, vol. 4, no. 4, pp. 249–262, 2010.

[115] R. H. Pletcher, J. C. Tannehill, and D. Anderson, *Computational fluid mechanics and heat transfer*. CRC Press, 2012.

[116] J. Dallon, "Multiscale modeling of cellular systems in biology," *Current Opinion in Colloid & Interface Science*, vol. 15, no. 1, pp. 24–31, 2010.

[117] L. Parker, D. Stathakis, and K. Arora, "Regulation of bmp and activin signaling in drosophila," in *Invertebrate Cytokines and the Phylogeny of Immunity*, pp. 73–101, Springer, 2004.

[118] P. K. Maini, "Mathematical models in morphogenesis," in *Mathematics inspired by biology*, pp. 151–189, Springer, 1999.

[119] B. Munsky and M. Khammash, "The finite state projection algorithm for the solution of the chemical master equation," *The Journal of chemical physics*, vol. 124, no. 4, p. 044104, 2006.

[120] A. D. Lander, Q. Nie, and F. Y. Wan, "Membrane-associated non-receptors and morphogen gradients," *Bull. Math. Biol.*, vol. 69, pp. 33–54, Jan 2007.

[121] L. Edelstein-Keshet, *Mathematical models in biology*, vol. 46. Siam, 1988.

[122] E. Bonabeau, "From classical models of morphogenesis to agent-based models of pattern formation," *Artificial life*, vol. 3, no. 3, pp. 191–211, 1997.

[123] J. Lewis, "From signals to patterns: space, time, and mathematics in developmental biology," *Science*, vol. 322, no. 5900, pp. 399–403, 2008.

[124] L. E. Reichl and I. Prigogine, *A modern course in statistical physics*, vol. 71. University of Texas press Austin, 1980.

[125] B. Bradie, *A friendly introduction to numerical analysis*. Prentice-Hall, 2006.

[126] A. R. Mitchell and D. F. Griffiths, *The finite difference method in partial differential equations*. John Wiley, 1980.

[127] O. C. Zienkiewicz, R. L. Taylor, O. C. Zienkiewicz, and R. L. Taylor, *The finite element method*, vol. 3. McGraw-hill London, 1977.

[128] R. Codina, "Comparison of some finite element methods for solving the diffusion-convection-reaction equation," *Computer Methods in Applied Mechanics and Engineering*, vol. 156, no. 1, pp. 185–210, 1998.

[129] R. Eymard, T. Gallouët, and R. Herbin, "Finite volume methods," *Handbook of numerical analysis*, vol. 7, pp. 713–1018, 2000.

[130] S. D. Cohen and A. C. Hindmarsh, "Cvode user guide," tech. rep., Technical Report UCRL-MA-118618, LLNL, 1994.

[131] L. Attisano and J. Wrana, "Signal transduction by the tgf-beta superfamily," *Science's STKE*, vol. 296, no. 5573, p. 1646, 2002.

[132] H. Miyazaki, T. Watabe, T. Kitamura, and K. Miyazono, "Bmp signals inhibit proliferation and in vivo tumor growth of androgen-insensitive prostate carcinoma cells," *Oncogene*, vol. 23, no. 58, pp. 9326–9335, 2004.

[133] D. Chen, M. Zhao, and G. Mundy, "Bone morphogenetic proteins," *Growth factors*, vol. 22, no. 4, pp. 233–241, 2004.

[134] G. Guasch, M. Schober, H. Pasolli, E. Conn, L. Polak, and E. Fuchs, "Loss of tgf [beta] signaling destabilizes homeostasis and promotes squamous cell carcinomas in stratified epithelia," *Cancer cell*, vol. 12, no. 4, pp. 313–327, 2007.

[135] J. Massagué, "Tgfβ in cancer," *Cell*, vol. 134, no. 2, pp. 215–230, 2008.

[136] R. Dillon and H. G. Othmer, "A mathematical model for outgrowth and spatial patterning of the vertebrate limb bud," *J Theor Biol*, vol. 197, no. 3, pp. 295–330, 1999.

[137] Y. Huang, S. Bharill, D. Karandur, S. M. Peterson, M. Marita, X. Shi, M. J. Kaliszewski, A. W. Smith, E. Y. Isacoff, and J. Kuriyan, "Molecular basis for multimerization in the activation of the epidermal growth factor receptor," *eLife*, vol. 5, p. e14107, 2016.

[138] S. Harth *et al.*, "Molecular recognition in bmp ligand-receptor interactions," *Fakultät für Biologie, Lehrstuhl für Physiologische Chemie II Julius-Maximilians-Universität Würzburg*, 2010.

[139] S. Kishigami and Y. Mishina, "Bmp signaling and early embryonic patterning," *Cytokine & growth factor reviews*, vol. 16, no. 3, pp. 265–278, 2005.

[140] Y. Wang and E. Ferguson, "Spatial bistability of dpp–receptor interactions during drosophila dorsal–ventral patterning," *Nature*, vol. 434, no. 7030, pp. 229–234, 2005.

[141] G. P. Allendorph, W. W. Vale, and S. Choe, "Structure of the ternary signaling complex of a tgf-β superfamily member," *Proceedings of the National Academy of Sciences*, vol. 103, no. 20, pp. 7643–7648, 2006.

[142] G. P. Allendorph, M. J. Isaacs, Y. Kawakami, J. C. Izpisua Belmonte, and S. Choe, "Bmp-3 and bmp-6 structures illuminate the nature of binding specificity with receptors," *Biochemistry*, vol. 46, no. 43, pp. 12238–12247, 2007.

[143] S. Harth, A. Kotzsch, J. Hu, W. Sebald, and T. D. Mueller, "A selection fit mechanism in bmp receptor ia as a possible source for bmp ligand-receptor promiscuity," *PloS one*, vol. 5, no. 9, p. e13049, 2010.

[144] A. Kotzsch, J. Nickel, A. Seher, W. Sebald, and T. D. Müller, "Crystal structure analysis reveals a spring-loaded latch as molecular mechanism for gdf-5–type i receptor specificity," *The EMBO journal*, vol. 28, no. 7, pp. 937–947, 2009.

[145] J. Nickel, A. Kotzsch, W. Sebald, and T. D. Mueller, "A single residue of gdf-5 defines binding specificity to bmp receptor ib," *Journal of molecular biology*, vol. 349, no. 5, pp. 933–947, 2005.

[146] D. Weber, A. Kotzsch, J. Nickel, S. Harth, A. Seher, U. Mueller, W. Sebald, and T. D. Mueller, "A silent h-bond can be mutationally activated for high-affinity interaction of bmp-2 and activin type iib receptor," *BMC structural biology*, vol. 7, no. 1, p. 1, 2007.

[147] W. Sebald, J. Nickel, J. L. Zhang, and T. D. Mueller, "Molecular recognition in bone morphogenetic protein (BMP)/receptor interaction," *Biol. Chem.*, vol. 385, pp. 697–710, 2004.

[148] A. Klimke, "Sparse grid interpolation toolbox–users guide," *IANS report*, vol. 17, 2007.

[149] S. Dal-Pra, M. Fürthauer, J. Van-Celst, B. Thisse, and C. Thisse, "Noggin1 and follistatin-like2 function redundantly to chordin to antagonize bmp activity," *Developmental biology*, vol. 298, no. 2, pp. 514–526, 2006.

[150] W. Zhu, J. Kim, C. Cheng, B. A. Rawlins, O. Boachie-Adjei, R. G. Crystal, and C. Hidaka, "Noggin regulation of bone morphogenetic protein (bmp) 2/7 heterodimer activity in vitro," *Bone*, vol. 39, no. 1, pp. 61–71, 2006.

[151] S. Piccolo, Y. Sasai, B. Lu, and E. M. De Robertis, "Dorsoventral patterning in xenopus: inhibition of ventral signals by direct binding of chordin to bmp-4," *Cell*, vol. 86, no. 4, pp. 589–598, 1996.

[152] M. Thattai and A. Van Oudenaarden, "Intrinsic noise in gene regulatory networks," *proceedings of the national academy of sciences of the united states of America*, vol. 98, no. 15, p. 8614, 2001.

[153] M. B. Elowitz, A. J. Levine, E. D. Siggia, and P. S. Swain, "Stochastic gene expression in a single cell," *Science*, vol. 297, no. 5584, pp. 1183–1186, 2002.

[154] S. Karim, G. T. Buzzard, and D. M. Umulis, "Efficient calculation of steady state probability distribution for stochastic biochemical reaction network," *BMC genomics*, vol. 13, no. Suppl 6, p. S10, 2012.

[155] J. Fox, "Human ipsc and esc translation potential debated," *Nature Biotechnology*, vol. 29, no. 5, pp. 375–376, 2011.

[156] M. Karim, "Steady state probability approximation applied to stochastic model of biological network," *The 2011 IEEE International Workshop on Genomic Signal Processing and Statistics*, 2011.

[157] E. M. De Robertis and H. Kuroda, "Dorsal-ventral patterning and neural induction in xenopus embryos," *Annual review of cell and developmental biology*, vol. 20, p. 285, 2004.

[158] A. Raj and A. van Oudenaarden, "Nature, nurture, or chance: stochastic gene expression and its consequences," *Cell*, vol. 135, no. 2, pp. 216–226, 2008.

[159] M. Samoilov, G. Price, and A. Arkin, "From fluctuations to phenotypes: the physiology of noise," *Science's STKE*, vol. 2006, no. 366, 2006.

[160] D. Gillespie, "A rigorous derivation of the chemical master equation," *Physica A: Statistical Mechanics and its Applications*, vol. 188, no. 1-3, pp. 404–425, 1992.

[161] D. Gillespie, "A general method for numerically simulating the stochastic time evolution of coupled chemical reactions," *Journal of computational physics*, vol. 22, no. 4, pp. 403–434, 1976.

[162] N. van Kampen, *Stochastic processes in physics and chemistry*. North Holland, 2007.

[163] D. Gillespie, "Exact stochastic simulation of coupled chemical reactions," *The journal of physical chemistry*, vol. 81, no. 25, pp. 2340–2361, 1977.

[164] M. Gibson and J. Bruck, "Efficient exact stochastic simulation of chemical systems with many species and many channels," *The journal of physical chemistry A*, vol. 104, no. 9, pp. 1876–1889, 2000.

[165] D. Gillespie, "Stochastic simulation of chemical kinetics," 2007.

[166] Y. Cao, D. T. Gillespie, and L. R. Petzold, "The slow-scale stochastic simulation algorithm," *The Journal of chemical physics*, vol. 122, no. 1, p. 014116, 2005.

[167] S. Peleš, B. Munsky, and M. Khammash, "Reduction and solution of the chemical master equation using time scale separation and finite state projection," *The Journal of chemical physics*, vol. 125, no. 20, p. 204104, 2006.

[168] D. Gillespie and L. Petzold, "Improved leap-size selection for accelerated stochastic simulation," *The Journal of Chemical Physics*, vol. 119, p. 8229, 2003.

[169] D. Gillespie, "Approximate accelerated stochastic simulation of chemically reacting systems," *The Journal of Chemical Physics*, vol. 115, p. 1716, 2001.

[170] R. Erban, J. Chapman, and P. Maini, "A practical guide to stochastic simulations of reaction-diffusion processes," *Arxiv preprint arXiv:0704.1908*, 2007.

[171] M. Hegland, C. Burden, L. Santoso, S. MacNamara, and H. Booth, "A solver for the stochastic master equation applied to gene regulatory networks," *Journal of Computational and Applied Mathematics*, vol. 205, no. 2, pp. 708–724, 2007.

[172] M. Hegland, A. Hellander, and P. L
"otstedt, "Sparse grids and hybrid methods for the chemical master equation," *BIT Numerical Mathematics*, vol. 48, no. 2, pp. 265–283, 2008.

[173] H. Schmidt and M. Jirstrand, "Systems biology toolbox for matlab: a computational platform for research in systems biology," *Bioinformatics*, vol. 22, no. 4, pp. 514–515, 2006.

[174] D. Ben-Zvi and N. Barkai, "Scaling of morphogen gradients by an expansion-repression integral feedback control," *Proceedings of the National Academy of Sciences*, vol. 107, no. 15, pp. 6924–6929, 2010.

[175] S. D. Cohen and A. C. Hindmarsh, "Cvode, a stiff/nonstiff ode solver in c," *Computers in physics*, vol. 10, no. 2, pp. 138–143, 1996.

[176] P. N. Brown and A. C. Hindmarsh, "Matrix-free methods for stiff systems of ode's," *SIAM Journal on Numerical Analysis*, vol. 23, no. 3, pp. 610–638, 1986.

[177] Y. Saad and M. H. Schultz, "Gmres: A generalized minimal residual algorithm for solving nonsymmetric linear systems," *SIAM Journal on scientific and statistical computing*, vol. 7, no. 3, pp. 856–869, 1986.

[178] T. Aegerter-Wilmsen, C. M. Aegerter, and T. Bisseling, "Model for the robust establishment of precise proportions in the early drosophila embryo," *Journal of theoretical biology*, vol. 234, no. 1, pp. 13–19, 2005.

[179] B. Houchmandzadeh, E. Wieschaus, and S. Leibler, "Precise domain specification in the developing Drosophila embryo," *Phys Rev E Stat Nonlin Soft Matter Phys*, vol. 72, p. 061920, Dec 2005.

[180] P. McHale, W.-J. Rappel, and H. Levine, "Embryonic pattern scaling achieved by oppositely directed morphogen gradients," *Physical biology*, vol. 3, no. 2, p. 107, 2006.

[181] M. Fujise, S. Takeo, K. Kamimura, T. Matsuo, T. Aigaki, S. Izumi, and H. Nakato, "Dally regulates dpp morphogen gradient formation in the drosophila wing," *Development*, vol. 130, no. 8, pp. 1515–1522, 2003.

[182] T. Lecuit and S. Cohen, "Dpp receptor levels contribute to shaping the Dpp morphogen gradient in the Drosophila wing imaginal disc," *Development*, vol. 125, no. 24, p. 4901, 1998.

[183] S. M. Jackson, H. Nakato, M. Sugiura, A. Jannuzi, R. Oakes, V. Kaluza, C. Golden, and S. B. Selleck, "dally, a drosophila glypican, controls cellular responses to the tgf-beta-related morphogen, dpp," *Development*, vol. 124, no. 20, pp. 4113–4120, 1997.

[184] S. Sarrazin, W. C. Lamanna, and J. D. Esko, "Heparan sulfate proteoglycans," *Cold Spring Harbor perspectives in biology*, vol. 3, no. 7, p. a004952, 2011.

[185] T. Akiyama, K. Kamimura, C. Firkus, S. Takeo, O. Shimmi, and H. Nakato, "Dally regulates dpp morphogen gradient formation by stabilizing dpp on the cell surface," *Developmental biology*, vol. 313, no. 1, pp. 408–419, 2008.

[186] H. Inomata, T. Haraguchi, and Y. Sasai, "Robust stability of the embryonic axial pattern requires a secreted scaffold for chordin degradation," *Cell*, vol. 134, no. 5, pp. 854–865, 2008.

[187] B. Reversade and E. De Robertis, "Regulation of admp and bmp2/4/7 at opposite embryonic poles generates a self-regulating morphogenetic field," *Cell*, vol. 123, no. 6, pp. 1147–1160, 2005.

[188] L. Brugnano and D. Trigiante, *On the characterization of stiffness for ODEs*. Watam Press, 1996.

[189] G. Wanner and E. Hairer, *Solving ordinary differential equations II*, vol. 1. Springer-Verlag, Berlin, 1991.

[190] D. J. Higham and L. N. Trefethen, "Stiffness of odes," *BIT Numerical Mathematics*, vol. 33, no. 2, pp. 285–303, 1993.

[191] L. F. Shampine and C. W. Gear, "A user's view of solving stiff ordinary differential equations," *SIAM review*, vol. 21, no. 1, pp. 1–17, 1979.

[192] A. C. Hindmarsh, P. N. Brown, K. E. Grant, S. L. Lee, R. Serban, D. E. Shumaker, and C. S. Woodward, "Sundials: Suite of nonlinear and differential/algebraic equation solvers," *ACM Transactions on Mathematical Software (TOMS)*, vol. 31, no. 3, pp. 363–396, 2005.

[193] C. T. Kelley, *Solving nonlinear equations with Newton's method*, vol. 1. Siam, 2003.

[194] G. D. Smith, *Numerical solution of partial differential equations: finite difference methods*. Oxford university press, 1985.

[195] C. W. Gear, "The automatic integration of ordinary differential equations," *Communications of the ACM*, vol. 14, no. 3, pp. 176–179, 1971.

[196] R. C. Team *et al.*, "R: A language and environment for statistical computing," 2013.

[197] A. Eldar, D. Rosin, B.-Z. Shilo, and N. Barkai, "Self-enhanced ligand degradation underlies robustness of morphogen gradients," *Developmental cell*, vol. 5, no. 4, pp. 635–646, 2003.

[198] N. Khare and S. Baumgartner, "Dally-like protein, a new Drosophila glypican with expression overlapping with wingless," *Mechanisms of Development*, vol. 99, no. 1-2, pp. 199–202, 2000.

[199] M. Yanagita, "Bmp antagonists: their roles in development and involvement in pathophysiology," *Cytokine & growth factor reviews*, vol. 16, no. 3, pp. 309–317, 2005.

[200] P. Christian and C. P. Stewart, "Maternal micronutrient deficiency, fetal development, and the risk of chronic disease," *The Journal of nutrition*, vol. 140, no. 3, pp. 437–445, 2010.

[201] G. Wu, F. W. Bazer, T. A. Cudd, C. J. Meininger, and T. E. Spencer, "Maternal nutrition and fetal development," *The Journal of nutrition*, vol. 134, no. 9, pp. 2169–2172, 2004.

[202] S. Andrews and D. Bray, "Stochastic simulation of chemical reactions with spatial resolution and single molecule detail," *Physical biology*, vol. 1, p. 137, 2004.

[203] T. Gardner, C. Cantor, and J. Collins, "Construction of a genetic toggle switch inescherichia coli," *Nature*, vol. 403, pp. 339–342, 2000.

APPENDICES

A. THE COMPLETE ODE MODEL FOR DIMER-RECEPTOR INTERACTIONS

A.1 Chemical reactions

As previously explained, we consider that no more than two same type of receptors can occupy positions in a tetrameric receptor association. So, tetrameric complexes with three same type of receptors, for example, $BMP : Alk3 : Alk3 : Alk3$ or $BMP : RII : RII : RII$, are not acceptable. Moreover, we also consider $BMP : RII : Alk8 = BMP : Alk8 : RII$, and such assumption is applied for all the trimeric and tetrameric complexes.

$$\mathrm{BMP2} + \mathrm{Alk3} \underset{k2\_1\mathrm{r}}{\overset{k2\_1}{\rightleftharpoons}} \mathrm{BMP2} : \mathrm{Alk3} \tag{A.1}$$

$$\mathrm{BMP2} + \mathrm{Alk8} \underset{k2\_2\mathrm{r}}{\overset{k2\_2}{\rightleftharpoons}} \mathrm{BMP2} : \mathrm{Alk8} \tag{A.2}$$

$$\mathrm{BMP2} + \mathrm{RII} \underset{k2\_3\mathrm{r}}{\overset{k2\_3}{\rightleftharpoons}} \mathrm{BMP2} : \mathrm{RII} \tag{A.3}$$

$$\mathrm{BMP2} : \mathrm{Alk3} + \mathrm{Alk3} \underset{k2\_4\mathrm{r}}{\overset{k2\_4}{\rightleftharpoons}} \mathrm{BMP2} : \mathrm{Alk3} : \mathrm{Alk3} \tag{A.4}$$

$$\mathrm{BMP2} : \mathrm{Alk3} + \mathrm{Alk8} \underset{k2\_5\mathrm{r}}{\overset{k2\_5}{\rightleftharpoons}} \mathrm{BMP2} : \mathrm{Alk3} : \mathrm{Alk8} \tag{A.5}$$

$$\mathrm{BMP2} : \mathrm{Alk3} + \mathrm{RII} \underset{k2\_6\mathrm{r}}{\overset{k2\_6}{\rightleftharpoons}} \mathrm{BMP2} : \mathrm{Alk3} : \mathrm{RII} \tag{A.6}$$

$$\mathrm{BMP2} : \mathrm{Alk8} + \mathrm{Alk3} \underset{k2\_7\mathrm{r}}{\overset{k2\_7}{\rightleftharpoons}} \mathrm{BMP2} : \mathrm{Alk3} : \mathrm{Alk8} \tag{A.7}$$

$$\mathrm{BMP2} : \mathrm{Alk8} + \mathrm{Alk8} \underset{k2\_8\mathrm{r}}{\overset{k2\_8}{\rightleftharpoons}} \mathrm{BMP2} : \mathrm{Alk8} : \mathrm{Alk8} \tag{A.8}$$

$$\mathrm{BMP2} : \mathrm{Alk8} + \mathrm{RII} \underset{k2\_9\mathrm{r}}{\overset{k2\_9}{\rightleftharpoons}} \mathrm{BMP2} : \mathrm{Alk8} : \mathrm{RII} \tag{A.9}$$

$$\mathrm{BMP2} : \mathrm{RII} + \mathrm{Alk3} \underset{k2\_10\mathrm{r}}{\overset{k2\_10}{\rightleftharpoons}} \mathrm{BMP2} : \mathrm{Alk3} : \mathrm{RII} \tag{A.10}$$

$$\mathrm{BMP2} : \mathrm{RII} + \mathrm{Alk8} \underset{k2\_11\mathrm{r}}{\overset{k2\_11}{\rightleftharpoons}} \mathrm{BMP2} : \mathrm{Alk8} : \mathrm{RII} \tag{A.11}$$

$$\mathrm{BMP2} : \mathrm{RII} + \mathrm{RII} \underset{k2\_12\mathrm{r}}{\overset{k2\_12}{\rightleftharpoons}} \mathrm{BMP2} : \mathrm{RII} : \mathrm{RII} \tag{A.12}$$

$$\mathrm{BMP2} : \mathrm{Alk8} : \mathrm{Alk8} + \mathrm{RII} \underset{k2\_13\mathrm{r}}{\overset{k2\_13}{\rightleftharpoons}} \mathrm{BMP2} : \mathrm{Alk8} : \mathrm{Alk8} : \mathrm{RII} \tag{A.13}$$

$$\mathrm{BMP2} : \mathrm{RII} : \mathrm{RII} + \mathrm{Alk3} \underset{k2\_14\mathrm{r}}{\overset{k2\_14}{\rightleftharpoons}} \mathrm{BMP2} : \mathrm{Alk3} : \mathrm{RII} : \mathrm{RII} \tag{A.14}$$

$$\mathrm{BMP2} : \mathrm{RII} : \mathrm{RII} + \mathrm{Alk8} \underset{k2\_15\mathrm{r}}{\overset{k2\_15}{\rightleftharpoons}} \mathrm{BMP2} : \mathrm{Alk8} : \mathrm{RII} : \mathrm{RII} \tag{A.15}$$

$$\mathrm{BMP2} : \mathrm{Alk3} : \mathrm{Alk3} + \mathrm{RII} \underset{k2\_16\mathrm{r}}{\overset{k2\_16}{\rightleftharpoons}} \mathrm{BMP2} : \mathrm{Alk3} : \mathrm{Alk3} : \mathrm{RII} \tag{A.16}$$

$$\mathrm{BMP2} : \mathrm{Alk3} : \mathrm{Alk8} + \mathrm{RII} \underset{k2\_17\mathrm{r}}{\overset{k2\_17}{\rightleftharpoons}} \mathrm{BMP2} : \mathrm{Alk3} : \mathrm{Alk8} : \mathrm{RII} \tag{A.17}$$

$$\text{BMP2} : \text{Alk3} : \text{RII} + \text{Alk3} \underset{k2\_18\text{r}}{\overset{k2\_18}{\rightleftharpoons}} \text{BMP2} : \text{Alk3} : \text{Alk3} : \text{RII} \quad \text{(A.18)}$$

$$\text{BMP2} : \text{Alk3} : \text{RII} + \text{Alk8} \underset{k2\_19\text{r}}{\overset{k2\_19}{\rightleftharpoons}} \text{BMP2} : \text{Alk3} : \text{Alk8} : \text{RII} \quad \text{(A.19)}$$

$$\text{BMP2} : \text{Alk3} : \text{RII} + \text{RII} \underset{k2\_20\text{r}}{\overset{k2\_20}{\rightleftharpoons}} \text{BMP2} : \text{Alk3} : \text{RII} : \text{RII} \quad \text{(A.20)}$$

$$\text{BMP2} : \text{Alk8} : \text{RII} + \text{Alk3} \underset{k2\_21\text{r}}{\overset{k2\_21}{\rightleftharpoons}} \text{BMP2} : \text{Alk3} : \text{Alk8} : \text{RII} \quad \text{(A.21)}$$

$$\text{BMP2} : \text{Alk8} : \text{RII} + \text{Alk8} \underset{k2\_22\text{r}}{\overset{k2\_22}{\rightleftharpoons}} \text{BMP2} : \text{Alk8} : \text{Alk8} : \text{RII} \quad \text{(A.22)}$$

$$\text{BMP2} : \text{Alk8} : \text{RII} + \text{RII} \underset{k2\_23\text{r}}{\overset{k2\_23}{\rightleftharpoons}} \text{BMP2} : \text{Alk8} : \text{RII} : \text{RII} \quad \text{(A.23)}$$

$$\text{BMP2} : \text{Alk3} : \text{Alk3} : \text{RII} + \text{RII} \underset{k2\_24\text{r}}{\overset{k2\_24}{\rightleftharpoons}} \text{BMP2} : \text{Alk3} : \text{Alk3} : \text{RII} : \text{RII} \quad \text{(A.24)}$$

$$\text{BMP2} : \text{Alk3} : \text{Alk8} : \text{RII} + \text{RII} \underset{k2\_25\text{r}}{\overset{k2\_25}{\rightleftharpoons}} \text{BMP2} : \text{Alk3} : \text{Alk8} : \text{RII} : \text{RII} \quad \text{(A.25)}$$

$$\text{BMP2} : \text{Alk3} : \text{RII} : \text{RII} + \text{Alk3} \underset{k2\_26\text{r}}{\overset{k2\_26}{\rightleftharpoons}} \text{BMP2} : \text{Alk3} : \text{Alk3} : \text{RII} : \text{RII} \quad \text{(A.26)}$$

$$\text{BMP2} : \text{Alk3} : \text{RII} : \text{RII} + \text{Alk8} \underset{k2\_27\text{r}}{\overset{k2\_27}{\rightleftharpoons}} \text{BMP2} : \text{Alk3} : \text{Alk8} : \text{RII} : \text{RII} \quad \text{(A.27)}$$

$$\text{BMP2} : \text{Alk8} : \text{Alk8} : \text{RII} + \text{RII} \underset{k2\_28\text{r}}{\overset{k2\_28}{\rightleftharpoons}} \text{BMP2} : \text{Alk8} : \text{Alk8} : \text{RII} : \text{RII} \quad \text{(A.28)}$$

$$\text{BMP2} : \text{Alk8} : \text{RII} : \text{RII} + \text{Alk3} \underset{k2\_29\text{r}}{\overset{k2\_29}{\rightleftharpoons}} \text{BMP2} : \text{Alk3} : \text{Alk8} : \text{RII} : \text{RII} \quad \text{(A.29)}$$

$$\text{BMP2} : \text{Alk8} : \text{RII} : \text{RII} + \text{Alk8} \underset{k2\_30\text{r}}{\overset{k2\_30}{\rightleftharpoons}} \text{BMP2} : \text{Alk8} : \text{Alk8} : \text{RII} : \text{RII} \quad \text{(A.30)}$$

Equations from A.1-A.30 are similar for other dimers, and can be obtained by replacing BMP2 with corresponding dimer.

A.2 ODE formulations

We show the ODE formulations for BMP2 homodimers only. The complete model can easily be devised by adding similar set of reactions for the other two dimers. In the below formulation, two copies of R_{II} are represented as $TypeII_1$ and $TypeII_2$.

$$
\begin{aligned}
r2\_1 &\equiv k2\_1 * BMP2 * Alk3 - k2\_1r * BMP2 : Alk3 \\
r2\_2 &\equiv k2\_2 * BMP2 * Alk8 - k2\_2r * BMP2 : Alk8 \\
r2\_3 &\equiv k2\_3 * BMP2 * TypeII\_1 - k2\_3r * BMP2 : TypeII_1 \\
r2\_4 &\equiv k2\_4 * BMP2 : Alk3 * Alk3 - k2\_4r * BMP2 : Alk3 : Alk3 \\
r2\_5 &\equiv k2\_5 * BMP2 : Alk3 * Alk8 - k2\_5r * BMP2 : Alk3 : Alk8 \\
r2\_6 &\equiv k2\_6 * BMP2 : Alk3 * TypeII_1 - k2\_6r * BMP2 : Alk3 : TypeII_1 \\
r2\_7 &\equiv k2\_7 * BMP2 : Alk8 * Alk3 - k2\_7r * BMP2 : Alk3 : Alk8 \\
r2\_8 &\equiv k2\_8 * BMP2 : Alk8 * Alk8 - k2\_8r * BMP2 : Alk8 : Alk8 \\
r2\_9 &\equiv k2\_9 * BMP2 : Alk8 * TypeII_1 - k2\_9r * BMP2 : Alk8 : TypeII_1 \\
r2\_10 &\equiv k2\_10 * BMP2 : TypeII_1 * Alk3 - k2\_10r * BMP2 : Alk3 : TypeII_1 \\
r2\_11 &\equiv k2\_11 * BMP2 : TypeII_1 * Alk8 - k2\_11r * BMP2 : Alk8 : TypeII_1 \\
r2\_12 &\equiv k2\_12 * BMP2 : TypeII_1 * TypeII_2 - k2\_12r * BMP2 : TypeII_1 : TypeII_2 \\
r2\_13 &\equiv k2\_13 * BMP2 : Alk8 : Alk8 * TypeII_1 \\
&\quad -k2\_13r * BMP2 : Alk8 : TypeII_1 \\
r2\_14 &\equiv k2\_14 * BMP2 : TypeII_1 : TypeII_2 * Alk3 \\
&\quad -k2\_14r * BMP2 : TypeII_1 : TypeII_2 : Alk3 \\
r2\_15 &\equiv k2\_15 * BMP2 : TypeII_1 : TypeII_2 * Alk8 \\
&\quad -k2\_15r * BMP2 : TypeII_1 : TypeII_2 : Alk8 \\
r2\_16 &\equiv k2\_16 * BMP2 : Alk3 : Alk3 * TypeII_1 \\
&\quad -k2\_16r * BMP2 : Alk3 : Alk3 : TypeII_1
\end{aligned}
$$

$$
\begin{aligned}
r2\_17 \quad & \equiv k2\_17 * BMP2 : Alk3 : Alk8 * TypeII_1 \\
& -k2\_17r * BMP2 : Alk3 : Alk8 : TypeII_1 \\
r2\_18 \quad & \equiv k2\_18 * BMP2 : Alk3 : TypeII_1 * Alk3 \\
& -k2\_18r * BMP2 : Alk3 : Alk3 : TypeII_1 \\
r2\_19 \quad & \equiv k2\_19 * BMP2 : Alk3 : TypeII_1 * Alk8 \\
& -k2\_19r * BMP2 : Alk3 : Alk8 : TypeII_1 \\
r2\_20 \quad & \equiv k2\_20 * BMP2 : Alk3 : TypeII_1 * TypeII_2 \\
& -k2\_20r * BMP2 : Alk3 : TypeII_1 : TypeII_2 \\
r2\_21 \quad & \equiv k2\_21 * BMP2 : Alk8 : TypeII_1 * Alk3 \\
& -k2\_21r * BMP2 : Alk3 : Alk8 : TypeII_1 \\
r2\_22 \quad & \equiv k2\_22 * BMP2 : Alk8 : TypeII_1 * Alk8 \\
& -k2\_22r * BMP2 : Alk8 : Alk8 : TypeII_1 \\
r2\_23 \quad & \equiv k2\_23 * BMP2 : Alk8 : TypeII_1 * TypeII_2 \\
& -k2\_23r * BMP2 : Alk8 : TypeII_1 : TypeII_2 \\
r2\_24 \quad & \equiv k2\_24 * BMP2 : Alk8 : TypeII_1 * TypeII_2 \\
& -k2\_24r * BMP2 : Alk8 : TypeII_1 : TypeII_2 \\
r2\_25 \quad & \equiv k2\_25 * BMP2 : Alk3 : Alk8 : TypeII_1 * TypeII_2
\end{aligned}
$$

$$
\begin{aligned}
& -k2\_25r * BMP2 : Alk3 : Alk8 : TypeII_1 : TypeII_2 \\
r2\_26 \quad & \equiv k2\_26 * BMP2 : Alk3 : TypeII_1 : TypeII_2 * Alk8 \\
& -k2\_26r * BMP2 : Alk3 : Alk8 : TypeII_1 : TypeII_2 \\
r2\_27 \quad & \equiv k2\_27 * BMP2 : Alk3 : TypeII_1 : TypeII_2 * Alk8 \\
& -k2\_27r * BMP2 : Alk3 : Alk8 : TypeII_1 : TypeII_2 \\
r2\_28 \quad & \equiv k2\_28 * BMP2 : Alk8 : Alk8 : TypeII_1 * TypeII_2 \\
& -k2\_28r * BMP2 : Alk8 : Alk8 : TypeII_1 : TypeII_2 \\
r2\_29 \quad & \equiv k2\_29 * BMP2 : Alk8 : TypeII_1 : TypeII_2 * Alk3 \\
& -k2\_29r * BMP2 : Alk3 : Alk8 : TypeII_1 : TypeII_2 \\
r2\_30 \quad & \equiv k2\_30 * BMP2 : Alk8 : TypeII_1 : TypeII_2 * Alk8 \\
& -k2\_30r * BMP2 : Alk8 : Alk8 : TypeII_2 : TypeII_2
\end{aligned}
$$

Using the mass-action kinetic equation, the set of ODE are as follows:

$$\frac{\mathrm{d}(BMP2{:}Alk3)}{\mathrm{d}\,t} = r2\_1 - r2\_4 - r2\_5 - r2\_6 - \delta_e BMP2 : Alk3$$

$$\frac{\mathrm{d}(BMP2{:}Alk8)}{\mathrm{d}\,t} = r2\_2 - r2\_7 - r2\_8 - r2\_9 - \delta_e BMP2 : Alk8$$

$$\frac{\mathrm{d}(BMP2{:}TypeII)}{\mathrm{d}\,t} = r2\_3 - r2\_10 - r2\_11 - r2\_12 - \delta_e BMP2 : TypeII$$

$$\frac{\mathrm{d}(BMP2{:}Alk3{:}Alk3)}{\mathrm{d}\,t} = r2\_4 - r2\_16 - \delta_e BMP2 : Alk3 : Alk3$$

$$\frac{\mathrm{d}(BMP2{:}Alk3{:}Alk8)}{\mathrm{d}\,t} = r2\_5 + r2\_7 - r2\_17 - \delta_e BMP2 : Alk3 : Alk8$$

$$\frac{\mathrm{d}(BMP2{:}Alk3{:}TypeII)}{\mathrm{d}\,t} = r2\_6 + r2\_10 - r2\_18 - r2\_19 - r2\_20$$
$$-\delta_e BMP2 : Alk3 : TypeII$$

$$\frac{\mathrm{d}(BMP2{:}Alk8{:}Alk8)}{\mathrm{d}\,t} = r2\_8 - r2\_13 - \delta_e BMP2 : Alk8 : Alk8$$

$$\frac{\mathrm{d}(BMP2{:}Alk8{:}TypeII)}{\mathrm{d}\,t} = r2\_9 + r2\_11 - r2\_21 - r2\_22 - r2\_23$$
$$-\delta_e BMP2 : Alk8 : TypeII$$

$$\frac{\mathrm{d}(BMP2{:}TypeII{:}TypeII)}{\mathrm{d}\,t} = r2\_12 - r2\_14 - r2\_15$$
$$-\delta_e BMP2 : TypeII : TypeII$$

$$\frac{\mathrm{d}(BMP2{:}Alk8{:}Alk8{:}TypeII)}{\mathrm{d}\,t} = r2\_13 + r2\_22 - r2\_28 - \delta_e BMP2 : Alk8 : Alk8 : TypeII$$

$$\frac{\mathrm{d}(BMP2{:}Alk3{:}TypeII{:}TypeII)}{\mathrm{d}\,t} = r2\_14 + r2\_20 - r2\_26 - r2\_27$$
$$-\delta_e BMP2 : Alk3 : TypeII : TypeII$$

$$\frac{\mathrm{d}(BMP2{:}Alk8{:}TypeII{:}TypeII)}{\mathrm{d}\,t} = r2\_15 + r2\_23 - r2\_29 - r2\_30$$
$$-\delta_e BMP2 : Alk8 : TypeII : TypeII$$

$$\frac{\mathrm{d}(BMP2{:}Alk3{:}Alk3{:}TypeII)}{\mathrm{d}\,t} = r2\_16 + r2\_18 - r2\_24$$
$$-\delta_e BMP2 : Alk3 : Alk3 : TypeII$$
$$\frac{\mathrm{d}(BMP2{:}Alk3{:}Alk8{:}TypeII)}{\mathrm{d}\,t} = r2\_17 + r2\_21 + r2\_19$$
$$-r2\_25 - \delta_e BMP2 : Alk3 : Alk8 : TypeII$$
$$\frac{\mathrm{d}(BMP2{:}Alk3{:}Alk3{:}TypeII{:}TypeII)}{\mathrm{d}\,t} = r2\_24 + r2\_26 - \delta_e BMP2 : Alk3 : Alk3 : TypeII$$
$$\frac{\mathrm{d}(BMP2{:}Alk3{:}Alk8{:}TypeII{:}TypeII)}{\mathrm{d}\,t} = r2\_25 + r2\_27 + r2\_29$$
$$-\delta_e BMP2 : Alk3 : Alk8 : TypeII$$
$$\frac{\mathrm{d}(BMP2{:}Alk3{:}Alk8{:}TypeII{:}TypeII)}{\mathrm{d}\,t} = r2\_28 + r2\_30 - \delta_e BMP2 : Alk8 : Alk8 : TypeII$$

where δ_e is the first order degradation rate of any species with unit s^{-1}. A complete dimer-receptor systems has three dimers, where each dimer, in theory, can participate in all the possible biochemical interaction as shown in Fig.2.2. Therefore, the complete ODE model of the oligomerization process includes a total of 90 bi-directional interactions, and a total of 51 ODEs are used to represent the transient dynamics of the system.

B. DIMER-RECEPTOR INTERACTIONS NETWORK WITH DIMER AS A VARIABLE

In the original dimer-receptor network, we treated all the dimers as system parameters and therefore, a constant concentration of dimer was made available each time a dimer-receptor interaction occurred in the system. In order to see whether treating dimer as a system variable the affinity based hierarchy of putative complex formation was preserved, we changed our previous implementation. In the new implementation, unlike the previous model where dimers were treated as parameters, the new model treated dimers as separate species in the Ordinary Differential Equation (ODE) model of dimer-receptor interactions. Because of this modification, the complete dimer-receptor system comprised of 93 bidirectional interactions and a total of 54 ODEs. Conversion of the dimer from a system parameter to a system variable is done as follows:

B.1 Equation for dimer

Let's assume that each dimer (B) is produced at a rate ϕ_B, and interacts with all the receptors according to second order mass-action kinetics. Then, a generic equation for any dimer in the system would be as follows:

$$\begin{aligned} \frac{dB}{dt} &= \phi_B - k_1[B][R_3] - k_2[B][R_8] - k_3[B][R_{II}] \\ &+ k_{-1}[B:R_3] - k_2[B:R_8] - k_3[B:R_{II}] - \delta_B[B] \end{aligned} \tag{B.1}$$

where, k_1, k_2, k_3 and k_{-1}, k_{-2}, k_{-3} are the forward and reverse reaction rate constant with units $nM^{-1}s^{-1}$ and s^{-1}, for recruitment and decoupling of $Alk3/6, Alk2/8, TypeII$

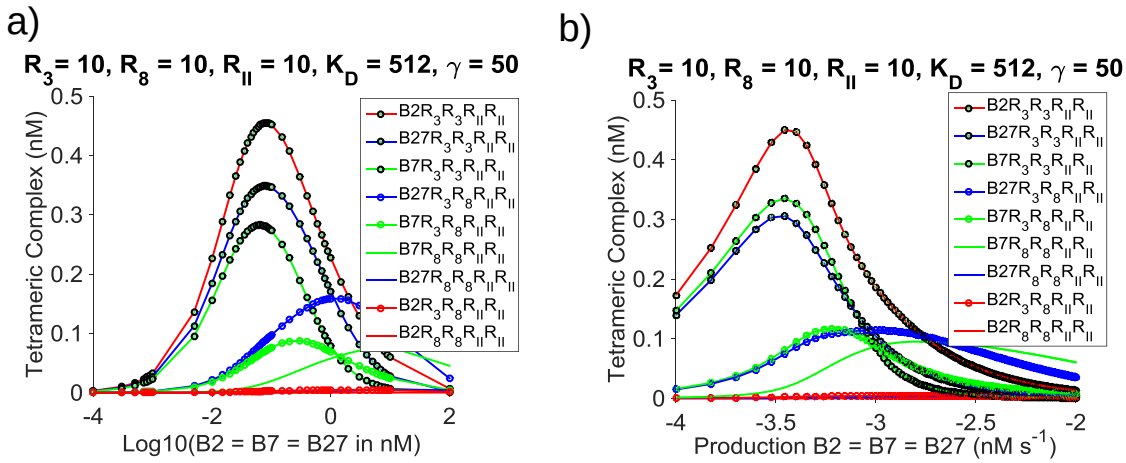

Fig. B.1. Affinity based hierarchy of putative complexes: Two different implementations are considered here- i) dimers are system parameter, and ii) dimers are treated as system variable. When dimers are system variable, a constant production rate is constant for each dimers. Similar to the initial implementation, we consider equal production rate of all the dimers. That is, production rate ϕ_{B2}, ϕ_{B7}, and ϕ_{B27} are equal in these simulations. a) Dimers are treated as system parameters, b) Dimers are treated as system variable. As we see here, concentration of putative signaling complexes follow a descending order set by the affinities of dimer-receptor interactions. For instance, the most prevalent complex in both implementation is $Bmp2-BmpR1-BmpR1-TypeII-TypeII$. The stipulated signaling complex $Bmp2/7-BmpR1-Acvr1-TypeII-TypeII$ is placed at the fourth most prevalent complex in both the implementation.

receptors respectively. In the complete dimer-receptor model, equal decay rate for all the dimers is considered.

B.2 Hierarchy of putative complexes

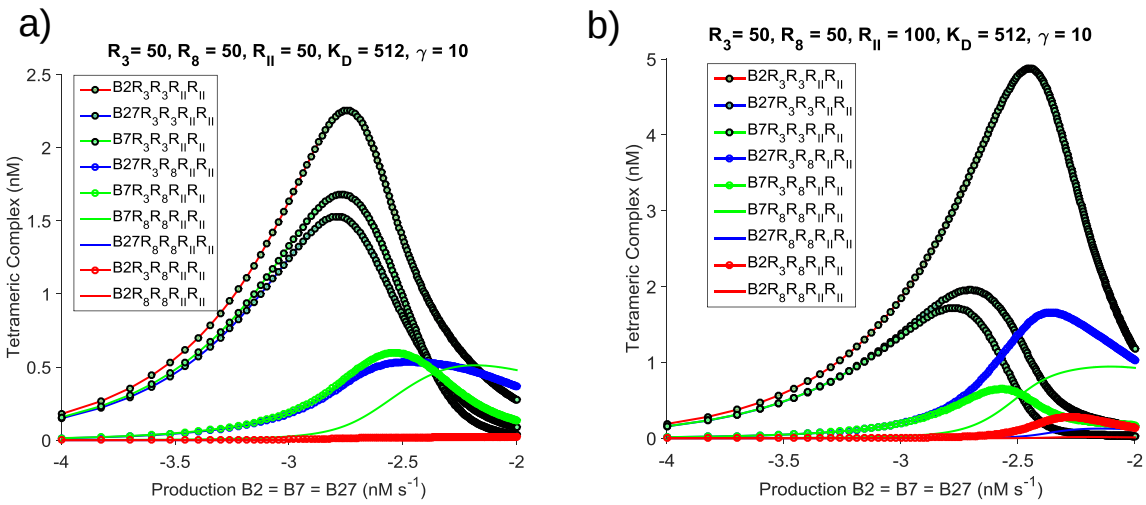

Fig. B.2. Hierarchy of tetrameric complexes formation considering dimers as the system variable: In this implementation, all the dimers have equal production rate. This is similar to Fig.B.2, but here the hierarchy of putative signaling complexes are captured for a reduced γ (surface enhancement factor) value. Also, the receptor strengths are increased in this plot. As seen from the simulated data, the affinity based hierarchy as observed previously, is preserved.

C. REGULATORY MOTIFS AND CORRESPONDING SYSTEM OF PDES

For the regulation of diffusion coefficient and reaction rate of both morphogen and modulator, we considered positive, negative, no regulation cases that generate a total of 81 different combinations. In this section, we listed out all the possible regulatory motifs and corresponding PDE equations associated with the TCS model. In all the motifs, flat-head edge is for negative regulation, arrow-head edge is for positive regulation, and no edge represents no regulation. Here, m and M denote morphogen and modulator respectively.

Motifs	Equations	
	Morphogen	Modulator
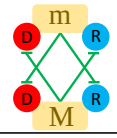	$\frac{\partial m}{\partial t} = D_{m0}(1+\alpha_m M)^{-1}\frac{\partial^2 m}{\partial x^2} + \left((-1)\alpha_m D_{m0}(1+\alpha_m M)^{-2}\right)\frac{\partial m}{\partial x}\frac{\partial M}{\partial x} - k_{\delta m}(\gamma_m^R+\beta_m^R M)^{-1}[m]$	$\frac{\partial M}{\partial t} = D_{M0}(1+\alpha_M m)^{-1}\frac{\partial^2 M}{\partial x^2} + \left((-1)\alpha_M D_{M0}(1+\alpha_M m)^{-2}\right)\frac{\partial m}{\partial x}\frac{\partial M}{\partial x} - k_{\delta M}(\gamma_M^R+\beta_M^R m)^{-1}[M]$
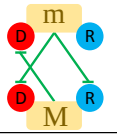	$\frac{\partial m}{\partial t} = D_{m0}(1+\alpha_m M)^{-1}\frac{\partial^2 m}{\partial x^2} + \left((-1)\alpha_m D_{m0}(1+\alpha_m M)^{-2}\right)\frac{\partial m}{\partial x}\frac{\partial M}{\partial x} - k_{\delta m}[m]$	$\frac{\partial M}{\partial t} = D_{M0}(1+\alpha_M m)^{-1}\frac{\partial^2 M}{\partial x^2} + \left((-1)\alpha_M D_{M0}(1+\alpha_M m)^{-2}\right)\frac{\partial m}{\partial x}\frac{\partial M}{\partial x} - k_{\delta M}(\gamma_M^R+\beta_M^R m)^{-1}[M]$
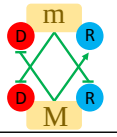	$\frac{\partial m}{\partial t} = D_{m0}(1+\alpha_m M)^{-1}\frac{\partial^2 m}{\partial x^2} + \left((-1)\alpha_m D_{m0}(1+\alpha_m M)^{-2}\right)\frac{\partial m}{\partial x}\frac{\partial M}{\partial x} - k_{\delta m}(\gamma_m^R+\beta_m^R M)[m]$	$\frac{\partial M}{\partial t} = D_{M0}(1+\alpha_M m)^{-1}\frac{\partial^2 M}{\partial x^2} + \left((-1)\alpha_M D_{M0}(1+\alpha_M m)^{-2}\right)\frac{\partial m}{\partial x}\frac{\partial M}{\partial x} - k_{\delta M}(\gamma_M^R+\beta_M^R m)^{-1}[M]$
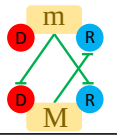	$\frac{\partial m}{\partial t} = D_{m0}\frac{\partial^2 m}{\partial x^2} + 0 - k_{\delta m}(\gamma_m^R+\beta_m^R M)^{-1}[m]$	$\frac{\partial M}{\partial t} = D_{M0}(1+\alpha_M m)^{-1}\frac{\partial^2 M}{\partial x^2} + \left((-1)\alpha_M D_{M0}(1+\alpha_M m)^{-2}\right)\frac{\partial m}{\partial x}\frac{\partial M}{\partial x} - k_{\delta M}(\gamma_M^R+\beta_M^R m)^{-1}[M]$
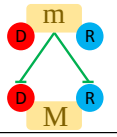	$\frac{\partial m}{\partial t} = D_{m0}\frac{\partial^2 m}{\partial x^2} + 0 - k_{\delta m}[m]$	$\frac{\partial M}{\partial t} = D_{M0}(1+\alpha_M m)^{-1}\frac{\partial^2 M}{\partial x^2} + \left((-1)\alpha_M D_{M0}(1+\alpha_M m)^{-2}\right)\frac{\partial m}{\partial x}\frac{\partial M}{\partial x} - k_{\delta M}(\gamma_M^R+\beta_M^R m)^{-1}[M]$
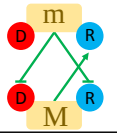	$\frac{\partial m}{\partial t} = D_{m0}\frac{\partial^2 m}{\partial x^2} + 0 - k_{\delta m}(\gamma_m^R+\beta_m M)[m]$	$\frac{\partial M}{\partial t} = D_{M0}(1+\alpha_M m)^{-1}\frac{\partial^2 M}{\partial x^2} + \left((-1)\alpha_M D_{M0}(1+\alpha_M m)^{-2}\right)\frac{\partial m}{\partial x}\frac{\partial M}{\partial x} - k_{\delta M}(\gamma_M^R+\beta_M^R m)^{-1}[M]$
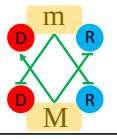	$\frac{\partial m}{\partial t} = D_{m0}(1+\alpha_m M)\frac{\partial^2 m}{\partial x^2} + (\alpha_m D_{m0})\frac{\partial m}{\partial x}\frac{\partial M}{\partial x} - k_{\delta m}(\gamma_m^R+\beta_m^R M)^{-1}[m]$	$\frac{\partial M}{\partial t} = D_{M0}(1+\alpha_M m)^{-1}\frac{\partial^2 M}{\partial x^2} + \left((-1)\alpha_M D_{M0}(1+\alpha_M m)^{-2}\right)\frac{\partial m}{\partial x}\frac{\partial M}{\partial x} - k_{\delta M}(\gamma_M^R+\beta_M^R m)^{-1}[M]$
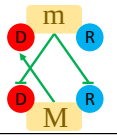	$\frac{\partial m}{\partial t} = D_{m0}(1+\alpha_m M)\frac{\partial^2 m}{\partial x^2} + (\alpha_m D_{m0})\frac{\partial m}{\partial x}\frac{\partial M}{\partial x} - k_{\delta m}[m]$	$\frac{\partial M}{\partial t} = D_{M0}(1+\alpha_M m)^{-1}\frac{\partial^2 M}{\partial x^2} + \left((-1)\alpha_M D_{M0}(1+\alpha_M m)^{-2}\right)\frac{\partial m}{\partial x}\frac{\partial M}{\partial x} - k_{\delta M}(\gamma_M^R+\beta_M^R m)^{-1}[M]$
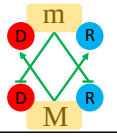	$\frac{\partial m}{\partial t} = D_{m0}(1+\alpha_m M)\frac{\partial^2 m}{\partial x^2} + (\alpha_m D_{m0})\frac{\partial m}{\partial x}\frac{\partial M}{\partial x} - k_{\delta m}(\gamma_m^R+\beta_m^R M)[m]$	$\frac{\partial M}{\partial t} = D_{M0}(1+\alpha_M m)^{-1}\frac{\partial^2 M}{\partial x^2} + \left((-1)\alpha_M D_{M0}(1+\alpha_M m)^{-2}\right)\frac{\partial m}{\partial x}\frac{\partial M}{\partial x} - k_{\delta M}(\gamma_M^R+\beta_M^R m)^{-1}[M]$

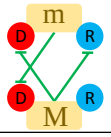	$\frac{\partial m}{\partial t} = D_{m0}(1+\alpha_m M)^{-1}\frac{\partial^2 m}{\partial x^2} + \left((-1)\alpha_m D_{m0}(1+\alpha_m M)^{-2}\right)\frac{\partial m}{\partial x}\frac{\partial M}{\partial x} - k_{\delta m}(\gamma_m^R+\beta_m^R M)^{-1}[m]$	$\frac{\partial M}{\partial t} = D_{M0}(1+\alpha_M m)^{-1}\frac{\partial^2 M}{\partial x^2} + \left((-1)\alpha_M D_{M0}(1+\alpha_M m)^{-2}\right)\frac{\partial m}{\partial x}\frac{\partial M}{\partial x} - k_{\delta M}[M]$
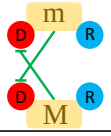	$\frac{\partial m}{\partial t} = D_{m0}(1+\alpha_m M)^{-1}\frac{\partial^2 m}{\partial x^2} + \left((-1)\alpha_m D_{m0}(1+\alpha_m M)^{-2}\right)\frac{\partial m}{\partial x}\frac{\partial M}{\partial x} - k_{\delta m}[m]$	$\frac{\partial M}{\partial t} = D_{M0}(1+\alpha_M m)^{-1}\frac{\partial^2 M}{\partial x^2} + \left((-1)\alpha_M D_{M0}(1+\alpha_M m)^{-2}\right)\frac{\partial m}{\partial x}\frac{\partial M}{\partial x} - k_{\delta M}[M]$
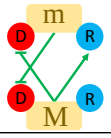	$\frac{\partial m}{\partial t} = D_{m0}(1+\alpha_m M)^{-1}\frac{\partial^2 m}{\partial x^2} + \left((-1)\alpha_m D_{m0}(1+\alpha_m M)^{-2}\right)\frac{\partial m}{\partial x}\frac{\partial M}{\partial x} - k_{\delta m}(\gamma_m^R+\beta_m^R M)[m]$	$\frac{\partial M}{\partial t} = D_{M0}(1+\alpha_M m)^{-1}\frac{\partial^2 M}{\partial x^2} + \left((-1)\alpha_M D_{M0}(1+\alpha_M m)^{-2}\right)\frac{\partial m}{\partial x}\frac{\partial M}{\partial x} - k_{\delta M}[M]$
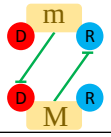	$\frac{\partial m}{\partial t} = D_{m0}\frac{\partial^2 m}{\partial x^2} + 0 - k_{\delta m}(\gamma_m^R+\beta_m M)^{-1}[m]$	$\frac{\partial M}{\partial t} = D_{M0}(1+\alpha_M m)^{-1}\frac{\partial^2 M}{\partial x^2} + \left((-1)\alpha_M D_{M0}(1+\alpha_M m)^{-2}\right)\frac{\partial m}{\partial x}\frac{\partial M}{\partial x} - k_{\delta M}[M]$
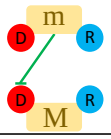	$\frac{\partial m}{\partial t} = D_{m0}\frac{\partial^2 m}{\partial x^2} + 0 - k_{\delta m}[m]$	$\frac{\partial M}{\partial t} = D_{M0}(1+\alpha_M m)^{-1}\frac{\partial^2 M}{\partial x^2} + \left((-1)\alpha_M D_{M0}(1+\alpha_M m)^{-2}\right)\frac{\partial m}{\partial x}\frac{\partial M}{\partial x} - k_{\delta M}[M]$
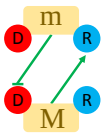	$\frac{\partial m}{\partial t} = D_{m0}\frac{\partial^2 m}{\partial x^2} + 0 - k_{\delta m}(\gamma_m^R+\beta_m^R M)[m]$	$\frac{\partial M}{\partial t} = D_{M0}(1+\alpha_M m)^{-1}\frac{\partial^2 M}{\partial x^2} + \left((-1)\alpha_M D_{M0}(1+\alpha_M m)^{-2}\right)\frac{\partial m}{\partial x}\frac{\partial M}{\partial x} - k_{\delta M}[M]$
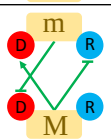	$\frac{\partial m}{\partial t} = D_{m0}(1+\alpha_m M)\frac{\partial^2 m}{\partial x^2} + (\alpha_m D_{m0})\frac{\partial m}{\partial x}\frac{\partial M}{\partial x} - k_{\delta m}(\gamma_m^R+\beta_m^R M)^{-1}[m]$	$\frac{\partial M}{\partial t} = D_{M0}(1+\alpha_M m)^{-1}\frac{\partial^2 M}{\partial x^2} + \left((-1)\alpha_M D_{M0}(1+\alpha_M m)^{-2}\right)\frac{\partial m}{\partial x}\frac{\partial M}{\partial x} - k_{\delta M}[M]$
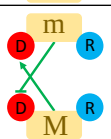	$\frac{\partial m}{\partial t} = D_{m0}(1+\alpha_m M)\frac{\partial^2 m}{\partial x^2} + (\alpha_m D_{m0})\frac{\partial m}{\partial x}\frac{\partial M}{\partial x} - k_{\delta m}[m]$	$\frac{\partial M}{\partial t} = D_{M0}(1+\alpha_M m)^{-1}\frac{\partial^2 M}{\partial x^2} + \left((-1)\alpha_M D_{M0}(1+\alpha_M m)^{-2}\right)\frac{\partial m}{\partial x}\frac{\partial M}{\partial x} - k_{\delta M}[M]$
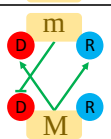	$\frac{\partial m}{\partial t} = D_{m0}(1+\alpha_m)\frac{\partial^2 m}{\partial x^2} + (\alpha_m D_{m0})\frac{\partial m}{\partial x}\frac{\partial M}{\partial x} - k_{\delta m}(\gamma_m^R+\beta_m^R M)[m]$	$\frac{\partial M}{\partial t} = D_{M0}(1+\alpha_M m)^{-1}\frac{\partial^2 M}{\partial x^2} + \left((-1)\alpha_M D_{M0}(1+\alpha_M m)^{-2}\right)\frac{\partial m}{\partial x}\frac{\partial M}{\partial x} - k_{\delta M}[M]$

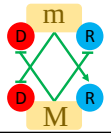	$\frac{\partial m}{\partial t} = D_{m0}(1+\alpha_m M)^{-1}\frac{\partial^2 m}{\partial x^2} + \left((-1)\alpha_m D_{m0}(1+\alpha_m M)^{-2}\right)\frac{\partial m}{\partial x}\frac{\partial M}{\partial x} - k_{\delta m}(\gamma_m^R+\beta_m^R M)^{-1}[m]$	$\frac{\partial M}{\partial t} = D_{M0}(1+\alpha_M m)^{-1}\frac{\partial^2 M}{\partial x^2} + \left((-1)\alpha_M D_{M0}(1+\alpha_M m)^{-2}\right)\frac{\partial m}{\partial x}\frac{\partial M}{\partial x} - k_{\delta M}(\gamma_M^R+\beta_M^R m)[M]$
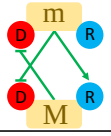	$\frac{\partial m}{\partial t} = D_{m0}(1+\alpha_m M)^{-1}\frac{\partial^2 m}{\partial x^2} + \left((-1)\alpha_m D_{m0}(1+\alpha_m M)^{-2}\right)\frac{\partial m}{\partial x}\frac{\partial M}{\partial x} - k_{\delta m}[m]$	$\frac{\partial M}{\partial t} = D_{M0}(1+\alpha_M m)^{-1}\frac{\partial^2 M}{\partial x^2} + \left((-1)\alpha_M D_{M0}(1+\alpha_M m)^{-2}\right)\frac{\partial m}{\partial x}\frac{\partial M}{\partial x} - k_{\delta M}(\gamma_M^R+\beta_M^R m)[M]$
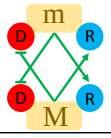	$\frac{\partial m}{\partial t} = D_{m0}(1+\alpha_m M)^{-1}\frac{\partial^2 m}{\partial x^2} + \left((-1)\alpha_m D_{m0}(1+\alpha_m M)^{-2}\right)\frac{\partial m}{\partial x}\frac{\partial M}{\partial x} - k_{\delta m}(\gamma_m^R+\beta_m^R M)[m]$	$\frac{\partial M}{\partial t} = D_{M0}(1+\alpha_M m)^{-1}\frac{\partial^2 M}{\partial x^2} + \left((-1)\alpha_M D_{M0}(1+\alpha_M m)^{-2}\right)\frac{\partial m}{\partial x}\frac{\partial M}{\partial x} - k_{\delta M}(\gamma_M^R+\beta_M^R m)[M]$
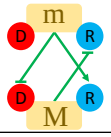	$\frac{\partial m}{\partial t} = D_{m0}\frac{\partial^2 m}{\partial x^2} + 0 - k_{\delta m}(\gamma_m^R+\beta_m^R M)^{-1}[m]$	$\frac{\partial M}{\partial t} = D_{M0}(1+\alpha_M m)^{-1}\frac{\partial^2 M}{\partial x^2} + \left((-1)\alpha_M D_{M0}(1+\alpha_M m)^{-2}\right)\frac{\partial m}{\partial x}\frac{\partial M}{\partial x} - k_{\delta M}(\gamma_M^R+\beta_M^R m)[M]$
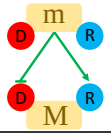	$\frac{\partial m}{\partial t} = D_{m0}\frac{\partial^2 m}{\partial x^2} + 0 - k_{\delta m}[m]$	$\frac{\partial M}{\partial t} = D_{M0}(1+\alpha_M m)^{-1}\frac{\partial^2 M}{\partial x^2} + \left((-1)\alpha_M D_{M0}(1+\alpha_M m)^{-2}\right)\frac{\partial m}{\partial x}\frac{\partial M}{\partial x} - k_{\delta M}(\gamma_M^R+\beta_M^R m)[M]$
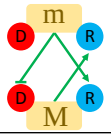	$\frac{\partial m}{\partial t} = D_{m0}\frac{\partial^2 m}{\partial x^2} + 0 - k_{\delta m}(\gamma_m^R+\beta_m^R M)[m]$	$\frac{\partial M}{\partial t} = D_{M0}(1+\alpha_M m)^{-1}\frac{\partial^2 M}{\partial x^2} + \left((-1)\alpha_M D_{M0}(1+\alpha_M m)^{-2}\right)\frac{\partial m}{\partial x}\frac{\partial M}{\partial x} - k_{\delta M}(\gamma_M^R+\beta_M^R m)[M]$
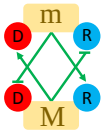	$\frac{\partial m}{\partial t} = D_{m0}(1+\alpha_m M)\frac{\partial^2 m}{\partial x^2} + (\alpha_m D_{m0})\frac{\partial m}{\partial x}\frac{\partial M}{\partial x} - k_{\delta m}(\gamma_m^R+\beta_m^R M)^{-1}[m]$	$\frac{\partial M}{\partial t} = D_{M0}(1+\alpha_M m)^{-1}\frac{\partial^2 M}{\partial x^2} + \left((-1)\alpha_M D_{M0}(1+\alpha_M m)^{-2}\right)\frac{\partial m}{\partial x}\frac{\partial M}{\partial x} - k_{\delta M}(\gamma_M^R+\beta_M^R m)[M]$
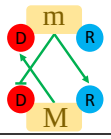	$\frac{\partial m}{\partial t} = D_{m0}(1+\alpha_m M)\frac{\partial^2 m}{\partial x^2} + (\alpha_m D_{m0})\frac{\partial m}{\partial x}\frac{\partial M}{\partial x} - k_{\delta m}[m]$	$\frac{\partial M}{\partial t} = D_{M0}(1+\alpha_M m)^{-1}\frac{\partial^2 M}{\partial x^2} + \left((-1)\alpha_M D_{M0}(1+\alpha_M m)^{-2}\right)\frac{\partial m}{\partial x}\frac{\partial M}{\partial x} - k_{\delta M}(\gamma_M^R+\beta_M^R m)[M]$
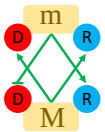	$\frac{\partial m}{\partial t} = D_{m0}(1+\alpha_m M)\frac{\partial^2 m}{\partial x^2} + (\alpha_m D_{m0})\frac{\partial m}{\partial x}\frac{\partial M}{\partial x} - k_{\delta m}(\gamma_m^R+\beta_m^R M)[m]$	$\frac{\partial M}{\partial t} = D_{M0}(1+\alpha_M m)^{-1}\frac{\partial^2 M}{\partial x^2} + \left((-1)\alpha_M D_{M0}(1+\alpha_M m)^{-2}\right)\frac{\partial m}{\partial x}\frac{\partial M}{\partial x} - k_{\delta M}(\gamma_M^R+\beta_M^R m)[M]$

Schematic	Equations	
	Morphogen	Modulator
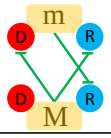	$\frac{\partial m}{\partial t} = D_{m0}(1+\alpha_m M)^{-1}\frac{\partial^2 m}{\partial x^2} + \left((-1)\alpha_m D_{m0}(1+\alpha M)^{-2}\right)\frac{\partial m}{\partial x}\frac{\partial M}{\partial x} - k_{\delta m}(\gamma_m^R+\beta_m M)^{-1}[m]$	$\frac{\partial M}{\partial t} = D_{M0}\frac{\partial^2 M}{\partial x^2} + 0 - k_{\delta M}(\gamma_M^R+\beta_M m)^{-1}[M]$
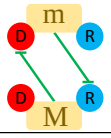	$\frac{\partial m}{\partial t} = D_{m0}(1+\alpha_m M)^{-1}\frac{\partial^2 m}{\partial x^2} + \left((-1)\alpha_m D_{m0}(1+\alpha M)^{-2}\right)\frac{\partial m}{\partial x}\frac{\partial M}{\partial x} - k_{\delta m}[m]$	$\frac{\partial M}{\partial t} = D_{M0}\frac{\partial^2 M}{\partial x^2} + 0 - k_{\delta M}(\gamma_M^R+\beta_M m)^{-1}[M]$
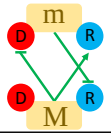	$\frac{\partial m}{\partial t} = D_{m0}(1+\alpha_m M)^{-1}\frac{\partial^2 m}{\partial x^2} + \left((-1)\alpha_m D_{m0}(1+\alpha M)^{-2}\right)\frac{\partial m}{\partial x}\frac{\partial M}{\partial x} - k_{\delta m}(\gamma_m^R+\beta_m M)[m]$	$\frac{\partial M}{\partial t} = D_{M0}\frac{\partial^2 M}{\partial x^2} + 0 - k_{\delta M}(\gamma_M^R+\beta_M m)^{-1}[M]$
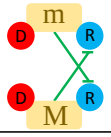	$\frac{\partial m}{\partial t} = D_{m0}\frac{\partial^2 m}{\partial x^2} + 0 - k_{\delta m}(\gamma_m^R+\beta_m M)^{-1}[m]$	$\frac{\partial M}{\partial t} = D_{M0}\frac{\partial^2 M}{\partial x^2} + 0 - k_{\delta M}(\gamma_M^R+\beta_M m)^{-1}[M]$
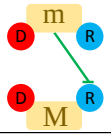	$\frac{\partial m}{\partial t} = D_{m0}\frac{\partial^2 m}{\partial x^2} + 0 - k_{\delta m}[m]$	$\frac{\partial M}{\partial t} = D_{M0}\frac{\partial^2 M}{\partial x^2} + 0 - k_{\delta M}(\gamma_M^R+\beta_M m)^{-1}[M]$
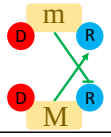	$\frac{\partial m}{\partial t} = D_{m0}\frac{\partial^2 m}{\partial x^2} + 0 - k_{\delta m}(\gamma_m^R+\beta_m M)[m]$	$\frac{\partial M}{\partial t} = D_{M0}\frac{\partial^2 M}{\partial x^2} + 0 - k_{\delta M}(\gamma_M^R+\beta_M m)^{-1}[M]$
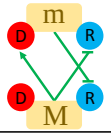	$\frac{\partial m}{\partial t} = D_{m0}(1+\alpha_m M)\frac{\partial^2 m}{\partial x^2} + (\alpha_m D_{m0})\frac{\partial m}{\partial x}\frac{\partial M}{\partial x} - k_{\delta m}(\gamma_m^R+\beta_m M)^{-1}[m]$	$\frac{\partial M}{\partial t} = D_{M0}\frac{\partial^2 M}{\partial x^2} + 0 - k_{\delta M}(\gamma_M^R+\beta_M m)^{-1}[M]$
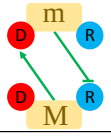	$\frac{\partial m}{\partial t} = D_{m0}(1+\alpha_m M)\frac{\partial^2 m}{\partial x^2} + (\alpha_m D_{m0})\frac{\partial m}{\partial x}\frac{\partial M}{\partial x} - k_{\delta m}[m]$	$\frac{\partial M}{\partial t} = D_{M0}\frac{\partial^2 M}{\partial x^2} + 0 - k_{\delta M}(\gamma_M^R+\beta_M m)^{-1}[M]$
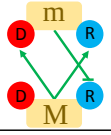	$\frac{\partial m}{\partial t} = D_{m0}(1+\alpha_m M)\frac{\partial^2 m}{\partial x^2} + (\alpha_m D_{m0})\frac{\partial m}{\partial x}\frac{\partial M}{\partial x} - k_{\delta m}(\gamma_m^R+\beta_m M)[m]$	$\frac{\partial M}{\partial t} = D_{M0}\frac{\partial^2 M}{\partial x^2} + 0 - k_{\delta M}(\gamma_M^R+\beta_M m)^{-1}[M]$

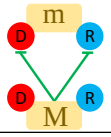	$\frac{\partial m}{\partial t} = D_{m0}(1+\alpha_m M)^{-1}\frac{\partial^2 m}{\partial x^2} + \left((-1)\alpha_m D_{m0}(1+\alpha M)^{-2}\right)\frac{\partial m}{\partial x}\frac{\partial M}{\partial x} - k_{\delta m}(\gamma_m^R+\beta_m M)^{-1}[m]$	$\frac{\partial M}{\partial t} = D_{M0}\frac{\partial^2 M}{\partial x^2} + 0 - k_{\delta M}[M]$
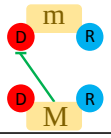	$\frac{\partial m}{\partial t} = D_{m0}(1+\alpha_m M)^{-1}\frac{\partial^2 m}{\partial x^2} + \left((-1)\alpha_m D_{m0}(1+\alpha M)^{-2}\right)\frac{\partial m}{\partial x}\frac{\partial M}{\partial x} - k_{\delta m}[m]$	$\frac{\partial M}{\partial t} = D_{M0}\frac{\partial^2 M}{\partial x^2} + 0 - k_{\delta M}[M]$
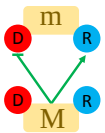	$\frac{\partial m}{\partial t} = D_{m0}(1+\alpha_m M)^{-1}\frac{\partial^2 m}{\partial x^2} + \left((-1)\alpha_m D_{m0}(1+\alpha M)^{-2}\right)\frac{\partial m}{\partial x}\frac{\partial M}{\partial x} - k_{\delta m}(\gamma_m^R+\beta_m M)[m]$	$\frac{\partial M}{\partial t} = D_{M0}\frac{\partial^2 M}{\partial x^2} + 0 - k_{\delta M}[M]$
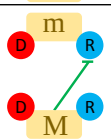	$\frac{\partial m}{\partial t} = D_{m0}\frac{\partial^2 m}{\partial x^2} + 0 - k_{\delta m}(\gamma_m^R+\beta_m M)^{-1}[m]$	$\frac{\partial M}{\partial t} = D_{M0}\frac{\partial^2 M}{\partial x^2} + 0 - k_{\delta M}[M]$
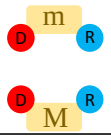	$\frac{\partial m}{\partial t} = D_{m0}\frac{\partial^2 m}{\partial x^2} + 0 - k_{\delta m}[m]$	$\frac{\partial M}{\partial t} = D_{M0}\frac{\partial^2 M}{\partial x^2} + 0 - k_{\delta M}[M]$
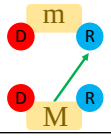	$\frac{\partial m}{\partial t} = D_{m0}\frac{\partial^2 m}{\partial x^2} + 0 - k_{\delta m}(\gamma_m^R+\beta_m M)[m]$	$\frac{\partial M}{\partial t} = D_{M0}\frac{\partial^2 M}{\partial x^2} + 0 - k_{\delta M}[M]$
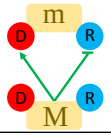	$\frac{\partial m}{\partial t} = D_{m0}(1+\alpha_m M)\frac{\partial^2 m}{\partial x^2} + (\alpha_m D_{m0})\frac{\partial m}{\partial x}\frac{\partial M}{\partial x} - k_{\delta m}(\gamma_m^R+\beta_m M)^{-1}[m]$	$\frac{\partial M}{\partial t} = D_{M0}\frac{\partial^2 M}{\partial x^2} + 0 - k_{\delta M}[M]$
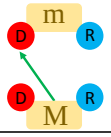	$\frac{\partial m}{\partial t} = D_{m0}(1+\alpha_m M)\frac{\partial^2 m}{\partial x^2} + (\alpha_m D_{m0})\frac{\partial m}{\partial x}\frac{\partial M}{\partial x} - k_{\delta m}[m]$	$\frac{\partial M}{\partial t} = D_{M0}\frac{\partial^2 M}{\partial x^2} + 0 - k_{\delta M}[M]$
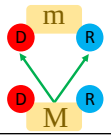	$\frac{\partial m}{\partial t} = D_{m0}(1+\alpha_m M)\frac{\partial^2 m}{\partial x^2} + (\alpha_m D_{m0})\frac{\partial m}{\partial x}\frac{\partial M}{\partial x} - k_{\delta m}(\gamma_m^R+\beta_m M)[m]$	$\frac{\partial M}{\partial t} = D_{M0}\frac{\partial^2 M}{\partial x^2} + 0 - k_{\delta M}[M]$

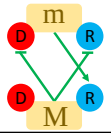	$\frac{\partial m}{\partial t} = D_{m0}(1+\alpha_m M)^{-1}\frac{\partial^2 m}{\partial x^2} + \left((-1)\alpha_m D_{m0}(1+\alpha M)^{-2}\right)\frac{\partial m}{\partial x}\frac{\partial M}{\partial x} - k_{\delta m}(\gamma_m^R+\beta_m M)^{-1}[m][M]$	$\frac{\partial M}{\partial t} = D_{M0}\frac{\partial^2 M}{\partial x^2} + 0 - k_{\delta M}(\gamma_M^R+\beta_M^R m)[M]$
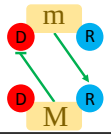	$\frac{\partial m}{\partial t} = D_{m0}(1+\alpha_m M)^{-1}\frac{\partial^2 m}{\partial x^2} + \left((-1)\alpha_m D_{m0}(1+\alpha M)^{-2}\right)\frac{\partial m}{\partial x}\frac{\partial M}{\partial x} - k_{\delta m}[m][M]$	$\frac{\partial M}{\partial t} = D_{M0}\frac{\partial^2 M}{\partial x^2} + 0 - k_{\delta M}(\gamma_M^R+\beta_M^R m)[M]$
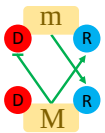	$\frac{\partial m}{\partial t} = D_{m0}(1+\alpha_m M)^{-1}\frac{\partial^2 m}{\partial x^2} + \left((-1)\alpha_m D_{m0}(1+\alpha M)^{-2}\right)\frac{\partial m}{\partial x}\frac{\partial M}{\partial x} - k_{\delta m}(\gamma_m^R+\beta_m M)[m][M]$	$\frac{\partial M}{\partial t} = D_{M0}\frac{\partial^2 M}{\partial x^2} + 0 - k_{\delta M}(\gamma_M^R+\beta_M^R m)[M]$
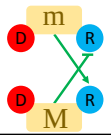	$\frac{\partial m}{\partial t} = D_{m0}\frac{\partial^2 m}{\partial x^2} + 0 - k_{\delta m}(\gamma_m^R+\beta_m M)^{-1}[m][M]$	$\frac{\partial M}{\partial t} = D_{M0}\frac{\partial^2 M}{\partial x^2} + 0 - k_{\delta M}(\gamma_M^R+\beta_M^R m)[M]$
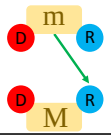	$\frac{\partial m}{\partial t} = D_{m0}\frac{\partial^2 m}{\partial x^2} + 0 - k_{\delta m}[m][M]$	$\frac{\partial M}{\partial t} = D_{M0}\frac{\partial^2 M}{\partial x^2} + 0 - k_{\delta M}(\gamma_M^R+\beta_M^R m)[M]$
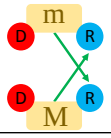	$\frac{\partial m}{\partial t} = D_{m0}\frac{\partial^2 m}{\partial x^2} + 0 - k_{\delta m}(\gamma_m^R+\beta_m M)[m][M]$	$\frac{\partial M}{\partial t} = D_{M0}\frac{\partial^2 M}{\partial x^2} + 0 - k_{\delta M}(\gamma_M^R+\beta_M^R m)[M]$
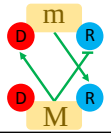	$\frac{\partial m}{\partial t} = D_{m0}(1+\alpha_m M)\frac{\partial^2 m}{\partial x^2} + (\alpha_m D_{m0})\frac{\partial m}{\partial x}\frac{\partial M}{\partial x} - k_{\delta m}(\gamma_m^R+\beta_m M)^{-1}[m][M]$	$\frac{\partial M}{\partial t} = D_{M0}\frac{\partial^2 M}{\partial x^2} + 0 - k_{\delta M}(\gamma_M^R+\beta_M^R m)[M]$
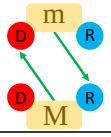	$\frac{\partial m}{\partial t} = D_{m0}(1+\alpha_m M)\frac{\partial^2 m}{\partial x^2} + (\alpha_m D_{m0})\frac{\partial m}{\partial x}\frac{\partial M}{\partial x} - k_{\delta m}[m][M]$	$\frac{\partial M}{\partial t} = D_{M0}\frac{\partial^2 M}{\partial x^2} + 0 - k_{\delta M}(\gamma_M^R+\beta_M^R m)[M]$
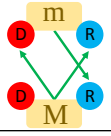	$\frac{\partial m}{\partial t} = D_{m0}(1+\alpha_m M)\frac{\partial^2 m}{\partial x^2} + (\alpha_m D_{m0})\frac{\partial m}{\partial x}\frac{\partial M}{\partial x} - k_{\delta m}(\gamma_m^R+\beta_m M)[m][M]$	$\frac{\partial M}{\partial t} = D_{M0}\frac{\partial^2 M}{\partial x^2} + 0 - k_{\delta M}(\gamma_M^R+\beta_M^R m)[M]$

Schematic	Equations	
	Morphogen	Modulator
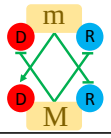	$\frac{\partial m}{\partial t} = D_{m0}(1+\alpha_m M)^{-1}\frac{\partial^2 m}{\partial x^2} + \left((-1)\alpha_m D_{m0}(1+\alpha M)^{-2}\right)\frac{\partial m}{\partial x}\frac{\partial M}{\partial x} - k_{\delta m}(\gamma_m^R+\beta_m M)^{-1}[m]$	$\frac{\partial M}{\partial t} = D_{M0}(1+\alpha_M m)\frac{\partial^2 M}{\partial x^2} + (\alpha_M D_{M0})\frac{\partial m}{\partial x}\frac{\partial M}{\partial x} - k_{\delta M}(\gamma_M^R+\beta_M^R m)^{-1}[M]$
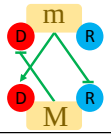	$\frac{\partial m}{\partial t} = D_{m0}(1+\alpha_m M)^{-1}\frac{\partial^2 m}{\partial x^2} + \left((-1)\alpha_m D_{m0}(1+\alpha M)^{-2}\right)\frac{\partial m}{\partial x}\frac{\partial M}{\partial x} - k_{\delta m}[m]$	$\frac{\partial M}{\partial t} = D_{M0}(1+\alpha_M m)\frac{\partial^2 M}{\partial x^2} + (\alpha_M D_{M0})\frac{\partial m}{\partial x}\frac{\partial M}{\partial x} - k_{\delta M}(\gamma_M^R+\beta_M^R m)^{-1}[M]$
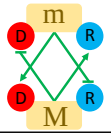	$\frac{\partial m}{\partial t} = D_{m0}(1+\alpha_m M)^{-1}\frac{\partial^2 m}{\partial x^2} + \left((-1)\alpha_m D_{m0}(1+\alpha M)^{-2}\right)\frac{\partial m}{\partial x}\frac{\partial M}{\partial x} - k_{\delta m}(\gamma_m^R+\beta_m M)[m]$	$\frac{\partial M}{\partial t} = D_{M0}(1+\alpha_M m)\frac{\partial^2 M}{\partial x^2} + (\alpha_M D_{M0})\frac{\partial m}{\partial x}\frac{\partial M}{\partial x} - k_{\delta M}(\gamma_M^R+\beta_M^R m)^{-1}[M]$
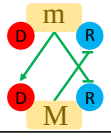	$\frac{\partial m}{\partial t} = D_{m0}\frac{\partial^2 m}{\partial x^2} + 0 - k_{\delta m}(\gamma_m^R+\beta_m M)^{-1}[m]$	$\frac{\partial M}{\partial t} = D_{M0}(1+\alpha_M m)\frac{\partial^2 M}{\partial x^2} + (\alpha_M D_{M0})\frac{\partial m}{\partial x}\frac{\partial M}{\partial x} - k_{\delta M}(\gamma_M^R+\beta_M^R m)^{-1}[M]$
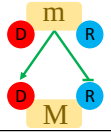	$\frac{\partial m}{\partial t} = D_{m0}\frac{\partial^2 m}{\partial x^2} + 0 - k_{\delta m}[m]$	$\frac{\partial M}{\partial t} = D_{M0}(1+\alpha_M m)\frac{\partial^2 M}{\partial x^2} + (\alpha_M D_{M0})\frac{\partial m}{\partial x}\frac{\partial M}{\partial x} - k_{\delta M}(\gamma_M^R+\beta_M^R m)^{-1}[M]$
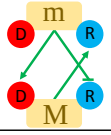	$\frac{\partial m}{\partial t} = D_{m0}\frac{\partial^2 m}{\partial x^2} + 0 - k_{\delta m}(\gamma_m^R+\beta_m M)[m]$	$\frac{\partial M}{\partial t} = D_{M0}(1+\alpha_M m)\frac{\partial^2 M}{\partial x^2} + (\alpha_M D_{M0})\frac{\partial m}{\partial x}\frac{\partial M}{\partial x} - k_{\delta M}(\gamma_M^R+\beta_M^R m)^{-1}[M]$
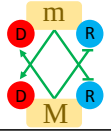	$\frac{\partial m}{\partial t} = D_{m0}(1+\alpha_m M)\frac{\partial^2 m}{\partial x^2} + (\alpha_m D_{m0})\frac{\partial m}{\partial x}\frac{\partial M}{\partial x} - k_{\delta m}(\gamma_m^R+\beta_m M)^{-1}[m]$	$\frac{\partial M}{\partial t} = D_{M0}(1+\alpha_M m)\frac{\partial^2 M}{\partial x^2} + (\alpha_M D_{M0})\frac{\partial m}{\partial x}\frac{\partial M}{\partial x} - k_{\delta M}(\gamma_M^R+\beta_M^R m)^{-1}[M]$
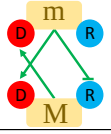	$\frac{\partial m}{\partial t} = D_{m0}(1+\alpha_m M)\frac{\partial^2 m}{\partial x^2} + (\alpha_m D_{m0})\frac{\partial m}{\partial x}\frac{\partial M}{\partial x} - k_{\delta m}[m]$	$\frac{\partial M}{\partial t} = D_{M0}(1+\alpha_M m)\frac{\partial^2 M}{\partial x^2} + (\alpha_M D_{M0})\frac{\partial m}{\partial x}\frac{\partial M}{\partial x} - k_{\delta M}(\gamma_M^R+\beta_M^R m)^{-1}[M]$
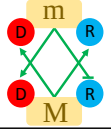	$\frac{\partial m}{\partial t} = D_{m0}(1+\alpha_m M)\frac{\partial^2 m}{\partial x^2} + (\alpha_m D_{m0})\frac{\partial m}{\partial x}\frac{\partial M}{\partial x} - k_{\delta m}(\gamma_m^R+\beta_m M)[m]$	$\frac{\partial M}{\partial t} = D_{M0}(1+\alpha_M m)\frac{\partial^2 M}{\partial x^2} + (\alpha_M D_{M0})\frac{\partial m}{\partial x}\frac{\partial M}{\partial x} - k_{\delta M}(\gamma_M^R+\beta_M^R m)^{-1}[M]$

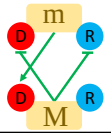	$\frac{\partial m}{\partial t} = D_{m0}(1+\alpha_m M)^{-1}\frac{\partial^2 m}{\partial x^2} + \left((-1)\alpha_m D_{m0}(1+\alpha M)^{-2}\right)\frac{\partial m}{\partial x}\frac{\partial M}{\partial x} - k_{\delta m}(\gamma_m^R+\beta_m M)^{-1}[m][M]$	$\frac{\partial M}{\partial t} = D_{M0}(1+\alpha_M m)\frac{\partial^2 M}{\partial x^2} + (\alpha_M D_{M0})\frac{\partial m}{\partial x}\frac{\partial M}{\partial x} - k_{\delta M}[M]$
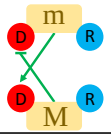	$\frac{\partial m}{\partial t} = D_{m0}(1+\alpha_m M)^{-1}\frac{\partial^2 m}{\partial x^2} + \left((-1)\alpha_m D_{m0}(1+\alpha M)^{-2}\right)\frac{\partial m}{\partial x}\frac{\partial M}{\partial x} - k_{\delta m}[m][M]$	$\frac{\partial M}{\partial t} = D_{M0}(1+\alpha_M m)\frac{\partial^2 M}{\partial x^2} + (\alpha_M D_{M0})\frac{\partial m}{\partial x}\frac{\partial M}{\partial x} - k_{\delta M}[M]$
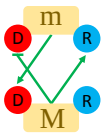	$\frac{\partial m}{\partial t} = D_{m0}(1+\alpha_m M)^{-1}\frac{\partial^2 m}{\partial x^2} + \left((-1)\alpha_m D_{m0}(1+\alpha M)^{-2}\right)\frac{\partial m}{\partial x}\frac{\partial M}{\partial x} - k_{\delta m}(\gamma_m^R+\beta_m M)[m][M]$	$\frac{\partial M}{\partial t} = D_{M0}(1+\alpha_M m)\frac{\partial^2 M}{\partial x^2} + (\alpha_M D_{M0})\frac{\partial m}{\partial x}\frac{\partial M}{\partial x} - k_{\delta M}[M]$
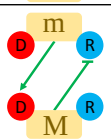	$\frac{\partial m}{\partial t} = D_{m0}\frac{\partial^2 m}{\partial x^2} + 0 - k_{\delta m}(\gamma_m^R+\beta_m M)^{-1}[m][M]$	$\frac{\partial M}{\partial t} = D_{M0}(1+\alpha_M m)\frac{\partial^2 M}{\partial x^2} + (\alpha_M D_{M0})\frac{\partial m}{\partial x}\frac{\partial M}{\partial x} - k_{\delta M}[M]$
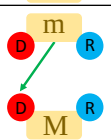	$\frac{\partial m}{\partial t} = D_{m0}\frac{\partial^2 m}{\partial x^2} + 0 - k_{\delta m}[m][M]$	$\frac{\partial M}{\partial t} = D_{M0}(1+\alpha_M m)\frac{\partial^2 M}{\partial x^2} + (\alpha_M D_{M0})\frac{\partial m}{\partial x}\frac{\partial M}{\partial x} - k_{\delta M}[M]$
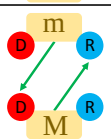	$\frac{\partial m}{\partial t} = D_{m0}\frac{\partial^2 m}{\partial x^2} + 0 - k_{\delta m}(\gamma_m^R+\beta_m M)[m][M]$	$\frac{\partial M}{\partial t} = D_{M0}(1+\alpha_M m)\frac{\partial^2 M}{\partial x^2} + (\alpha_M D_{M0})\frac{\partial m}{\partial x}\frac{\partial M}{\partial x} - k_{\delta M}[M]$
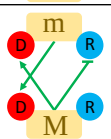	$\frac{\partial m}{\partial t} = D_{m0}(1+\alpha_m M)\frac{\partial^2 m}{\partial x^2} + (\alpha_m D_{m0})\frac{\partial m}{\partial x}\frac{\partial M}{\partial x} - k_{\delta m}(\gamma_m^R+\beta_m M)^{-1}[m][M]$	$\frac{\partial M}{\partial t} = D_{M0}(1+\alpha_M m)\frac{\partial^2 M}{\partial x^2} + (\alpha_M D_{M0})\frac{\partial m}{\partial x}\frac{\partial M}{\partial x} - k_{\delta M}[M]$
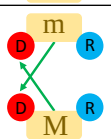	$\frac{\partial m}{\partial t} = D_{m0}(1+\alpha_m M)\frac{\partial^2 m}{\partial x^2} + (\alpha_m D_{m0})\frac{\partial m}{\partial x}\frac{\partial M}{\partial x} - k_{\delta m}[m][M]$	$\frac{\partial M}{\partial t} = D_{M0}(1+\alpha_M m)\frac{\partial^2 M}{\partial x^2} + (\alpha_M D_{M0})\frac{\partial m}{\partial x}\frac{\partial M}{\partial x} - k_{\delta M}[M]$
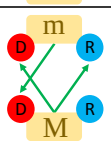	$\frac{\partial m}{\partial t} = D_{m0}(1+\alpha_m M)\frac{\partial^2 m}{\partial x^2} + (\alpha_m D_{m0})\frac{\partial m}{\partial x}\frac{\partial M}{\partial x} - k_{\delta m}(\gamma_m^R+\beta_m M)[m][M]$	$\frac{\partial M}{\partial t} = D_{M0}(1+\alpha_M m)\frac{\partial^2 M}{\partial x^2} + (\alpha_M D_{M0})\frac{\partial m}{\partial x}\frac{\partial M}{\partial x} - k_{\delta M}[M]$

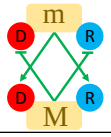	$\frac{\partial m}{\partial t} = D_{m0}(1+\alpha_m M)^{-1}\frac{\partial^2 m}{\partial x^2} + \left((-1)\alpha_m D_{m0}(1+\alpha M)^{-2}\right)\frac{\partial m}{\partial x}\frac{\partial M}{\partial x} - k_{\delta m}(\gamma_m^R+\beta_m M)^{-1}[m]$	$\frac{\partial M}{\partial t} = D_{M0}(1+\alpha_M m)\frac{\partial^2 M}{\partial x^2} + (\alpha_M D_{M0})\frac{\partial m}{\partial x}\frac{\partial M}{\partial x} - k_{\delta M}(\gamma_M^R+\beta_M^R m)[M]$
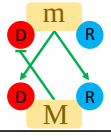	$\frac{\partial m}{\partial t} = D_{m0}(1+\alpha_m M)^{-1}\frac{\partial^2 m}{\partial x^2} + \left((-1)\alpha_m D_{m0}(1+\alpha M)^{-2}\right)\frac{\partial m}{\partial x}\frac{\partial M}{\partial x} - k_{\delta m}[m]$	$\frac{\partial M}{\partial t} = D_{M0}(1+\alpha_M m)\frac{\partial^2 M}{\partial x^2} + (\alpha_M D_{M0})\frac{\partial m}{\partial x}\frac{\partial M}{\partial x} - k_{\delta M}(\gamma_M^R+\beta_M^R m)[M]$
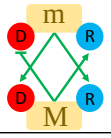	$\frac{\partial m}{\partial t} = D_{m0}(1+\alpha_m M)^{-1}\frac{\partial^2 m}{\partial x^2} + \left((-1)\alpha_m D_{m0}(1+\alpha M)^{-2}\right)\frac{\partial m}{\partial x}\frac{\partial M}{\partial x} - k_{\delta m}(\gamma_m^R+\beta_m M)[m]$	$\frac{\partial M}{\partial t} = D_{M0}(1+\alpha_M m)\frac{\partial^2 M}{\partial x^2} + (\alpha_M D_{M0})\frac{\partial m}{\partial x}\frac{\partial M}{\partial x} - k_{\delta M}(\gamma_M^R+\beta_M^R m)[M]$
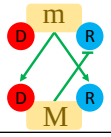	$\frac{\partial m}{\partial t} = D_{m0}\frac{\partial^2 m}{\partial x^2} + 0 - k_{\delta m}(\gamma_m^R+\beta_m M)^{-1}[m]$	$\frac{\partial M}{\partial t} = D_{M0}(1+\alpha_M m)\frac{\partial^2 M}{\partial x^2} + (\alpha_M D_{M0})\frac{\partial m}{\partial x}\frac{\partial M}{\partial x} - k_{\delta M}(\gamma_M^R+\beta_M^R m)[M]$
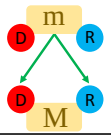	$\frac{\partial m}{\partial t} = D_{m0}\frac{\partial^2 m}{\partial x^2} + 0 - k_{\delta m}[m]$	$\frac{\partial M}{\partial t} = D_{M0}(1+\alpha_M m)\frac{\partial^2 M}{\partial x^2} + (\alpha_M D_{M0})\frac{\partial m}{\partial x}\frac{\partial M}{\partial x} - k_{\delta M}(\gamma_M^R+\beta_M^R m)[M]$
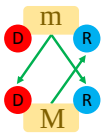	$\frac{\partial m}{\partial t} = D_{m0}\frac{\partial^2 m}{\partial x^2} + 0 - k_{\delta m}(\gamma_m^R+\beta_m M)[m]$	$\frac{\partial M}{\partial t} = D_{M0}(1+\alpha_M m)\frac{\partial^2 M}{\partial x^2} + (\alpha_M D_{M0})\frac{\partial m}{\partial x}\frac{\partial M}{\partial x} - k_{\delta M}(\gamma_M^R+\beta_M^R m)[M]$
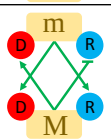	$\frac{\partial m}{\partial t} = D_{m0}(1+\alpha_m M)\frac{\partial^2 m}{\partial x^2} + (\alpha_m D_{m0})\frac{\partial m}{\partial x}\frac{\partial M}{\partial x} - k_{\delta m}(\gamma_m^R+\beta_m M)^{-1}[m]$	$\frac{\partial M}{\partial t} = D_{M0}(1+\alpha_M m)\frac{\partial^2 M}{\partial x^2} + (\alpha_M D_{M0})\frac{\partial m}{\partial x}\frac{\partial M}{\partial x} - k_{\delta M}(\gamma_M^R+\beta_M^R m)[M]$
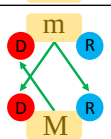	$\frac{\partial m}{\partial t} = D_{m0}(1+\alpha_m M)\frac{\partial^2 m}{\partial x^2} + (\alpha_m D_{m0})\frac{\partial m}{\partial x}\frac{\partial M}{\partial x} - k_{\delta m}[m]$	$\frac{\partial M}{\partial t} = D_{M0}(1+\alpha_M m)\frac{\partial^2 M}{\partial x^2} + (\alpha_M D_{M0})\frac{\partial m}{\partial x}\frac{\partial M}{\partial x} - k_{\delta M}(\gamma_M^R+\beta_M^R m)[M]$
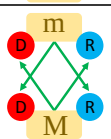	$\frac{\partial m}{\partial t} = D_{m0}(1+\alpha_m M)\frac{\partial^2 m}{\partial x^2} + (\alpha_m D_{m0})\frac{\partial m}{\partial x}\frac{\partial M}{\partial x} - k_{\delta m}(\gamma_m^R+\beta_m M)[m]$	$\frac{\partial M}{\partial t} = D_{M0}(1+\alpha_M m)\frac{\partial^2 M}{\partial x^2} + (\alpha_M D_{M0})\frac{\partial m}{\partial x}\frac{\partial M}{\partial x} - k_{\delta M}(\gamma_M^R+\beta_M^R m)[M]$

D. EVALUATION OF NUMERICAL APPROACHES: CONSERVATION OF MASS AND CONVERGENCE STATISTICS OF CVODE IMPLMENTATION OF THE TCS MODEL

D.1 Conservation of Mass

To find a numerical approximation approach that is able to generate trustworthy data for TCS, we compare the performances of both divergence (i.e., DV) and non-divergence (EC), considering an example of mass-conservation. We investigate whether the conservation of mass rule is satisfied by our adopted discretization process, and to do so, we took a simplistic model of morphogen and modulator transport. In this example, we consider two diffusive particles, m and M, with reflected boundary conditions [125, 193] for each at the left ($X = 0$) and right ($X = L$) boundaries. Here, the diffusivity of species m at any location is directly dependent on species M at that location, and vice-versa. In fact, this model is a simplified version of the TCS model we propose. The model equations are as follows:

D.1.1 Model 1: Source of morphogen and modulator at x = 0

$$Morphogen : \frac{\partial m}{\partial t} = \frac{\partial}{\partial x}\left(D_m(M)\frac{\partial m}{\partial x}\right) \tag{D.1}$$

$$B.C : -D_m(M)\frac{\partial m}{\partial x}\bigg|_{x=0} = 0, \frac{\partial m}{\partial x}\bigg|_{x=L} = 0 \tag{D.2}$$

$$I.C : m(t = 0, x) = e^{-\theta x} \tag{D.3}$$

$$Modulator : \frac{\partial M}{\partial t} = \frac{\partial}{\partial x}\left(D_M(m)\frac{\partial M}{\partial x}\right) \tag{D.4}$$

$$B.C : -D_M(m)\frac{\partial M}{\partial x}\bigg|_{x=0} = 0, \frac{\partial M}{\partial x}\bigg|_{x=L} = 0 \tag{D.5}$$

$$I.C : M(t=0,x) = e^{-\theta x} \tag{D.6}$$

As the transport properties are spatially dependent on the modulator concentration at any given point, the equation for moodulation of transport properties is considered as:

$$D_m(M) = D_{m0}(1+\alpha M)^{\nu} \tag{D.7}$$

The system is non-dimensionalized by defining $\xi = \frac{x}{L}$, where L is the system length. Both the I.C and B.C are non-dimenstionalized as well. For example, initial condition $m(t=0,x) = e^{-\theta x}$ is non-dimensionalized as $m(t=0,\xi) = e^{-\theta\frac{x}{L}}$

We consider two approaches to implement the above system– i) chain-rule of derivative is applied to expand Eq.D.8 and Eq.D.9, ii) Divergence form (chain-rule of the derivative is not applied). These two approaches are compared with data obtained through COMSOL implementation in order differentiate any possible differences in the performances of the two aforesaid approaches.

D.1.2 Steady-state analysis

For the steady state analysis, the term $\frac{\partial m}{\partial t}$ is set to zero and the model becomes:

$$\begin{aligned} &Morphogen : 0 = \frac{\partial}{\partial x}\left(D_m(M)\frac{\partial m}{\partial x}\right) \\ &B.C : -D_m(M)\frac{\partial m}{\partial x}\bigg|_{x=0} = 0, \frac{\partial m}{\partial x}\bigg|_{x=L} = 0 \\ &I.C : m(t=0,x) = e^{-\theta x} \end{aligned} \tag{D.8}$$

$$\begin{aligned} &Modulator : 0 = \frac{\partial}{\partial x}\left(D_M(m)\frac{\partial M}{\partial x}\right) \\ &B.C : -D_M(m)\frac{\partial M}{\partial x}\bigg|_{x=0} = 0, \frac{\partial M}{\partial x}\bigg|_{x=L} = 0 \\ &I.C : M(t=0,x) = e^{-\theta x} \end{aligned} \tag{D.9}$$

By integrating once and then using the boundary condition we obtain:

$$\frac{\partial}{\partial x}\left(D_m(M)\frac{\partial m}{\partial x}\right) = 0 \tag{D.10}$$

$$\Rightarrow \left(D_m(M)\frac{\partial m}{\partial x}\right) = 0 \tag{D.11}$$

$$\Rightarrow \frac{\partial m}{\partial x} = 0 \tag{D.12}$$

$$\Rightarrow m = constant \tag{D.13}$$

The steady-state distribution of morphogen or modulatior is constant, which means an uniform level of morphogen throughout the space. We also consider an approximate time-scale calculation for the steady state analysis. The time-scale is $\frac{L^2}{D_m(M)}$, where L is the system length and $D_m(M) = D_{m0}(1+\alpha_m M)^{\nu_m^D}$. For example, if the intrinsic diffusion coefficient is $D_{m0} = 0.01\mu m^2 s^{-1}$, system length($L = 300\mu m$) without modulation the time-scale of the dynamics is about 2500 hrs. So, to test the conservation of mass maximum time to reach steady-state should be significantly large.

To show how similar the steady-state distribution as obtained from different numerical approaches, we compare the morphogen and modulator distribution with analytical results and COMSOL Multiphysics data. Also, mass conservation for each species is verified by calculating the area under the initial and steady-state concentration profile.

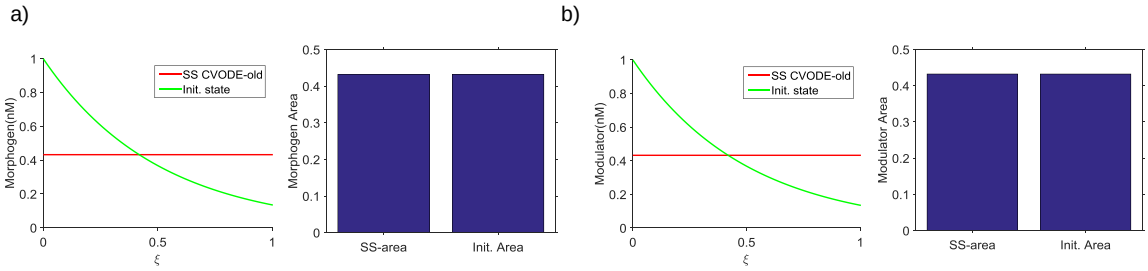

Fig. D.1. EC data for the first-order positive regulation of diffusion coefficient : Intrinsic diffusion coefficients are $D_{m0} = 1\mu m^2 s^{-1}$ and $D_{M0} = 0.1\mu m^2 s^{-1}$ for morphogen and modulator respectively. In graph a) and b), Line plots are for the concentration distribution, where the red line is for the exact initial profile supplied to the system. As seen from the graphs, both the different approaches (EC and DIV) generate similar outcomes that do not deviate from the initial area. This implies that the discretization of the domain satisfy the conservation of mass criteria. Analytical solution as devised earlier showed that the steady state profile should be constant, which is reproduced by simulation as well. Second order regulation also achieves a steady state data that is uniform over the spatial domain, however, the data is not shown here. We also tried equal intrinsic diffusion coefficient ($D_{m0} = D_{M0} = 1\mu m^2 s^{-1}$) to see if the steady-state is qualitatively similar to the analytically obtained traits, and the mass of the system is conserved.

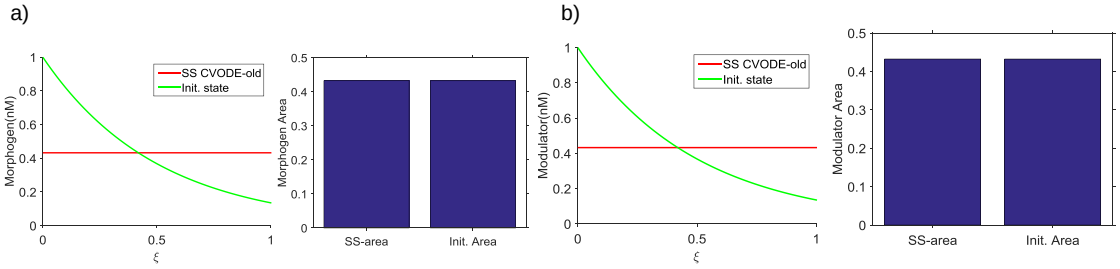

Fig. D.2. EC data for the first-order negative regulation of diffusion coefficient : Intrinsic diffusion coefficients are $D_{m0} = 1\mu m^2 s^{-1}$ and $D_{M0} = 0.1\mu m^2 s^{-1}$ for morphogen and modulator respectively. Same as Fig.1, but shown here for negative regulation. As seen from the area comparison between initial and steady-state profile, modulator distribution also satisfies the mass-conservation.

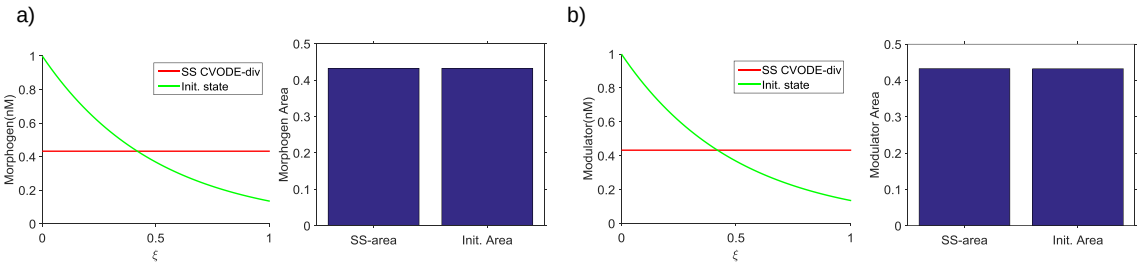

Fig. D.3. DIV data for the first-order positive regulation of diffusion coefficient: Intrinsic diffusion coefficients are $D_{m0} = 1\mu m^2 s^{-1}$ and $D_{M0} = 0.1\mu m^2 s^{-1}$ for morphogen and modulator respectively.

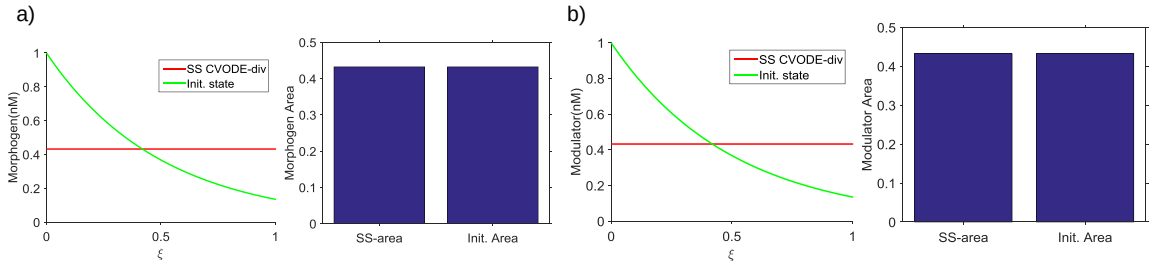

Fig. D.4. DIV data for the first-order negative regulation of diffusion coefficient: Intrinsic diffusion coefficients are $D_{m0} = 1\mu m^2 s^{-1}$ and $D_{M0} = 0.1\mu m^2 s^{-1}$ for morphogen and modulator respectively.

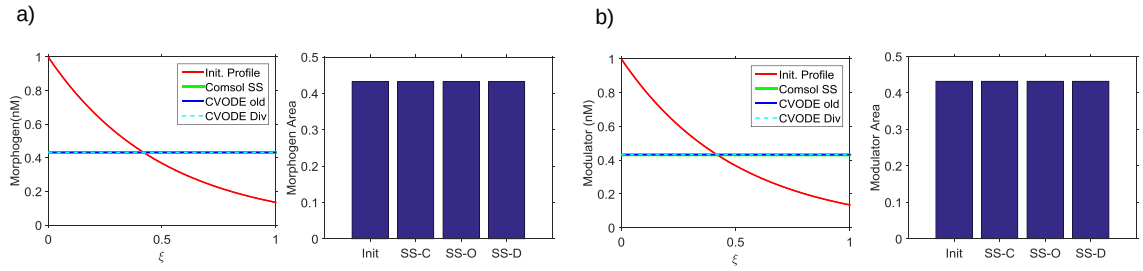

Fig. D.5. Comparison of CVODE data with COMSOL: Intrinsic diffusion coefficients are $D_{m0} = 1\mu m^2 s^{-1}$ and $D_{M0} = 0.1\mu m^2 s^{-1}$ for morphogen and modulator respectively. Steady-state profile of concentration obtained by three approaches are compared. Here, the COMSOL data is treated as the reference to compare the performance of EC and DIV approaches. a) Comparison for morphogen data, b) Comparison for modulator data. The bar plots show the area under the concentration curve as demonstrated by the different approaches. As we see, EC and DIV both match with COMSOL data perfectly.

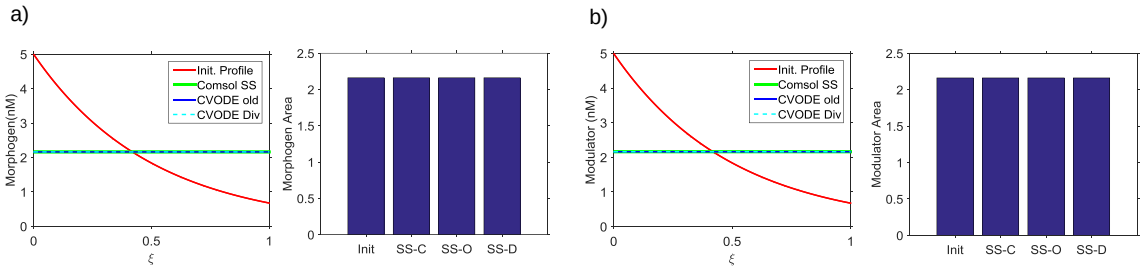

Fig. D.6. Comparison of CVODE data with COMSOL: Initial profile of morphogen and modulator is changed from $m(t=0,\xi) = M(t=0,\xi) = e^{-600\frac{\xi}{L}}$ to $m(t=0,\xi) = M(t=0,\xi) = 5e^{-600\frac{\xi}{L}}$. Intrinsic diffusion coefficients are $D_{m0} = 1\mu m^2 s^{-1}$ and $D_{M0} = 0.1\mu m^2 s^{-1}$ for morphogen and modulator respectively. Steady-state distribution is 5 times the steady-state data obtained for previous initial condition. Qualitative behavior of this simulation is similar to Fig. D.6.

D.2 Different initial profile: $m(t=0,\xi) = M(t=0,\xi) = 5e^{-600\frac{\xi}{L}}$

In all these simulations, initial profile is $m(t=0,\xi) = M(t=0,\xi) = e^{-600\frac{\xi}{L}}$, which is changed by a factor of 5 in subsequent simulation. Because the initial profile remains qualitatively same, the area of the distribution will be 5 times the previous area. So, if the steady state uniform distribution is 0.4343, in the new simulation the uniform distribution will be at $5*0.4343$. We would like to see if all the approaches can attain the steady-state uniform distribution with amplitude equivalent to $5 * 0.4343$.

It is clear from Fig.D.6 that for the new initial condition, the EC and DIV implementation demonstrate conservation of mass. Also, the steady state profile in both implementations match with analytically obtained distribution of morphogen and modulator. In all these simulations, spatial domain was discretized into 301 mesh points.

Table D.1
For an initial parameter space, simulation time and failures for both EC and DIV implementation of TCS

Regulation	Grid Pts	Time		SIV Failures				RBST Failures			
				L_1		L_2		ϕ_1		ϕ_2	
		EC	D	EC	D	EC	D	EC	D	EC	D
POS	2000	20m	28m	0	0	0	0	0	0	0	0
NO	2000	25.2m	29.3m	0	0	0	0	0	0	0	0
NEG	2000	25.5m	26m	0	0	0	1	0	0	0	9

D.2.1 Accuracy: DIV vs. EC approach

In order to compare EC and DIV approaches of TCS implementation, we consider a system length $L = 600\mu m$, and choose negative regulation of biophysical properties. Outcomes reveal that when morphogen and modulator are mostly confined near the source of their production, DIV implementation of TCS approximates the reference concentration (COMSOL Multiphysics data is treated as) near the origin more accurately (comparison between green line and cyan circles) than it does by the EC form of implementation. However, if the species concentration is distributed over the spatial domain both approaches perform well when compared against the COMSOL Multiphysics data.

D.3 Comparison of simulation statistics:expanded chain-rule vs. divergence form of TCS implementation

For an initial comparison (as shown in Table D.1) we consider 2000 grid points for each of the regulation type– i) Positive regulation of diffusion and reaction, ii) No regulation of reaction and diffusion, iii) Negative regulation of reaction and diffusion. While all regulatory parameters associated with reaction and difussion are kept

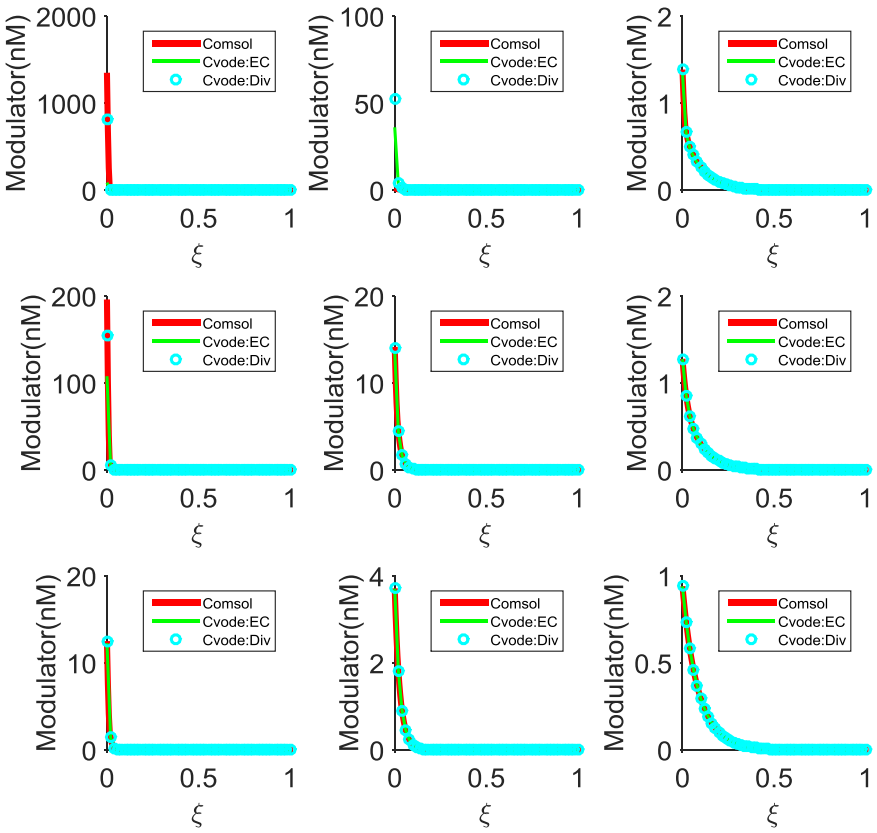

Fig. D.7. Comparison of modulator concentration for negative regulation: The two CVODE approaches (EC and DIV) are compared for a system length $L = 600$, and the COMSOL data is treated as the reference to perform the comparison. When D_{m0} and D_{M0} are low, distribution of the modulator concentration is primarily concentrated near the source, and CVODE implementations fail to match the concentration obtained through COMSOL perfectly at the source. When compared between DIV and EC, it's found that DIV performs better than EC version near the source of modulator. In this concentration comparison, data represented in red are obtained from COMSOL Multiphysics implementation of TCS, and this set of data is treated as the standard to compare EC and DIV.

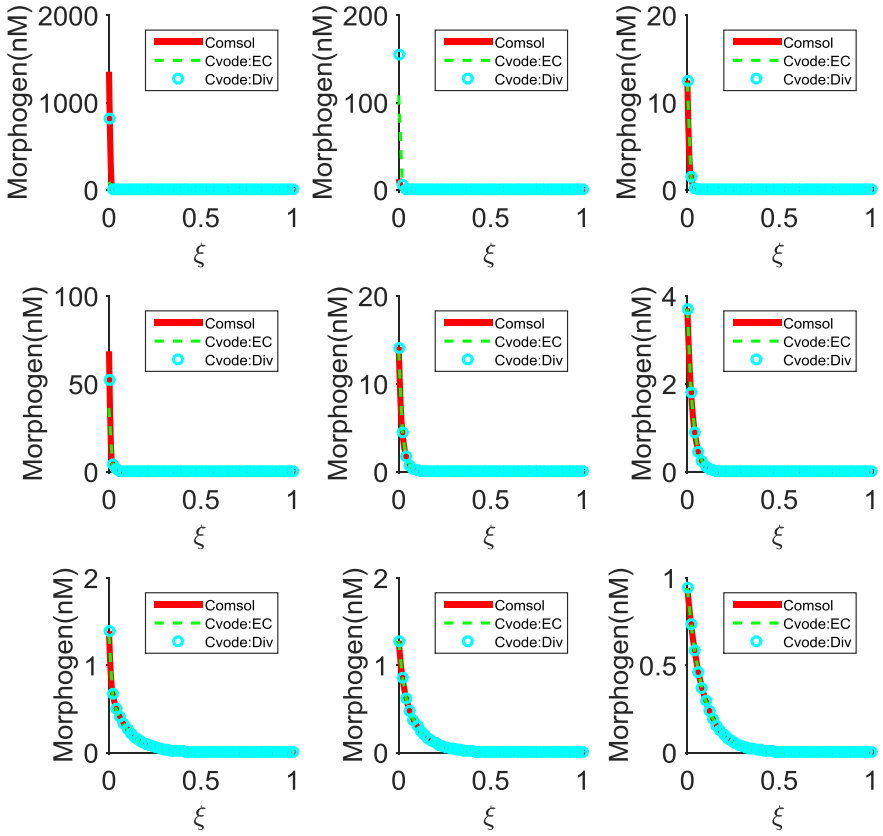

Fig. D.8. Comparison of morphogen for Negative Regulation, L = 600: Similar to previous Fig. D.7, but morphogen data is compared in this plot.

Table D.2
For alternative parameter space: simulation time taken by EC and DIV, and the statistics of simulation failures for mesh size 501

Regulation	Grid Pts	Time		SIV Failures				RBST Failures			
				L_1		L_2		ϕ_1		ϕ_2	
		EC	D	EC	D	EC	D	EC	D	EC	D
POS	1000	78m	82m12s	6	6	0	0	6	6	53	48
NEG	1000	7m43s	7m21s	0	0	0	0	0	0	0	0
NO	1000	4m49s	6m3s	0	0	0	0	0	0	0	0

Table D.3
For alternative parameter space: simulation time taken by EC and DIV, and the statistics of simulation failures for mesh size 301

Regulation	Grid Pts	Time		SIV Failures				RBST Failures			
				L_1		L_2		ϕ_1		ϕ_2	
		EC	D	EC	D	EC	D	EC	D	EC	D
POS	1000	22m47s	26m27s	0	4	0	0	0	4	2	5
NEG	1000	4m14s	3m54s	0	0	13 (NaN)	0	0	0	0	0
NO	1000	2m48s	3m10s	0	0	0	0	0	0	0	0

unchanged, other parameters are varied to obtain the grid points. Both expanded chain-rule and divergence form are used to simulate the system for two performance objectives namely, scale-invariance (SIV) and robustness (RBST).

In another comparison between EC and DIV approaches for a different parameter space, we consider 1000 grid points for each of the regulation type i) Positive regulation of diffusion coefficient and reaction rate, ii) No regulation, iii) Negative regulation of diffusion coefficient and reaction rate. While all regulatory parameters associated with reaction and diffusion are kept unchanged, other parameters are varied to obtain the new grid points. Both expanded chain-rule (EC) and divergence (DIV) forms are used to simulate the system for two performance objectives, namely, scale-invariance (SIV) and robustness (RBST). The simulation statistics, for two different mesh size (301 and 501), are shown in Table. D.3 and Table D.2 respectively.

Comparison of accuracy and simulation time of different approaches (EC and DIV) reveal that they perform almost similarly when accuracy is compared. It is shown by comparing both absolute error and root mean square error against different mesh size that the DIV and EC forms of implementation of TCS demonstrate similar trend. However, the approaches differ in simulation time and simulation failures. For example, EC performs better when all the regulations are positive, whereas DIV works better for negative regulations (mesh 301 case). The EC form of implementation experiences more simulation failures for mesh size 301. Hence, we intend to reduce the mesh size from 501 to a lower value without compromising the accuracy. As found after a number of trials, DIV generates fewer failures than EC. Furthermore, if the two approaches are compared against the time taken to simulate about 1000 grid points it is seen that EC requires less time than DIV (Table D.2 and Table D.3). Because DIV tends to generate fewer failures, and we would prefer to obtain more instances of successful data, DIV is chosen to generate data for the analysis of different versions of TCS.

VITA

VITA

Md. Shahriar Karim was born in Bera, Pabna. He did his elementary education from Santhia Primary School and Santhia High School, Santhia, Pabna. Shahriar completed his 12th grade education from Notre Dame College, Dhaka, Bangladesh. Later, he received his bachelor of technology in Electronics Engineering from Motilal Nehru National Institute of Technology, Allahabad, India in 2005. From 2005 through 2008, he worked in Ericsson Bangladesh Ltd., and Motorola Inc., Bangladesh as a system engineer. Shahriar returned to graduate school in 2009, and pursued a master of science in biological engineering from the department of agricultural and biological engineering at Purdue University with Professor David M. Umulis towards identifying the mechanisms of noise suppression in morphogen signaling.

In 2012, Shahriar started pursuing his doctoral degree in the computational biology lab of Professor David M. Umulis. Shahriar is also a part of the computational life science (CLS) program at Purdue University. His research focus is to identify mechanisms that contribute to achieve precise and robust pattern formation during different stages of species development. During his graduate research, Shahriar has published two journal papers, two conference papers, and a few of his journals papers are currently under preparation. Shahriar presented his work at various conferences and workshops as both oral and poster presentations.